

N° d'ordre : 42279



THESE DE DOCTORAT

Présentée à

L'UNIVERSITE DE LILLE 1- SCIENCES ET TECHNOLOGIES

Ecole Doctorale Régionale Sciences Pour l'Ingénieur Lille Nord-de-France

pour obtenir le grade de

DOCTEUR EN SCIENCES

Spécialité Micro et Nano Technologies, Acoustique et Télécommunications

par

**Sijia GU**

Title

**CONTRIBUTION TO BROADBAND  
LOCAL CHARACTERIZATION OF MATERIALS BY  
NEAR-FIELD MICROWAVE MICROSCOPY**

Soutenue le 12 Décembre 2016

Laurent CHUSSEAU	DR CNRS Université de Montpellier	Rapporteur
Florence PODEVIN	MCF HDR Grenoble INP	Rapporteur
Antoine DIET	MCF CentraleSupélec	Examinateur
David GLAY	MCF Université de Lille 1	Examinateur
Henri HAPPY	Professeur Université de Lille 1	Examinateur
Tuami LASRI	Professeur Université de Lille 1	Directeur de thèse



## **Acknowledgements**

First, I would like to thank Mr Lionel BUCHAILLOT, Director at Institut d'Electronique de Microelectronique et de Nanotechnologie (IEMN) for having welcomed me into the laboratory.

I gratefully acknowledge the funding received towards my PhD from Lille 1 University and Région Nord Pas-de-Calais.

I would like to express my special appreciation and thanks to my advisor, Mr Tuami LASRI, Professor at University of Lille 1 and director of the SPI doctoral school at Lille 1, for providing me this PhD opportunity. I am grateful for his patience, motivation, and immense knowledge. His guidance helped me in every step of my PhD work. He has been very present during my research time, every preparation of papers and conferences and writing of this thesis. I will remember our discussions for a long time.

Besides my advisor, I would like to thank my thesis committee, Mrs Florence PODEVIN, Maitre de conférences at Grenoble INP, and Mr Laurent CHUSSEAU, CNRS Directeur de recherche at Université de Montpellier, for their insightful comments and suggestions. My thanks also goes to Mr. Henri HAPPY, Professor at University of Lille 1, Mr. David GLAY, Maitre de conférences at University of Lille 1, and Antoine DIET, Maitre de conférences at CentraleSupélec for having accepted to examine my work.

I would like to thank all the MITEC team for giving me the benefit of their relevant remarks and their knowledge. Especially, I would like to express my thanks to Mr. Kamel HADDADI, Maitre de conférences at University of Lille 1 for his help, advice in the beginning stage.

I would also like to express my gratitude my colleagues, Xin, Tianjun, Ghizlane, Nadine, Hind, Amine, Soufiane, Abdallah, Abdel and Zahir, for the help they have given me and for their sympathy and friendship. It is a very nice experience to work

with them. Especially, I would like to thank Dr. Xin Zhou for her help and guidance for my thesis project. We have many interesting discussions in calculations and measurements. Also, a special thanks to my colleague, Mr Tianjun Lin, we have worked together for more than two years and I have learned many things from him.

I do not forget my friends, Zhu Tianqi, Hao Jianping, Ding Xiaokun, Wei wei, Zhou Di, Zhang Tianchen, Li Shuo, Chen Shiqi, Xu Tao, Li sizhe, Yan Xin, Qi Haoling, Jiang Zhifang and et al. Unfortunately I cannot thank them all individually here, but be assured of my gratitude for all the good times spent together.

I would like express appreciation to my Jiaying who has always believed in me and incented me to strive towards my goal.

Finally, my deepest thanks to my parents, words cannot express how grateful I am for their support and encouragement.

## *Outline*

<b>General introduction .....</b>	<b>1</b>
<b>Chapter I Overview of near-field microwave microscopy .....</b>	<b>5</b>
I.1 Introduction to near-field microwave microscopy.....	5
I.2 Near-field microwave microscopy platforms and applications .....	8
I.2.1 Introduction .....	8
I.2.2 Near-field microwave microscope platforms .....	8
I.2.2.1 Coaxial probe-based platform .....	9
I.2.2.2 Waveguide-based platform .....	9
I.2.2.3 Microstrip line-based platform.....	10
I.2.2.4 Magnetic-probe-based platform .....	12
I.2.2.5 AFM-based platform .....	13
I.2.2.6 STM tip-based platform .....	14
I.2.3 Applications of near-field microwave microscope .....	15
I.2.3.1 Solid dielectric materials characterization .....	16
I.2.3.2 Semiconductor samples testing .....	16
I.2.3.3 Chemical and biological samples characterization .....	17
I.2.3.4 Graphene characterization.....	17
I.2.3.5 Subsurface imaging .....	18
I.2.4 Conclusion.....	18
I.3 Quantification methodology of near-field microwave microscopy .....	20
I.3.1 Introduction .....	20
I.3.2 Modeling of tip-sample interaction .....	20
I.3.3 Capacitance modeling of tip-sample interaction .....	23
I.3.3.1 Image method .....	24
I.3.3.2 Surface integration method .....	25
I.3.4 Calibration methods .....	27
I.3.4.1 Cavity perturbation method.....	28

I.3.4.2 Transmission line method .....	29
I.3.5 Conclusion.....	30
I.4 Conclusion .....	31
I.5 References.....	33
<b>Chapter II Interferometer-based near-field microwave microscope (iNFMM) ..</b>	<b>39</b>
II.1 Introduction .....	39
II.2 Description of the interferometer-based microwave microscope.....	42
II.2.1 Introduction.....	42
II.2.2 Mismatch issue between the EMP and the VNA.....	42
II.2.3 Configuration of the interferometer-based NFMM .....	44
II.2.4 Electromagnetic simulations of the microwave microscope .....	46
II.2.4.1 Simulation of the EMP by Ansys <sup>TM</sup> /HFSS .....	46
II.2.4.2 Simulation of the iNFMM by Keysight <sup>TM</sup> /ADS .....	49
II.2.5 Conclusion .....	51
II.3 Characterization of the microwave microscope .....	52
II.3.1 Introduction.....	52
II.3.2 Characterization of the interferometer .....	52
II.3.2.1 Characterization of the hybrid coupler .....	52
II.3.2.2 Characterization of the attenuator .....	55
II.3.2.3 Characterization of the delay line .....	57
II.3.2.4 Characterization of the evanescent microwave probe .....	60
II.3.3 Performance of the interferometric technique .....	61
II.3.3.1 Validation of the wave-cancelling process .....	61
II.3.3.2 Evaluation of the measurement sensitivity .....	65
II.3.4 Conclusion .....	66
II.4 Setting parameters influence on the repeatability of the iNFMM.....	67
II.4.1 Introduction.....	67
II.4.2 Interferometer-based near-field microwave microscope setup.....	68
II.4.3 Setting parameters impact on repeatability tests.....	68
II.4.3.1 VNA intermediate frequency bandwidth (IFBW) .....	69
II.4.3.2 Zero level of the transmission coefficient.....	72
II.4.4 Scanning repeatability study .....	76

II.4.4.1 Extraction of scanning errors in 1D scanning.....	76
II.4.4.2 2D nondestructive microwave imaging .....	77
II.4.5 Conclusion .....	81
II.5 Conclusion .....	82
II.6 References .....	84
<b>Chapter III Materials characterization by iNFMM.....</b>	<b>88</b>
III.1 Introduction .....	88
III.2 Study of 1D and 2D spatial resolutions study of the iNFMM .....	90
III.2.1 Introduction .....	90
III.2.2 Test conditions for the scanning process .....	91
III.2.3 Influence of the scanning parameters on the 1D scanning resolution.....	92
III.2.4 2D imaging sensitivity of iNFMM .....	99
III.2.5 Influence of the scanning parameters on the 2D imaging resolution .....	101
III.2.6 Resolution enhancement by position/signal difference method .....	107
III.2.7 Conclusion .....	110
III.3 Broadband microwave characterization of liquids by iNFMM .....	112
III.3.1 Introduction .....	112
III.3.2 Permittivity study of saline solutions .....	113
III.3.3 Simulation of the probe-liquid interaction.....	116
III.3.4 EMP position control in liquid .....	119
III.3.5 Evaluation of the measurement sensitivity .....	120
III.3.6 Experimental retrieval of the complex permittivity .....	124
III.3.6.1 Permittivity extraction by transmission line method.....	125
III.3.6.2 Permittivity extraction by cavity perturbation method.....	127
III.3.7 Conclusion .....	134
III.4 Broadband non-contact characterization of graphene by iNFMM.....	136
III.4.1 Introduction .....	136
III.4.2 Electromagnetic simulation of the probe-sample interaction .....	137
III.4.3 Calibration procedure of iNFMM.....	141
III.4.3.1 Modeling of the probe-sample interaction.....	141
III.4.3.2 iNFMM calibration procedure.....	142

III.4.4 Results and discussions .....	144
III.4.4.1 Evaluation of the measurement sensitivity .....	144
III.4.4.2 Extraction of the materials under test impedance.....	146
III.4.5 Conclusion .....	149
III.5 Conclusion.....	150
III.6 References .....	152
<b>General conclusion and perspectives .....</b>	<b>158</b>
<b>List of publications.....</b>	<b>163</b>

## *List of figures*

<b>Fig. I-1:</b> Schematic of the coaxial line-based microwave microscope [CHI 12] .....	9
<b>Fig. I-2:</b> Schematic of the platform with a waveguide-fed thin slit microwave probe [GOL 00] .....	10
<b>Fig. I-3:</b> Microstrip line resonator with tapered tip [TAB 99b], [TAB 99c].....	11
<b>Fig. I-4:</b> Schematic of the experimental setup [TAB 99b], [TAB 99c] .....	12
<b>Fig. I-5:</b> Schematic of the magnetic microwave probe [WAN 07].....	13
<b>Fig. I-6:</b> Schematic of the AFM-based set up [GRA 14].....	14
<b>Fig. I-7:</b> Schematic of the STM based-NFMM [FAR 11a] [FAR 12b] .....	15
<b>Fig. I-8:</b> Lumped element model of tip-sample interaction (a) and equivalent circuit (b).....	21
<b>Fig. I-9:</b> Iterative image charges in tip–bulk sample system [GAO 98] [GAO 99].....	24
<b>Fig. I-10:</b> Tip-infinite flat metallic surface system [HUD 98] .....	26
<b>Fig. I-11:</b> Calculation of $C_c$ by two methods: image method (Gao’s model in round symbols [GAO 98]) and surface integration method (Hudlet’s model in solid lines [HUD 98]); three tip radius are considered: $1\mu\text{m}$ , $10\mu\text{m}$ and $100\mu\text{m}$ .....	27
<b>Fig. II-1:</b> Reflection coefficient $\Gamma$ as a function of a pure resistive impedance measured by means of a $50\ \Omega$ VNA .....	43
<b>Fig. II-2:</b> Schematic of the interferometer-based microwave microscope.....	44
<b>Fig. II-3:</b> Wave cancellation process by combining $\Gamma_{\text{EMP}}$ and $\Gamma_{\text{TUN}}$ .....	45
<b>Fig. II-4:</b> Impedance tuner included in the iNFMM .....	45
<b>Fig. II-5:</b> Simulation of the electric field magnitude for different EMP in free space by using Ansys <sup>TM</sup> /HFSS; (a): EMP with planar end ( $D = 260\ \mu\text{m}$ ), (b): EMP with rounded end ( $D = 260\ \mu\text{m}$ ), (c): EMP with rounded end ( $D = 66\ \mu\text{m}$ ), these images are taken at the cross-section along the probe, $f = 2\ \text{GHz}$ .....	47
<b>Fig. II-6:</b> Variation of E-field with the distance to the tip (Ansys <sup>TM</sup> /HFSS); (a) distance from 0 to $500\ \mu\text{m}$ , (b) distance range zoomed from 0 to $200\ \mu\text{m}$ , $f = 2\ \text{GHz}$ .....	47
<b>Fig. II-7:</b> Variation of electric ( $O$ ) and magnetic ( $\diamond$ ) fields as a function of the distance to the tip (Ansys <sup>TM</sup> /HFSS); (a): Probe with apex size $D = 66\ \mu\text{m}$ , (b): probe with apex size $D = 260\ \mu\text{m}$ , $f = 2\ \text{GHz}$ .....	48

<b>Fig. II-8:</b> Schematic of the different configurations simulated by Keysight <sup>TM</sup> /ADS, (a): without interferometer, (b): with interferometer .....	49
<b>Fig. II-9:</b> Simulation (Keysight <sup>TM</sup> /ADS) of the wave-cancelling process under two configurations: with and without the interferometer; (a): frequency range from 2 to 3 GHz, (b): frequency range from 2.459 to 2.464 GHz, $P_0 = 0$ dBm .....	50
<b>Fig. II-10:</b> Characteristics of the [2-10 GHz] hybrid coupler; (a): matching and isolation; (b): directivity and coupling parameters .....	53
<b>Fig. II-11:</b> Phase-shift between the direct and coupled paths of the hybrid coupler; dash lines represents $90^\circ$ and $-90^\circ$ .....	53
<b>Fig. II-12:</b> Characteristic of the [6-20 GHz] hybrid coupler; (a): matching and isolation; (b): directivity and coupling parameters .....	54
<b>Fig. II-13:</b> Phase-shift between the direct and coupled paths of the hybrid coupler; dash lines represents $90^\circ$ .....	55
<b>Fig. II-14:</b> Magnitude of the reflection coefficient $S_{11}$ of the attenuator; minimum and maximum attenuations are presented in blue and red lines, respectively .....	56
<b>Fig. II-15:</b> Magnitude (a) and phase-shift (b) of the transmission coefficient $S_{21}$ of the attenuator; minimum and maximum attenuations are presented in blue and red lines, respectively .....	57
<b>Fig. II-16:</b> Insertion loss and return loss of the delay line; (a): no delay (0 ps); (b): maximum delay (625 ps) .....	58
<b>Fig. II-17:</b> Phase-shift of corresponding delay time (5 ps, 10 ps and 50 ps); the theoretically calculated values and measured ones are presented in dotted symbols and solid lines, respectively .....	59
<b>Fig. II-18:</b> (a): EMP made of a tapered-ended metallic conductor and a SMA support, (b): magnitude of the reflection coefficient $S_{11}$ of the evanescent microwave probe (EMP), two probe apex sizes are considered: $66 \mu\text{m}$ and $260 \mu\text{m}$ .....	60
<b>Fig. II-19:</b> Measured (solid lines) and simulated (dotted lines) magnitude spectra in two cases: with (in black) and without (in red) interferometer; $P_0 = 0$ dBm, IFBW = 100Hz, EMP apex = $66 \mu\text{m}$ .....	62
<b>Fig. II-20:</b> (b): Measured (solid line) and simulated (dotted line) $ S_{21} $ spectra from 2.459 to 2.464 GHz; $P_0 = 0$ dBm, IFBW = 100Hz, EMP apex = $66 \mu\text{m}$ .....	63
<b>Fig. II-21:</b> Measured magnitude spectra of the transmission coefficient $S_{21}$ , (a): different $ S_{21} $ levels (-45 dB, -60 dB, -75 dB and -90 dB) obtained by tuning the attenuator, (b): resonance shift (around 0.8 MHz) achieved by adding a short time delay (1 ps) .....	64
<b>Fig. II-22:</b> Quality factors measured (in red) as a function of the frequency considering the zero level around -75 dB (in blue); (a): results by using the [2-10 GHz] coupler; (b): results by	

using the [6-20 GHz] coupler; the wave-cancelling process is done considering the probe in air.....	65
<b>Fig. II-23:</b> Interferometer-based near-field microwave microscope setup .....	68
<b>Fig. II-24:</b> Measured transmission coefficient $S_{21}$ as a function of the intermediate frequency bandwidth (IFBW), $P_0 = 0$ dBm (Keysight <sup>TM</sup> PNA-X 5242A) .....	70
<b>Fig. II-25:</b> Transmission coefficient magnitude (a) and phase-shift (b) versus time for 3 zero levels (around -30dB, -50 dB and -70 dB), $f = 2$ GHz, IFBW = 100 Hz, number of points = 600 .....	73
<b>Fig. II-26:</b> Standard deviation of the transmission coefficient as a function of acquisition time under three zero levels, $f = 2$ GHz, IFBW = 100 Hz, number of points = 600 .....	75
<b>Fig. II-27:</b> Repeatability tests of the motorized stage in x/y directions (a) and in z direction (b), the displacement is performed in a step of 1000 $\mu\text{m}$ .....	77
<b>Fig. II-28:</b> Image of the chip area ( $11 \times 8 \text{ mm}^2$ ) of a common chip card, (a): the chip region is metalized and the rest of the card is in plastic, (b): zoomed slot line width (optical image) and (c): 2D scanning path .....	78
<b>Fig. II-29:</b> 2D images on chip area ( $5.5 \times 8 \text{ mm}^2$ ) of a card with a step of 50 $\mu\text{m}$ , (a) and (b): magnitude images with the same test conditions, (c): subtraction between (a) and (b), (d) and (e): phase-shift images with the same test conditions, (f): subtraction between (d) and (e); tip-sample separation=10 $\mu\text{m}$ , $f=2$ GHz, IFBW = 100 Hz, zero level = -50 dB.....	79
<b>Fig. II-30:</b> Averaged variation of transmission coefficient magnitude and phase-shift calculated every 50 $\mu\text{m}$ , (a) and (b): mean in x direction, (c) and (d): mean in y direction ....	80
<b>Fig. III-1:</b> Image of the chip area ( $11 \times 8 \text{ mm}^2$ ) of a common chip card, the chip region is metalized and the rest of the card is in plastic, the 1D scanning process is along the line XX' where the dielectric slot line width stands for 220.2 $\mu\text{m}$ .....	91
<b>Fig. III-2:</b> 1D scanning along the line XX' (1000 $\mu\text{m}$ ) as a function of probe distance H, (a) and (b): magnitude and phase-shift of $S_{21}$ for H varying from 1 to 260 $\mu\text{m}$ , (c) and (d): magnitude and phase-shift of $S_{21}$ for H varying from 1 to 50 $\mu\text{m}$ , $f = 2$ GHz, IFBW = 100 Hz, $P_0 = 0$ dBm, zero level = -50 dB, $S = 1 \mu\text{m}$ , $D = 260 \mu\text{m}$ .....	93
<b>Fig. III-3:</b> 1D scanning along the line XX' at a probe-sample distance $H = 10 \mu\text{m}$ , (a): magnitude of $S_{21}$ , (b): phase-shift of $S_{21}$ , $f = 2$ GHz, IFBW = 100 Hz, $P_0 = 0$ dBm, $S = 1 \mu\text{m}$ , $D = 260 \mu\text{m}$ , zero level = -50 dB.....	94
<b>Fig. III-4:</b> Measured width as a function of probe stand-off distance H, $f = 2$ GHz, IFBW = 100 Hz, $P_0 = 0$ dBm, zero level = -50 dB, $S = 1 \mu\text{m}$ , $D = 260 \mu\text{m}$ .....	95
<b>Fig. III-5:</b> Measured width as a function of scanning step size S, (a): step size varying from 1 to 200 $\mu\text{m}$ , (b): step size from 1 to 50 $\mu\text{m}$ , $f = 2$ GHz, IFBW = 100 Hz, $P_0 = 0$ dBm, zero level = -50 dB, $H = 10 \mu\text{m}$ , $D = 260 \mu\text{m}$ .....	96

- Fig. III-6:** Comparison of the width measured by two probes with different apices: 66 and 260  $\mu\text{m}$ ;  $f = 2 \text{ GHz}$ ,  $\text{IFBW} = 100 \text{ Hz}$ ,  $P_0 = 0 \text{ dBm}$ , zero level = -50 dB,  $S = 1 \mu\text{m}$ ..... 97
- Fig. III-7:** Comparison of the width measured by two probes with different apices: 66 and 260  $\mu\text{m}$ ,  $f = 2 \text{ GHz}$ ,  $\text{IFBW} = 100 \text{ Hz}$ ,  $P_0 = 0 \text{ dBm}$ , zero level = -50 dB,  $H = 10 \mu\text{m}$  ..... 98
- Fig. III-8:** Measured magnitude and phase-shift of the S parameters in two system configurations, (a) and (b): without interferometer ( $S_{11}$  measured), (c) and (d): with interferometer ( $S_{21}$  measured);  $f = 2 \text{ GHz}$ ,  $\text{IFBW} = 100 \text{ Hz}$ , zero level = -50 dB,  $P_0 = 0 \text{ dBm}$ ,  $H = 10 \mu\text{m}$ ,  $S = 50 \mu\text{m}$ ,  $D = 260 \mu\text{m}$  ..... 100
- Fig. III-9:** Measured magnitude of the transmission coefficient  $S_{21}$  for three zero levels, (a): -30 dB, (b): -50 dB and (c): -70 dB,  $f = 2 \text{ GHz}$ ,  $\text{IFBW} = 100\text{Hz}$ ,  $P_0 = 0 \text{ dBm}$ ,  $H = 10 \mu\text{m}$ ,  $S = 50 \mu\text{m}$ ,  $D = 260 \mu\text{m}$  ..... 101
- Fig. III-10:** Measured magnitude of the transmission coefficient  $S_{21}$  over the chip area for three stand-off distances, (a): 10  $\mu\text{m}$ , (b): 250  $\mu\text{m}$  and (c): 1000  $\mu\text{m}$ ;  $f = 2 \text{ GHz}$ ,  $\text{IFBW} = 100 \text{ Hz}$ ,  $P_0 = 0 \text{ dBm}$ , zero level = - 50 dB,  $S = 50 \mu\text{m}$ ,  $D = 260 \mu\text{m}$  ..... 103
- Fig. III-11:** Measured magnitude of the transmission coefficient  $S_{21}$  over the chip area as a function of different scanning step sizes; (a): 50  $\mu\text{m}$ , (b): 100  $\mu\text{m}$ , (c): 200  $\mu\text{m}$  and (d): 500  $\mu\text{m}$ ,  $f = 2 \text{ GHz}$ ,  $\text{IFBW} = 100\text{Hz}$ ,  $P_0 = 0 \text{ dBm}$ , zero level = -50 dB,  $H = 10 \mu\text{m}$ ,  $D = 260 \mu\text{m}$  ..... 104
- Fig. III-12:** Measured magnitude of the transmission coefficient over the chip area for two different probe apex sizes, (a): 260  $\mu\text{m}$  and (b): 66  $\mu\text{m}$ ,  $f = 2 \text{ GHz}$ ,  $\text{IFBW} = 100\text{Hz}$ ,  $P_0 = 0 \text{ dBm}$ , zero level = -50 dB,  $H = 10 \mu\text{m}$ ,  $S = 50 \mu\text{m}$  ..... 105
- Fig. III-13:** Measured magnitude of the transmission coefficient  $S_{21}$  over the chip area for two different step sizes; (a): 260  $\mu\text{m}$  and (b): 66  $\mu\text{m}$ ,  $f = 2 \text{ GHz}$ ,  $\text{IFBW} = 100\text{Hz}$ ,  $P_0 = 0 \text{ dBm}$ , zero level = -50 dB,  $H = 10 \mu\text{m}$ ,  $D = 66 \mu\text{m}$  ..... 106
- Fig. III-14:** Resolution enhancement as a result of signal differences acquired for different tip-sample heights, the images represent the magnitude of the signal ( $S_{21}$ ); (a): Magnitude plot for height  $H = 10 \mu\text{m}$ , (b): magnitude plot for height  $H = 50 \mu\text{m}$ , (c): complex difference of magnitude plots (a) and (b); (d), (e) and (f) represent the zoomed area ( $2.5 \times 1.5 \text{ mm}^2$ ) of magnitude plots (a), (b) and (c) respectively;  $f = 2 \text{ GHz}$ ,  $\text{IFBW} = 100\text{Hz}$ ,  $P_0 = 0 \text{ dBm}$ , zero level = -50 dB,  $D = 260 \mu\text{m}$ ,  $S_1 = 50 \mu\text{m}$  for (a), (b) and (c);  $S_2 = 10 \mu\text{m}$  for (d), (e) and (f) ..... 109
- Fig. III-15:** Complex permittivity of saline solutions based on Cole-Cole model at 25  $^\circ\text{C}$ , (a): frequency dependence of the complex permittivity for water,  $\tan\delta$  is given in the inset, (b): Cole-Cole plot for different saline concentrations (0, 9, 50 and 160 mg/ml)..... 114
- Fig. III-16:** Complex permittivity of saline aqueous solutions calculated by Cole-Cole model, (a): NaCl concentration range from 0 to 160 mg/ml, (b): NaCl concentration range from 0 to 9 mg/ml,  $T = 25 \text{ }^\circ\text{C}$ ,  $f = 2 \text{ GHz}$ ..... 115
- Fig. III-17:** Numerical simulation (ANSYS/HFSS<sup>TM</sup>) of the EMP (apex = 260  $\mu\text{m}$ ) electric field magnitude at three probe positions, (a): probe at 300  $\mu\text{m}$  over the liquid surface, (b): probe in contact with the liquid surface, (c): probe into the liquid at a depth of 300  $\mu\text{m}$ , the

images are taken at the cross section along the probe, liquid under test is DI water,  $T = 25\text{ }^{\circ}\text{C}$ ,  $f = 2\text{ GHz}$ ..... 117

**Fig. III-18:** Simulation (ANSYS/HFSS<sup>TM</sup>) of the microwave probe (apex = 260  $\mu\text{m}$ ) electric field magnitude for different saline concentration levels, (a): 0 mg/ml, (b): 9 mg/ml, (c): 80 mg/ml and (d): 160 mg/ml, (e): E-field as a function of the distance  $H$  from the tip, probe immersed in liquid at a depth of 300  $\mu\text{m}$ ,  $T = 25\text{ }^{\circ}\text{C}$ ,  $f = 2\text{ GHz}$ ..... 118

**Fig. III-19:** Transmission coefficient magnitude and phase-shift measured as a function of probe tip position, (a): from -300 to 300  $\mu\text{m}$ , (b): zoomed region from -10 to 10  $\mu\text{m}$ , liquid under test is DI water,  $T = 25\text{ }^{\circ}\text{C}$ ,  $f = 2\text{ GHz}$ , IFBW= 100 Hz,  $P_0 = 0\text{ dBm}$  ..... 120

**Fig. III-20:** Measured reflection coefficient  $S_{11}$  of different saline aqueous solutions from 0 mg/ml to 9 mg/ml, (a): magnitude plot, (b): phase-shift plot,  $f = 2\text{ GHz}$ ,  $P_0 = 0\text{ dBm}$ , IFBW = 100 Hz,  $T = 25\text{ }^{\circ}\text{C}$  ..... 121

**Fig. III-21:** Measured transmission coefficient  $S_{21}$  for different saline solutions from 0 to 9 mg/ml, (a): magnitude plot, (b): phase-shift plot, 0 mg/ml (DI water) represents reference value,  $f = 2\text{ GHz}$ ,  $P_0 = 0\text{ dBm}$ , IFBW = 100 Hz, zero level = -55 dB,  $T = 25\text{ }^{\circ}\text{C}$  ..... 122

**Fig. III-22:** Measured transmission coefficient for saline concentrations [0-160 mg/ml], zero level is tuned to -55 dB considering 0mg/ml (DI water) as a reference value,  $f = 2\text{ GHz}$ ,  $T = 25\text{ }^{\circ}\text{C}$ , IFBW= 100 Hz,  $P_0 = 0\text{ dBm}$  ..... 124

**Fig. III-23:** Frequency-dependent dielectric constant (a) and dielectric losses (b) for different saline concentrations from 0 to 160 mg/ml, Solid lines represent values based on the Cole-Cole model, Symbols are values retrieved by using the inversion procedure,  $T = 25\text{ }^{\circ}\text{C}$ , IFBW=100 Hz,  $P_0 = 0\text{ dBm}$ , zero level = -55 dB ..... 126

**Fig. III-24:** Resonance peak parameters obtained from the measured transmission coefficient  $|S_{21}|$  as a function of saline concentration, (a): resonance frequency shift  $\Delta f$ , (b): quality factor  $Q$ , 0 mg/ml = reference value,  $f_{\text{ref}} = 2\text{ GHz}$ ,  $P_0 = 0\text{ dBm}$ , IFBW = 100 Hz, zero level = -55 dB ..... 127

**Fig. III-25:** Resonance peak parameters obtained from the measured transmission coefficient  $|S_{21}|$  as a function of saline concentration, (a):  $\Delta f/f_{\text{ref}}$ , (b):  $\Delta(1/Q)$ , Dashed lines represent the fitted polynomial line at first order, 0 mg/ml is the reference value,  $f_{\text{ref}} = 2\text{ GHz}$ ,  $P_0 = 0\text{ dBm}$ , IFBW = 100 Hz, zero level = -55 dB ..... 128

**Fig. III-26:** Complex permittivity as a function of saline concentration, (a): dielectric constant  $\epsilon'$ , (b): dielectric loss  $\epsilon''$ , round symbols represent values based on the Cole-Cole model, square symbols represent measured values, 0 mg/ml is the reference value,  $f_{\text{ref}} = 2\text{ GHz}$ ,  $P_0 = 0\text{ dBm}$ , IFBW = 100 Hz, zero level = -55 dB..... 129

**Fig. III-27:** Complex permittivity as a function of saline concentration, (a): dielectric constant  $\epsilon'$ , (b): dielectric loss  $\epsilon''$ , round symbols represent values based on the Cole-Cole model, square symbols represent measured values, 0 mg/ml is the reference value,  $f_{\text{ref}} = 2\text{ GHz}$ ,  $P_0 = 0\text{ dBm}$ , IFBW = 100 Hz, zero level = -55 dB..... 130

- Fig. III-28:** Quality factor as a function of saline solutions considering different reference solutions: 0, 58, 100 and 160 mg/ml,  $f_{\text{ref}} = 2\text{GHz}$ ,  $P_0 = 0\text{ dBm}$ ,  $\text{IFBW} = 100\text{ Hz}$ , zero level = -55 dB ..... 131
- Fig. III-29:** Complex permittivity for 4 NaCl reference concentrations: 0, 58, 100 and 160 mg/ml, (a): dielectric constant  $\epsilon'$ , (b): dielectric loss  $\epsilon''$ , Solid lines represent values based on the Cole-Cole model, symbols represent measured values, zero level equals to -55 dB for the 4 reference concentrations,  $f_{\text{ref}} = 2\text{GHz}$ ,  $P_0 = 0\text{ dBm}$ ,  $\text{IFBW} = 100\text{ Hz}$ ..... 132
- Fig. III-30:** (a): Configuration of the samples tested: silicon carbide (SiC) substrate, epitaxial graphene on SiC substrate (SiCG,) metallized SiC substrate with gold layer on the top (MSiC) and SiCG structure with  $\text{Al}_2\text{O}_3$  layer on the top (SiCGAlO), (b): simulations of electric field at the cross-section along the probe, zoomed image of tip-sample (SiC) coupling and (c): electric field penetration in the samples (stand-off distance fixed at  $10\text{ }\mu\text{m}$ ),  $f = 2\text{ GHz}$ , simulation tool: Ansys<sup>TM</sup>/HFSS..... 139
- Fig. III-31:** Electric field distribution for the samples as a function of the tip end to the sample surface,  $f = 2\text{ GHz}$  ..... 140
- Fig. III-32:** Schematic of a lumped element model of probe-sample interaction. Here,  $C_c$  is the coupling capacitance between the tip and the sample,  $Z_s$  is the material impedance to be measured, including the resistance  $R_s$ , inductance  $L_s$  and capacitance  $C_s$ .  $C_{\text{str}}$  (or  $C_{\text{out}}$ ) is the stray capacitance [GAO 98], [ANL 07]..... 141
- Fig. III-33:** Calibration procedure of iNFMM (a) and extraction of the material impedance (b) ..... 142
- Fig. III-34:** Measured quality factor (a) and resonance frequency shift (b) of measured transmission coefficient  $|S_{21}|$  as a function of the stand-off distance,  $f_{\text{ref}} = 2\text{ GHz}$ ,  $\text{IFBW} = 100\text{ Hz}$ ,  $P_0 = 0\text{ dBm}$ , the wave-cancelling process is done considering the probe in air with zero level = -75 dB ..... 145
- Fig. III-35:** Measured magnitude and phase-shift of the transmission coefficient  $S_{21}$  as a function of the stand-off distance,  $f_0 = 2\text{ GHz}$ ,  $\text{IFBW} = 100\text{ Hz}$ ,  $P_0 = 0\text{ dBm}$ , the wave-cancelling process is done considering the probe in air with zero level = -75 dB ..... 146
- Fig. III-36:** Extracted dielectric parameters of SiC after the calibration procedure, (a):  $\epsilon'$  and  $\tan\delta$  as a function of the stand-off distance  $h$  at  $2\text{ GHz}$ , (b):  $\epsilon'$  and  $\tan\delta$  as a function of the frequency when the stand-off distance is kept to  $10\text{ }\mu\text{m}$  ..... 147
- Fig. III-37:** Modeling of the probe-SiCG interaction (a) and extracted complex impedance of graphene (b) as a function of frequency from  $2\text{ GHz}$  to  $18\text{ GHz}$  ..... 148

## *List of tables*

<b>Table II-1:</b> Standard deviation of the transmission coefficient $S_{21}$ as a function of IFBW; zero level = -50 dB, $f = 2$ GHz, acquisition time = 60 s, number of points = 60 .....	71
<b>Table II-2:</b> Standard deviation of the transmission coefficient $S_{21}$ as a function of IFBW; zero level = -50 dB, $f = 2$ GHz, acquisition time = 60s.....	71
<b>Table II-3:</b> Standard deviation of the transmission coefficient $S_{21}$ as a function of the zero level; $f = 2$ GHz; $P_0 = 0$ dBm, IFBW = 100 Hz, acquisition time = 5 minutes, number of points = 600 .....	73
<b>Table II-4:</b> Standard deviation for three zero levels of the transmission coefficient $S_{21}$ , $f = 2$ GHz, $P_0 = 0$ dBm, IFBW = 100 Hz, acquisition time = 5 hours, number of points = 600 .....	74
<b>Table III-1:</b> Measured width as a function of probe stand-off distance H and the difference compared with the actual width, $f = 2$ GHz, IFBW = 100 Hz, $P_0 = 0$ dBm, zero level = -50 dB, $S = 1 \mu\text{m}$ , $D = 260 \mu\text{m}$ .....	95
<b>Table III-2:</b> (a): Measured width as a function of the stand-off distance, (b): width as a result of the signal/position difference method applied to different tip-sample separation distances, $f = 2$ GHz, IFBW = 100Hz, $P_0 = 0$ dBm, zero level = - 50 dB, $S = 1 \mu\text{m}$ , $D = 260 \mu\text{m}$ .....	107
<b>Table III-3:</b> Measurement sensitivity to saline concentration levels from 0 to 9 mg/ml with the two configurations considered: without interferometer (reflection mode) and with interferometer (transmission mode), $f = 2$ GHz, $P_0 = 0$ dBm, IFBW = 100 Hz.....	123
<b>Table III-4:</b> Averaged errors in percentage for different reference concentration levels (0, 58, 100 and 160 mg/ml), $f_{\text{ref}} = 2$ GHz, $P_0 = 0$ dBm, IFBW = 100 Hz, zero level = -55 dB .....	133
<b>Table III-5:</b> Averaged errors in percentage of two complex permittivity extraction methods, $f_{\text{ref}} = 2$ GHz, $P_0 = 0$ dBm, IFBW = 100 Hz, zero level = -55 dB.....	134

## ***List of acronyms and abbreviations***

ADC: Analog-to-digital converter

ADS: Advanced design system

AFM: Atomic force microscope

DC: Direct current

DNA: Deoxyribonucleic acid

DSP: Digital signal processor

DUT: Device under test

EMP: Evanescent microwave probe

FWHM: Full width at half maximum

HFSS: High frequency structural simulator

IC: Integrated circuit

IFBW: Intermediate frequency bandwidth

iNFMM: Interferometer-based near field microwave microscope

LO: Local oscillator

MEMS: Micro-electro-mechanical system

MOS: Metal-oxide-semiconductor

MSiC: Gold-metallized silicon carbide substrate

NFMM: Near-field microwave microscope

NSOM: Near-field scanning optical microscope

SEM: Scanning electron microscope

SiC: Silicon carbide

SiCG: Graphene fabricated by epitaxial method on SiC substrate

SiCGALO: SiCG with a Al<sub>2</sub>O<sub>3</sub> layer on the top

SMA: Sub miniature version A

SMM: Scanning microwave microscope

SPM: Scanning probe microscope

STM: Scanning tunneling microscope

VNA: Vector network analyzer



## **General introduction**

The microscope is an essential instrument to visualize objects that are too small to be observed with the naked eye. For centuries, considerable and continuous efforts have been made to design and develop various kinds of microscopes with ever increasing performance. Today different types of microscopes are available for diverse uses in a variety of fields. They can be classified in many different ways. For example, microscopes such as the atomic force microscope (AFM), the scanning electron microscope (SEM), the scanning tunneling microscope (STM) are now very well-known instruments for their high spatial resolution in nanometric scale; they are widely found in industrial and academic laboratories. These platforms are tools of choice to address a large scope of applications in different fields like materials characterization, biological sciences, medical research and food security inspection, to name just a few of them. Microscopes can also be categorized by means of their operating frequency. In case of AFM, SEM and STM they are able to investigate materials/devices at MHz frequencies or even lower. So, one of the challenge in the microscopy field is to propose solutions for characterizations at higher frequency. It is worth noting that recently, platforms working in the terahertz frequency band have been developed such as the near-field scanning optical microscope (NSOM) which has established its ability in the local evaluation of materials under test. Indeed, the exploitation of these characterization tools helps to acquire different kind of materials properties. However, one can notice that dedicated instruments working in a routine manner are still lacking in the gap between MHz and THz frequency bands. This work is a contribution to the efforts made in developing microwave microscopes to fill this gap.

One advantage of the microwave technology is the penetration ability of the microwave signals into the materials/devices under test, offering the possibility to collect information at the surface but also in depth. Thanks to this possibility, characterization tools like resonant cavities, waveguides and transmission lines have been developed to estimate the electrical properties of materials/devices such as dielectric parameters and impedance. However, it is well known that the spatial resolution given by these conventional microwave methods is theoretically limited to

around half of wavelength. To bypass this limit, known as the Abbe limit, and achieve a sub-wavelength resolution, the near-field microwave microscope (NFMM) is under development. The NFMMs are equipped with microwave near-field probes that confine evanescent fields to regions which are significantly smaller than the wavelength of the operating frequency. Therefore, these microscopes are able to resolve sub-wavelength features, providing resolution much higher than the classical Abbe limit. Thus, the NFMM appears as a useful tool for the local characterizations of materials. Nevertheless, microwave probes usually present a high impedance (several  $k\Omega$ ) compared to the  $50 \Omega$  characteristic impedance of the microwave measurement instrument (i.e. vector network analyzer / VNA). This mismatch, resulting in a poor measurement sensitivity, is one of the main bottlenecks of this characterization mean. Different techniques of matching have been proposed to solve this impedance mismatch but practically all of them are narrow frequency bandwidth.

In this thesis, to overcome this difficulty and thus improve the measurement sensitivity an interferometric technique is used. The proposed method is evaluated for broadband characterization with high sensitivity of diverse materials/structures such as metals, semiconductors, dielectrics and liquids. Furthermore, a microwave probe which generates evanescent waves at a short probe-sample separation distance is used to perform a non-destructive evaluation with a sub-wavelength resolution. The possibility of a broadband local quantitative analysis of materials is demonstrated through some applications in the materials characterization field.

The manuscript is organized in three chapters. In the Chapter I, relying on a brief state of the art of the near-field microwave microscope, several typical platforms are described in terms of different probing techniques. Then, some of the applications of NFMMs in materials and life sciences fields are discussed. After detailing the measuring principle of NFMM, we focus on the study of the probe-sample interaction in near field. Finally, an electrical model corresponding to this interaction is proposed and methods to relate the measured parameters to the local electromagnetic properties of the samples under test are provided.

In chapter II, we concentrate on the performance of the microwave microscope proposed by our group. To clarify the context of this work, the mismatch problem between the high-impedance load and the microwave instrument is firstly described. In response to the requirements mentioned above, an interferometric technique is

proposed for its integration into the microwave microscope. After carefully characterizing the microwave components of the microscope architecture, we demonstrate a large enhancement of the measurement sensitivity brought by the interferometric method. Furthermore, a major asset of the technique is its capacity to operate over a wide frequency range, [2-18 GHz], which is hardly feasible with conventional microwave approaches. To guarantee a reliable measurement, the performance of the system is also evaluated through the study of the measurement repeatability. This later is estimated by the computation of the complex standard deviation. The errors related to the platform are effectively quantified. Two types of situation are investigated, the first one considers a static measurement (x-y-z stage fixed), and the other one takes into account the platform displacement (for 1D and 2D scanning). Finally, a set of key parameters is investigated for 1D scanning and 2D microwave imaging applications. After the demonstration that the interferometer-based near-field microwave microscope (iNFMM) has potentials to perform numerous kinds of characterizations with a high measurement sensitivity over a broad frequency range, a few examples are presented in the next chapter.

In chapter III, two important applications which are the non-contact surface imaging and the local characterization of materials/structures are discussed. We start with the scanning resolution study through 1D and 2D experiments. The influence of scanning parameters (the tip-sample distance  $H$ , the scanning step size  $S$  of the x-y-z stage and the probe size  $D$ ) on the scanning quality is carefully investigated. A set of scanning parameters ( $H$ ,  $S$  and  $D$ ) is defined to establish the best scanning performance of the iNFMM. Furthermore, we study the possibility to improve the scanning quality by a simple signal processing method.

Afterwards, the possibility of a broadband local characterization from 2 to 18 GHz of different kinds of materials is demonstrated. First, we evaluate the potential offered by the interferometric technique for liquids characterization. As a common and widely available example used when dealing with bio-samples, solutions prepared with deionized water and different concentrations of sodium chloride are characterized. The choice of these techniques is mainly motivated by advantages such as the low volume of investigation and a good measurement sensitivity even in immersion mode. The complex permittivity of the saline solutions is extracted by two different methods. The experimental permittivities retrieved are compared to the

theoretical values calculated by Cole-Cole model to appreciate the performance of these methods. Finally, a non-contact and non-destructive investigation of solid materials/structures is presented. In this part we are aiming to characterize materials whose properties are not well known in the microwave frequency range. This is the case of most of the new nanomaterials, in particular 2D nanomaterials. As some of 2D materials have shown interesting features for a potential use in microwaves, the knowledge of their electromagnetic properties is of prime importance. So, in the last part of the manuscript the complex impedance of graphene fabricated by epitaxial method is quantified in the frequency band [2-18 GHz].

## Chapter I

### Overview of near-field microwave microscopy

#### I.1 Introduction to near-field microwave microscopy

The rapid advances in microelectronics and in microfabrication technologies, in particular, have led to a fast and continuous miniaturization of devices. For example, in the semiconductor industry, the number of transistors in a dense integrated circuit doubles approximately every 18 months, in accordance with the famous Moore's law [MOO 65]. Thus, the feature size of the transistors decreases and meanwhile the operating frequency increases remarkably. Moreover, the rise of a large number of new materials such as nanotubes, nanowires and nanomaterials in general promotes the development of fabrication and characterization techniques towards the nanoscale. These developments have been accompanied by a will of an increase of the operating frequency. Generally speaking, one can say that there is a high demand for characterization tools at ever-increasing performance in terms of both the size of the materials/devices to be tested and the operating frequency.

In fact, instruments that offer spatial resolutions in the order of the nanometer and a high frequency are targeted. Actually, numerous metrology tools with high spatial resolution have been developed in the MHz region or at ultra-high measurement frequencies (~THz). Indeed in the MHz frequency range, imaging platforms such as the atomic force microscope (AFM), the scanning electron microscope (SEM) and the scanning tunneling microscope (STM) have successfully addressed the requirements of nanoscale spatial resolutions. However, for these instruments, the measurement of miniaturized materials/devices at high frequency is a great challenge. In the same way in the terahertz region, the advent of the near-field scanning optical microscope (NSOM) offers the possibility to investigate the local electromagnetic properties of samples [IMT 14a]. But in-between these two frequencies domains there is a gap where there is no standard tool really available yet. Therefore, there is an urgent need for solutions to fill this gap between MHz and THz frequency bands.

As just mentioned above, there is a demand to fulfill the requirements of tools working at a few GHz and being able to locally characterize the physical properties of materials/devices such as dielectric constants and impedance. Actually, microwave sensing and characterization techniques have shown great potentials in a wide range of applications [KHA 07]. Indeed, as microwave frequency signals can penetrate materials, they offer the possibility to inspect the surface and subsurface of samples. Such advantages include the fact that these methods are nondestructive, and enable one-side and noncontact testing. Nevertheless, traditional microwave techniques based on transmission lines or resonant cavities [IMT 14a] have an important limitation related to the spatial resolution achievable set by the diffraction limit, in the order of half of the wavelength of operation. Actually, in the microwave spectrum, the spatial resolution for conventional tools is at best in the order of the millimeter [TAB 99a]. Therefore, to address the applications where a sub-millimeter resolution is needed, this diffraction limit must be overcome.

A solution to bypass this diffraction limit is to make use of microscopy methods based on the near-field evanescent waves rather than the propagating ones [ANL 07]. Synge *et al.* firstly proposed a near-field scanning method to overcome this diffraction problem in 1928 [SYN 28]. Fraint and Soohoo extended Synge's idea and performed near-field microwave characterizations with open-ended cavities in 1959 [FRA 59] and 1962 [SOO 62], respectively. Ash *et al.* 10 years later experimentally studied materials dielectric properties by means of a waveguide structure [ASH 72]. In these setups, waveguide probes were used. However, these probes have poor measurement sensitivity when operating below the cut-off frequency [SOO 62]. Bryant *et al.* were probably the first (1965) to use a tapered coaxial transmission line probe to study the local conductivity of materials in the GHz region (with a spatial resolution in the order of millimeters) [BRY 65]. The coaxial transmission line probe is a better candidate for the microwave microscopy as there is no cut-off frequency in transmission line [BRY 65]. Wang *et al.* in 1990 demonstrated a near-field microwave microscope (NFMM) based on a resonator with a tapered microstrip line at 10 GHz [WAN 90]. Then, Tabib-Azar performed microwave images by using a similar structure with a spatial resolution of 0.4  $\mu\text{m}$  at 1 GHz [TAB 99a]. More recently, at the beginning of the 21<sup>th</sup> century, the atomic force microscope (AFM) and scanning tunneling microscope (STM)-based NFMMs were developed [TAB 04], [FAR 11a].

Thanks to these well-defined platforms, the local electrical properties can be investigated with high spatial resolution (in the order of nanometers). Furthermore, NFMM has successfully established its potentials to locally characterize materials in various fields such as dielectrics [HOF 14], semiconductors [GRA 14], metals [STE 98] and biological samples [FAR 11a], to name just a few of them.

In this chapter, we first briefly present the NFMM developed in the past decades in terms of different probe techniques including coaxial probes, waveguides, microstrip lines, magnetic probes, AFM tips and STM tips. Then, some of the applications of NFMM in materials and life sciences are discussed. As the objective of the NFMM is to relate the measured parameters to the local electrical properties of samples under test, quantification methodologies of NFMM are studied in the last section of this chapter.

## **I.2 Near-field microwave microscopy platforms and applications**

### **I.2.1 Introduction**

Near-field microwave microscopes are usually composed of three parts: an evanescent microwave probe (EMP), a microwave source and a probe positioning system. During the measurement, the materials/devices under test are illuminated with the microwave emitted by the EMP, generally a metallic probe, at a short distance. The diffraction limit can be overcome and thus a local characterization can be performed by the microwave microscope. The physics of near-field microwaves is as follows: in the microwave frequency range, connecting a source to a sharp probe with tip radius  $R_0 \ll \lambda$  (wavelength in free space) will generate evanescent waves whose wave vectors  $k_r$  is around  $1/R_0$  and the spatial resolution given by  $R_0$  [GAO 04a]. Actually, these evanescent waves only exist very near the EMP surface and decay exponentially away from the surface. The interaction between the EMP tip and a sample will change the field configuration near the tip and its equivalent capacitance. Thus the stand-off distance between the EMP and the sample ( $z$ ) should be kept much smaller than the wavelength to assure high resolution and sensitivity provided by the evanescent waves [OMA 15]. Almost all near-field microwave probes are based on this principle. Therefore, in the following part, we present the NFMM in terms of different kinds of evanescent microwave probes.

### **I.2.2 Near-field microwave microscope platforms**

As said before, the near-field microwave microscopy is generally based on a microwave probe whose apex size is much smaller than the wavelength in free space ( $\lambda$ ). The probe is positioned very close to the material under test to ensure a maximum tip-sample interaction. It is connected to a detector system which collects the electromagnetic information from the materials under test. The microwave response can be presented in different manners such as resonant frequency ( $F$ ) and quality factor ( $Q$ ) in resonator-based microscopy, or real and imaginary parts of the reflection/transmission coefficients in other cases. In this part, different NFMM platforms are presented in terms of a variety of probes such as coaxial probes, waveguides, transmission lines probes, magnetic probes, AFM tips and STM tips.

### I.2.2.1 Coaxial probe-based platform

The probe widely used in the NFMM field is based on the coaxial line [STE 98]. It is usually made of a coaxial connector with a center conductor extruded [LU 97]. In this configuration, the electric field generated by the probe is coupled to the material under test. Usually a resonator structure is added between the measurement instrument and the probe to improve the measurement sensitivity. As shown in the Fig. I-1, the platform is equipped with a sharpened tip, a half wavelength resonator, a microwave source and a lock-in system.

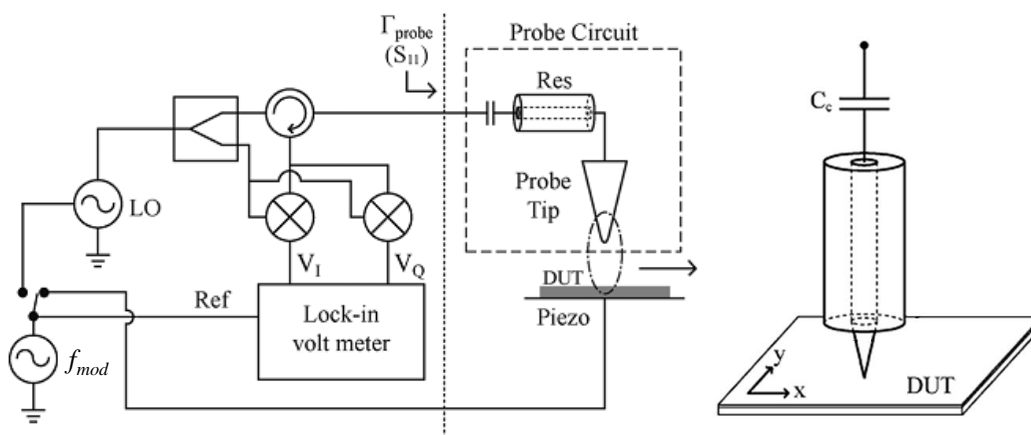


**Fig. I-1:** Schematic of the coaxial line-based microwave microscope [CHI 12]

The electrical properties of the sample affect the resonant frequency and quality factor when the sample is investigated by the microwave probe. The resonant frequency shift ( $\Delta F$ ) and the variation of the quality factor ( $\Delta Q$ ) are exploited to determine the dielectric properties of the sample [CHI 12]. As the electric field is concentrated around the tip apex, the spatial resolution of this type of probe is in the order of the smallest dimension of the tip (in the order of microns [CHI 12]). This resolution also depends on the separation between the probe and the sample under test. This type of probe has been used to measure the properties of different materials such as metals [STE 98], dielectrics [LU 97] and semiconductors [CHI 12]. The typical scanning speed of the coaxial line-based platform is 10 ms per pixel [CHI 12].

### I.2.2.2 Waveguide-based platform

Open-ended waveguide probes are widely used in microwave nondestructive testing [QAD 07] [HAD 12]. As shown in the Fig. I-2, Golosovsky *et al.* demonstrated

a typical waveguide-based microwave microscope equipped with a rectangular waveguide, a microwave source, a matching network and a x-y-z positioning system [GOL 00].

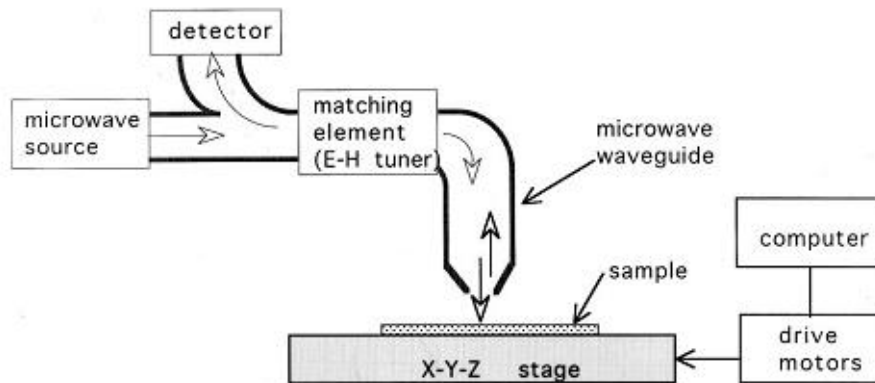


**Fig. I-2:** Schematic of the platform with a waveguide-fed thin slit microwave probe [GOL 00]

The spatial resolution of the open-ended waveguide probes is limited by the waveguide cross section whose size is around a half wave-length [MAL 16]. Therefore for higher spatial resolution, higher operating frequencies are required, which leads to higher cost and complexity of equipment and, in general, higher measurement noise level. The best spatial resolution of the waveguide setup is in the order of hundreds of microns and a typical scanning speed is in the order of 70 pixels per minutes [GOL 00].

### I.2.2.3 Microstrip line-based platform

In this case, as shown in Fig. I-3, a  $\lambda/4$  microstrip line is tapered at its end to form the near-field probe [TAB 99b], [TAB 99c]. This microstrip line is then coupled to a short feed line.

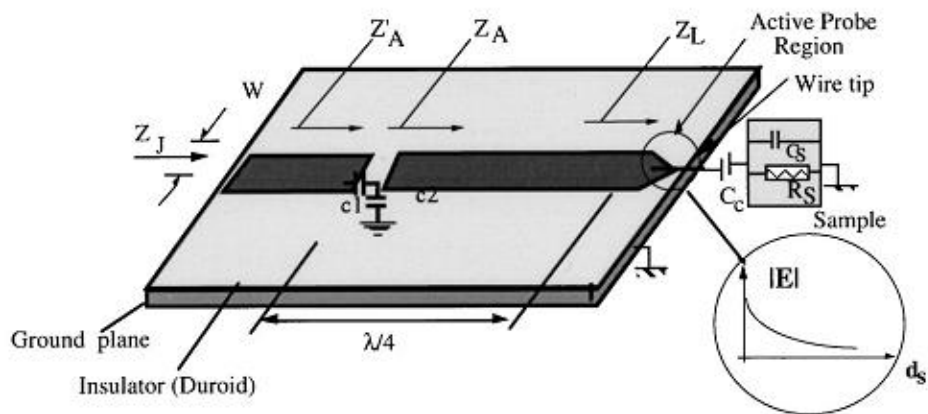


**Fig. I-3:** Microstrip line resonator with tapered tip [TAB 99b], [TAB 99c]

The feed line is connected to a three-port circulator, which circulates the signal from the radio frequency source to the resonator, and directs the reflected wave to a crystal detector. The sample is mounted on an x-y stage and scanned underneath the probe tip (see Fig. I-4). To quantitatively map the surface conductivity, there is a reflectance-compensated fiber optic distance sensor right next the tip of the probe, and a distance feedback control (in z direction) to alleviate dependence of the probe output on the topography of the sample surface. The accuracy of the distance control is  $0.5 \mu\text{m}$  [TAB 99a].

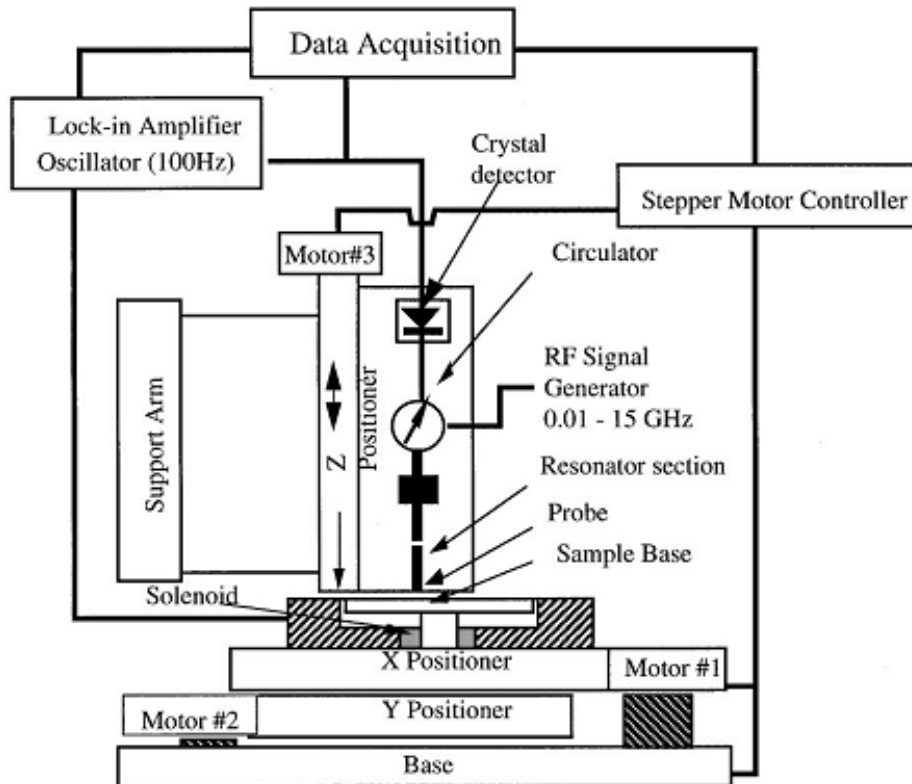


**Fig. I-4:** Schematic of the experimental setup [TAB 99b], [TAB 99c]

The materials under test are usually metal plates or dielectrics. Both the resonance frequency and the quality factor of the resonator are affected by the presence of the sample [TAB 99c] [TAL 09]. The spatial resolution of this type of probe depends on the geometry of the tip, the coupling between the resonator and the transmission line and the permittivity of the substrate of the microstrip line [HAD 13]. A typical spatial resolution of this kind of setup is in the order of several hundreds of nanometers [TAB 99a].

#### I.2.2.4 Magnetic-probe-based platform

Magnetic probe can be achieved by extending a conductive loop from the inner conductor to the ground from a transmission line probe [WAN 05] [WAN 07] or an open ended coaxial probe [TAI 11]. As an example, a microstrip-based magnetic microwave probe is shown in Fig. I-5. In that case, the probe is a driven resonant transmission line fabricated on RT Duroid substrate, coupled to a feedline. One end of the stripline is connected to a copper loop which is formed by shorting the

micro-stripline resonator to the ground. The platform configuration is the same as illustrated in Fig. I-4.

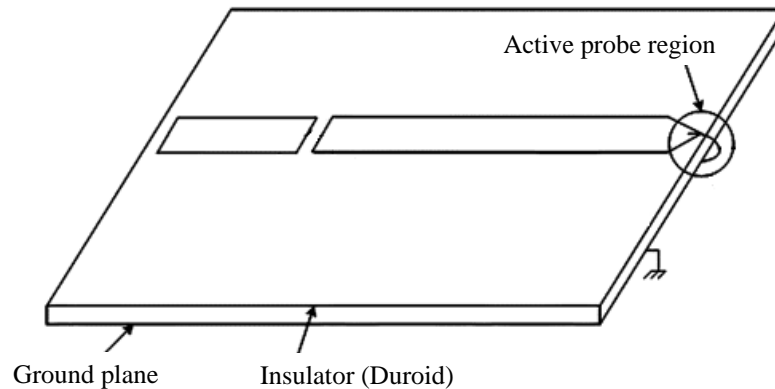


**Fig. I-5:** Schematic of the magnetic microwave probe [WAN 07]

In this case, magnetic evanescent fields are created around the loop. A near-field magnetic-dipole probe is suitable for noncontact and nondestructive imaging of metals [WAN 05] while the electric-dipole probe is better suited for insulator and semiconductor materials measurement.

#### **I.2.2.5 AFM-based platform**

In this configuration, the probe of an atomic force microscope (AFM) is connected to the microwave source [TAB 04]. The stand-off distance between the tip and the sample can be very precisely controlled because the sensitivity of the AFM optical detection method is typically 0.01 nm in the z-direction [TAB 04]. The typical lateral resolution is around 100 nm. The microwave images in terms of real and imaginary parts can be obtained simultaneously with the topography. An illustration of the commercial AFM-based NFMM developed by Keysight™ is shown in Fig. I-6.

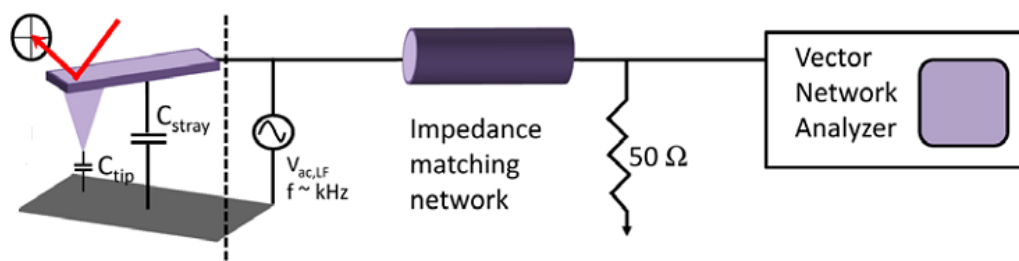


**Fig. I-6:** Schematic of the AFM-based set up [GRA 14]

The vector network analyzer (VNA) measures the ratio between the incident and reflected signals at the tip, the so-called scattering  $S_{11}$ -parameter. The micrometric tip-sample system forms a low capacitance of a few femto Farads, causing a high reflection coefficient and therefore a loss of measurement resolution of the VNA.

The imaginary and real parts are proportional to changes of the tip-sample capacitance and reactance which can ultimately be converted to the local properties ( $\epsilon, \sigma$ ) of the material under test [HUM 11]. However, the major drawback of this type of probe is the lack of sensitivity attributed to the parasitic capacitance between the cantilever and the sample [LAI 09a], [LAI 11]. The shielded cantilever probe was proposed to localize the tip-sample interaction near the tip apex. Compared with STM-based platform, AFM-assisted system allows simpler landing, especially over poorly conductive (or insulating) samples [FAR 12a].

### **I.2.2.6 STM tip-based platform**

More recently, the scanning tunneling microscope (STM) tip is used as microwave probe and it is capacitively coupled to a coaxial connector which is then connected to a vector network analyzer [FAR 11a] [FAR 12b]. An example of STM-based setup is shown in the Fig. I-7. The STM current is recorded in the feedback chain in order to maintain the tip-sample distance, while providing in the same time a topographical image of the sample being characterized.

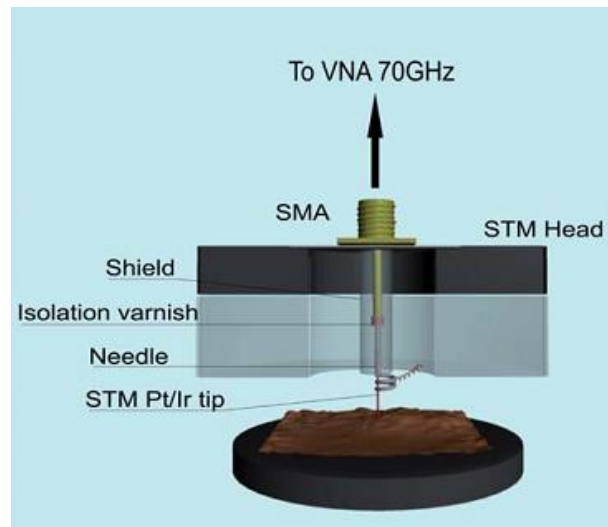


**Fig. I-7:** Schematic of the STM based-NFMM [FAR 11a] [FAR 12b]

One of the biggest advantages of the STM-based setup is that a nano-metric spatial resolution can be achieved [FAR 11a]. However, the sample under test is supposed to be conductive and some preparation such as depositing electrodes on the sample surface before the measurement must be performed. This sample preparation process might influence the electric properties of the material.

As one can see there are various kinds of NFMM platforms in terms of microwave probes including coaxial probes, waveguides, transmission lines, magnetic probes, AFM tips and STM tips. Thanks to the high spatial resolution and measurement sensitivity provided by these probes, several kinds of applications which are discussed in the following part have been addressed in many domains.

### **I.2.3 Applications of near-field microwave microscope**

Thanks to the high spatial resolution and measurement sensitivity provided by the NFMM [BIA 16], [BER 15], [GRE 16], various applications have been well addressed such as characterization of dielectric films, integrated circuits (IC), semiconductors, graphene, aqueous solutions and biological tissues. Furthermore, because of the penetration of microwaves into the materials under test, the electrical properties (conductivity, permittivity) can be extracted from the reflected wave and 2D electrical property images can be performed simultaneously with the sample topography, which is unattainable by conventional optical microscopes or AFMs. Additionally, microwave subsurface imaging can also be achieved by NFMM, which extends the

NFMM applications field to more important capabilities such as detection of buried structures in materials [OPT 14]. To better highlight the numerous possibilities allowed, a short overview of the NFMM applications is given in this part.

### **I.2.3.1 Solid dielectric materials characterization**

Dielectric materials whose permittivity varies from 1 (free space) to hundreds (high-k materials) are widely used. For example, low permittivity materials are being sought to allow smaller scale circuits [CHI 12] while minimizing undesirable stray capacitance between wires. Regarding high permittivity materials, they are under study in order to fabricate smaller capacitors while minimizing leakage. Steinhauer *et al.* described the use of an open-ended coaxial probe based-NFMM to image the permittivity of bulk and thin film dielectric samples on a length scale of about 1 mm [STE 00]. The dielectric loss is also an important issue when characterizing materials. Hoffmann *et al.* presented an algorithm for measuring the relative permittivity of thick dielectric (low loss) substrates [HOF 14]. The complex permittivity of high loss dielectric materials at microwave frequencies is measured by a resonant cavity based NFMM [GRE 16]. The local characterization offered by this kind of techniques is a big advantage compared with the conventional methods. Karbassi *et al.* performed a localized thin film dielectric constant measurement on low resistivity silicon substrates [KAR 08]. An observation of electronic inhomogeneity in indium selenide ( $\text{In}_2\text{Se}_3$ ) nanoribbons with spatial resolution around 100 nm was reported in [LAI 09b].

### **I.2.3.2 Semiconductor samples testing**

Semiconductors based integrated circuit (IC) represents almost all of today's technology. The characterization of semiconductors is always an important issue. The conventional measurement methods of semiconductors require pre-measurement preparation of sample which might influence the material properties [IMT 14b]. For example, the four-point method which is commonly used for the measurement of the surface resistivity of silicon wafer requires metallic pads deposited on the silicon surface. On the contrary, the NFMM enables non-destructive testing over material surface without any sample preparation. Imtiaz *et al.* performed visualization (detection) of the p-n junction location of a nanowire on a Si substrate [IMT 14b]. The capacitance and resistance images over silicon wafer were also obtained in [BRI 15].

Weber *et al.* presented a transmission line based NFMM that had been configured for inhomogeneous photovoltaic samples imaging [WEB 12]. Berweger *et al.* performed microwave imaging over 2D semiconductor materials where the change of image contrast by controlling the sample charge carrier concentration through the applied tip bias was observed [BER 15].

### **I.2.3.3 Chemical and biological samples characterization**

The characterization of chemical and biological materials requires sensing tools with high sensitivity and spatial resolution. The NFMM has been successfully used to evaluate chemical components and bio-samples. Tabib-Azar *et al.* demonstrated the ability of the evanescent microwave probe (EMP) in detecting minute changes over chemical materials [TAB 00]. An original sub-surface, high spatial resolution tomographic technique based on scanning microwave microscopy was used to visualize in-depth materials with different chemical compositions [OPT 14]. Wu *et al.* performed 2D imaging maps on biological samples [WU 15]. Park *et al.* presented the application of a resonator-based SMM to the characterization of biological samples [PAR 05]. Since dielectric properties of most biological samples originate mainly from the water they contain, the authors have measured the electrical properties of water in the microwave region. Kim *et al.* demonstrated a resonator-based NFMM in liquid environment [KIM 05]. In that case, the topographic and NFMM images of DNA samples in liquid were successfully obtained. The permittivity of a single bacterial cell, at microwave frequencies and nanoscale spatial resolution, has been quantified by means of AFM-based platform [BIA 16] [TUC 16].

### **I.2.3.4 Graphene characterization**

In the last decade, graphene has emerged as a promising material for radio-frequency analog circuits and for large-area transparent conductors. Microwave microscopy provides a non-destructive nanoscale characterization of graphene [TSE 13]. Kundhikanjana *et al.* investigated a pristine graphene layer on Si substrate by using the AFM-based NFMM, and demonstrated the possibility of detection of local inhomogeneities in the chemically derived graphene [KUN 09]. Talanov *et al.* performed a transmission line based NFMM for quantitative imaging of the local impedance for monolayer and few-layers graphene [TAL 10]. More recently, Monti *et*

*al.* conducted a non-contact measurement of the sheet resistance of a multilayer material composed by a dielectric film and a few layers of graphene [MON 12], [MON 13]. Additionally, an imaging of buried inhomogeneities of graphene on SiC was reported in [TSE 13].

### **I.2.3.5 Subsurface imaging**

As microwaves penetrate into the materials, subsurface imaging can be achieved by NFMM. An example of such capability is the use of microwaves to monitor the local ion concentration in a sealed lab-on-a-chip system to study chemical reactions within a confined geometry [SUN 14]. They can be employed in the on-site failure analysis of sophisticated sensors fabricated with the micro-electro -mechanical-system (MEMS) technology, without opening the device package. The subsurface lateral resolution and measurement sensitivity of the microscope have been studied in [SUN 14]. Actually, the best spatial resolution can be obtained when the thickness of the cover layer is thinner than the probe apex. For instance, the structure under a dielectric layer (thickness = 25  $\mu\text{m}$ ) was effectively detected by using a probe with an apex of 50  $\mu\text{m}$  [SUN 14]. More recently, capacitance images of flat Si test samples with varying dopant density and covered with dielectric thin films of SiO<sub>2</sub> (100–400 nm thick) were measured [GRA 15].

### **I.2.4 Conclusion**

NFMM has wide applications in material and life sciences. In this part, we have given only a representative sample of the numerous possibilities offered by this technique. Indeed, one can mention many advantages of NFMM compared with conventional microwave methods. First, microwave microscopy is able to perform local quantitative measurements of electrical properties such as dielectric constant and resistivity of the material under test. Thanks to this possibility of local characterization, electronic inhomogeneities of materials can be carefully studied with nano-metric spatial resolution. Secondly, the microwave generated by the probe can penetrate the sample to some extent, allowing imaging of subsurface structures. Another advantage offered by NFMM is the nondestructive characterization of materials which protects the sample surface from any scratch. Furthermore, comparing to the conventional

methods, this method does not require large area samples or any particular sample preparation including the deposition of thin film electrodes, cleavage and cross-sectioning on the materials surfaces. Thus it is easily applicable to various semiconductors and materials science investigations. However, there are some inconveniences of NFMM. For example, as most microwave microscopes are resonator-based, poor measurement sensitivity is obtained in the presence of liquid samples because liquids are high loss materials.

## **I.3 Quantification methodology of near-field microwave microscopy**

### **I.3.1 Introduction**

Two major trends in NFMM are the waveguide and sharp-tip approaches. For the study of micro-and nano-scale materials/devices, the sharp-tip approach is preferred to the waveguide one because of the much higher spatial resolution achievable. However, although NFMM has been used for nanoscale characterization, quantitative analysis is still difficult because of the complicated electromagnetic interaction between the evanescent waves and the material under investigation. In this part, we investigate the interaction of the sharp tip with materials when it is brought into the near field of different bulk samples.

The measurement parameters of the NFMM system such as reflection/transmission coefficients, quality factor and resonant frequency depend on the electrical properties of the materials/devices under test including complex permittivity and permeability. The ultimate goal for theoretical analysis of a near-field microwave probe is to find a relationship between these detectable quantities and the sample properties. Generally, there are two calculation methods: cavity perturbation method and transmission line method. The first approach relates the measured quality factor and resonant frequency of resonator-based NFMM to the electrical parameters of materials while the second one extract these electrical parameters through the real and imaginary parts of the measured reflection/transmission coefficients. To this end, the modeling of tip-sample interaction is first studied. Then, the capacitance model between the tip and a metallic surface is investigated by integrating the field contribution between the tip and the sample based on the image or surface integration methods. Finally, the electrical properties are related to the tip-sample model by using both cavity perturbation method and transmission line method.

### **I.3.2 Modeling of tip-sample interaction**

Generally, the NFMM is equipped with a sharp tip (radius  $\ll \lambda$ ) which generates non-propagating evanescent waves at small tip-sample separation distances. In this case, the probe consists of a sharpened metal tip mounted on the center conductor of a coaxial connector. The working frequency is out of the resonance frequency range of

the probe, which shields the propagating far-field waves. The probe-sample interaction is shown in the Fig. I-8. As the sample is placed in the near-field range of the tip and the tip radius is much smaller than the wavelength, the electromagnetic wave can be considered as quasi-static.

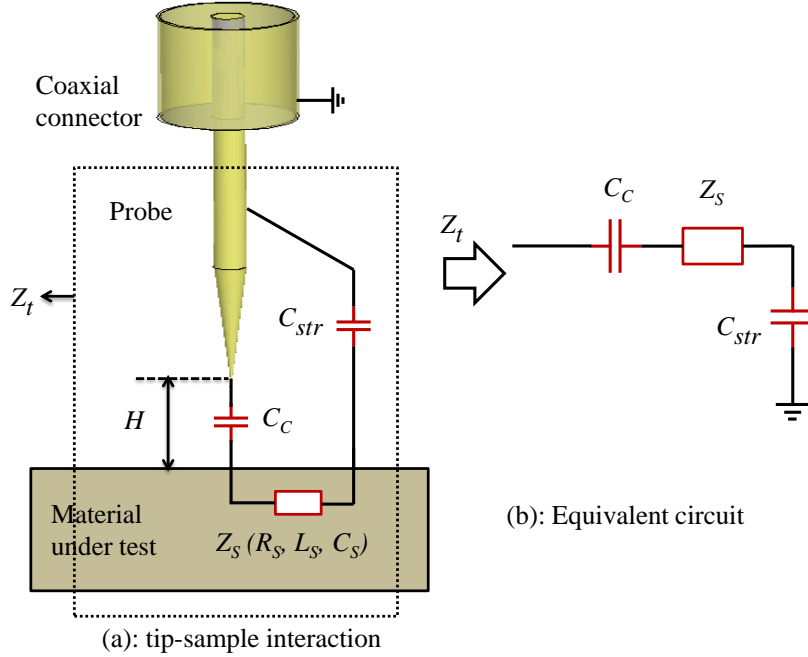


**Fig. I-8:** Lumped element model of tip-sample interaction (a) and equivalent circuit (b)

Generically, the impedance  $Z_t$  of an electric sharp tip can be represented as a network (Fig. I-8.b) made of the tip-to-sample coupling capacitance  $C_c$ , the sample “near-field” impedance  $Z_S$  including the resistance  $R_S$ , inductance  $L_S$  and capacitance  $C_S$  of the material, and the tip stray capacitance  $C_{str}$  (or  $C_{out}$ ) [GAO 98], [ANL 07].

$$Z_t = \frac{1}{j\omega C_c} + Z_S + \frac{1}{j\omega C_{str}} \quad (\text{I-1})$$

$Z_S$  is due to the energy stored and/or dissipated in the sample under test. Both  $C_c$  and  $C_{str}$  depend on the tip-sample distance  $H$ . To obtain high enough sensitivity to the sample properties (i.e., to make  $Z_t \sim Z_S$ ), it is imperative to have both  $1/\omega C_c \ll Z_S$  and  $\omega C_{str} \ll Z_S$ , which can typically be achieved by making  $H \ll D$  where  $D$  is the characteristic tip size. In the near-field,  $Z_S$  can be expressed as [ANL 07]:

$$Z_S = \frac{1}{j\omega \epsilon_0 \epsilon_S D} \quad (\text{I-2})$$

which is basically the impedance of a capacitor with a geometrical capacitance  $\epsilon_0 D$  filled up with a material of complex relative permittivity  $\epsilon_s = \epsilon' - j\epsilon''$ . Let us now illustrate this concept for a variety of materials.

### a) Dielectrics

If the sample is a low-loss dielectric with  $\epsilon_s = \epsilon' (1 - j \tan\delta)$  and  $\tan\delta \ll 1$ , then the near-field impedance is:

$$Z_s = \frac{\tan \delta}{\omega \epsilon_0 \epsilon' D} - j \frac{1}{\omega \epsilon_0 \epsilon' D} \quad (\text{I-3})$$

Its reactive part is capacitive and the probe is sensitive to the sample dielectric constant as well as the loss tangent ( $\tan\delta$ ).

### b) Semiconductors

At microwave frequencies semiconductors can exhibit  $\epsilon' \sim \epsilon'' = 1/\epsilon_0 \omega \rho$ , where  $\rho$  represents the resistance of the semiconductor. In the near field the impedance is [ANL 07]:

$$Z_s = \frac{1}{\frac{D}{\rho} + j\omega \epsilon_0 \epsilon' D} \quad (\text{I-4})$$

### c) Metals

A conductive metal can be characterized by the relative permittivity  $\epsilon_s \approx -i/\epsilon_0 \omega \rho$ . Thus  $Z_s$  represents the dc resistance of the tip-sample interaction:

$$Z_s = \frac{\rho}{D} \quad (\text{I-5})$$

$Z_s$  has no reactive part because the geometrical inductance is negligible in the case of an electric probe. This equation implies that when  $D$  is much smaller than the metal skin-depth the probe spatial resolution is governed by the tip size rather than the sample skin-depth. This creates a unique opportunity for near-field microwave microscopy to study just the subsurface portion of the material, unlike conventional far-field techniques that are sensitive to the entire skin-depth layer.

As the measured results of NFMM largely depend on the tip-sample interaction, quantification methods are used to retrieve the electric properties (complex permittivity, conductivity) from these measured parameters. However, all these

quantification methods require calibration process with well-defined standards [FAR 11b]. Generally, metallic materials such as metal plates and high conductive substrates are chosen as standard loads [IMT 05], [IMT 07], [GAO 04a], [GRA 14]. In the following part, the metallic plate is selected as material under test and we focus on the coupling capacitance between the tip and the sample surface.

### **I.3.3 Capacitance modeling of tip-sample interaction**

The series-RLC lumped element model is shown in the Fig. I-8. As already said, the impedance  $Z_S$  of the material under test is composed of a resistance  $R_S$ , an inductance  $L_S$  and a capacitance  $C_S$ . Here, the sample under test is a metal plate, thus the capacitance  $C_S$  is neglected. In the first order of approximation, the metal resistance  $R_S$  and the inductance  $L_S$  are not taken into consideration because only the tip-sample interaction is under investigation. Actually, the inductance  $L_S$  becomes important for superconducting samples [IMT 07]. Additionally, the capacitance  $C_{str}$  between the outer conductor of the resonator and the bulk sample can be safely ignored, since  $C_{str} \gg C_c$  [IMT 05] [IMT 07]. Therefore, the loading impedance  $Z_t$  of the sample is modeled as a pure capacitor  $C_c$  [IMT 05], [IMT 07], [GAO 04a], [GRA 14]. There are basically two methods to analytically solve this capacitance: the image method [GAO 98] and the surface integration method [HUD 98].

Two critical approximations are made in obtaining these analytical solutions [GAO 04a]. First, the probe tip is regarded as a spherical tip because the main part of the probe interacting with the sample is the tip cap. Actually, this is a good approximation, especially when the probe is held at a distance from the sample shorter than the probe radius. Secondly, the electric field between the tip and the material surface is approximately quasi-electrostatic because the effective region with significant non-zero field distribution is several orders smaller than the relatively long wavelength of the microwave, the phase effect can be neglected. Under these two approximations, the problem is simplified to solve the static electric field distribution in the sample under two boundary conditions: equipotential surface of the sphere and continuity at the sample surface. Then the tip-sample capacitance can be solved by the image method and the surface integration method.

### I.3.3.1 Image method

The first analytical quantitative microscopy theory for NFMM was proposed by Gao's group by using the electrostatic approximation and a perfect conducting sphere [GAO 98] [GAO 99]. The charge redistribution on the tip caused by the probe-sample interaction can be represented by a series of iterative image charges as shown in Fig. I-9.

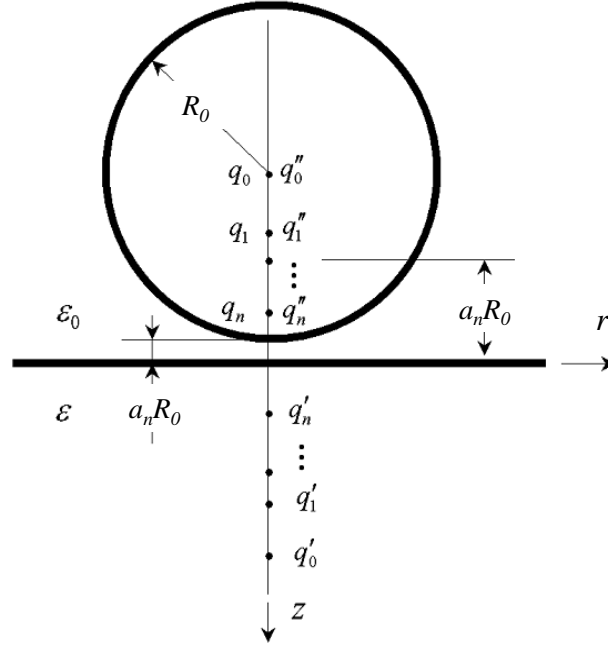


**Fig. I-9:** Iterative image charges in tip-bulk sample system [GAO 98] [GAO 99]

The electric field in the tip-sample region can be calculated by the following expression [GAO 98] [GAO 99]:

$$\mathbf{E} = \frac{1}{4\pi\epsilon_0} \sum_{n=1}^{\infty} q_n \left\{ \frac{r\mathbf{e}_r + (z + a_n R_0)\mathbf{e}_z}{[r^2 + (z + a_n R_0)^2]^{3/2}} - \frac{r\mathbf{e}_r + (z - a_n)\mathbf{e}_z}{[r^2 + (z - a_n R_0)^2]^{3/2}} \right\} \quad (\text{I-6})$$

$\mathbf{e}_r$  and  $\mathbf{e}_z$  are the unit vectors along the directions of the cylindrical coordinates  $r$  and  $z$ .  $R_0$  is the tip radius.  $a_n R_0$  represents the distance of the  $n_{th}$  image charge from the sample surface.  $q_n = t_n q_1$  is the  $n_{th}$  image charge inside the tip. And  $q_1 = 4\pi\epsilon_0 R_0 V_0$ , where  $V_0$  is the tip voltage.

$a_n$  and  $t_n$  have the following iterative relations.

$$\begin{aligned}
 a_n &= \begin{cases} 1 + a - \frac{1}{1 + a + a_{n-1}}, & z > 0 \\ \frac{1}{n}, & z = 0 \end{cases} \\
 t_n &= \begin{cases} \frac{b}{1 + a + a_{n-1}} t_{n-1}, & z > 0 \\ \frac{b^{n-1}}{n}, & z = 0 \end{cases}
 \end{aligned} \tag{I-7}$$

The initial conditions for the iterations are:  $a_1 = 1 + a$  and  $t_1 = 1$ . The parameter  $b$  equals  $(\varepsilon - \varepsilon_0)/(\varepsilon + \varepsilon_0)$  ( $\varepsilon$  and  $\varepsilon_0$  are the permittivities of the sample and free space, respectively).

When a conducting material is placed near the tip (modelled as a conducting sphere), it will interact with the tip causing charge and field redistributions. An expression of the capacitance between a sphere and a metallic plane is given thereafter [DUR 66] [GAO 99]:

$$C_c = 4\pi\varepsilon_0 R_0 \sinh(\alpha) \sum_{n=2}^{\infty} \frac{1}{\sinh(n\alpha)} \tag{I-8}$$

where  $\alpha = \cosh^{-1}(1 + a')$  with  $a' = H/R_0$ .

### I.3.3.2 Surface integration method

For the surface integration method, the tip surface is assumed as a superposition of infinitesimal surfaces obtained by faceting. Then, the electric field created between this faceted conductor and the plane surface is evaluated (Fig. I-10). Hudlet *et al.* derived an approximate analytical formula for predicting the capacitance of a conductive sharp tip above a metallic surface [HUD 98]. Law *et al.* extended the Hudlet's model, employing an additional capacitive term. Thanks to more data collection, they were able to more effectively validate their model [LAW 02].



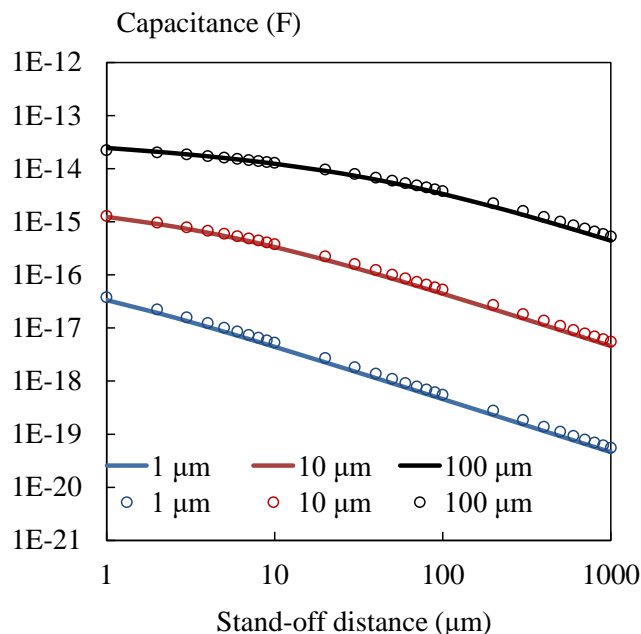


**Fig. I-11:** Calculation of  $C_c$  by two methods: image method (Gao's model in round symbols [GAO 98]) and surface integration method (Hudlet's model in solid lines [HUD 98]); three tip radius are considered: 1  $\mu\text{m}$ , 10  $\mu\text{m}$  and 100  $\mu\text{m}$

As can be seen from the Fig. I-11, the two models agree well with each other for the three tip radius considered (1  $\mu\text{m}$ , 10  $\mu\text{m}$  and 100  $\mu\text{m}$ ). Moreover, it is retrieved that the capacitance value decreases with the increasing stand-off distance. Especially, smaller tips lead to lower capacitances.

Both the charge image method and the geometrical integration method need calibration process to relate the measured data (resonance frequency, quality factor and reflection/transmission coefficient) to the desired electric properties such as complex permittivity [GAO 04a]. These models are discussed in the following section.

### I.3.4 Calibration methods

In order to obtain quantitative and reproducible measures of the intrinsic material properties a calibration of the NFMM system is required. A theoretical model for the detection circuit of NFMM can be based either on a cavity perturbation technique, a transmission line method or other approaches. In this study, two main methods which are the cavity perturbation method and the transmission line method are discussed. Actually, the majority of  $\lambda/4$  or  $\lambda/2$  coaxial resonators based NFMMs usually utilize the quality factor and resonant frequency to retrieve the information of

materials/devices under test [REZ 14]. Since recently, the transmission line method is widely found in AFM-based NFMM [HUB 10], [GRA 14].

### I.3.4.1 Cavity perturbation method

The interaction between the tip and a sample, containing the sample complex electrical impedance, is measured as changes in the quality factor ( $Q$ ) and resonant frequency ( $f$ ) of the resonator-based NFMM. In near field, the probe does not emit significant energy and therefore needs very high  $Q$  to boost the sensitivity. The evanescent waves on the tip will interact with the materials only when the tip is close to the sample. This interaction leads to the change of  $Q$  and  $f$  from the unloaded value of the resonator ( $Q_0, f_0$ ) and contains the information of the electrical impedance [IMT 07] [REZ 14]. The quality factor contains the loss information of the sample while the resonant frequency depends on the capacitance between the tip and sample surface [STE 98].

Gao *et al.* obtained analytic solutions of the electric field near the tip for bulk materials [GAO 98] [GAO 99]. Based on the field distribution, they calculated the shifts of the resonant frequency and the quality factor of the resonator probe due to the tip–sample interaction and derived the dielectric constant and the loss tangent of samples quantitatively with simple boundary conditions. More recently, Gao *et al.* proposed a recursive algorithm to calculate the total charges on the tip–film–substrate system and to derive the dielectric constant and the thickness of the film [GAO 04b].

Hereafter, the relations between the quality factor and the frequency shifts of the resonator and the dielectric parameters of the sample, based on the perturbation theory [POZ 12], [GAO 98], [GAO 99], are given:

$$\frac{\Delta f}{f} = \frac{f - f_0}{f_0} = \begin{cases} -A \sum_{n=1}^{\infty} \frac{bt_n}{a_1 + a_n}, & H > 0 \\ A \left[ \frac{\ln(1-b)}{b} + 1 \right], & H = 0 \end{cases} \quad (\text{I-11})$$

$$\Delta \left( \frac{1}{Q} \right) = \frac{1}{Q} - \frac{1}{Q_0} = -(B_Q + B'_Q \tan \delta) \frac{\Delta f}{f} \quad (\text{I-12})$$

where  $A$ ,  $B_Q$  and  $B'_Q$  are constants determined by the tip-resonator geometry, and  $f_0$  and  $Q_0$  are respectively the resonant frequency and quality factor of the resonator without a sample present near the tip.

### I.3.4.2 Transmission line method

Apart from the cavity perturbation that relates the  $Q$  and  $f$  to the electrical properties of the material under test, in the following a transmission line method is developed to determine quantitative electrical properties of nanoscale samples through reflection/transmission coefficients measurements [GRA 14]. As a matter of fact, the impedance  $Z_S$  of the probe-sample interaction can be related to the reflection coefficient  $\Gamma_S$  [HUB 10] [MOE 14]:

$$\Gamma_S = \frac{Z_S - Z_0}{Z_S + Z_0} \quad (\text{I-13})$$

with  $Z_0$  the vector network analyzer (VNA) characteristic impedance ( $50 \Omega$ ). The relation between the tip impedance  $Z_S$  and the permittivity of material  $\varepsilon^*$  has already been given by Eqn. I-2. Especially, when only the coupling capacitance of the tip-metal is considered,  $Z_S$  can be written as:

$$Z_S = \frac{1}{j\omega C_c} \quad (\text{I-14})$$

Here, we consider the case when the microwave characterization is performed by means of the reflection coefficient ( $S_{11m}$ ). In this case, a one-port vector calibration model is used to make the link between the reflection coefficient  $S_{11m}$  measured by the VNA and the reflection coefficient  $\Gamma_S$ . The relation can be expressed in the following form:

$$S_{11m} = e_{00} + \frac{(e_{10}e_{01})\Gamma_S}{1 - \Gamma_S e_{11}} \quad (\text{I-15})$$

$e_{00}$ ,  $e_{11}$  and  $e_{10}e_{01}$  are three complex errors parameters which have to be obtained from the calibration process. These three terms can be extracted by measuring three reflection coefficients for three known calibration standards  $Z_{S1}$ ,  $Z_{S2}$  and  $Z_{S3}$  with reflection coefficients  $\Gamma_{S1}$ ,  $\Gamma_{S2}$  and  $\Gamma_{S3}$ . Once these three calibration terms are determined, the electrical properties can be calculated by exploiting the Eqns. I-13 and I-15.

### **I.3.5 Conclusion**

In this part, first the modeling of the tip-sample interaction is carefully discussed. As the tip radius and the tip-sample distance are much smaller than the wavelength, the tip-sample electric field can be solved by the electrostatic model. Thus the lumped element model can be applied to represent the materials under test including dielectrics, semiconductors and metals. Additionally, the coupling capacitance of tip-sample interaction is investigated when considering a metal plate as the material under test. In order to quantify this coupling capacitance, there are generally two approaches which are the image and surface integration methods. By analyzing the capacitance calculated by these two methods, it is found that the two models agree well with each other for the different tip radius investigated. As the typical tip apex is in the micrometer-size, the corresponding capacitance value is in the level of femto Farad. Furthermore, the capacitance value decreases when the stand-off distance increases. After studying the tip-sample interaction through an electrostatic model, we can quantify the local electrical properties (i.e. complex permittivity, conductivity) from the measurement data (resonant frequency, quality factor and reflection/transmission coefficient), which is the aim of the NFMM. Thus two most widely used quantification methods which are cavity perturbation and transmission line methods are discussed. The cavity perturbation method relates the measured Q and F to the electrical properties while the transmission line method uses the reflection/transmission coefficients. Standard loads should be carefully defined as reference or calibration kits for these two methods [IMT 05], [IMT 07], [GAO 04a], [GRA 14].

## **I.4 Conclusion**

At the beginning of this chapter, a brief introduction to the history of the near-field microwave microscope is given. As the near-field microwave microscope is basically built on the combination of an evanescent microwave probe, a microwave source and a positioning controlling unit, we present in the second section microwave microscopes platforms in terms of different probes categories including coaxial probe, waveguide-based probe, microstrip line-based probe, magnetic-based probe, AFM-based probe, and STM-based probe. NFMM has exhibited great potentials in the characterizations of various kinds of materials/devices such as dielectric films, integrated circuits (IC), semiconductors, graphene, aqueous solutions and biological tissues. Indeed, compared with conventional microwave methods, the NFMM has great advantages to address non-destructive and non-contact characterizations of materials with high spatial resolution and sensitivity. Especially, thanks to this possibility of local characterization, electronic inhomogeneities of materials or structures can be carefully evaluated. Additionally, the microwaves generated by the probe can penetrate the sample to some extent, allowing imaging of subsurface structures.

In the third section of this chapter, the lumped model is used to interpret the tip-sample impedance as in the near-field region, the tip-sample interaction can be solved in electrostatic method. A metal is selected as the material under test for an example. Thus, the tip-metal interaction is simplified as a coupling capacitance. Generally, there are two mathematical methods allowing to quantify this capacitance: image and surface integration methods. Afterwards, to retrieve the electrical properties (complex permittivity, conductivity) of the materials under test, two main quantification methods of NFMM (cavity perturbation and transmission line methods) are discussed. Especially, the perturbation method is usually based on the quality factor and resonance frequency while the transmission method is closely related to the reflection/transmission coefficient. Finally, both approaches require well defined loads as reference or calibration standards. Moreover, the coupling capacitance mentioned above is commonly used as a calibration standard.

In the following chapter, the mismatch problem between the network analyzer and the microwave probe is described and an interferometric technique is proposed as

a matching network to guarantee a good measurement sensitivity. Then, the interferometer-based NFMM is presented and the microwave parts of the platform are carefully characterized. Finally, the performance of the system is evaluated through the repeatability study.

## I.5 References

(73 references, Classified in alphabetical order)

- [ANL 07] S. M. Anlage, V. V. Talanov and A. R. Schwartz, “Principles of near-field microwave microscopy,” *Scanning probe microscopy*, Springer New York, pp. 215-253, 2007.
- [ASH 72] E. A. Ash and G. Nicholls, “Super-resolution aperture scanning microscope.,” *Nature*, vol. 237, n<sup>o</sup>. 5357, pp. 510–512, 1972.
- [BER 15] S. Berweger, J. C. Weber, J. John, J. M. Velazquez, A. Pieterick, N. A. Sanford, A. V. Davydov, B. Brunshwig, N. S. Lewis, T. M. Wallis, and P. Kabos, “Microwave Near-Field Imaging of Two-Dimensional Semiconductors,” *Nano Lett.*, vol. 15, n<sup>o</sup>. 2, pp. 1122–1127, 2015.
- [BIA 16] M. C. Biagi, R. Fabregas, G. Gramse, M. Van Der Hofstadt, A. Juárez, F. Kienberger, L. Fumagalli, and G. Gomila, “Nanoscale Electric Permittivity of Single Bacterial Cells at Gigahertz Frequencies by Scanning Microwave Microscopy,” *ACS Nano*, vol. 10, n<sup>o</sup>. 1, pp. 280–288, 2016.
- [BRI 15] E. Brinciotti, G. Gramse, S. Hommel, T. Schweinboeck, A. Altes, M. A. Fenner, J. Smoliner, M. Kasper, G. Badino, S. S. Tuca, and F. Kienberger, “Probing resistivity and doping concentration of semiconductors at the nanoscale using scanning microwave microscopy,” *Nanoscale*, vol. 7, n<sup>o</sup>. 35, pp. 14715–14722, 2015.
- [BRY 65] C. A. Bryant and J. B. Gunn, “Noncontact Technique for the Local Measurement of Semiconductor Resistivity,” *Rev. Sci. Instrum.*, vol. 36, p. 1614, 1965.
- [CHI 12] J. D. Chisum and Z. Popovi, “Performance limitations and measurement analysis of a near-field microwave microscope for nondestructive and subsurface detection,” *IEEE Trans. Microw. Theory Tech.*, vol. 60, n<sup>o</sup>. 8, pp. 2605–2615, 2012.
- [DUR 66] E. Durand, *Electrostatique Tome II. Problèmes Généraux Conducteurs*. Masson, 1966.
- [FAR 11a] M. Farina, A. Lucesoli, T. Pietrangelo, A. di Donato, S. Fabiani, G. Venanzoni, D. Mencarelli, T. Rozzi, and A. Morini, “Disentangling time in a near-field approach to scanning probe microscopy,” *Nanoscale*, vol. 3, n<sup>o</sup>. 9, pp. 3589–93, 2011.
- [FAR 11b] M. Farina, D. Mencarelli, A. Di Donato, G. Venanzoni, and A. Morini, “Calibration Protocol for Broadband Near-Field Microwave Microscopy,” *IEEE Trans. Microw. Theory Tech.*, vol. 59, n<sup>o</sup>. 10, pp. 2769–2776, 2011.
- [FAR 12a] M. Farina, A. Di Donato, T. Monti, T. Pietrangelo, T. Da Ros, A. Turco, G. Venanzoni, and A. Morini, “Tomographic effects of near-field microwave microscopy in the investigation of muscle cells interacting with multi-walled carbon nanotubes,” *Appl. Phys. Lett.*, vol. 101, n<sup>o</sup>. 20, 2012.
- [FAR 12b] M. Farina, A. Di Donato, D. Mencarelli, G. Venanzoni, and A. Morini, “High resolution scanning microwave microscopy for applications in liquid environment,” *IEEE Microw. Wirel. Components Lett.*, vol. 22, n<sup>o</sup>. 11, pp. 595–597, 2012.

- [FRA 59] Z. Frait, “The use of high-frequency modulation in studying ferromagnetic resonance,” *Czechoslov. J. Phys.*, vol. 9, n<sup>o</sup>. 3, pp. 403–404, 1959.
- [GAO 98] C. Gao and X. Xiang, “Quantitative microwave near-field microscopy of dielectric properties,” *Rev. Sci. Instrum.*, vol. 69, n<sup>o</sup>. 11, pp. 3846–3849, 1998.
- [GAO 99] C. Gao, F. Duewer, X. Xiang, C. Gao, F. Duewer, and X. Xiang, “Quantitative microwave evanescent microscopy,” *Appl. Phys. Lett.*, vol. 75, n<sup>o</sup>. 19, p. 3005, 1999.
- [GAO 04a] C. Gao, B. Hu, I. Takeuchi, K. Chang, X. Xiang, and G. Wang, “Quantitative scanning evanescent microwave microscopy and its applications in characterization of functional materials libraries,” *Meas. Sci. Technol.*, vol. 16, n<sup>o</sup>. 1, pp. 248–260, 2004.
- [GAO 04b] C. Gao, B. Hu, P. Zhang, M. Huang, W. Liu, I. Takeuchi, “Quantitative microwave evanescent microscopy of dielectric thin films using a recursive image charge approach,” *Appl. Phys. Lett.*, vol. 84, n<sup>o</sup>. 23, pp. 4647–4649, 2004.
- [GOL 00] M. Golosovsky, a. F. Lann, D. Davidov, and a. Frenkel, “Microwave near-field imaging of conducting objects of a simple geometric shape,” *Rev. Sci. Instrum.*, vol. 71, n<sup>o</sup>. 10, p. 3927, 2000.
- [GRA 14] G. Gramse, M. Kasper, L. Fumagalli, G. Gomila, P. Hinterdorfer, and F. Kienberger, “Calibrated complex impedance and permittivity measurements with scanning microwave microscopy,” *Nanotechnology*, vol. 25, n<sup>o</sup>. 14, p. 145703, 2014.
- [GRA 15] G. Gramse, E. Brinciotti, A. Lucibello, S. B. Patil, M. Kasper, C. Rankl, R. Giridharagopal, P. Hinterdorfer, R. Marcelli, and F. Kienberger, “Quantitative sub-surface and non-contact imaging using scanning microwave microscopy,” *Nanotechnology*, vol. 26, n<sup>o</sup>. 13, p. 135701, 2015.
- [GRE 16] A. P. Gregory, J. F. Blackburn, K. Lees, R. N. Clarke, T. E. Hodgetts, S. M. Hanham, and N. Klein, “Measurement of the permittivity and loss of high-loss materials using a Near-Field Scanning Microwave Microscope,” *Ultramicroscopy*, vol. 161, pp. 137–145, 2016.
- [HAD 12] K. Haddadi and T. Lasri, “60-GHz Near-Field Six-Port Microscope Using a Scanning Slit Probe for Subsurface Sensing,” *IEEE Sens. J.*, vol. 12, n<sup>o</sup>. 8, pp. 2575–2576, 2012.
- [HAD 13] K. Haddadi and T. Lasri, “Scanning microwave near-field microscope based on the multiport technology,” *IEEE Trans. Instrum. Meas.*, vol. 62, n<sup>o</sup>. 12, pp. 3189–3193, 2013.
- [HOF 14] J. Hoffmann, G. Gramse, J. Niegemann, M. Zeier, and F. Kienberger, “Measuring low loss dielectric substrates with scanning probe microscopes,” *Appl. Phys. Lett.*, vol. 105, n<sup>o</sup>. 1, pp. 1–5, 2014.
- [HUB 10] H. P. Huber, M. Moertelmaier, T. M. Wallis, C. J. Chiang, M. Hochleitner, A. Imtiaz, Y. J. Oh, K. Schilcher, M. Dieudonne, J. Smoliner, P. Hinterdorfer, S. J. Rosner, H. Tanbakuchi, P. Kabos, and F. Kienberger, “Calibrated nanoscale capacitance measurements using a scanning microwave microscope,” *Rev. Sci. Instrum.*, vol. 81, n<sup>o</sup>. 11, 2010.

- [HUD 98] S. Hudlet, M. Saint Jean, C. Guthmann, and J. Berger, "Evaluation of the capacitive force between an atomic force microscopy tip and a metallic surface," *Eur. Phys. J. B*, vol. 10, n<sup>o</sup>. 1, pp. 5–10, 1998.
- [HUM 11] I. Humer, O. Bethge, M. Bodnarchuk, M. Kovalenko, M. Yarema, W. Heiss, H. P. Huber, M. Hochleitner, P. Hinterdorfer, F. Kienberger, and J. Smoliner, "Scanning microwave microscopy and scanning capacitance microscopy on colloidal nanocrystals," *J. Appl. Phys.*, vol. 109, n<sup>o</sup>. 6, 2011.
- [IMT 05] A. Imtiaz, M. Pollak, S. M. Anlage, J. D. Barry, J. Melngailis, "Near-field microwave microscopy on nanometer length scales," *J. Appl. Phys.*, vol. 97, n<sup>o</sup>. 4, 2011.
- [IMT 07] A. Imtiaz, T. Baldwin, H. T. Nembach, T. M. Wallis, P. Kabos, "Near-field microwave microscope measurements to characterize bulk material properties," *Appl. Phys. Lett.*, vol. 90, n<sup>o</sup>. 24, 2007.
- [IMT 14a] A. Imtiaz, T. M. Wallis, and P. Kabos, "Near-Field Scanning Microwave Microscopy," *IEEE Microw. Mag.*, n<sup>o</sup>. 2, pp. 52–64, 2014.
- [IMT 14b] A. Imtiaz, T. M. Wallis, J. C. Weber, K. J. Coakley, M. D. Brubaker, P. T. Blanchard, K. A. Bertness, N. A. Sanford, and P. Kabos, "Imaging the p-n junction in a gallium nitride nanowire with a scanning microwave microscope," *Appl. Phys. Lett.*, vol. 104, n<sup>o</sup>. 26, 2014.
- [KAR 08] A. Karbassi, D. Ruf, A. D. Bettermann, C. A. Paulson, D. W. Van Der Weide, H. Tanbakuchi, and R. Stancliff, "Quantitative scanning near-field microwave microscopy for thin film dielectric constant measurement," *Rev. Sci. Instrum.*, vol. 79, n<sup>o</sup>. 9, 2008.
- [KHA 07] S. Kharkovsky and R. Zoughi, "Microwave and millimeter wave nondestructive testing and evaluation - overview and recent advances," *IEEE Instrum. Meas. Mag.*, vol. 10, n<sup>o</sup>. 2, pp. 26–38, 2007.
- [KIM 05] S. Kim, H. Yoo, K. Lee, B. Friedman, M. A. Gaspar, and R. Levicky, "Distance control for a near-field scanning microwave microscope in liquid using a quartz tuning fork," *Appl. Phys. Lett.*, vol. 86, n<sup>o</sup>. 15, pp. 1–3, 2005.
- [KUN 09] W. Kundhikanjana, K. Lai, H. Wang, H. Dai, M. A. Kelly, and Z. X. Shen, "Hierarchy of electronic properties of chemically derived and pristine graphene probed by microwave imaging," *Nano Lett.*, vol. 9, n<sup>o</sup>. 11, pp. 3762–3765, 2009.
- [LAI 09a] K. Lai, W. Kundhikanjana, H. Peng, Y. Cui, M. A. Kelly, and Z. X. Shen, "Tapping mode microwave impedance microscopy," *Rev. Sci. Instrum.*, vol. 80, n<sup>o</sup>. 4, p. 043707, 2009.
- [LAI 09b] K. Lai, H. Peng, W. Kundhikanjana, D. T. Schoen, C. Xie, S. Meister, Y. Cui, M. A. Kelly, and Z. X. Shen, "Nanoscale electronic inhomogeneity in In<sub>2</sub>Se<sub>3</sub> nanoribbons revealed by microwave impedance microscopy," *Nano Lett.*, vol. 9, n<sup>o</sup>. 3, pp. 1265–1269, 2009.
- [LAI 11] K. Lai, W. Kundhikanjana, M. A. Kelly, and Z.-X. Shen, "Nanoscale microwave microscopy using shielded cantilever probes," *Applied Nanoscience*, vol. 1, n<sup>o</sup>. 1, pp. 13–18, 2011.
- [LAW 02] B. M. Law and F. Rieutord, "Electrostatic forces in atomic force microscopy," *Phys. Rev. B*, vol. 66, n<sup>o</sup>. 3, pp. 2–7, 2002.

- [LU 97] Y. Lu, T. Wei, F. Duewer, Y. Lu, N. Ben Ming, P. G. Schultz, and X. D. Xiang, “Nondestructive Imaging of Dielectric-Constant Profiles and Ferroelectric Domains with a Scanning-Tip Microwave Near-Field Microscope,” *Science*, vol. 276, n<sup>o</sup>. 5321, pp. 2004–2006, 1997.
- [MAL 16] O. Malyuskin and V. F. Fusco, “High-Resolution Microwave Near-Field Surface Imaging Using Resonance Probes,” *IEEE Trans. Instrum. Meas.*, vol. 65, n<sup>o</sup>. 1, pp. 189–200, 2016.
- [MOE 14] M. Moertelmaier, H. P. Huber, C. Rankl, and F. Kienberger, “Continuous capacitance-voltage spectroscopy mapping for scanning microwave microscopy,” *Ultramicroscopy*, vol. 136, pp. 67–72, 2014.
- [MON 12] T. Monti, A. Di Donato, and M. Farina, “High resolution imaging of few-layer graphene by Near-Field Scanning Microwave Microscopy,” *J. Appl. Phys.*, vol. 111, n<sup>o</sup>. 6, p. 064305, 2012.
- [MON 13] T. Monti, A. Di Donato, D. Mencarelli, G. Venanzoni, A. Morini, and M. Farina, “Near-field microwave investigation of electrical properties of graphene-ITO electrodes for LED applications,” *IEEE/OSA J. Disp. Technol.*, vol. 9, n<sup>o</sup>. 6, pp. 504–510, 2013.
- [MOO 65] G.E Moore, “Cramming more components onto integrated circuits,” *IEEE Solid-State Circuits Newsletter*, vol. 3, n<sup>o</sup>. 20, pp. 33-35, 1965.
- [OMA 15] R. Omarouayache, P. Payet, J. Raoult, and L. Chusseau, “Millimeter-wave near-field imaging with bow-tie antennas”, *Optics express*, vol. 23, n<sup>o</sup>. 9, pp.12144-12151, 2015
- [OPT 14] V. Optasanu, E. Bourillot, P. Vitry, C. Plassard, L. Beurenaut, P. Jacquinet, F. Herbst, P. Berger, E. Lesniewska, and T. Montessin, “High-resolution characterization of the diffusion of light chemical elements in metallic components by scanning microwave microscopy,” *Nanoscale*, vol. 6, n<sup>o</sup>. 24, pp. 14932–14938, 2014.
- [PAR 05] J. Park, S. Hyun, A. Kim, T. Kim, and K. Char, “Observation of biological samples using a scanning microwave microscope,” *Ultramicroscopy*, vol. 102, n<sup>o</sup>. 2, pp. 101–106, 2005.
- [POZ 12] D. Pozar, *Microwave Engineering Fourth Edition*. Wiley, 2012.
- [QAD 07] N. N. Qaddoumi, W. M. Saleh, and M. Abou-Khousa, “Innovative Near-Field Microwave Nondestructive Testing of Corroded Metallic Structures Utilizing,” *IEEE Trans. Instrum. Meas.*, vol. 56, n<sup>o</sup>. 5, pp. 1961–1966, 2007.
- [REZ 14] A. N. Reznik, “Electromagnetic model for near-field microwave microscope with atomic resolution: Determination of tunnel junction impedance  
Electromagnetic model for near-field microwave microscope with atomic resolution: Determination of tunnel junction impedance,” *Appl. Phys. Lett.*, vol. 105, n<sup>o</sup>. 8, 2014.
- [SOO 62] R. F. Soohoo, “A Microwave Magnetic Microscope”, vol. 33, pp. 1276, 1962.,” *J. Appl. Phys.*, vol. 33, p. 1276, 1962.
- [STE 98] D. E. Steinhauer, C. P. Vlahacos, S. K. Dutta, B. J. Feenstra, F. C. Wellstood, and S. M. Anlage, “Quantitative imaging of sheet resistance with a scanning near-field microwave microscope,” *Appl. Phys. Lett.*, vol. 72, n<sup>o</sup>. 7, pp. 861–863, 1998.

- [STE 00] D. E. Steinhauer, C. P. Vlahacos, F. C. Wellstood, S. M. Anlage, C. Canedy, R. Ramesh, A. Stanishevsky, and J. Melngailis, “Quantitative imaging of dielectric permittivity and tunability with a near-field scanning microwave microscope,” *Rev. Sci. Instrum.*, vol. 2751, n<sup>o</sup>. 2000, 12, 2000.
- [SUN 14] W. Sun, Y. Yang, Z. Wu, T. Feng, Q. Zhuang, L. M. Peng, S. Xu, and C. K. Ong, “Penetrative imaging of sub-surface microstructures with a near-field microwave microscope,” *J. Appl. Phys.*, vol. 116, n<sup>o</sup>. 4, 2014.
- [SYN 28] E. H. Sygne, “A Suggested Method for Extending Microscopic Resolution into the Ultra- Microscopic Region,” *Philos. Mag.*, vol. 6, p. 356, 1928.
- [TAB 99a] M. Tabib-Azar, D. Su, A. Pohar, S. R. LeClair, and G. Ponchak, “0.4  $\mu\text{m}$  spatial resolution with 1 GHz ( $\lambda=30$  cm) evanescent microwave probe,” *Rev. Sci. Instrum.*, vol. 70, n<sup>o</sup>. 3, pp. 1725–1729, 1999.
- [TAB 99b] M. Tabib-Azar, D. Akinwande, G. E. Ponchak, and S. R. LeClair, “Evanescent Microwave Probes on High-Resistivity Silicon and its Application in Characterization of Semiconductors,” *Rev. Sci. Instrum.*, vol. 70, n<sup>o</sup>. 7, pp. 3083–3086, 1999.
- [TAB 99c] M. Tabib-Azar, D. Akinwande, G. Ponchak, and S. R. LeClair, “Novel physical sensors using evanescent microwave probes,” *Rev. Sci. Instrum.*, vol. 70, n<sup>o</sup>. 8, p. 3381, 1999.
- [TAB 00] M. Tabib-Azar and S. R. Leclair, “Applications of evanescent microwave probes in gas and chemical sensors,” *Sensors Actuators, B Chem.*, vol. 67, n<sup>o</sup>. 1, pp. 112–121, 2000.
- [TAB 04] M. Tabib-Azar and Y. Wang, “Design and fabrication of scanning near-field microwave probes compatible with atomic force microscopy to image embedded nanostructures,” *IEEE Trans. Microw. Theory Tech.*, vol. 52, n<sup>o</sup>. 3, pp. 971–979, 2004.
- [TAI 11] T. Tai, X. X. Xi, C. G. Zhuang, D. I. Mircea, and S. M. Anlage, “Nonlinear near-field microwave microscope for RF defect localization in superconductors,” *IEEE Trans. Appl. Supercond.*, vol. 21, n<sup>o</sup>. 3, pp. 2615–2618, 2011.
- [TAK 15] H. Takahashi, Y. Imai, and A. Maeda, “Near-field microwave imaging of inhomogeneous  $\text{K}_x\text{Fe}_y\text{Se}_2$ : Separation of topographic and electric features,” *Appl. Phys. Lett.*, vol. 106, n<sup>o</sup>. 23, 2015.
- [TAL 09] V. V. Talanov and A. R. Schwartz, “Near-field scanning microwave microscope for interline capacitance characterization of nanoelectronics interconnect,” *IEEE Trans. Microw. Theory Tech.*, vol. 57, n<sup>o</sup>. 5, pp. 1224–1229, 2009.
- [TAL 10] V. V. Talanov, C. Del Barga, L. Wickey, I. Kalichava, E. Gonzales, E. A. Shaner, A. V. Gin, and N. G. Kalugin, “Few-Layer Graphene Characterization by Near-Field Scanning Microwave Microscopy,” *ACS Nano*, vol. 4, n<sup>o</sup>. 7, pp. 3831–3838, 2010.
- [TSE 07] A. Tselev, S. M. Anlage, Z. Ma, and J. Melngailis, “Broadband dielectric microwave microscopy on micron length scales,” *Rev. Sci. Instrum.*, vol. 78, n<sup>o</sup>. 4, 2007.

- [TSE 13] A. Tselev, V. K. Sangwan, D. Jariwala, T. J. Marks, L. J. Lauhon, M. C. Hersam, and S. V. Kalinin, “Near-field microwave microscopy of high-oxides grown on graphene with an organic seeding layer,” *Appl. Phys. Lett.*, vol. 103, n<sup>o</sup>. 24, pp. 10–15, 2013.
- [TUC 16] S. S. Tuca, G. Badino, G. Gramse, E. Brinciotti, M. Kasper, Y. J. Oh, R. Zhu, C. Rankl, P. Hinterdorfer, and F. Kienberger, “Calibrated complex impedance of CHO cells and *E. coli* bacteria at GHz frequencies using scanning microwave microscopy,” *Nanotechnology*, vol. 27, n<sup>o</sup>. 13, p. 135702, 2016.
- [WAN 90] M. S. Wang and J. M. Borrego, “High-Resolution Scanning Microwave Electric-Field Probe for Dielectric Constant Uniformity Measurement,” *Mater. Eval.*, pp. 1106–1109, 1990.
- [WAN 05] R. Wang, F. Li, and M. Tabib-Azar, “Calibration methods of a 2 GHz evanescent microwave magnetic probe for noncontact and nondestructive metal characterization for corrosion, defects, conductivity, and thickness nonuniformities,” *Rev. Sci. Instrum.*, vol. 76, n<sup>o</sup>. 5, pp. 0–13, 2005.
- [WAN 07] R. Wang and M. Tabib-Azar, “Noncontact Evanescent Microwave Magnetic Dipole Probe Imaging of Ferromagnets,” *IEEE Trans. Magn.*, vol. 43, n<sup>o</sup>. 7, pp. 3165–3170, 2007.
- [WEB 12] J. C. Weber, J. B. Schlager, N. A. Sanford, A. Imtiaz, T. M. Wallis, L. M. Mansfield, K. J. Coakley, K. A. Bertness, P. Kabos, and V. M. Bright, “A near-field scanning microwave microscope for characterization of inhomogeneous photovoltaics,” *Rev. Sci. Instrum.*, vol. 83, n<sup>o</sup>. 8, 2012.
- [WU 15] Z. Wu, W. Q. Sun, T. Feng, S. W. Tang, G. Li, K. L. Jiang, S. Y. Xu, and C. K. Ong, “Imaging of soft material with carbon nanotube tip using near-field scanning microwave microscopy,” *Ultramicroscopy*, vol. 148, pp. 75–80, 2015.

## **Chapter II**

# **Interferometer-based near-field microwave microscope (iNFMM)**

### **II.1 Introduction**

Although the near-field microwave microscopy (NFMM) has established its great potential in local characterizations of numerous kinds of materials with nanoscale resolution, there are still some obstacles to be overcome for a routine use. Actually, as mentioned in Chapter I, the microwave microscope usually combines an evanescent microwave probe (EMP) with impedance in the range of tens or hundreds of  $k\Omega$  [HAD 12], [MIC 15], with a microwave measurement system (e.g. VNA) with intrinsic impedance of  $50 \Omega$ . Hence, a mismatch problem appears when directly connecting the EMP to the VNA, resulting in a reflection coefficient close to one and a poor measurement sensitivity. Because the VNA works at its best sensitivity when the load impedance is around  $50 \Omega$ , matching techniques should be developed to transform the high impedance load down to  $50 \Omega$ .

Generally speaking, microwave approaches to match the high impedance probe to VNA can be ranged in two classes: resonator-based methods and interferometer-based techniques. Actually, the resonator-based NFMMs including cavity-based and  $\lambda/4$  transmission line-based structures are widely found in the literature [TAL 09], [CHI 12], [GRA 15], as already discussed in Chapter I. Nonetheless, most of the resonator-based microscopes operate at limited frequency bands because the resonator is usually designed at only one or a few resonant frequencies. Even though some researches have demonstrated dielectric characterizations in a wide frequency range [TSE 07], the sensitivity reported is not equally high in the entire frequency band investigated. Another limitation of this method is the fall of the quality factor of the resonator in the presence of high-loss materials such as liquids [KIM 05], [PAR 05]. This limitation brings difficulties for resonator-based structures to precisely analyze biological tissues and fluids.

Recently, more attention is paid to another type of matching method: the interferometric technique. Actually, this technique is realized by adding an interferometric circuit into the microwave system. The general principle of the circuit is to generate a signal to compensate the reflected signal of the high impedance probe. This signal provided by the interferometer should have an equal magnitude and an opposite phase-shift compared to the reflected signal of the probe. The resulting combined signal becomes the reference signal, called “zero level signal”. By applying this wave-cancelling process, the high impedance probe can be well matched to the VNA. Afterwards, a very small variation of signal around this zero level can be detected by the VNA, leading to an increased measurement sensitivity and a better accuracy for the characterization of high-impedance DUT.

There has been many research works focused on the interferometer-based NFMM platforms. In fact, at IEMN (Institute of Electronics, Microelectronics and Nanotechnologies), many advanced studies are devoted to the development and improvement of this kind of structures. For example, Debroucke *et al.* measured the capacitance (300 aF) at 4 GHz of Metal-Oxide-Semiconductor (MOS) varactors by using an interferometer-based probing system [DEB 10], [DEB 11]. Especially, in MITEC Group, a home-made microwave microscope integrating an interferometric technique is developed and many applications have been addressed [HAD 11], [HAD 12], [HAD 14], [BAK 13], [BAK 14]. High measurement sensitivity was found when investigating aqueous saline solutions at 2.45 GHz [HAD 12]. Afterwards, some surface scanning applications over metallic and dielectric materials were demonstrated by using the same platform at 2.5 GHz [HAD 14]. Based on a similar configuration, Bakli *et al.* obtained good measurement sensitivity over metallic samples in a wider frequency range [2-6 GHz] [BAK 14]. Apart from these home-made structures, in very recent years, commercial NFMMs developed by Keysight<sup>TM</sup> have been modified by integrating interferometric setup around 4 GHz [DAR 13]. High measurement sensitivity and dynamic range were obtained when evaluating semiconductor samples [DAR 13], [MIC 15]. All these results demonstrate the versatility, applicability and possibilities offered by interferometer-based instruments.

In this work, a home-made NFMM including an interferometric setup is proposed. This study is consecutive to Bakli's work in MITEC group. This chapter dedicated to the interferometer-based near-field microwave microscope (iNFMM) developed is divided into three sections. First, the description of the iNFMM platform is established. To this end, the mismatch issue between the VNA and the high impedance probe is discussed and then the principle of the interferometer is presented. After that, the configuration of the iNFMM setup, including the microwave components (the couplers, the attenuator, the delay line and the microwave probe) and the measurement instrument (VNA) are characterized. After giving these basic information on the iNFMM proposed, the working principle of the EMP and the wave-cancellation process are also theoretically analyzed by using electromagnetic simulation tools such as Ansys<sup>TM</sup>/HFSS and Keysight<sup>TM</sup>/ADS, respectively. In the second section, to better understand the principle of the iNFMM, these important microwave components which compose the system are carefully characterized. Afterwards, the performance of the whole microscope is evaluated by analyzing the measurement sensitivity over the frequency band of interest. Finally, in the last section of this chapter, the measurement repeatability which is one of the most important issues of NFMM is analyzed. This feature greatly influences the stability and accuracy of the measurement results. It is worth noting that this kind of complete study is not generally found in the literature. Thus, a fine analysis of the measurement errors in terms of repeatability is carefully established to provide a guide for best practice in near-field microwave microscopy.

## **II.2 Description of the interferometer-based microwave microscope**

### **II.2.1 Introduction**

To describe the principle of the interferometer-based microwave microscope, we separate this section into three parts. First, we discuss the mismatch problem when connecting the high impedance EMP to the VNA. Some examples are listed to explain the poor measurement sensitivity induced by this problem. As mentioned in the introduction, there are generally two matching techniques: the resonator method and the interferometric method. This study is based on the second one. Thus, in the second part of this section, the principle of the iNFMM is presented. In the third part, we use electromagnetic simulation platforms such as Ansys<sup>TM</sup>/HFSS and Keysight<sup>TM</sup>/ADS to theoretically study the principle of the iNFMM proposed. Especially, the distribution of the electromagnetic field is simulated by Ansys<sup>TM</sup>/HFSS. Then, the performance of the whole system is simulated by Keysight<sup>TM</sup>/ADS.

### **II.2.2 Mismatch issue between the EMP and the VNA**

The main measurement limitation in microwave microscopy applications is the impedance mismatch between the VNA intrinsic impedance, close to  $50 \Omega$  ( $Z_0$ ), and the EMP impedance [GU 14], [GU 15a]. For the demonstration, we first consider a DUT, whose impedance is variable, connected to a VNA. As illustrated in Fig. II-1, when very high impedances (or very low) are considered, most of the incident wave on the DUT is reflected back. For simplicity, a pure resistive impedance is considered.

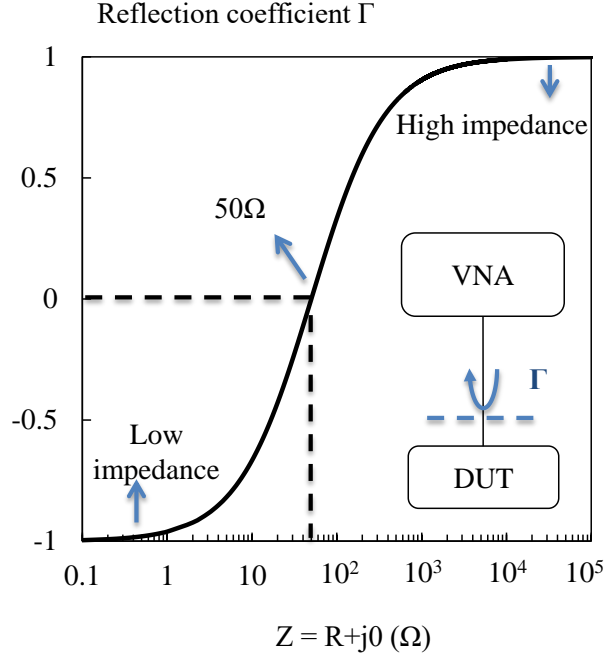


**Fig. II-1:** Reflection coefficient  $\Gamma$  as a function of a pure resistive impedance measured by means of a  $50\ \Omega$  VNA

As can be seen in Fig. II-1, the reflection coefficient  $\Gamma$  is close to -1 for any impedance much lower than  $50\ \Omega$  and close to 1 for any value much higher than  $50\ \Omega$  which is the characteristic impedance of the VNA. However,  $\Gamma$  stays around zero when the DUT is in the order of  $50\ \Omega$  which represents the best sensitive region for the VNA. Indeed, as the reflection coefficient  $\Gamma$  is related to the impedance  $Z_{DUT}$  by the following equation [DAR 13] [WEB 14]:

$$\Gamma = \frac{Z_{DUT} - Z_0}{Z_{DUT} + Z_0}$$

The sensitivity can be evaluated by calculating the derivative of  $\Gamma$  with respect to  $Z_{DUT}$ :

$$\frac{d\Gamma}{dZ_{DUT}} = \frac{d}{dZ_{DUT}} \left[ \frac{Z_{DUT} - Z_0}{Z_{DUT} + Z_0} \right]$$

$$\Delta\Gamma = \left[ \frac{2Z_0}{(Z_{DUT} + Z_0)^2} \right] \Delta Z_{DUT}$$

Actually, for a given  $\Delta Z_{DUT}$ ,  $\Delta \Gamma$  decreases with  $Z_{DUT}^2$ , which means that the sensitivity is strongly degraded when considering a high  $Z_{DUT}$  [DAR 13]. In this work, an interferometric technique is proposed to match the high impedance of the EMP to  $50 \Omega$  under any configurations. The principle of the iNFMM is presented in the following part.

### II.2.3 Configuration of the interferometer-based NFMM

The interferometer-based microwave microscope built up with a VNA, a hybrid coupler, an impedance tuner and an EMP is proposed in Fig. II-2.

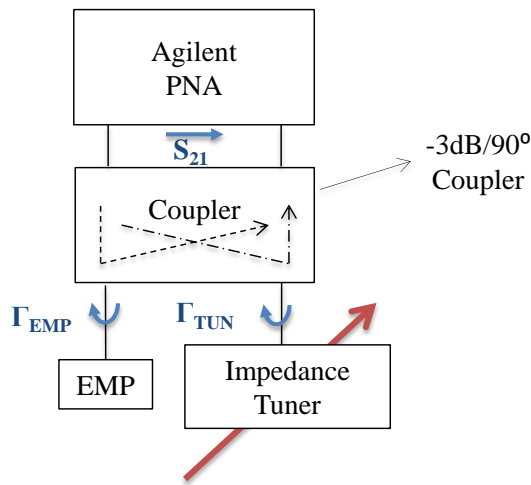


**Fig. II-2:** Schematic of the interferometer-based microwave microscope

The hybrid coupler is connected to the ports 1 and 2 of the VNA. The direct and coupled paths are connected to the EMP (with reflection coefficient  $\Gamma_{EMP}$ ) and to the impedance tuner (with reflection coefficient  $\Gamma_{TUN}$ ) respectively. In this configuration, the coupler has two functions. First, it acts as a reflectometer that separates the incident signal from the one reflected by the EMP. Secondly, by combining the reflected signal with the wave coming from the impedance tuner, it gives the possibility to tune the resulting signal to a very low level. Particularly,  $\Gamma_{TUN}$  is carefully adjusted to compensate  $\Gamma_{EMP}$  by adequately choosing attenuator and phase-shifter positions that lead to a signal with an equal magnitude and an opposite phase-shift when comparing to  $\Gamma_{EMP}$ . This tuning process is illustrated in Fig. II-3.

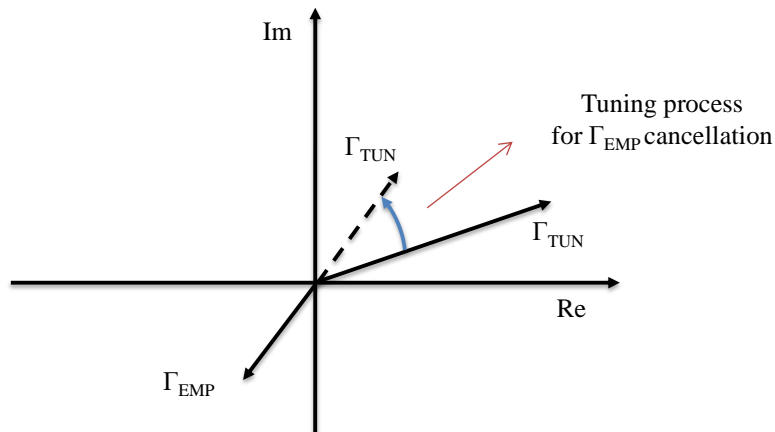


**Fig. II-3:** Wave cancellation process by combining  $\Gamma_{EMP}$  and  $\Gamma_{TUN}$

Thus, the measured transmission coefficient (zero-level signal) is given by:

$$S_{21} = \frac{1}{2}(\Gamma_{EMP} + \Gamma_{TUN}) = 0$$

Ideally, the wave-cancellation technique should be done at any desired operating frequency. This signal is measured in a transmission mode ( $S_{21}$ ) to overcome the main limitation encountered when using VNAs in terms of directivity errors, especially on the measurement of small signals. Thus, the technique gives the possibility to operate in the ultimate sensitivity range of the VNA. The proposed impedance tuner is given in Fig. II-4.

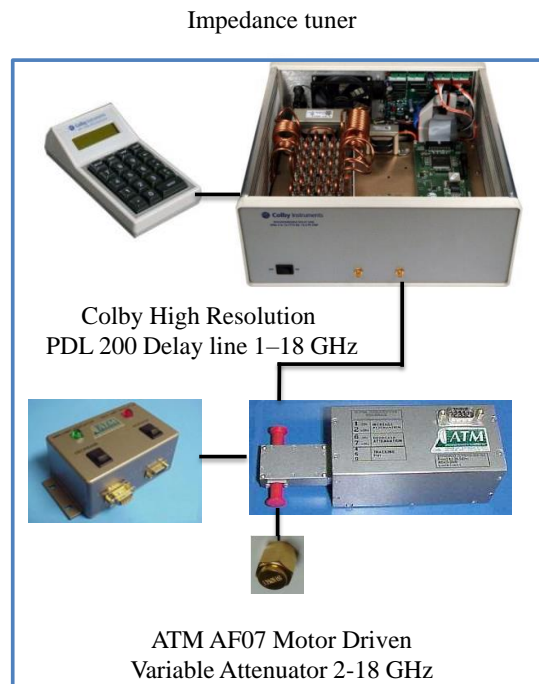


**Fig. II-4:** Impedance tuner included in the iNFMM

It is built up with a high-resolution programmable delay line (Colby Instruments PDL-200A Series) connected to a motor-driven variable attenuator (ATM AF 074H-10-28). The output port of the attenuator is shortcut with a SMA short termination to operate in reflection mode. In the following, the principle of the iNFMM system is theoretically simulated by commercial tools such as Ansys<sup>TM</sup>/HFSS and Keysight<sup>TM</sup>/ADS.

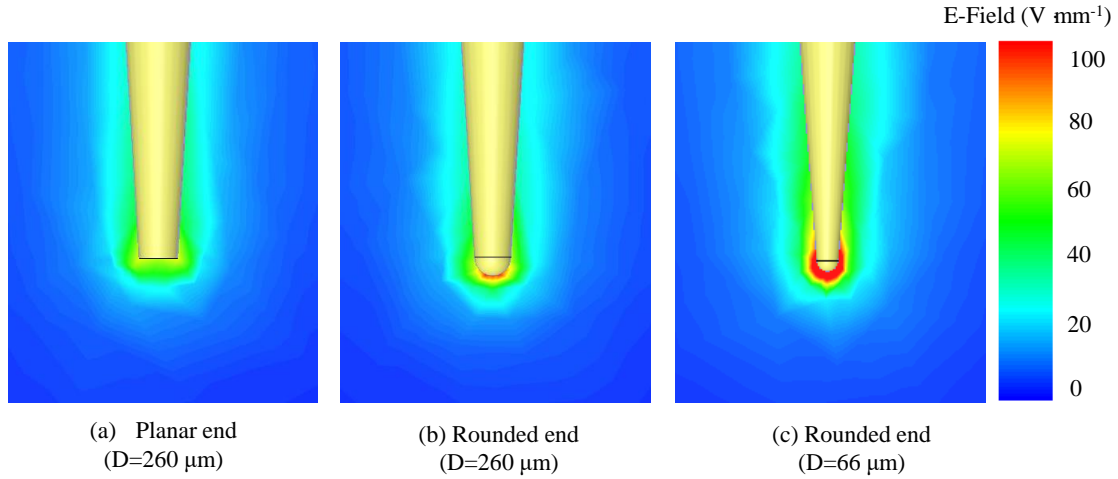
#### **II.2.4 Electromagnetic simulations of the microwave microscope**

Electromagnetic simulation platforms are effective ways to compute the electrical properties of materials, devices and structures for a better understanding of their functioning. In this part, to theoretically analyze the performance of the iNFMM, two commercial simulation tools are exploited: Ansys<sup>TM</sup>/HFSS and Keysight<sup>TM</sup>/ADS. First, the electromagnetic field distribution of the EMP is determined by using Ansys<sup>TM</sup>/HFSS, which permits us to highlight the local characterization possibility provided by the EMP. Afterwards, the behavior of the whole interferometer-based microwave microscope system is simulated by using the Keysight<sup>TM</sup>/ADS platform. The performance of the iNFMM system is studied in two configurations: with and without interferometer.

##### **II.2.4.1 Simulation of the EMP by Ansys<sup>TM</sup>/HFSS**

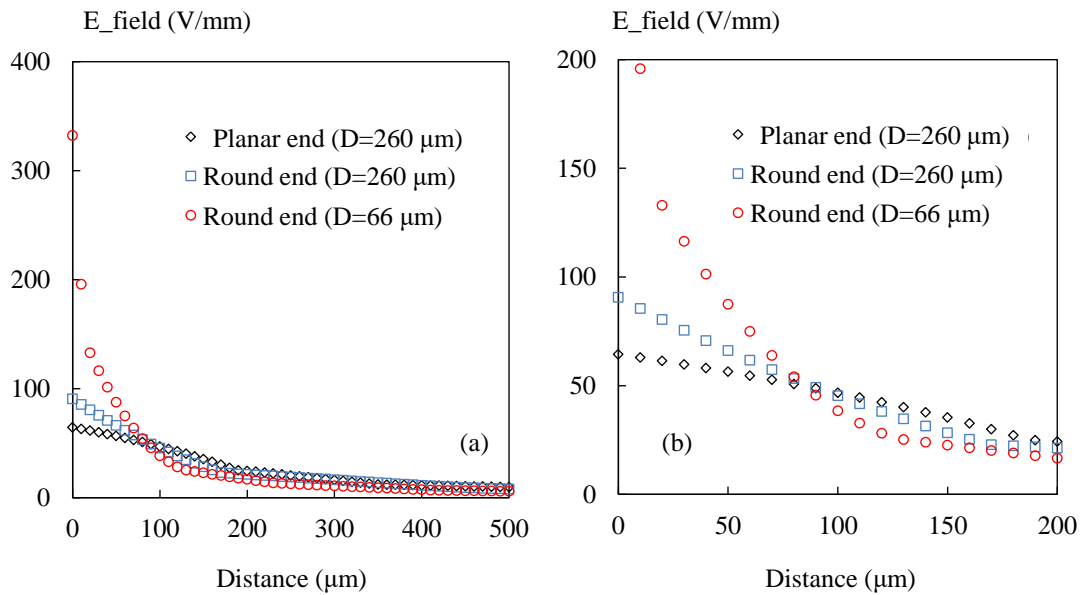
During the measurement, two round end tips ( $D = 260/66 \mu\text{m}$ ) are employed to locally characterize materials. Therefore, the distribution of the electromagnetic energy in the vicinity of the probe tip should be studied.

Fig. II-5 shows the electric field distribution in free-space conditions at 2 GHz for different tip ends: tip with planar end ( $D = 260 \mu\text{m}$ ) and tip with rounded end ( $D = 260/66 \mu\text{m}$ ).



**Fig. II-5:** Simulation of the electric field magnitude for different EMP in free space by using Ansys<sup>TM</sup>/HFSS; (a): EMP with planar end ( $D = 260 \mu\text{m}$ ), (b): EMP with rounded end ( $D = 260 \mu\text{m}$ ), (c): EMP with rounded end ( $D = 66 \mu\text{m}$ ), these images are taken at the cross-section along the probe,  $f = 2 \text{ GHz}$

Based on these simulation results, different conclusions can be drawn. As shown in Fig. II-5, the electric field is confined around the apex of the probe [OLA 13], [OLA 14]. When comparing the planar tip (Fig. II-5.a) and the round tip (Fig. II-5.b), it is noted that the round end tip is a better candidate to focus the electromagnetic energy at the tip end. Furthermore, a smaller probe (Fig. II-5.c) concentrates more field energy, which allows a better local characterization. Thereafter, the E-field is presented as a function of the distance to the tip (Fig. II-6).



**Fig. II-6:** Variation of E-field with the distance to the tip (Ansys<sup>TM</sup>/HFSS); (a) distance from 0 to  $500 \mu\text{m}$ , (b) distance range zoomed from 0 to  $200 \mu\text{m}$ ,  $f = 2 \text{ GHz}$

One can note from Fig. II-6.a that the E-field decays exponentially with the distance to the tip. Particularly, the maximum E-field value for the 66  $\mu\text{m}$ -tip is higher than the value of the 260  $\mu\text{m}$ -tip by a factor of 3.6 (for a distance = 0  $\mu\text{m}$ ) which also corresponds to the apex size ratio between these two tips. From the zoomed stand-off distance window (0 to 200  $\mu\text{m}$ ) in Fig. II-6.b, it is noted that the E-field of the smaller tip (66  $\mu\text{m}$ ) decays faster than the one calculated for the bigger probe. Indeed, the lateral spatial resolution is highly related to the tip apex [COR 15]. For example, considering a tip apex of 66  $\mu\text{m}$ , the corresponding resolution (in the order of apex) is about  $\lambda_0/2270$  at 2 GHz (where  $\lambda_0$  is the free-space wavelength). Furthermore, these results prove the fact that the smaller round tip focuses more E-field around tip apex and allows a better local measurement. So to benefit of the better sensitivity of the probe, the material under investigation must be placed in this near-zone (in the order of the tip apex size).

In the same way, the magnetic field of the two round end probes ( $D = 66/260 \mu\text{m}$ ) is investigated in Fig. II-7.

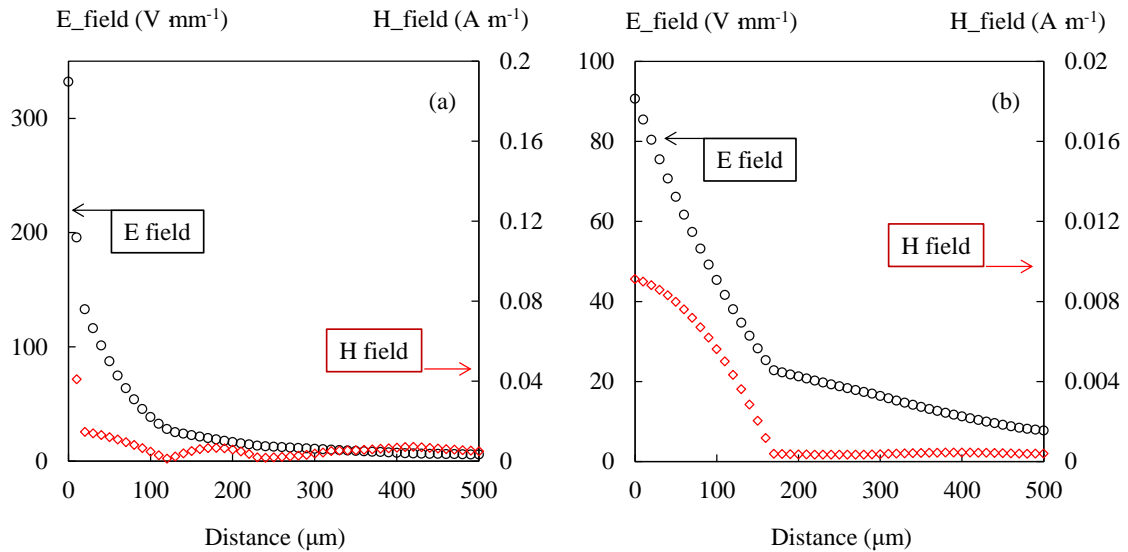


**Fig. II-7:** Variation of electric ( $\circ$ ) and magnetic ( $\diamond$ ) fields as a function of the distance to the tip (Ansys<sup>TM</sup>/HFSS); (a): Probe with apex size  $D = 66 \mu\text{m}$ , (b): probe with apex size  $D = 260 \mu\text{m}$ ,  $f = 2 \text{ GHz}$

Fig. II-7 presents the magnitude of the electric and magnetic fields as a function of the distance to the probe. We can notice that the H-field decays with the distance to the probe. It also indicates that the magnetic field magnitude in the region of the apex

is negligible compared to the electric field. The ratio of the electric and magnetic fields' magnitudes ( $|E|/|H|$ ) is therefore much greater than the vacuum impedance.

The study of the electromagnetic field of the evanescent microwave probe demonstrates that both the electric and magnetic fields decay as a function of distance. Furthermore, the E-field is well focused around the probe tip, which shows the possibility of local characterization provided by the probe. In the following, the behavior of the interferometer-based microwave microscope is simulated by using the Keysight™/ADS platform.

#### II.2.4.2 Simulation of the iNFMM by Keysight™/ADS

To estimate the performance of the interferometric technique, we simulate the whole microwave microscope by using Keysight™/ADS (Fig. II-8). For comparison, the configuration without interferometer is also shown in Fig. II-8. It should be mentioned that for the microwave components such as the attenuator, the phase-shifter and cables, ideal circuit models provided by Keysight™/ADS are considered. Nevertheless, as there is no suitable hybrid coupler in ADS elements library, we have built a data box for the hybrid coupler whose values (scattering parameters as a function of frequency) are extracted from measurement results. Additionally, as the probe presents a high impedance in free space, it is considered as an open circuit.

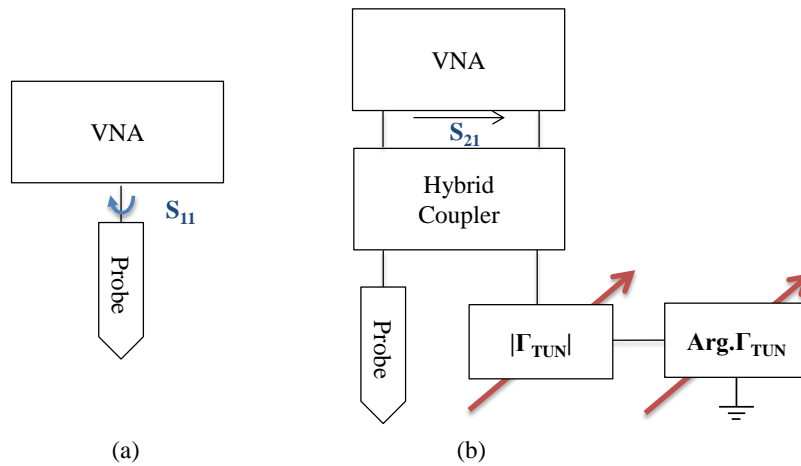


**Fig. II-8:** Schematic of the different configurations simulated by Keysight™/ADS, (a): without interferometer, (b): with interferometer

To demonstrate the performance of the interferometric technique, two microwave microscope configurations are considered: without (Fig. II-8.a) and with the interferometer (Fig. II-8.b). In the setup without interferometer, one port of the VNA is directly connected to the EMP and the reflection coefficient  $S_{11}$  is simulated. In the case with interferometer, as shown in Fig. II-8.b, the transmission coefficient  $S_{21}$  is simulated. As an example, a small frequency range [2-3 GHz] at the beginning of the frequency range available [2-18 GHz] is selected to demonstrate the wave-cancelling process (Fig. II-9.a). Furthermore, in Fig. II-9.b, a selection of a resonant frequency window of  $S_{21}$  from 2.459 to 2.464 GHz is also presented.

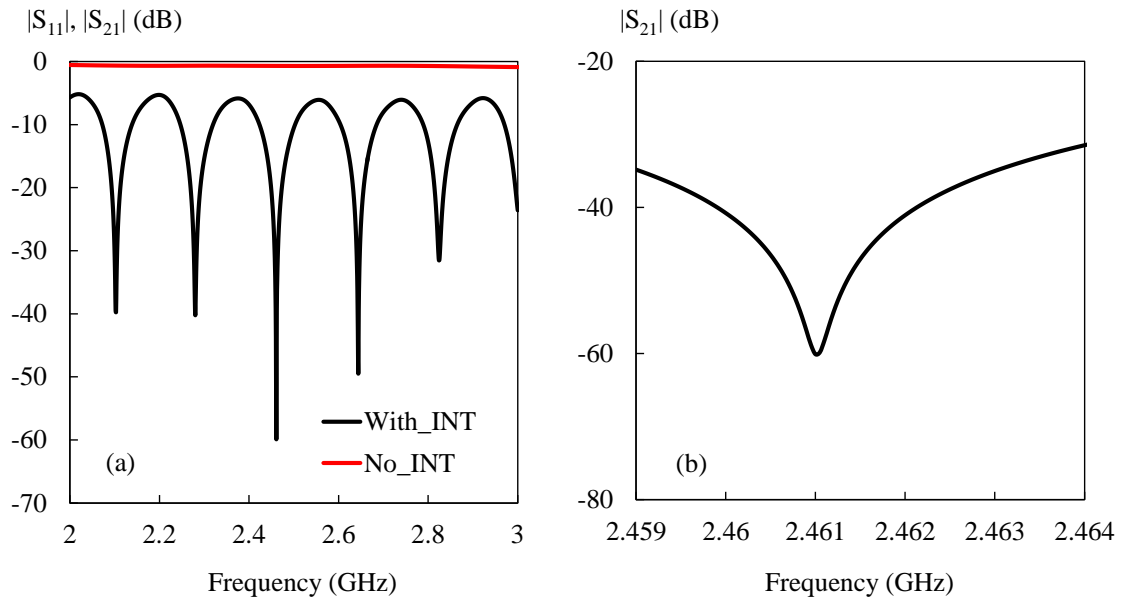


**Fig. II-9:** Simulation (Keysight<sup>TM</sup>/ADS) of the wave-cancelling process under two configurations: with and without the interferometer; (a): frequency range from 2 to 3 GHz, (b): frequency range from 2.459 to 2.464 GHz,  $P_0 = 0$  dBm

As clearly shown in Fig. II-9.a, in the case where no-interferometer is used, the simulation results ( $S_{11}$ ) are very close to 0 dB due to the mismatch problem, which leads to a poor sensitivity. However, by including an interferometer into the NFMM platform, the zero level can be tuned to a low value, (for example, -60 dB, Fig. II-9.a). Actually, this signal can be lower depending on applications. Especially, from 2 to 3 GHz, six successive resonances are observed in this figure. The resonances occur every 170 MHz. To better visualize the resonance peak, we consider the frequency around 2.46 GHz as an example (third peak observed when stepping from 2 GHz to 3 GHz, Fig. II-9.a). From a zoomed frequency window, we observe in Fig. II-9.b that

the probe is actually matched down to -60 dB (35 dB above the noise floor of the VNA) at 2.461 GHz. Additionally, the corresponding quality factor of this resonance is as high as 10254. Thus, the proposed technique largely improves the sensitivity.

### **II.2.5 Conclusion**

In this section, we have first discussed the mismatch problem when connecting directly the high impedance probe to the VNA. To solve this problem, an interferometric technique is proposed in our NFMM configuration. The iNFMM proposed is thus carefully discussed. Afterwards, the simulation tools Ansys<sup>TM</sup>/HFSS and Keysight<sup>TM</sup>/ADS are employed to analyze the performance of the NFMM. First, the distribution of the electromagnetic field of the EMP is demonstrated by Ansys<sup>TM</sup>/HFSS. It is found that the E-field is concentrated around tip apex to enable a very local characterization. Furthermore, the probe with smaller apex is shown to focus more E-field energy around the tip apex, leading to a better spatial resolution. Thereafter, the whole iNFMM system including the coupler, the attenuator, the delay line and the EMP is simulated by using Keysight<sup>TM</sup>/ADS. The wave-cancellation process is demonstrated in the frequency range [2-3 GHz]. All these simulation results allow a finer understanding of the iNFMM system, especially the EMP and the principle of the wave-cancelling process associated to the interferometric technique.

After these theoretical studies of the electromagnetic distribution and the wave-cancelling process provided by the interferometric technique, we present in the next section the characterization of the iNFMM system.

## **II.3 Characterization of the microwave microscope**

### **II.3.1 Introduction**

To better understand the microwave response of the proposed system, in this section we present the characterization of the microwave components which compose the iNFMM such as the couplers, the attenuator, the delay line and the EMP by using the Keysight™ PNA-X 5242A network analyzer covering the frequency range [10 MHz- 26.5 GHz]. The characteristics of these components help to select the frequency band assuring the best functioning of each component and also to better understand the principle of the system. Then, the performance of the whole system is investigated and the zero level of the transmission coefficient is recorded under different conditions of the wave-cancelling process. In this part, for all the tests, the output power of the VNA is set to 0 dBm and the IFBW to 100 Hz.

### **II.3.2 Characterization of the interferometer**

#### **II.3.2.1 Characterization of the hybrid coupler**

The hybrid coupler plays an important role in the iNFMM as it combines the signal reflected by the EMP and the wave reflected by the impedance tuner. It is inside the coupler that takes place the wave-cancelling process, thus the characteristics of the coupler directly influence the quality of the wave-cancellation process. In our configuration, two couplers are needed to cover the entire operating frequency band of the system: one covering the frequency range [2-10 GHz] and another one covering a higher frequency range [6-20 GHz]. Actually in these measurements, critical characteristics of the couplers such as the matching, the isolation, the directivity, the coupling factor and the 90 °phase-shift between the direct and coupled path are investigated.

#### **a) 2-10 GHz coupler**

Although the coupler is measured in the frequency range [10 MHz - 20 GHz], only the band [2-10 GHz] is of interest for this coupler. The matching properties and the isolation of the coupler are shown in the Fig. II-10.a. Both are well above 15 dB

from 2 to 10 GHz. In Fig. II-10.b, the insertion loss varies from 3.5 dB to 6 dB from 2 to 10 GHz while in the same frequency range, the coupling factor varies from 1.5 dB to 3.5 dB. The directivity is higher than 14 dB in this range.

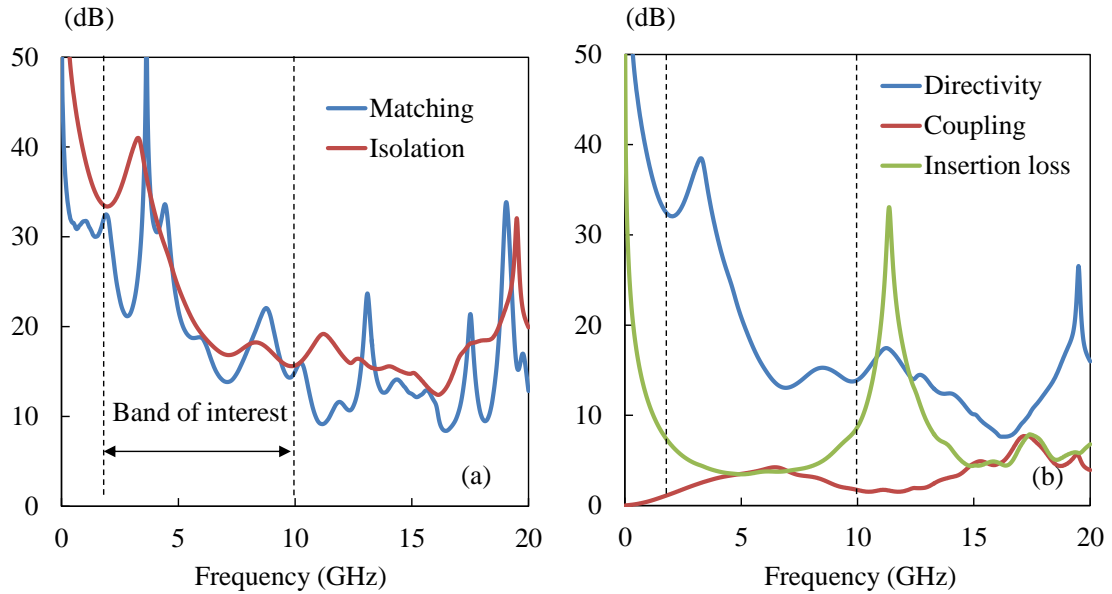


**Fig. II-10:** Characteristics of the [2-10 GHz] hybrid coupler; (a): matching and isolation; (b): directivity and coupling parameters

The phase-shift between the direct and coupled paths is shown in Fig. II-11. This phase-shift varies from 91 °to 99 °in the frequency band [2-10 GHz].

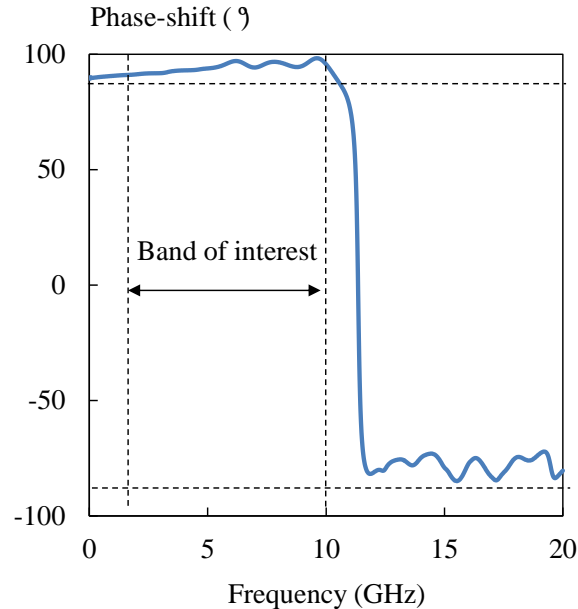


**Fig. II-11:** Phase-shift between the direct and coupled paths of the hybrid coupler; dash lines represents 90 °and -90 °

Based on these measurements, we confirm that the coupler operates correctly in the frequency range [2-10 GHz].

### b) 6-20 GHz coupler

Similar tests are performed for the second coupler. The matching, isolation, directivity and coupling properties are shown in Fig. II-12.

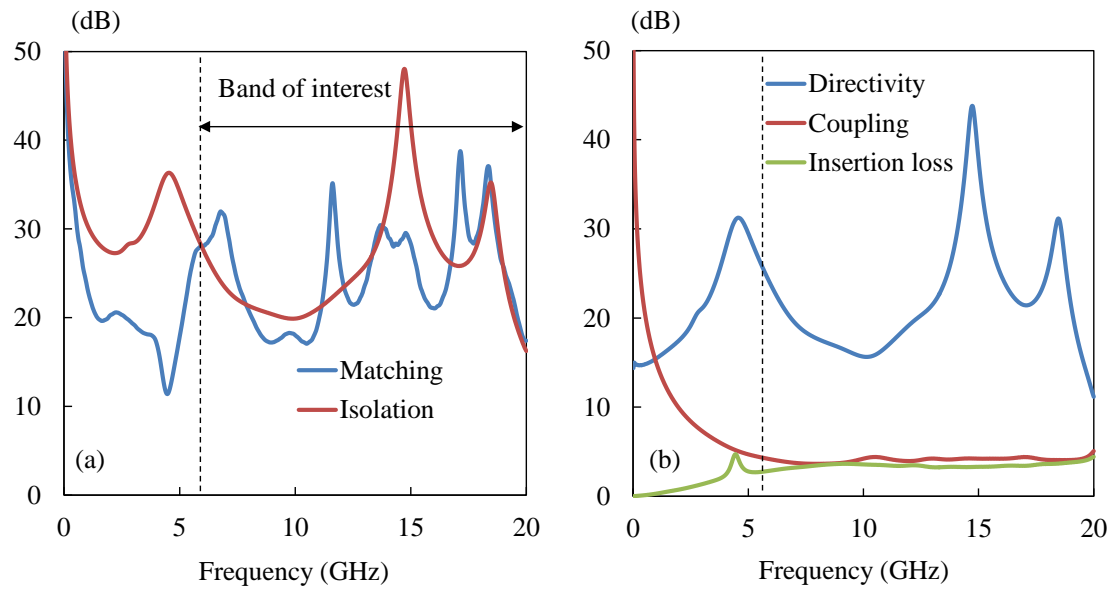


**Fig. II-12:** Characteristic of the [6-20 GHz] hybrid coupler; (a): matching and isolation; (b): directivity and coupling parameters

As can be seen in Fig. II-12.a, the matching and the isolation coefficients are well above 18 dB for the frequency range [6-20 GHz]. In Fig. II-12.b, the insertion and the coupling factor are almost flat and around 4 dB from 6 to 20 GHz. The directivity is above 13 dB in this range.

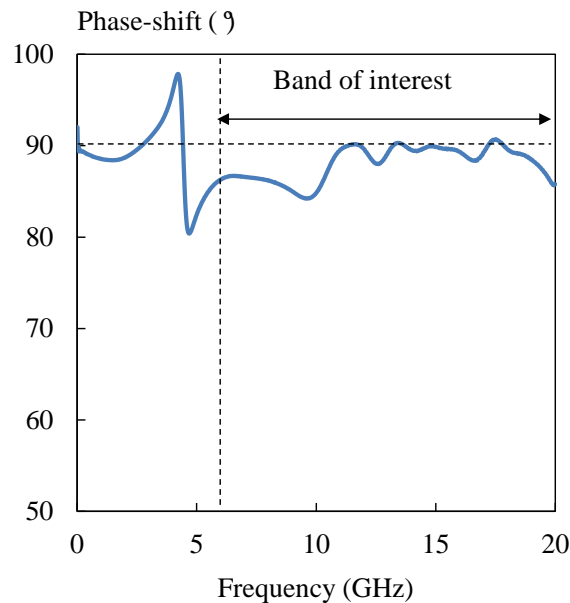


**Fig. II-13:** Phase-shift between the direct and coupled paths of the hybrid coupler; dash lines represents  $90^\circ$

The phase-shift (Fig. II-13) between the direct and the coupled paths is between  $85^\circ$  and  $91^\circ$  from 6 to 20 GHz.

As a conclusion, two couplers are characterized in this part and they operate correctly in the frequency band [2-10 GHz] and [6-20 GHz], respectively. One can note that the operating frequencies of the couplers covers a common range from 6 to 10 GHz. Particularly, to guarantee a good performance of the couplers, the measurements in [6-8 GHz] are done preferentially by the first coupler, and the measurements in [8-10 GHz] are rather conducted by the second coupler.

In the following, the performance of the attenuator is evaluated.

### II.3.2.2 Characterization of the attenuator

The impedance tuner is an essential component in our setup. Actually, the measurement sensitivity of the system highly depends on its performance. The impedance tuner includes an attenuator and a delay line that have to be characterized in the frequency band of interest. We first study the properties of the attenuator in terms of matching and attenuation. To assure a fine and automatic control of the attenuation, the variable attenuator is controlled by a motor. Fig. II-14 presents the reflection coefficient  $S_{11}$  of the attenuator for both the maximum and minimum attenuations available.

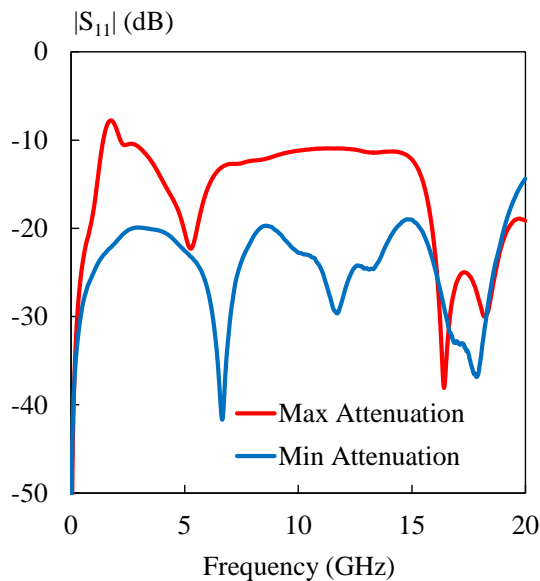


**Fig. II-14:** Magnitude of the reflection coefficient  $S_{11}$  of the attenuator; minimum and maximum attenuations are presented in blue and red lines, respectively

As shown in Fig. II-14,  $|S_{11}|$  is well below -20 dB when there is no attenuation considered (0 dB, blue line), leading to a good matching on the entire frequency range [10 MHz-20 GHz]. Concerning the maximum attenuation (red line in Fig. II-14), the  $S_{11}$  magnitude is below -13 dB in [3-20 GHz]. Especially, in [1.5-3 GHz],  $|S_{11}|$  is around -10 dB, which is still acceptable in terms of matching properties.

The insertion loss of the attenuator is plotted in the Fig. II-15 considering two conditions: minimum attenuation and maximum attenuation.

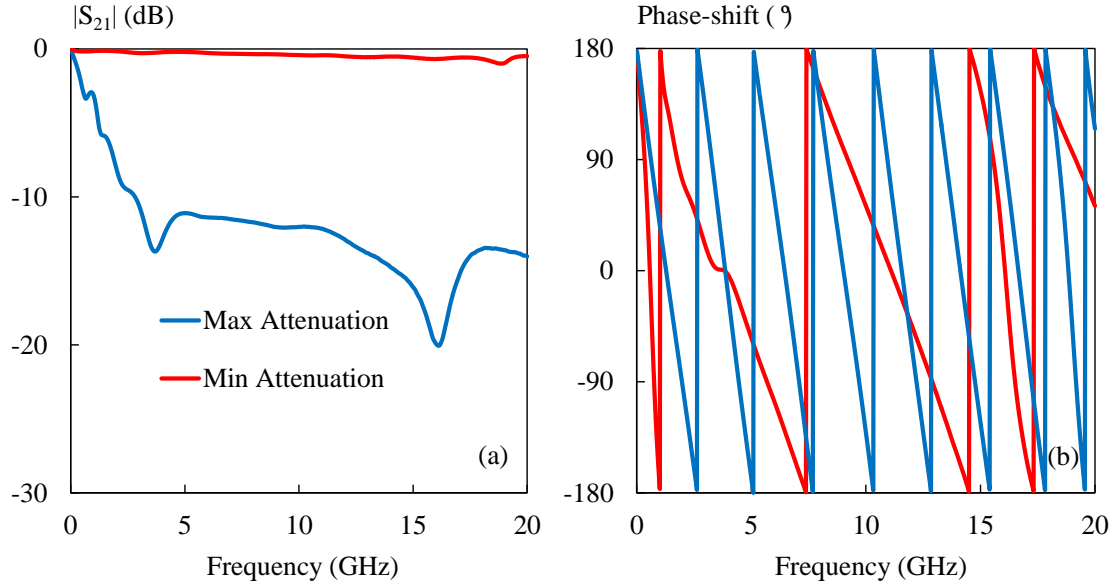


**Fig. II-15:** Magnitude (a) and phase-shift (b) of the transmission coefficient  $S_{21}$  of the attenuator; minimum and maximum attenuations are presented in blue and red lines, respectively

As illustrated in Fig. II-15.a, the insertion loss is less than 1 dB when no attenuation is applied. When considering the maximum attenuation,  $|S_{21}|$  varies from -10 to -18 dB in [2-20 GHz]. Actually, in the configuration of the proposed iNFMM, the impedance tuner is terminated by a short circuit, and the attenuator operates in reflection mode. So, the maximum attenuation varies in fact from 20 to 36 dB, which is largely sufficient for the wave-cancelling process. Furthermore, as the attenuator is motorized, the attenuation can be precisely controlled. Additionally, it is noticed that the attenuator introduces a phase-shift into the system (Fig. II-15.b).

### II.3.2.3 Characterization of the delay line

The delay line, also named phase shifter, is investigated in this part. The delay time of this instrument ranges from 0 to 625 ps with a minimum step of 0.5 ps. Its return loss and insertion loss are shown in Fig. II-16.

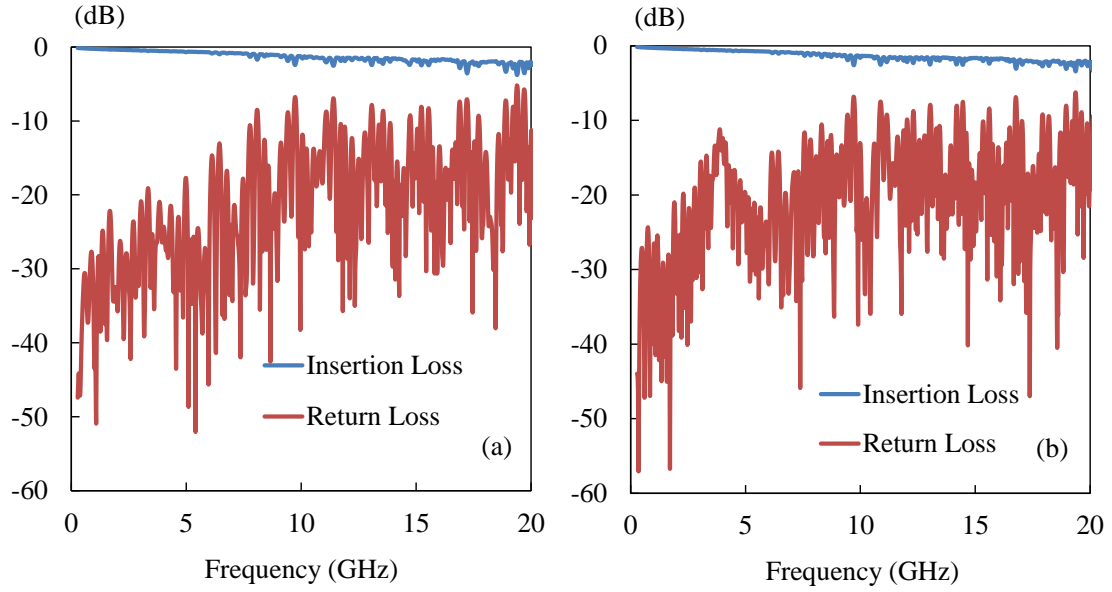


**Fig. II-16:** Insertion loss and return loss of the delay line; (a): no delay (0 ps); (b): maximum delay (625 ps)

From Fig. II-16, we find that the return loss varies from 10 to 57 dB in the frequency band [10MHz-20 GHz] for two conditions: no delay (0 ps) and maximum delay available (625 ps). It can also be noted that insertion loss is very flat and smaller than 3 dB for the entire frequency band. These results return good matching and transmission properties of the delay line. In the following, the exact phase-shift is calculated from the measurement delay time.

The relationship between the phase-shift  $\varphi$  and the delay time  $t$  in free space is expressed as below.

$$\varphi = k \cdot d = k \cdot c \cdot t$$

where  $k$  is the wave number of the wave,  $d$  is the length of cable and  $c$  is the speed of light in free space. The wave number is related to the wavelength  $\lambda$  by the equation:

$$k = \frac{2\pi}{\lambda}$$

Actually,  $k$  describes how many oscillations the wave completes per unit of space.

So it is quite easy to calculate the phase-shift from a given delay time. As an example, we consider a delay time of 1 ps at 10 GHz. The phase-shift is given by:

$$\varphi = \frac{2\pi \cdot f}{c} \cdot c \cdot t = 2\pi \cdot f \cdot t$$

$$\varphi = 2\pi \cdot 10^{10} \cdot 10^{-12}$$

$$\varphi = 0.0628 \text{ rad} = 3.6^\circ$$

Thus a delay time of 1 ps at 10 GHz corresponds to a phase-shift of 3.6 °

Particularly, the phase-shift in degrees that corresponds to a given delay time can be expressed by

$$\varphi (\text{deg}) = 360^\circ \cdot f \cdot t$$

By using the equation above, the phase-shift can be calculated at any frequency for a certain delay time. In Fig. II-17, as a demonstration, three delay times (5 ps, 10 ps and 50 ps) are considered and a comparison between the theoretical phase-shift and the one measured is presented.

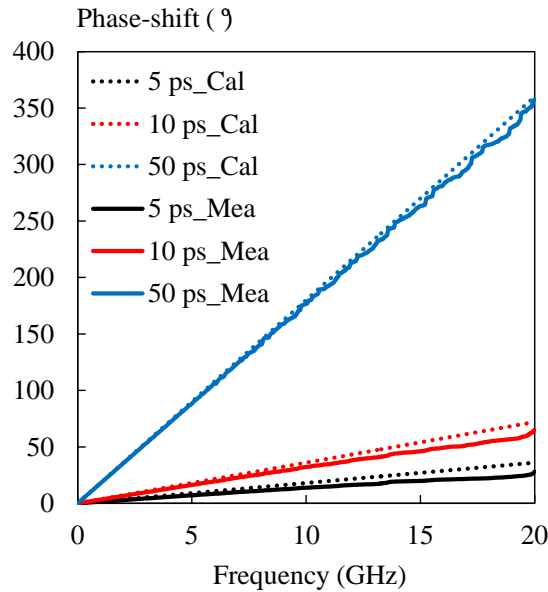


**Fig. II-17:** Phase-shift of corresponding delay time (5 ps, 10 ps and 50 ps); the theoretically calculated values and measured ones are presented in dotted symbols and solid lines, respectively

As shown in Fig. II-17, one can note that the phase-shift is proportional to the working frequency from 10 MHz to 20 GHz. It can also be retrieved that for a particular operating frequency, a longer delay time results in a larger phase-shift. In addition, a good agreement is found between theory and measurement data. Thus, the

impedance tuner is precisely controlled by a numeric pad in the range [0-625 ps], which enables a fine adjustment of the phase-shift of the impedance tuner.

After the evaluation of the performance of the delay line, the frequency response of the EMP is investigated in the following.

### II.3.2.4 Characterization of the evanescent microwave probe

The evanescent microwave probe (EMP) is a crucial part of the microscope because the EMP directly interacts with the device/material under test. It is worth noting that the probe is constituted by a tapered-ended metallic conductor extruded from a SMA support (Fig. II-18.a). To analyze the performance of the probe, we measure its reflection coefficient. As shown in Fig. II-18.b, two probes of different apex sizes: 66  $\mu\text{m}$  and 260  $\mu\text{m}$  are investigated. During the measurement, the probe is fixed in free space and it is connected directly to the network analyzer.

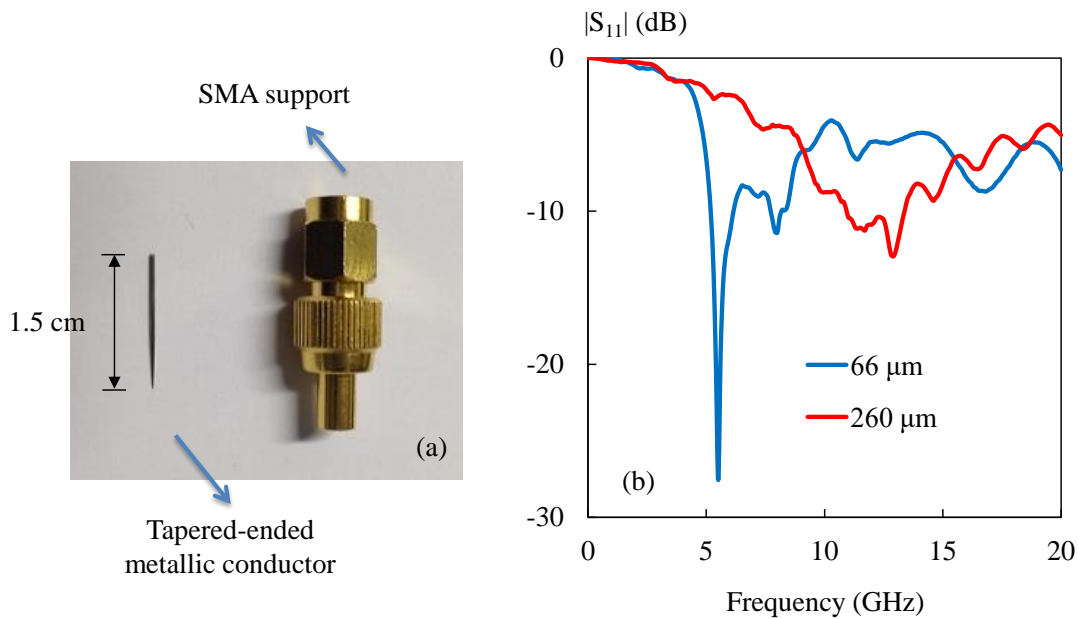


**Fig. II-18:** (a): EMP made of a tapered-ended metallic conductor and a SMA support, (b): magnitude of the reflection coefficient  $S_{11}$  of the evanescent microwave probe (EMP), two probe apex sizes are considered: 66  $\mu\text{m}$  and 260  $\mu\text{m}$

As shown in Fig. II-18.b, resonance peaks are found at 5.3 GHz and 12.7 GHz for probe apex of 66  $\mu\text{m}$  and 260  $\mu\text{m}$  respectively. Actually, as the EMP is composed of a central conductor and a SMA support, the probe works like a quarter-wave monopole, in which the antenna is approximately 1/4 wavelength ( $\lambda_0$ ) of the microwaves. For the probe with apex size of 66  $\mu\text{m}$ , the length of the central

conductor is 1.5 cm (Fig. II-18.a) which is close to the length of the 1/4 wavelength ( $\lambda_0 = 5.7$  cm) antenna with a resonance frequency of 5.3 GHz (Fig. II-18.b). Similarly, for the probe apex of 260  $\mu\text{m}$ , the length of the central conductor is 0.7 cm, corresponding to the length of the 1/4 of the wavelength ( $\lambda_0 = 2.4$  cm) antenna with a resonance frequency of 12.7 GHz (Fig. II-18.b). One can note that high sensitivity is guaranteed around the resonance frequencies, while for other frequencies, for example at 2 GHz, the reflection coefficients of the two probes are very close to 0 dB. This poor matching means the majority of the wave is reflected back from the SMA support of the EMP and there is almost no wave transmitted into the probe. Thus, the EMP is only sensitive in its resonance frequency range. However, the simulation results in section II.2.4 prove that by incorporating an interferometer between the VNA and the probe, the sensitivity can be largely improved. Thus, in the following part, the tuning process associated to this technique and the performance of the whole microscope are experimentally validated.

### **II.3.3 Performance of the interferometric technique**

#### **II.3.3.1 Validation of the wave-cancelling process**

According to the characteristics of the microwave components of the system presented just before, the microwave microscope proposed operates in a broad frequency band [2-18 GHz]. Thus, in this part, we evaluate the performance of the whole microscope. Practically, the potentialities of the interferometric technique are verified through some basic experiments.

The accuracy of the tuning process is first verified. To that end, we considered the EMP (apex = 260  $\mu\text{m}$ ) in free-space. The source power of the VNA is set to 0 dBm and the IFBW to 100 Hz. In this configuration, the noise floor of the VNA is around -95 dB. The resonant peak of the transmission coefficient is then easily adjusted by tuning the phase-shift of the delay line. All measurements are done at room temperature around 20 °C. As a demonstration, the data are acquired in the frequency range [2-3 GHz] with a frequency step of 10 kHz (Fig. II-19). We present the performance of the platform with two configurations: with and without interferometer (Fig. II-8). As mentioned before, in the case with interferometer, the parameter measured is the transmission

coefficient  $S_{21}$ . In case of the setup without interferometer, one port of the VNA is directly connected to the EMP and the reflection coefficient  $S_{11}$  is acquired.

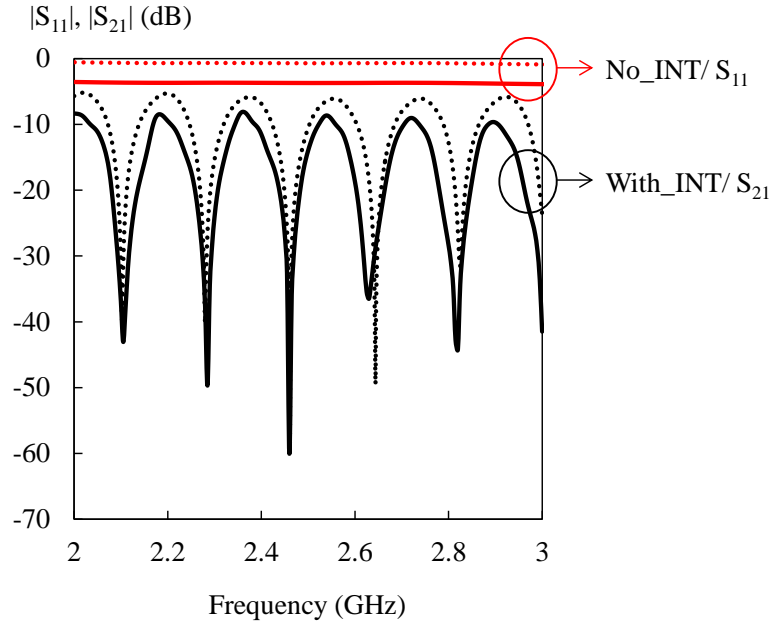


**Fig. II-19:** Measured (solid lines) and simulated (dotted lines) magnitude spectra in two cases: with (in black) and without (in red) interferometer;  $P_0 = 0$  dBm, IFBW = 100Hz, EMP apex =  $66 \mu\text{m}$

In Fig. II-19, for the setup without interferometer, the reflection coefficient response  $|S_{11}|$  is flat in the frequency range [2-3 GHz]. However, in the setup with interferometer, several resonances which occur every 170 MHz are observed, in the frequency range [2-3 GHz]. These resonances guarantee a good measurement sensitivity. It can also be observed from Fig. II-19 that there is a difference between the measured (solid lines) and simulated (dotted lines) results because losses are not considered in the simulation. These losses are associated to the cables, connections and microwave components of the system. In this case, losses mainly come from the cables. For example, in the setup without interferometer (red lines in Fig. II-19), the measured  $S_{11}$  spectrum is around 3 dB below the simulated one due to the cable loss (in the order of 1.5 dB). In the case with interferometer, there is also a 3 dB difference of  $S_{21}$  spectrum because two cables are employed to connect two ports of the coupler to the VNA.

Afterwards, to better visualize the resonance peak of  $S_{21}$ , the frequency window is reduced to 5 MHz around 2.46 GHz (Fig. II-20).

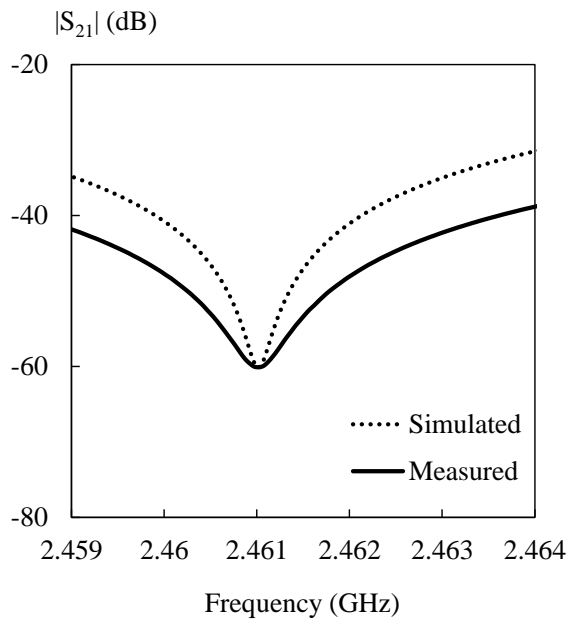


**Fig. II-20:** (b): Measured (solid line) and simulated (dotted line)  $|S_{21}|$  spectra from 2.459 to 2.464 GHz;  $P_0 = 0$  dBm, IFBW = 100Hz, EMP apex = 66  $\mu\text{m}$

As shown in Fig. II-20, the quality factor obtained by simulation (10254) is about twice as the value measured (4922). After giving some basic results on the wave-cancelling process, in the following, the behavior of the impedance tuner which plays an important role in the interferometric technique is investigated (Fig. II-21). Especially, in Fig. II-21.a, different cancellation levels are obtained by tuning carefully the attenuator.

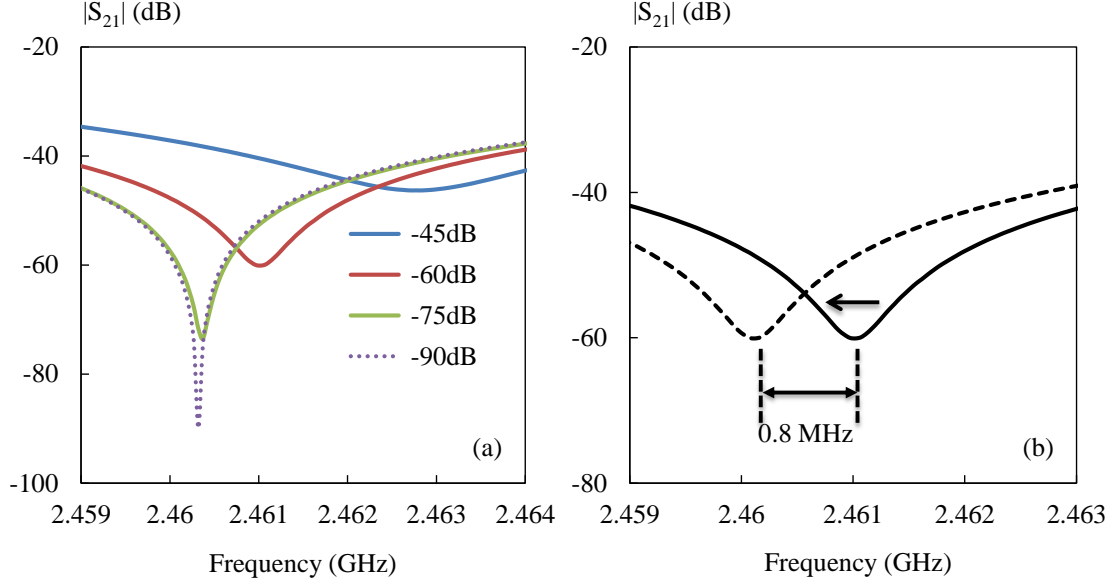


**Fig. II-21:** Measured magnitude spectra of the transmission coefficient  $S_{21}$ , (a): different  $|S_{21}|$  levels (-45 dB, -60 dB, -75 dB and -90 dB) obtained by tuning the attenuator, (b): resonance shift (around 0.8 MHz) achieved by adding a short time delay (1 ps)

As shown in Fig. II-21.a, a fine adjustment of  $\Gamma_{TUN}$  allows setting  $|S_{21}|$  at a zero level equal to -90 dB (only 5 dB upper than the noise floor of the VNA). Actually, such a low zero level leads to a high quality factor (Q) and a better sensitivity. For example, the calculated Q for the different zero levels selected (-45 dB, -60 dB, -75 dB and -90 dB) are 1172, 4922, 24603 and 98412 respectively. Indeed, the high measurement sensitivity can be easily adjusted by tuning the motorized attenuator. Then the influence of the time delay on the tuning process is also investigated. As shown in Fig. II-21.b, a time delay of 1 ps is added into the system by the delay line, and consequently a resonance shift of 0.8 MHz of  $|S_{21}|$  is obtained. Furthermore, as the electrical length of the system is slightly extended because of the time delay (1 ps) inserted this resonance peak shifts to the left side. So, generally speaking, thanks to the delay line, the operating resonance frequency can be precisely selected in a wide frequency band [2-18 GHz] with a step around 1 MHz. Therefore, compared to other NFMM operating at very limited frequency [HUM 12] [TOR 12], the iNFMM proposed enables a quasi-continuous frequency band [GU 16b].

In the following, the measurement sensitivity over a broad frequency band is under evaluation.

### II.3.3.2 Evaluation of the measurement sensitivity

The quality factor of the iNFMM represents one of the most effective manner to demonstrate the measurement sensitivity [STE 98], [LAI 09]. As reported in the literature, the transmission-line-based structures usually exhibit a quality factor in the order of 1000 [TAB 00], [KLE 06], [WEB 12]; while the resonator-based platforms present higher Q values around 5000 [SUN 14], [GRE 16]. Another limitation for resonator-based NFMM is the difficulty to obtain a good measurement sensitivity for a broad frequency range [TSE 07]. On the contrary, an interferometer-based structure has potentials to achieve a good sensitivity in broad frequency band. For example, Bakli *et al.* obtained a Q varying from 5300 to 9400 in the frequency band [2-6 GHz] in free space [BAK 14]. In this work, we extend the working frequency to 18 GHz with an excellent sensitivity.

As presented in Fig. II-22, the zero level is set around -75 dB by carefully tuning the attenuator and the delay line, and the corresponding quality factors are calculated as a function of frequency. The probe is placed in air. As mentioned in section II.3.2, there are two couplers covering different frequency ranges. Q values are presented separately for these two couplers in Fig. II-22.a and Fig. II-22.b.

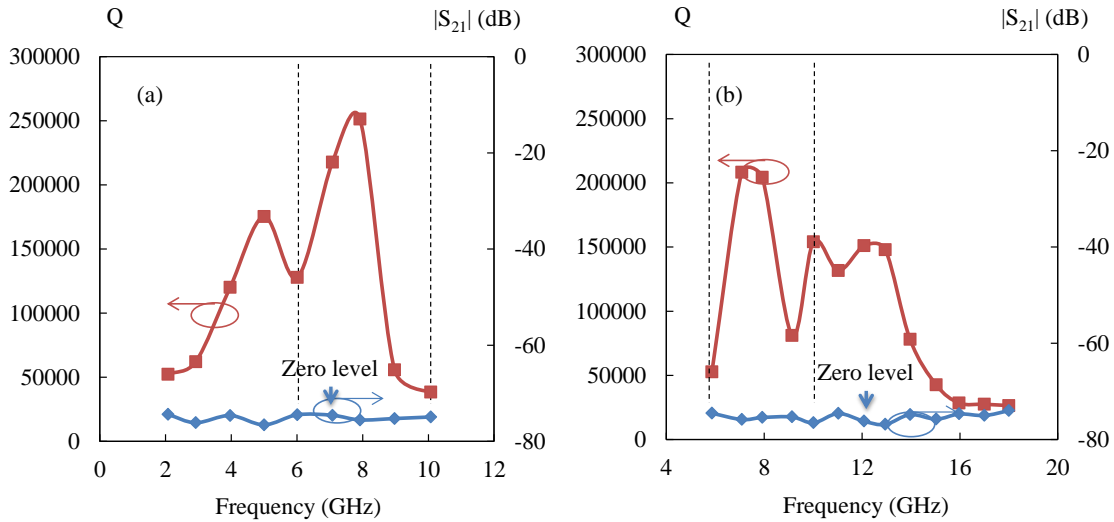


**Fig. II-22:** Quality factors measured (in red) as a function of the frequency considering the zero level around -75 dB (in blue); (a): results by using the [2-10 GHz] coupler; (b): results by using the [6-20 GHz] coupler; the wave-cancelling process is done considering the probe in air

As shown in Fig. II-22, the quality factor obtained varies from 25000 to 260000 which is much higher than the values ever reported in the literature. Especially, even

the minimum Q value obtained (25000) is higher than the Q given by the resonator-based structure (5000) by a factor of five. Thus, an excellent measurement sensitivity over a broad frequency range is guaranteed by the interferometric technique. One can note that the maximum quality factor is obtained around 8 GHz whatever the coupler is. This maximum value, 260000, is obtained by using the [2-10 GHz] coupler while the maximum Q value is 210000 using the [6-20 GHz] coupler. Thus we clearly see that Q values are influenced by the characteristics of the microwave components of the system, and mainly affected by the coupler features. Actually the couplers are not exploited in their entire working frequency but rather from 2 to 8 GHz for the first coupler, and from 8 to 18 GHz for the second coupler.

### **II.3.4 Conclusion**

In this section, we have presented the characterization of the properties of the critical elements of the iNFMM proposed including the hybrid coupler, the impedance tuner and the probe. It has been shown that the properties of these components guarantee a broad frequency of operation from 2 to 18 GHz. As an illustration, we have presented the results obtained for a tuning process performed in the frequency range [2-3 GHz] to demonstrate the performance of the interferometric technique. Particularly, we have shown that a low zero level with high quality factor can be easily obtained by carefully adjusting the attenuator. Furthermore, thanks to the motorized delay line, the platform is able to operate in a quasi-continuous frequency range [2-18 GHz] with a step of 0.8 MHz for a time delay of 1ps. The interferometer setup confirms a measurement sensitivity largely enhanced compared to the setup without interferometer. High quality factors are obtained by the interferometric technique for a wide frequency range. Therefore, compared to the resonator method, the interferometric technique represents a better candidate to operate in a broad frequency band, from 2 to 18 GHz in the present case, with high measurement sensitivity.

After the presentation of the performance of the microwave microscope which has been experimentally evaluated, in the following part we report on the performance of the whole iNFMM system including the microwave part and the mechanical part (x-y-z stage) in terms of measurement repeatability which is one of the most critical issues of the NFMM.

## **II.4 Setting parameters influence on the repeatability of the iNFMM**

### **II.4.1 Introduction**

Microwave microscopy has been demonstrated as a good candidate to address imaging applications with high spatial resolution. However, some scientific issues are still to be overcome. In particular, the main difficulty of NFMM lies in the measurement repeatability [TAB 99], [IMT 14], especially in micro- and/or nano-characterizations scenarios [HUB 10]. For this kind of experiments typical measurement uncertainties around 10 % to 20 % are reported [TAL 09], [HUB 10]. Even if there have been some repeatability analysis for scanning probe microscope (SPM) [EDW 98], [XIA 14], only a few works devoted to repeatability study of the microwave microscope have been identified [CHE 02], [HOF 14]. For this reason, there is an urgent need to address the repeatability issue of NFMM and to identify the errors sources related to this new characterization mean. Indeed, this kind of experimentations requires well-established measurement protocols to ensure reproducibility of the measured data and to improve the microwave microscopy performance. For instance, comprehensive works focusing on the influence of setting parameters, such as stand-off distance (distance between the material under test and the probe) and scanning step size, on the imaging quality have been achieved [CAS 11]. In our study, we concentrate on the impact of a large number of setting parameters (microwave source, impedance tuner, cables, x-y-z stage and measurement duration) and analyze their contributions to the measurement repeatability and imaging quality. This is a very fine study that intends to give a good picture of the performance allowed by the platform developed. The description of the iNFMM platform is given in Section II.4.2. In Section II.4.3, the impact of the VNA IFBW on the measurement repeatability is quantified in different scenarios. The drift of the iNFMM with time is also estimated for three different zero levels achieved by the interferometer. In Section II.4.4, these optimized key parameters (i.e. the IFBW and the zero level) are defined to configure the iNFMM for 1D scanning. The error generated during the scanning process is successfully extracted. Furthermore, a 2D microwave imaging application based on the optimized key parameters is proposed to evaluate the performance of this instrument.

## II.4.2 Interferometer-based near-field microwave microscope setup

We present in Fig. II-23 the whole setup of the proposed iNFMM including the microwave circuits (i.e. VNA, coupler, impedance tuner and EMP) and the mechanical part (x-y-z stage).

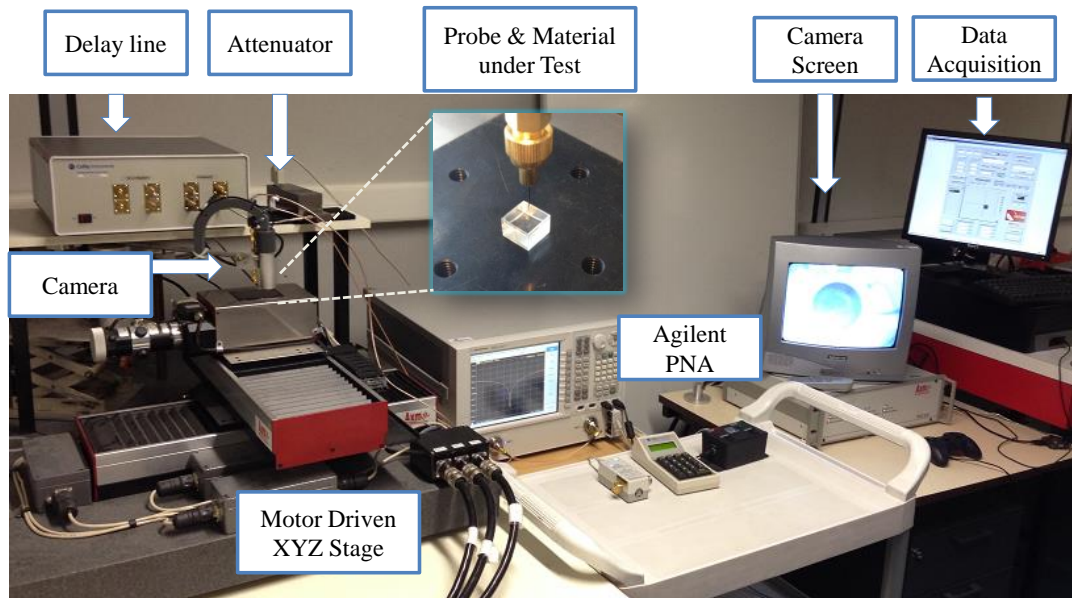


**Fig. II-23:** Interferometer-based near-field microwave microscope setup

As shown in Fig. II-23, the sample to be scanned is mounted on a motor-driven x-y-z stage. The probe is positioned vertically over the stage. The x-y-z stage consists of three independent motorized linear translation sub-stages with travelling distances of 25 cm in x/y axis and 1 cm in z axis respectively. The minimum increment step in the three directions is 1  $\mu\text{m}$ . The sample is placed on the chuck fixed on the stage whereas the microwave part of the microscope remains fixed. Consequently, a better stability is obtained by moving the sample under the probe tip instead of moving the probe. A camera is used for better visualization of the tip and the sample under test. Concerning the software part of the platform, a National Instruments Labview interface is developed to control the position of the sample, to set the network analyzer parameters, to measure the resulting transmission coefficient  $S_{21}$  and to display the results.

## II.4.3 Setting parameters impact on repeatability tests

In this part, a complete study related to the influence of different setting parameters on the quality of measurement is proposed [GU 16a]. The first part of the

analysis is focused on the measurement precision. This latter is related to the deviation of repeated measurements from the mean value. Consequently, to investigate the performance of the technique, the mean and the standard deviation of the transmission coefficient are considered. The mean of the transmission coefficient is given by:

$$\overline{S_{21}} = \frac{1}{n} \sum_{i=1}^n S_{21i}$$

with  $n$  the number of measurements.

The standard deviation of the complex transmission coefficient is defined by:

$$Std(S_{21}) = \left( \frac{1}{n-1} \sum_{i=1}^n [(S_{21i} - \overline{S_{21}}) \times (S_{21i} - \overline{S_{21}})^*] \right)^{\frac{1}{2}}$$

The relative standard deviation is given by:

$$Std(S_{21}) \% = 100 \% \times \frac{std(S_{21})}{|\overline{S_{21}}|}$$

The errors related to the electrical part of the system (VNA, impedance tuner, coupler, cables, etc.) and the mechanical repeatability (x-y-z stage) impact the measurement precision in an extent that has to be estimated. Concerning the contribution of the electrical part of the platform to the error budget, it is quite difficult to quantitatively analyze the influence of each component (impedance tuner, coupler and cables) separately. Thus, we have considered this electrical contribution as a whole. Nevertheless, to lower this source of error as already said, the microwave part of system remains fixed during the scanning and the environmental conditions are kept constant (in particular the temperature). We begin the description of this study with the influence of the IFBW and the zero level. Then, investigation related to the scanning error is reported. All measurements are done at room temperature around 20 °C.

#### **II.4.3.1 VNA intermediate frequency bandwidth (IFBW)**

In this part the influence of the VNA IFBW on the measured transmission coefficient is examined. The receiver architecture of a conventional VNA is based on a tuned receiver that makes use of a local oscillator (LO) to mix the received microwave

signal to a lower intermediate frequency (IF). The IF signal is bandpass filtered which narrows the receiver bandwidth and greatly improves the sensitivity, dynamic range and precision. The magnitude and phase information are extracted from the IF signal by means of an analog-to-digital converter (ADC) and digital-signal processor (DSP). Thus, as the measurement accuracy and sensitivity are mainly governed by the IF bandwidth of the VNA, the transmission coefficient noise floor is first determined as a function of this parameter. To that end, the source power of the VNA is set to  $P_0 = 0$  dBm and both measurement ports of the VNA are connected to match loads. The measured transmission noise floor corresponds to the average of the measured transmission coefficient magnitude on the whole frequency band of the VNA [10 MHz - 26.5 GHz] (Fig. II-24).

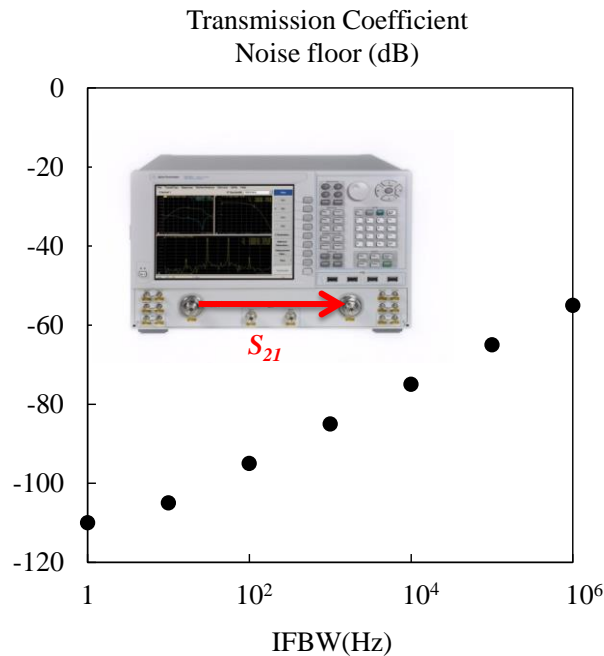


**Fig. II-24:** Measured transmission coefficient  $S_{21}$  as a function of the intermediate frequency bandwidth (IFBW),  $P_0 = 0$  dBm (Keysight™ PNA-X 5242A)

From this graph, it is clear that the noise floor can be significantly reduced by decreasing the IFBW. In the present case, a minimum value around -110 dB for an IFBW of 1 Hz is obtained. Nevertheless, a low IFBW results in a longer acquisition time. Consequently, the measure is more sensitive to drift errors. Experiments are proposed in the following to quantify the impact of the IFBW on the measurement precision. For these first tests, the coupler arms connected respectively to the probe and the impedance tuner are equilibrated by the interferometric method proposed so that the

zero level is set to a value around -50 dB at 2 GHz when the probe is in free-space. The acquisition time is set to 60 seconds (number of points: 60) and six values of IFBW between 1 Hz and 1000 Hz are considered.

We give in Table II-1 the standard deviation obtained for the different cases. As the transmission coefficient is a complex value, we have also given the standard deviation calculated for the magnitude and the phase-shift separately.

IFBW (Hz)	Std ( $S_{21}$ ) (%)	Std ( $ S_{21} $ ) (%)	Std ( $\arg.S_{21}$ ) (°)
1	0.47	0.4	0.14
10	0.62	0.4	0.28
50	0.79	0.49	0.35
100	0.83	0.53	0.37
500	0.89	0.55	0.4
1000	1.46	0.91	0.66

**Table II-1:** Standard deviation of the transmission coefficient  $S_{21}$  as a function of IFBW; zero level = -50 dB,  $f = 2$  GHz, acquisition time = 60 s, number of points = 60

From these data, we show that for given acquisition times and number of points the measurement precision diminishes when the IFBW increases. When the IFBW increases from 1 Hz to 1000 Hz, the standard deviation of the transmission coefficient is multiplied by a factor three, going from around 0.5 % to 1.5 %.

In the next experiment, the acquisition time remains equal to 60s while the sampling speed increases with IFBW. Obviously, a higher IFBW leads to a faster sampling speed and thus a higher number of points (32001 points for IFBW=1000 Hz). The data obtained are summarized in Table II-2.

IFBW (Hz)	Number of points	Std ( $S_{21}$ ) (%)	Std ( $ S_{21} $ ) (%)	Std ( $\arg.S_{21}$ ) (°)
1	60	0.47	0.4	0.14
10	600	0.58	0.4	0.24
50	3,000	0.73	0.43	0.32
100	6,000	0.75	0.49	0.33
500	30,000	0.78	0.49	0.35
1000	32,001	0.89	0.69	0.35

**Table II-2:** Standard deviation of the transmission coefficient  $S_{21}$  as a function of IFBW; zero level = -50 dB,  $f = 2$  GHz, acquisition time = 60s

One can retrieve, when comparing Table II-1 and Table II-2, that for given acquisition time and IFBW, the precision is obviously better when the number of points is higher. These experiments clearly demonstrate the influence of the VNA setting parameters on the measurement precision. So, to lower the impact of these parameters, a compromise between the IFBW, the number of points and the acquisition time has to be found.

#### **II.4.3.2 Zero level of the transmission coefficient**

In this part, the influence of the zero level of the transmission coefficient  $S_{21}$  set by the interferometer on the drift errors is under investigation. As already said, the EMP exhibits a very high impedance in comparison with the standard  $50 \Omega$  impedance of the VNA. Consequently, as already mentioned, if the EMP is connected directly to a measurement port of the VNA, the receiver becomes practically insensitive to the variations of the reflection coefficient. Therefore, the probe must be matched to the  $50 \Omega$  input impedance of the VNA. In the approach proposed, as described before, a broadband matching network based on an interferometric technique is inserted between the analyzer and the probe to enhance the measurement sensitivity/accuracy in the frequency range 2-18 GHz. Thus, the transmission coefficient  $S_{21}$  can be put at a very low-level to benefit from the sensitivity of the VNA. As the measured signal is subject to drift errors especially when very low signals are considered, the stability of the system as a function of acquisition time is quantified in the following for different zero levels. The input source power  $P_0$  of the VNA and the IFBW are set respectively to 0 dBm and 100 Hz (that corresponds to a transmission coefficient noise floor around -90 dB according to the Fig. II-24). In Table II-3, we present the standard deviations calculated for three zero levels (about -30 dB, -50 dB and -70 dB). A relatively short acquisition time is first considered (5 minutes). The measured data are acquired every 30 seconds.

$ S_{21} $ (dB)	Std ( $S_{21}$ ) (%)	Std ( $ S_{21} $ ) (%)	Std ( $\arg.S_{21}$ ) (°)
-30	0.121	0.10	0.038
-50	0.52	0.35	0.29
-70	5.36	4.280	1.85

**Table II-3:** Standard deviation of the transmission coefficient  $S_{21}$  as a function of the zero level;  $f = 2$  GHz;  $P_0 = 0$  dBm, IFBW = 100 Hz, acquisition time = 5 minutes, number of points = 600

It is retrieved in this table that the drift errors increase with a decrease of the signal level. A maximum deviation of 5.36 % is found for the lowest zero level tested (-70 dB), which is acceptable for short term measurements lasting a few minutes.

After analyzing the drift errors for a short time test, a measurement time of 5 hours is investigated in Fig. II-25. Indeed, one of the applications of the microwave microscopy platform proposed is to perform a 2D imaging over an object under test as it will be detailed at the end of the section. Because such process usually takes hours, the long term stability must be carefully studied. Besides, 5 hours is largely enough for measurements such as 2D scanning. As for the short time test, the measurement data are acquired every 30 seconds.

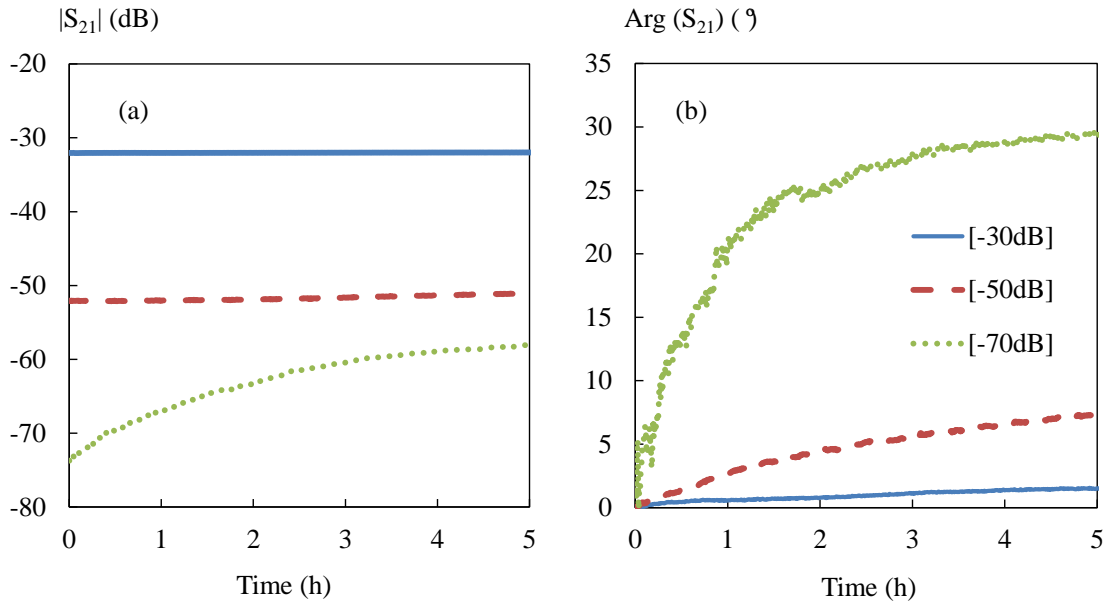


**Fig. II-25:** Transmission coefficient magnitude (a) and phase-shift (b) versus time for 3 zero levels (around -30dB, -50 dB and -70 dB),  $f = 2$  GHz, IFBW = 100 Hz, number of points = 600

These plots clearly indicate that the measured data are impacted by drift errors. A higher zero level (-30 dB and -50 dB) leads obviously to a better stability of the system. For example, when a cancellation level around -70 dB is considered, the measurement stability study shows variations after 5 hours of 15.5 dB and  $29.4^\circ$  for magnitude and phase-shift respectively (Fig. II-25). However, only slight variations of 0.1 dB and  $1.5^\circ$  respectively for magnitude and phase-shift are obtained after 5 hours when the zero level is around -30 dB. For a signal level in between (-50 dB), the variations observed in magnitude and phase-shift are respectively 0.9 dB and  $7.2^\circ$ . The standard deviations of the measured transmission coefficient are then derived (Table II-4).

$ S_{21} $ (dB)	Std ( $S_{21}$ ) (%)	Std ( $ S_{21} $ ) (%)	Std ( $\arg.S_{21}$ ) (°)
-30	0.72	0.25	0.39
-50	5.19	3.81	2.01
-70	41.17	40.26	6.62

**Table II-4:** Standard deviation for three zero levels of the transmission coefficient  $S_{21}$ ,  $f = 2$  GHz,  $P_0 = 0$  dBm, IFBW = 100 Hz, acquisition time = 5 hours, number of points = 600

It is retrieved that the standard deviation diminishes when the zero level increases, just as found in Table II-3. When comparing Table II-4 and Table II-3, it is evidenced that much more errors are found for all the transmission coefficients considered after a long term test. Therefore, the acquisition time that considerably affects the test stability is an important data when imaging applications are aimed.

After having done a complete study of a 5h-stability test, a further investigation is focused on standard deviation evolution with acquisition time as illustrated in Fig. II-26.

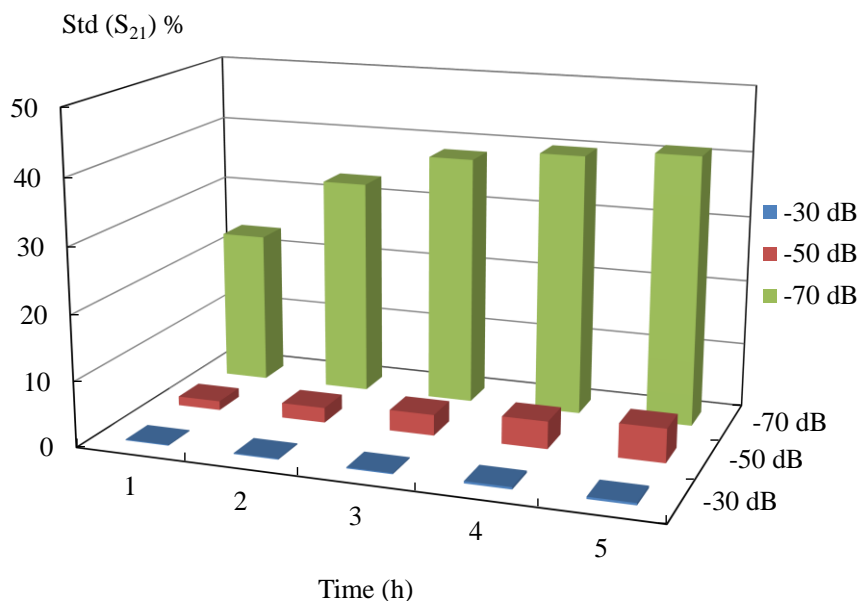


**Fig. II-26:** Standard deviation of the transmission coefficient as a function of acquisition time under three zero levels,  $f = 2$  GHz, IFBW = 100 Hz, number of points = 600

This study provides the distribution of the system drift errors versus acquisition time. As evidenced by the figure, the deviation first increases with acquisition time and then stabilizes for the three zero levels considered. It is clearly visible for the -70 dB response that the rate of the rise of the drift errors slows down with acquisition time. This indicates a gradual downward trend of the deviation increase. It can also be observed in this figure that, for the same period, the test results turn out to be much more repeatable for higher zero levels (-30 dB and -50 dB) than that for the lowest one (-70 dB). Generally, a low signal level (-70 dB) is supposed to be chosen to benefit of a larger dynamic range of the transmission coefficient. However, in that case, the standard deviation (Fig. II-26) of a 2-hour measurement for example is quite high (33.2 %). By contrast, for a higher zero level (-30 dB and -50 dB), the drift errors are much lower (0.15 % and 2.3 %) but at the expense of a smaller dynamic range. Thus, there is a hard compromise to be found between the zero level, the acquisition time and the dynamic range.

As a conclusion, given all the results obtained in this section, we demonstrate that key parameters such as IFBW, acquisition time and zero level have a great impact on the measurement repeatability. A magnitude of -50 dB of the zero level is believed to be a good candidate for applications where a long-term measurement lasting hours is

needed. By contrast, for short-term measurements typically lasting minutes, a level of -70 dB can be applied to benefit from the best dynamic range.

#### **II.4.4 Scanning repeatability study**

The optimized key parameters needed to perform short-term and/or long-term tests have been carefully discussed. It has been shown that the electrical components of the platform (VNA, coupler, impedance tuner etc.) have a strong impact on the measurement reproducibility. On the other hand, as mentioned above, the mechanical error is also related to the measurement repeatability. In this part, we first present the influence of the x-y-z stage on the measurement precision by analyzing 1D scanning tests. Afterwards, a 2D microwave imaging application is investigated to quantify the platform performance.

##### **II.4.4.1 Extraction of scanning errors in 1D scanning**

The 3D stage enables a large scanning area of  $200 \times 200 \text{ mm}^2$  in x/y directions and a displacement of 10 mm in z direction with a positioning uncertainty in the order of  $0.1 \text{ }\mu\text{m}$ . However, as the measured data are obtained by stepping the scanning motors point by point, even such a small positioning error can lower the repeatability of one-line or 2D scanning measurements. Therefore, the error generated during the scanning process has also to be evaluated.

The set-up configuration is such as the key parameters mentioned above, IFBW, acquisition time and zero level, are fixed to 100 Hz, 2 hours and -50 dB respectively to run a long-term test. The EMP is positioned  $10 \text{ }\mu\text{m}$  over a metallic surface, as displayed in Fig. II-27. To test the reliability of the stage, the sample is moved to another position along x/y directions in a step of  $1000 \text{ }\mu\text{m}$  which is much larger than the minimum step size of the stage ( $1 \text{ }\mu\text{m}$ ), and then moved back to the initial position (Fig. II-27.a). This process is conducted 10 times in 2 hours. Similarly, in z direction, a process of stand-off distance jumping up to  $1000 \text{ }\mu\text{m}$  and falling to  $10 \text{ }\mu\text{m}$  is repeated 10 times during the same period (Fig. II-27.b).

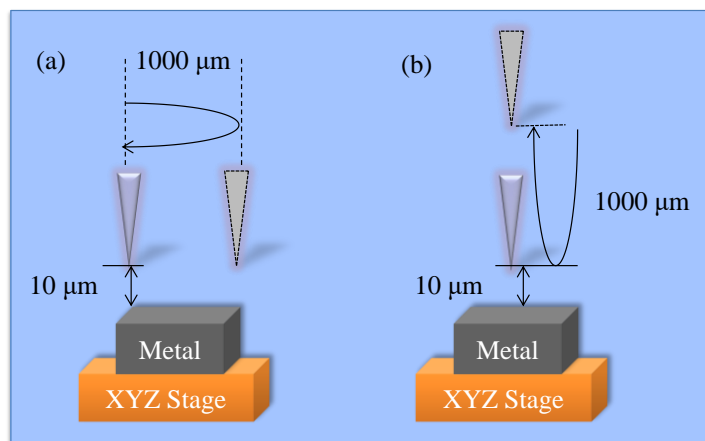


**Fig. II-27:** Repeatability tests of the motorized stage in x/y directions (a) and in z direction (b), the displacement is performed in a step of 1000 μm

As said before, the errors are studied in two different situations with and without movement of the stage. In case of 1D and 2D scanning, the errors are of two kinds, electrical and mechanical. At the probe initial position (10 μm as stand-off distance), standard deviations are calculated as 5.20 %, 5.44 % and 5.74 % for x, y and z directions respectively. For comparison, a close standard deviation in the order of 6 % for z direction was found in [GU 15b]. This uncertainty, taking into account electrical and mechanical errors, is acceptable for long term applications such as 2D microwave imaging. It is worth noting that the impact of environmental conditions such as temperature and humidity drifts have not been taken into account in this evaluation method of the errors occurring when using the platform in particular for long time lasting experiments.

#### II.4.4.2 2D nondestructive microwave imaging

The previous repeatability study has demonstrated excellent measurement reliability when using optimized key setting parameters. Indeed, even for a long term test, the relative deviations of the stage in x/y directions are only about 5 % after 2 hours-test. Consequently, the good stability and versatility offered by the iNFMM proposed allow us to envisage a wide range of applications in different fields. Particularly, we show that the platform is suitable for 2D nondestructive imaging with sub-wavelength spatial resolution. In these experiments the probe selected has an apex of 66 μm. As a demonstration, we have scanned a chip area of a widely available card (Fig. II-28.a). A microphotograph of a metallic slot is also shown in Fig. II-28.b.

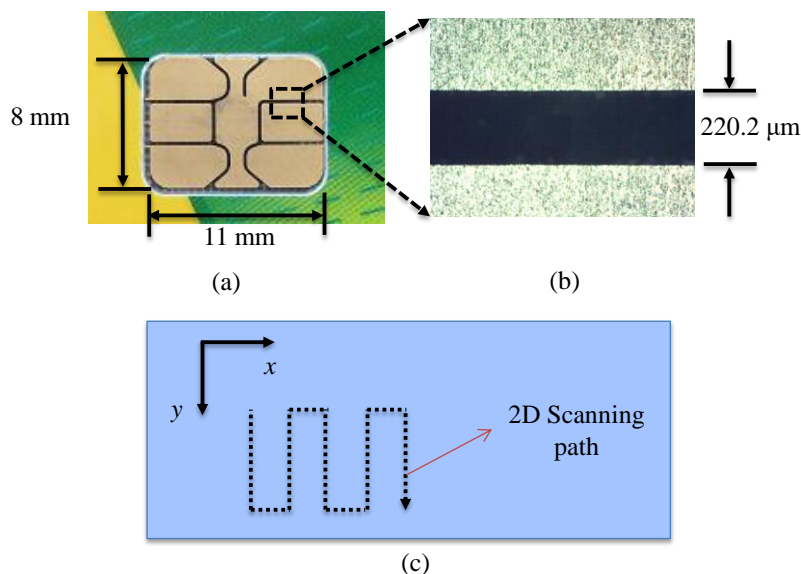


**Fig. II-28:** Image of the chip area ( $11 \times 8 \text{ mm}^2$ ) of a common chip card, (a): the chip region is metalized and the rest of the card is in plastic, (b): zoomed slot line width (optical image) and (c): 2D scanning path

As shown in Fig. II-28.c, the 2D image is completed by moving the x-y-z stage in a zigzag path (sweep in one direction on y-axis followed by a step in x direction and a sweep in the other direction on y-axis). Considering the drift errors increase with the measurement duration, we have kept for the IFBW and the zero level the values that have shown the optimized results in case of long term test (IFBW = 100 Hz, zero level = -50 dB). The sweep speed of the evanescent probe is set to 600 pixels per minute with a step size of 50 μm which is smaller than the tip apex (260 μm). The scanning area corresponds to half of the chip surface ( $11 \times 8 \text{ mm}^2$ ), resulting in a scanning duration of 1 hour. To assure the microscope operates in near-field region, the separation distance between the tip and the sample is set to 10 μm. To evaluate the accuracy and repeatability of the microscopy system, we investigate the difference between microwave images obtained by repeating the same scanning process several times (5 times). We show in Fig. II-29 the images ( $|S_{21}|$ ,  $\arg.S_{21}$ ) that present the largest difference observed. First, it can be noticed that both magnitude and phase-shift clearly return the chip area image. The maximum contrast for magnitude and phase-shift are 8 dB (Fig. II-29.a and b) and  $40^\circ$  (Fig. II-29.d and e) respectively. As illustrated on these images, the slot width retrieved, equal to 250 μm, is close to the value obtained by the optical image (220.2 μm, Fig. II-28). This width corresponds to about  $\lambda_0/600$  at 2 GHz

in free space. So, one conclusion that can be drawn after these tests is the achievement of images with subwavelength spatial resolution.

To better appreciate the difference between the 2D scans we have plotted the images obtained by subtracting pixel by pixel the results recorded for each case in terms of magnitude (Fig. II-29.c) and phase-shift (Fig. II-29.f).

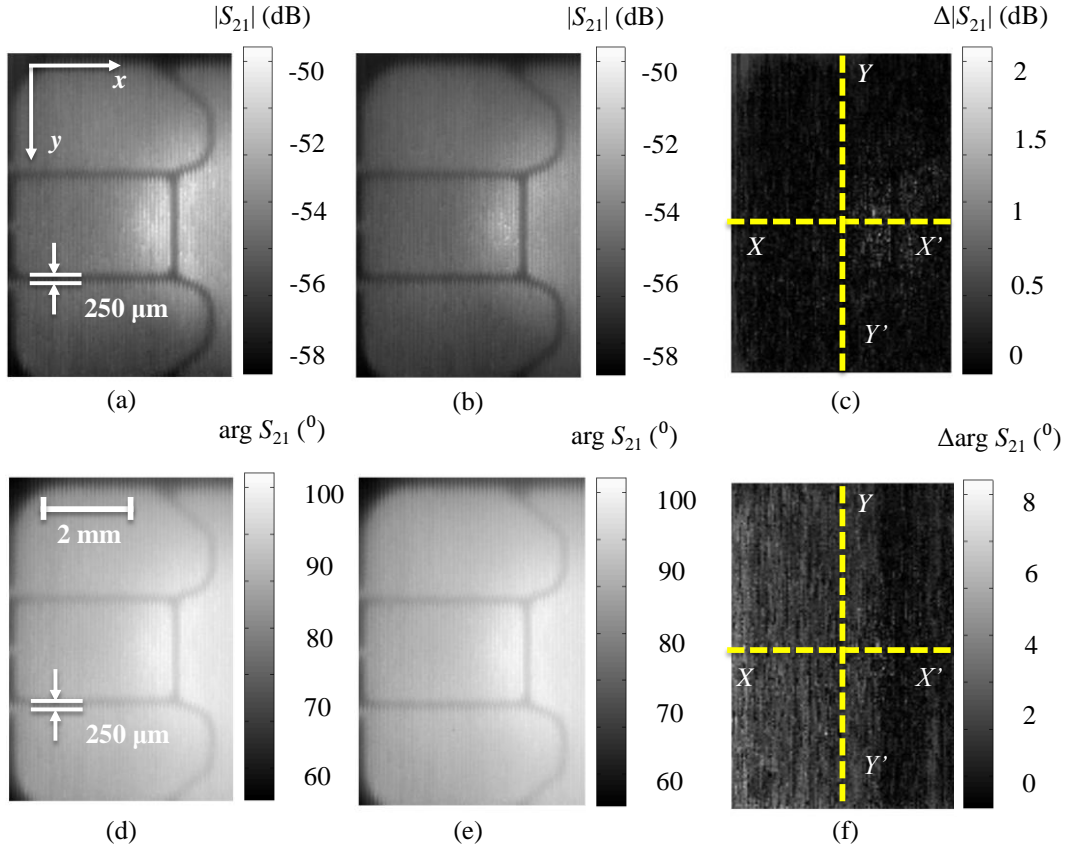


**Fig. II-29:** 2D images on chip area ( $5.5 \times 8 \text{ mm}^2$ ) of a card with a step of  $50 \mu\text{m}$ , (a) and (b): magnitude images with the same test conditions, (c): subtraction between (a) and (b), (d) and (e): phase-shift images with the same test conditions, (f): subtraction between (d) and (e); tip-sample separation= $10 \mu\text{m}$ ,  $f=2 \text{ GHz}$ , IFBW =  $100 \text{ Hz}$ , zero level =  $-50 \text{ dB}$

A maximum variation of  $2 \text{ dB}$  and  $8^\circ$  respectively for magnitude and phase-shift is noted. Because of the low zero level, the variation is not uniform on the entire scanned surface. So, we have collected the mean values for different positions materialized by the dashed lines on Fig. II-29.c and Fig. II-29.f. In fact to obtain the mean in x direction, we calculate the averaged values of every line along y direction. Then, the influence of the setting parameters is analyzed by varying the values around the optimized ones (IFBW= $100 \text{ Hz}$  and zero level =  $-50 \text{ dB}$ ). Two situations are considered, we change only one parameter, either IFBW or  $|S_{21}|$  is modified (1<sup>st</sup> case: IFBW= $1000$

Hz and zero level = -50 dB; 2<sup>nd</sup> case: IFBW=100 Hz and zero level = -70 dB). The results are reported in Fig. II-30.

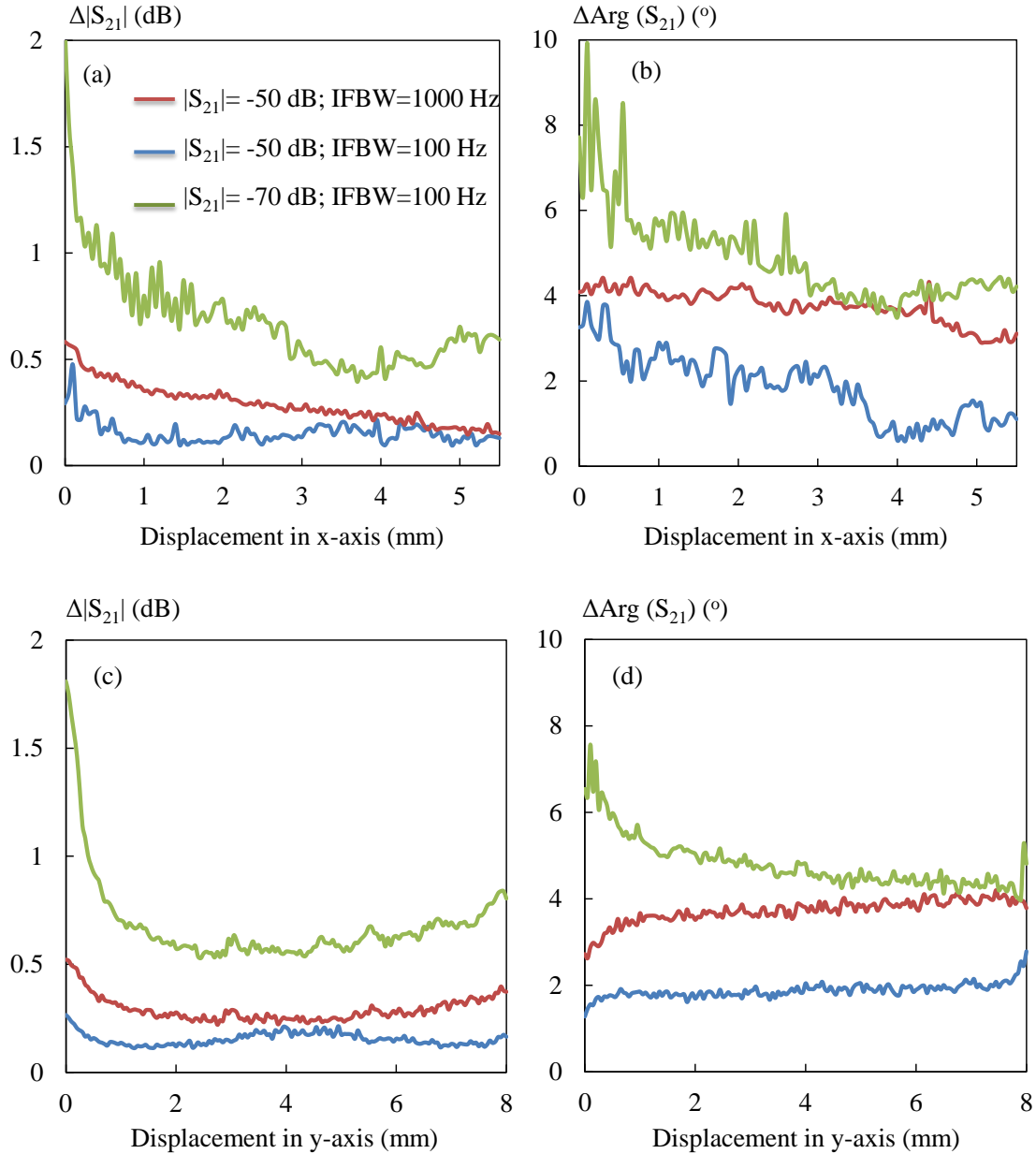


**Fig. II-30:** Averaged variation of transmission coefficient magnitude and phase-shift calculated every 50  $\mu\text{m}$ , (a) and (b): mean in x direction, (c) and (d): mean in y direction

This figure clearly exhibits the drift level that affects the 2D microwave imaging process. Because of the sweeping mechanism chosen (zigzag: continuous sweep along y-axis and stepped sweep along x-axis) the results are less noisy for the displacement on y-axis. We also confirm that the best results are obtained in case of optimized setting parameters (IFBW, zero level of  $|S_{21}|$ ) with fluctuations lower than 0.5 dB for the

magnitude and lower than  $3^\circ$  for the phase-shift. As highlighted by Fig. II-30, if we deviate from these optimized setting parameters the accuracy is strongly impacted; the errors are doubled at least. To perform these tests, only one parameter has been modified at once, it is quite obvious that the performance will be even lowered if both are changed in the same time. These results altogether demonstrate the influence of the setting parameters on the platform accuracy.

#### **II.4.5 Conclusion**

A near-field microwave microscopy platform based on an interferometric technique is evaluated through the study of key configuration parameters. Setting parameters such as IFBW, acquisition time, zero level set by the interferometer are investigated to determine the performance of the system in terms of accuracy and repeatability. It is demonstrated that the error measured for applications requiring displacement (1D and 2D scanning) is less than 6 %, while for characterizations with a fixed stage, it is less than 3 %. Moreover, the evaluation of a 2D imaging technique, with sub-wavelength spatial resolution, is performed. The 2D scanning images confirm that the best results are obtained in case of optimized setting parameters (IFBW = 100 Hz, zero level = -50 dB).

## **II.5 Conclusion**

In this chapter, we have discussed the principle of the proposed iNFMM and demonstrated its performance. First, to solve the mismatch issue between the high impedance EMP and the VNA (characteristic impedance = 50  $\Omega$ ), an interferometer based matching network is included into the NFMM. The interferometer made of a hybrid coupler and an impedance tuner, is used to introduce a wave-cancellation process into the system. It has been shown that this technique largely improves the measurement sensitivity.

Then, simulation tools including Ansys<sup>TM</sup>/HFSS and Keysight<sup>TM</sup>/ADS are employed to analyze the performance of the EMP and the whole iNFMM. It is shown, according to the distribution of the electromagnetic field, that the E-field energy is well confined around the probe apex and it decays rapidly with the distance to the tip in the near field region. In fact, this property enables a very local characterization of the material/device under test. Later, the wave-cancelling process provided by the interferometric technique is simulated by Keysight<sup>TM</sup>/ADS platform. All these simulation results lead to a better understanding of the iNFMM, especially the EMP behavior and the wave-cancelling process used in the interferometric technique.

Then, the microwave components that compose the iNFMM such as the coupler, the impedance tuner and the EMP are characterized. One can note that the properties of the components selected guarantee a broad frequency of operation from 2 to 18 GHz. Afterwards, the wave-cancelling process is experimentally validated by employing an impedance tuner made of motorized attenuator and a high resolution delay line. Particularly, we have shown that the zero level can be tuned to a very sharp resonance, which corresponds to a high quality factor, by carefully adjusting the attenuator. Furthermore, thanks to the motorized delay line, the platform is able to operate in a quasi-continuous frequency range [2-18 GHz] with a step of 0.8 MHz. Based on this wave-cancelling mechanism, the performance of the iNFMM is evaluated in terms of the quality factor. The results return an excellent measurement sensitivity in the whole frequency range compared to the resonator-based NFMM. Therefore, the matching technique selected brings advantages such as tuning simplicity and a relatively flexible choice of the operating frequency used for measurements compared to the conventional resonator-based matching method.

Additionally, it is worth mentioning that the interferometer is composed of passive components which lead to a low power consumption and good signal-to-noise ratio.

In the final section of this chapter, the influence of the setting parameters (zero level, IFBW and acquisition time) on the measurement accuracy is carefully studied through the evaluation of the performance of the iNFMM in terms of repeatability. Particularly, a low IFBW leads to a better measurement repeatability thanks to a low noise floor of the VNA, but results in a long acquisition time. Furthermore, a low zero level leads to a large measurement dynamic range and a better sensitivity, but a poor measurement accuracy and repeatability. In fact, there is a compromise between the measurement accuracy, the IFBW and the related acquisition time which has been carefully discussed in Section II.4.3. Depending on the application targeted, the IFBW, the frequency band of operation and the number of frequency points can be adjusted. Generally speaking, the key parameters can be set to: zero level = -50 dB and IFBW = 100 Hz for both short-term and long-term measurements. Based on the optimal setting parameters, the error measured for applications requiring displacement (1D and 2D scanning) is less than 6 %, while for characterizations with a fixed stage, it is less than 3 %. Then, the evaluation of a 2D imaging technique, with sub-wavelength spatial resolution, is performed. Finally, it is also clearly shown that if we deviate from the optimal setting parameters the measurement accuracy is strongly impacted.

After evaluating the performance of the proposed microwave microscope, in the following chapter, applications of the iNFMM including 2D imaging and material impedance characterizations will be addressed.

## II.6 References

(41 references, Classified in alphabetical order)

- [BAK 13] H. Bakli, K. Haddadi, and T. Lasri, "Interferometric technique for scanning near-field microwave microscopy applications," 5<sup>th</sup> International Instrumentation and Measurement Technology Conference (I<sup>2</sup>MTC), Minneapolis, USA, May 2013.
- [BAK 14] H. Bakli, K. Haddadi, and T. Lasri, "Interferometric technique for scanning near-field microwave microscopy applications," *IEEE Trans. Instrum. Meas.*, vol. 63, n<sup>o</sup>. 5, pp. 1281–1286, 2014.
- [CAS 11] J.T. Case, M.T. Ghasr, R. Zoughi, "Optimum Two-Dimensional Uniform Spatial Sampling for Microwave SAR-Based NDE Imaging Systems," *IEEE Trans. Instrum. Meas.*, vol. 60, n<sup>o</sup>.12, pp. 3806-3815, 2011.
- [CHE 02] Y. Chen, H. Cheng, G. Wang, X. Xiang, C. Lei and I. Lin, "Measurement of Dielectric Property by Evanescent Microwave Microscope", *Jpn. J. Appl. Phys.*, vol. 41 pp. 7214–7217, Nov. 2002.
- [CHI 12] J. D. Chisum and Z. Popovi, "Performance limitations and measurement analysis of a near-field microwave microscope for nondestructive and subsurface detection", *IEEE Trans. Microw. Theory Tech.*, vol. 60, n<sup>o</sup>. 8, pp. 2605–2615, 2012.
- [COR 15] M. F. Córdoba-Erazo and T. M. Weller, "Noncontact electrical characterization of printed resistors using microwave microscopy", *IEEE Trans. Instrum. Mea.* vol. 64, n<sup>o</sup>. 2, pp. 509-515, 2015.
- [DAR 13] T. Dargent, K. Haddadi, T. Lasri, N. Clement, D. Ducatteau, B. Legrand, H. Tanbakuchi, and D. Theron, "An interferometric scanning microwave microscope and calibration method for sub-fF microwave measurements," *Rev. Sci. Instrum.*, vol. 84, n<sup>o</sup>. 12, 2013.
- [DEB 10] R. Debroucke, J. Larchanche, D. Theron, D. Ducatteau, and H. Tanbakuchi, "Sub-femtoFarad MOS Varactor Characterization Tools," in *Microwave Conference (EuMC), 2010 European*, pp. 783–786, 2010.
- [DEB 11] R. Debroucke, D. Gloria, D. Ducatteau, D. Theron, H. Tanbakuchi, and C. Gaquiere, "attoF MOS varactor RF measurement VNA coupled with interferometer," in *2011 77th ARFTG Microwave Measurement Conference: Design and Measurement of Microwave Systems, ARFTG 2011*, pp. 1–2, 2011.
- [EDW 98] H. Edwards, R. McGlothlin, and E. U, "Vertical metrology using scanning-probe microscopes: Imaging distortions and measurement repeatability", *Jour. Appl. Phys.* vol. 83, 3952, 1998.
- [GRA 15] G. Gramse, E. Brinciotti, A. Lucibello, S. B. Patil, M. Kasper, C. Rankl, R. Giridharagopal, P. Hinterdorfer, R. Marcelli, and F. Kienberger, "Quantitative sub-surface and non-contact imaging using scanning microwave microscopy," *Nanotechnology*, vol. 26, n<sup>o</sup>. 13, 135701, 2015.
- [GRE 16] A. P. Gregory, J. F. Blackburn, K. Lees, R. N. Clarke, T. E. Hodgetts, S. M. Hanham, and N. Klein, "Measurement of the permittivity and loss of high-loss

- materials using a Near-Field Scanning Microwave Microscope,” *Ultramicroscopy*, vol. 161, pp. 137–145, 2016.
- [GU 14] S. Gu, K. Haddadi, and T. Lasri, “Near-field microwave microscopy for liquid characterization”, *European Microwave Conference (EuMC)*, pp. 628-631, Rome, Italy, Oct. 2014.
- [GU 15a] S. Gu, K. Haddadi, A. El Fellahi and T. Lasri, “Near-field scanning microwave microscope for subsurface non-destructive characterization”, *European Microwave Conference (EuMC)*, pp. 155-158, Paris, France, Sept. 2015.
- [GU 15b] S. Gu, K. Haddadi, A. El Fellahi, G. Dambrine and T. Lasri, “Measurement Accuracy and Repeatability in Near-Field Scanning Microwave Microscopy”, *International Instrumentation and Measurement Technology Conference (I<sup>2</sup>MTC)*, Pisa, Italy, May 2015.
- [GU 16a] S. Gu, K. Haddadi, A. El Fellahi and T. Lasri, “Setting Parameters Influence on Accuracy and Stability of Near-Field Scanning Microwave Microscopy Platform”, *IEEE Trans. Instrum. Meas.*, vol. 65, n<sup>o</sup>. 4, pp. 890–897, 2016.
- [GU 16b] S. Gu, T. Lin and T. Lasri, “Broadband dielectric characterization of aqueous saline solutions by an interferometer-based microwave microscope”, *Appl. Phys. Lett.* vol. 108, 242903, 2016.
- [HAD 11] K. Haddadi, D. Glay, and T. Lasri, “Near-field scanning microscopy in liquid media based on microwave interferometry,” *9<sup>th</sup> International Conference on Electromagnetic Wave Interaction with Water and Moist Substances (ISEMA)*, Kansas City, Missouri, USA, 2011.
- [HAD 12] K. Haddadi, H. Bakli, and T. Lasri, “Microwave liquid sensing based on interferometry and microscopy techniques,” *IEEE Microw. Wirel. Components Lett.*, vol. 22, n<sup>o</sup>. 10, pp. 542–544, 2012.
- [HAD 14] K. Haddadi and T. Lasri, “Interferometer-Based Microwave Microscopy Operating in Transmission Mode,” *IEEE Sens. J.*, vol. 14, n<sup>o</sup>. 7, pp. 2226–2227, 2014.
- [HOF 14] J. Hoffmann, G. Gramse, J. Niegemann, M. Zeier, and F. Kienberger, “Measuring low loss dielectric substrates with scanning probe microscopes,” *Appl. Phys. Lett.*, vol. 105, n<sup>o</sup>. 1, pp. 1–5, 2014.
- [HUB 10] H. P. Huber, M. Moertelmaier, T. M. Wallis, C. J. Chiang, M. Hochleitner, A. Imtiaz, Y. J. Oh, K. Schilcher, M. Dieudonne, J. Smoliner, P. Hinterdorfer, S. J. Rosner, H. Tanbakuchi, P. Kabos, and F. Kienberger, “Calibrated nanoscale capacitance measurements using a scanning microwave microscope”, *Rev. Sci. Instrum.*, vol. 81, 113701, 2010.
- [HUM 12] I. Humer, H. P. Huber, F. Kienberger, J. Danzberger, and J. Smoliner, "Phase and amplitude sensitive scanning microwave microscopy/spectroscopy on metal–oxide–semiconductor systems." *Jour. Appl. Phys.* vol. 111, 074313, 2012.
- [IMT 14] A. Imtiaz and al., "Near-Field Scanning Microwave Microscopy: An Emerging Research Tool for Nanoscale Metrology”, *IEEE Micro. Mag.*, vol.15, n<sup>o</sup>.1, pp.52-64, Jan. 2014.

- [KIM 05] S. Kim, H. Yoo, K. Lee, B. Friedman, M. A. Gaspar, and R. Levicky, "Distance control for a near-field scanning microwave microscope in liquid using a quartz tuning fork," *Appl. Phys. Lett.*, vol. 86, n<sup>o</sup>. 15, pp. 1–3, 2005.
- [KLE 06] R. A. Kleismit, M. K. Kazimierczuk and G. Kozlowski. "Sensitivity and resolution of evanescent microwave microscope." *IEEE trans. Microwave theo. Tech.* vol. 54, n<sup>o</sup>. 2, pp. 639-647, 2006.
- [LAI 09] K. Lai, W. Kundhikanjana, H. Peng, Y. Cui, M. A. Kelly, and Z. X. Shen, "Tapping mode microwave impedance microscopy," *Rev. Sci. Instrum.*, vol. 80, n<sup>o</sup>. 4, p. 043707, 2009.
- [MIC 15] L. Michalas, F. Wang, C. Brillard, N. Chevalier, J. M. Hartmann, R. Marcelli, and D. Theron, "Modeling and de-embedding the interferometric scanning microwave microscopy by means of dopant profile calibration," *Appl. Phys. Lett.*, vol. 107, n<sup>o</sup>. 22, 2015
- [OLA 13] A. O. Oladipo, M. Kasper, S. Lavdas, G. Gramse, F. Kienberger, and N. C. Panoiu, "Three-dimensional finite-element simulations of a scanning microwave microscope cantilever for imaging at the nanoscale", *Appl. Phys. Lett.*, vol. 103, 213106, 2013.
- [OLA 14] A. O. Oladipo, A. Lucibello, M. Kasper, S. Lavdas, G. M. Sardi, E. Proietti, F. Kienberger, R. Marcelli, and N. C. Panoiu, "Analysis of a transmission mode scanning microwave microscope for subsurface imaging at the nanoscale", *Appl. Phys. Lett.*, vol. 105, 133112, 2014.
- [PAR 05] J. Park, S. Hyun, A. Kim, T. Kim, and K. Char, "Observation of biological samples using a scanning microwave microscope," *Ultramicroscopy*, vol. 102, n<sup>o</sup>. 2, pp. 101–106, 2005.
- [STE 98] D. E. Steinhauer, C. P. Vlahacos, S. K. Dutta, B. J. Feenstra, F. C. Wellstood, and S. M. Anlage, "Quantitative imaging of sheet resistance with a scanning near-field microwave microscope," *Appl. Phys. Lett.*, vol. 72, n<sup>o</sup>. 7, pp. 861–863, 1998.
- [SUN 14] W. Sun, Y. Yang, Z. Wu, T. Feng, Q. Zhuang, L. M. Peng, S. Xu, and C. K. Ong, "Penetrative imaging of sub-surface microstructures with a near-field microwave microscope," *J. Appl. Phys.*, vol. 116, n<sup>o</sup>. 4, 2014.
- [TAB 99] M. Tabib-Azar, D.-P. Su, A. Pohar, S. R. LeClair, and G. Ponchak, "0.4  $\mu\text{m}$  spatial resolution with 1 GHz ( $\lambda=30\text{cm}$ ) evanescent microwave probe," *Rev. Sci. Instrum.*, vol. 70, n<sup>o</sup>. 3, pp. 1725–1729, 1999.
- [TAB 00] M. Tabib-Azar and S. R. Leclair, "Applications of evanescent microwave probes in gas and chemical sensors," *Sensors Actuators, B Chem.*, vol. 67, n<sup>o</sup>. 1, pp. 112–121, 2000.
- [TAL 09] V. V. Talanov and A. R. Schwartz, "Near-field scanning microwave microscope for interline capacitance characterization of nanoelectronics interconnect," *IEEE Trans. Microw. Theory Tech.*, vol. 57, n<sup>o</sup>. 5, pp. 1224–1229, 2009.
- [TOR 12] K. Torigoe, M. Arita, and T. Motooka, "Sensitivity analysis of scanning microwave microscopy for nano-scale dopant measurements in Si", *Jour. Appl. Phys.* vol. 112, 104325, 2012.

- [TSE 07] A. Tselev, S. M. Anlage, Z. Ma, and J. Melngailis, "Broadband dielectric microwave microscopy on micron length scales," *Rev. Sci. Instrum.*, vol. 78, n<sup>o</sup>. 4, 2007.
- [WEB 12] J. C. Weber, J. B. Schlager, N. A. Sanford, A. Imtiaz, T. M. Wallis, L. M. Mansfield, K. J. Coakley, K. A. Bertness, P. Kabos, and V. M. Bright, "A near-field scanning microwave microscope for characterization of inhomogeneous photovoltaics," *Rev. Sci. Instrum.*, vol. 83, n<sup>o</sup>. 8, 2012.
- [WEB 14] J. C. Weber, P. T. Blanchard, A. W. Sanders, A. Imtiaz, T. M. Wallis, K. J. Coakley, K. A. Bertness, P. Kabos, N. A. Sanford, and V. M. Bright. "Gallium nitride nanowire probe for near-field scanning microwave microscopy." *Appl. Phys. Lett.*, vol. 104, 023113, 2014.
- [XIA 14] Z. Xia, J. Wang, Y. Hou, and Q. Lu, "A high stability and repeatability electrochemical scanning tunneling microscope", *Rev. Sci. Instrum.*, vol. 85, 125103, 2014.



## Chapter III

### Materials characterization by iNFMM

#### III.1 Introduction

The near-field microwave microscope is now a valuable tool to locally investigate materials properties. Indeed, thanks to its high spatial resolution it has great potential for applications in different fields like biology, chemistry, materials sciences, microelectronics and so on [TAL 09], [FAR 12a], [ANL 07]. As previously mentioned, one of the main difficulties of the NFMM is the impedance mismatch issue between the high-impedance probe and the  $50 \Omega$  VNA. We have seen that the addition of an interferometer is a solution to provide the NFMM a high measurement sensitivity. In the Chapter II, the performance of the iNFMM has been validated and the setting parameters of the proposed iNFMM (IFBW, zero level and acquisition time) have been finely studied in terms of the repeatability of the platform. Based on these setting parameters, various applications including surface imaging and local characterization of materials/structures can be achieved. For the demonstration, some important applications of the iNFMM are presented in this chapter.

First, one of the essential capabilities of the iNFMM, which is the scanning spatial resolution, is investigated. To demonstrate the benefit of adding the interferometer in the NFMM, two configurations of the system are considered, without and with the interferometer. The influence of scanning parameters (including the tip-sample distance  $H$ , the scanning step size  $S$  of the  $x$ - $y$ - $z$  stage and the probe size  $D$ ) on the scanning quality is carefully investigated through 1D and 2D experiments. Furthermore, the set of the parameters ( $H$ ,  $S$  and  $D$ ) is determined to demonstrate the best scanning and imaging performance. Then, we exhibit the possibility to enhance the scanning quality of the iNFMM proposed by a signal processing method which reduces the background noise during the scanning process.

Secondly, the platform is evaluated for a possible characterization of bio-samples in a wide frequency band from 2 to 18 GHz. The material chosen for the tests is a widely used liquid when study bio-samples, namely a saline aqueous solution. The probe tip is immersed into the liquid to guarantee a good electromagnetic coupling

between the probe and the liquid. To ensure an accurate and a repeatable measurement, the probe position in liquid is carefully defined. Then the complex permittivity of the saline solutions is extracted by two different methods. Finally, the experimental permittivities are compared to the theoretical values calculated by Cole-Cole model to appreciate the performance of these methods.

After demonstrating the capability of liquids characterization in a wide frequency range by using the proposed iNFMM, the non-contact and non-destructive evaluation of 2D materials is presented in the final section of this chapter. For the demonstration, graphene is selected as the material under test. The choice of this 2D nanomaterial is motivated by its unique physical properties and numerous potential applications in electronics. The complex impedance of a graphene layer is extracted in the frequency range [2-18 GHz].

## III.2 Study of 1D and 2D spatial resolutions study of the iNFMM

### III.2.1 Introduction

Free-space microwave non-destructive sensing and surface imaging techniques have great potentials for a wide range of applications [GUI 11] [KHA 07]. Traditional non-destructive sensing techniques are generally based on transmission lines or free-space methods [HAD 11], [HAD 12a]. The spatial resolution achievable in case of these methods, set by the diffraction limit, is in the order of half the wavelength of operation. Thus, in the microwave spectrum, the spatial resolution is at best in the order of the millimeter.

In order to bypass the diffraction limit, microscopy methods based on evanescent waves rather than propagating ones can be used [ANL 07]. Actually, an evanescent wave is an oscillating electric and/or magnetic field which does not propagate as an electromagnetic wave but whose energy is spatially concentrated in the vicinity of the source (near-field region). Practically, near-field microwave microscopy has advanced the knowledge in the local characterization of materials and a variety of near-field probes have been reported [TAL 09], [FAB 11]. Evanescent probes based on tapered microstrip or coaxial transmission lines are very attractive owing to their simple structure and high spatial resolution.

In this section, 1D and 2D spatial resolutions, which are essential features of the proposed iNFMM, are carefully studied. Practically, the impacts on the spatial resolution of the scanning parameters, including the tip-sample distance  $H$ , the scanning step size  $S$  and the probe size  $D$ , are investigated. To demonstrate the measurement sensitivity brought by the interferometric technique, two configurations of the proposed system are evaluated: without and with interferometer. The scanning parameters ( $S$ ,  $H$  and  $D$ ) which permit the best scanning performance are determined. Then, in order to improve ever more the resolution, a simple signal processing technique is applied. Actually, this method reduces the background noise during the scanning process and results in an enhanced imaging quality.

### III.2.2 Test conditions for the scanning process

In this study we are interested in imaging samples which size is larger than  $1000 \times 1000 \mu\text{m}^2$  at a relatively high scanning speed (300 pixels/min). This kind of situation can be found when studying microelectronics circuits, characterizing materials and in the non-destructive testing field in general. Because of the applications targeted we are not looking for an extremely high resolution but rather a sufficient one taking into account requirements such as image construction duration and robustness of the probe. The scanning efficiency and the duration should answer to a compromise. Actually, for 1D scanning process, the measurement lasts usually several minutes or even shorter but a 2D imaging process usually takes hours. Thus, the step size should be carefully selected to avoid an excessive scanning duration. We have also selected probes robust enough to avoid too frequent impairment of the tip. The tips sizes considered are in the range of a few tens to a few hundreds of micrometers.

Given all these requirements, as a demonstration, we have scanned a chip area of a widely available card (Fig. III-1). It is the same card as the one considered in Chapter II.4 (slot width =  $220.2 \mu\text{m}$ ). In this case the surface available to be scanned is around  $100 \text{ mm}^2$  but a smaller one can be selected on the chip. This size is a common one met in the integrated circuits fields.

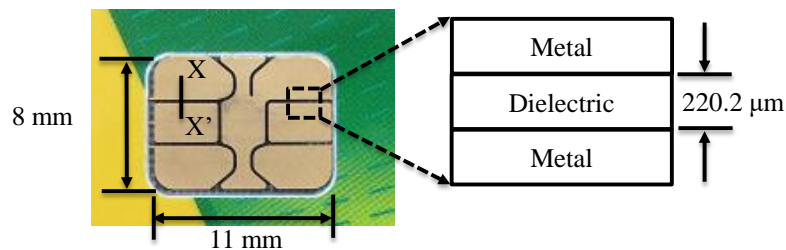


**Fig. III-1:** Image of the chip area ( $11 \times 8 \text{ mm}^2$ ) of a common chip card, the chip region is metalized and the rest of the card is in plastic, the 1D scanning process is along the line XX' where the dielectric slot line width stands for  $220.2 \mu\text{m}$

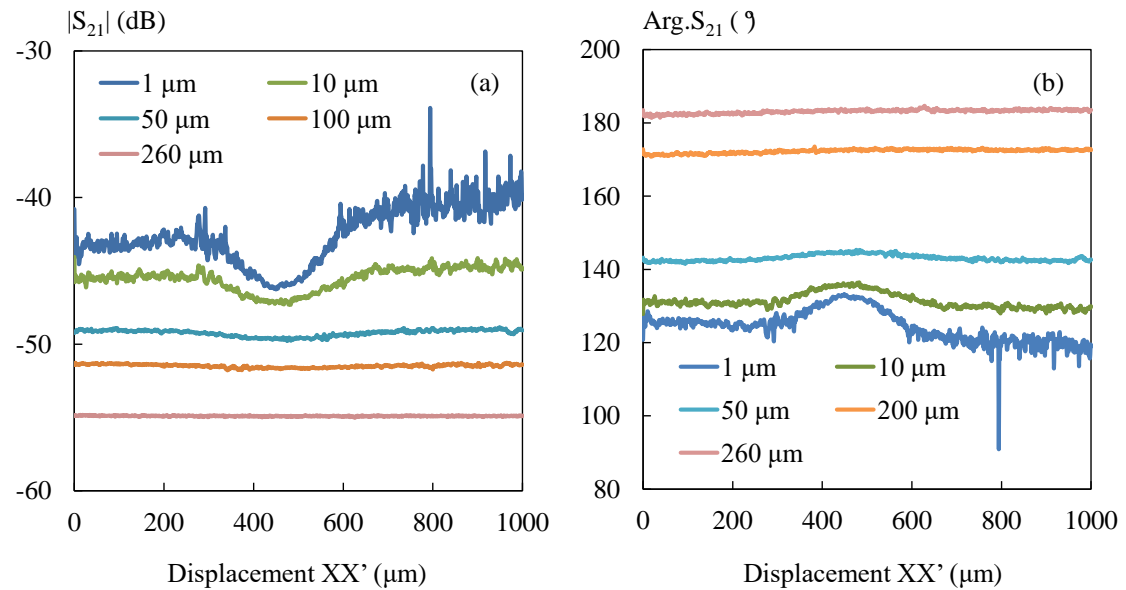
As the slot line width is  $220.2 \mu\text{m}$ , therefore, two probes are considered for the measurement: one slightly larger than the slot width (apex =  $260 \mu\text{m}$ ) and another one much smaller than the slot width (apex =  $66 \mu\text{m}$ ). Concerning the VNA, the setting parameters selected are 2 GHz for the frequency and 0 dBm for the power. In addition, the IFBW and zero level are selected as 100 Hz and -50 dB respectively for both 1D and 2D scanning for the reasons discussed in the Chapter II. In fact, we have to

precise that the zero level, tuned to -50 dB, is considered when the probe is on the plastic region of the chip card. In the following part, we start with the influence of the scanning parameters (H, S and D) on 1D spatial resolution. Actually, the 1D scanning is constructed on a line XX' that corresponds to a metal-dielectric-metal structure (Fig. III-1). This line whose length is 1000  $\mu\text{m}$  just crosses a slot (dielectric part) of 220.2  $\mu\text{m}$  width.

### III.2.3 Influence of the scanning parameters on the 1D scanning resolution

#### a) Probe-sample distance H

In this part, the influence of the probe-sample distance H on the scanning results is investigated. The scanning step is set to 1  $\mu\text{m}$  which is the minimum step offered by the motorized x-y-z stage of the system. The probe with an apex size of 260  $\mu\text{m}$  is selected for the scan. Particularly, for a scanning speed of 300 pixels/min, the scanning duration of the line XX' (Fig. III-1) is about 3 minutes. We present in Fig. III-2 the measured magnitude and phase-shift of the transmission coefficient obtained by linearly scanning the structure under test for different probe-sample distances at the test frequency of 2 GHz. The distance H varies from 1  $\mu\text{m}$  (minimum controllable distance of the stage) to 260  $\mu\text{m}$  (probe apex size). The results for five values of H (1, 5, 10, 25, 50, 100 and 260  $\mu\text{m}$ ) are selected to be presented in Fig. III-2.



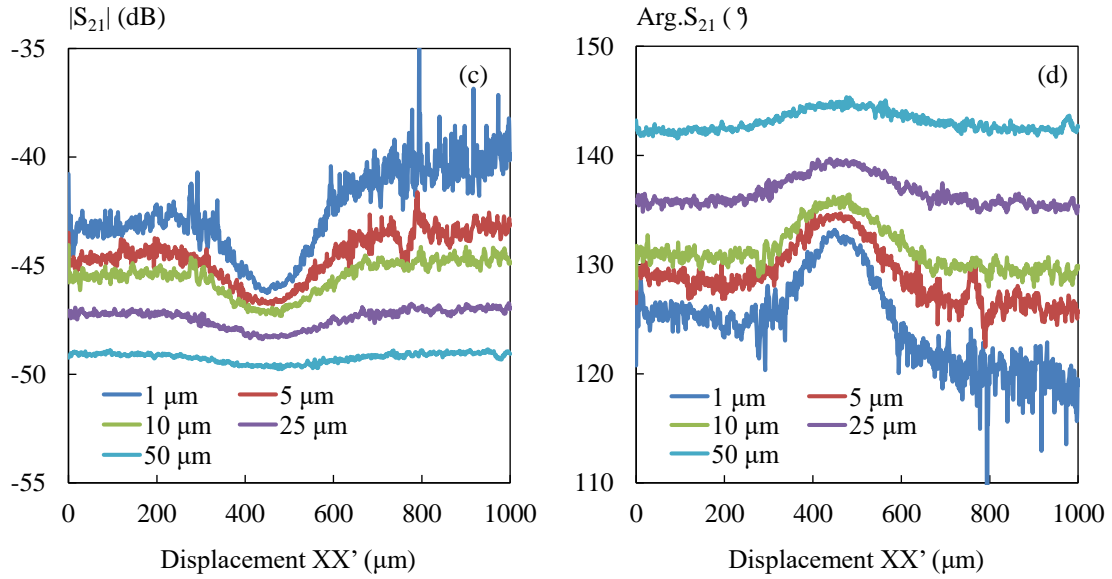


**Fig. III-2:** 1D scanning along the line  $XX'$  ( $1000 \mu\text{m}$ ) as a function of probe distance  $H$ , (a) and (b): magnitude and phase-shift of  $S_{21}$  for  $H$  varying from 1 to  $260 \mu\text{m}$ , (c) and (d): magnitude and phase-shift of  $S_{21}$  for  $H$  varying from 1 to  $50 \mu\text{m}$ ,  $f = 2 \text{ GHz}$ ,  $\text{IFBW} = 100 \text{ Hz}$ ,  $P_0 = 0 \text{ dBm}$ , zero level =  $-50 \text{ dB}$ ,  $S = 1 \mu\text{m}$ ,  $D = 260 \mu\text{m}$

As can be seen in Fig. III-2, the slot is clearly detected both in the magnitude and phase-shift of the transmission coefficient responses for small  $H$  (e.g.  $H = 1, 5, 10$  and  $25 \mu\text{m}$ , Fig. III-2.c and Fig. III-2.d). The slot becomes less detectable when the tip-sample distance  $H$  increases. Indeed, the collimation of the evanescent electrical fields diminishes with the height  $H$  [OMA 15a] [OMA 15b]. Especially, for  $H$  larger than  $50 \mu\text{m}$ , the slot can hardly be detected. Thus, to ensure a good lateral resolution, the stand-off distance must be kept relatively low (e.g.  $\leq 10 \mu\text{m}$ ). One can also note that a highest sensitivity can be obtained at the minimum height of  $1 \mu\text{m}$  (Fig. III-2). However, the closer the probe is to the surface of the structure, a more noisy result can be found in both Fig. III-2.c and Fig. III-2.d. So, considering the results obtained, a good compromise between the detectability and the scanning noise is  $10 \mu\text{m}$  for the stand-off distance. In addition, the inclination of the  $x$ - $y$ - $z$  stage can be observed especially for small stand-off distances in Fig. III-2, in particular for  $1 \mu\text{m}$  the presence of a tilt is clearly observed (Fig. III-2.c and Fig. III-2.d).

In this measurement, the slot width measured is defined by the full width at half maximum (FWHM) approach. This method represents the width corresponding to the half of maximum amplitude. For a demonstration, the magnitude in linear and the phase-shift for stand-off distance equal to  $10 \mu\text{m}$  are presented in Fig. III-3.

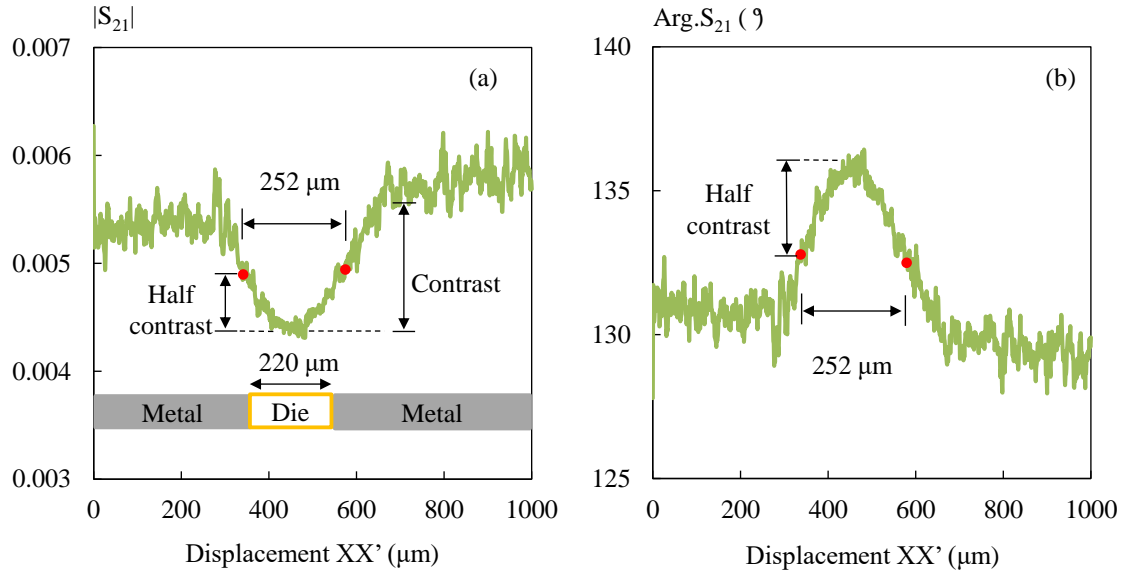


**Fig. III-3:** 1D scanning along the line XX' at a probe-sample distance  $H = 10 \mu\text{m}$ , (a): magnitude of  $S_{21}$ , (b): phase-shift of  $S_{21}$ ,  $f = 2 \text{ GHz}$ ,  $\text{IFBW} = 100 \text{ Hz}$ ,  $P_0 = 0 \text{ dBm}$ ,  $S = 1 \mu\text{m}$ ,  $D = 260 \mu\text{m}$ , zero level =  $-50 \text{ dB}$

In Fig. III-3.a, for the stand-off distance of  $10 \mu\text{m}$ , the magnitude at the middle of the slot region (dielectric material) is  $0.0043$  ( $-47.6 \text{ dB}$ ) is slight difference from the zero level value measured ( $-50 \text{ dB}$ ) in case of the plastic region. This variation is due to dielectric material in the slot region which is structurally different from the plastic plane near the chip region where the zero level is established. One can also note that when the tip is on the metal part, the signal magnitude returns  $0.0053$  ( $-45.5 \text{ dB}$ ) whereas this value turns to  $0.0043$  ( $-47.6 \text{ dB}$ ) at the middle of the slot region. We define the magnitude contrast as the difference between the magnitudes when the probe is on the metal ( $0.0053$ ) and when the probe is at the middle of the slot ( $0.0043$ ). In the present case a contrast of  $0.001$  ( $2 \text{ dB}$ ) is obtained (Fig. III-3.a). Similarly, the phase-shift contrast is found to be around  $7^\circ$  in Fig. III-3.b. According to the NFWHM method, the measured slot width is defined as the interval related to the positions corresponding to the half of the contrast value, as shown in Fig. III-3 [GU 15b]. After applying this evaluation method, the magnitude and the phase-shift plots demonstrate the same measured width that is  $252 \mu\text{m}$ . Obviously, the stand-off distance will influence the measurement test. To appreciate this influence, the width is presented as a function of the probe stand-off distance in Fig. III-4 and Table III-1. As the magnitude and the phase-shift plots offer comparable scanning results, to ease the presentation, all the results in the following are given only for the magnitude.

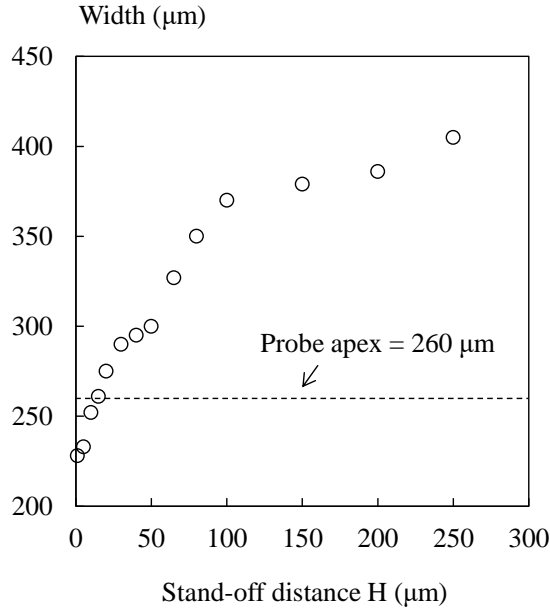


**Fig. III-4:** Measured width as a function of probe stand-off distance  $H$ ,  $f = 2$  GHz, IFBW = 100 Hz,  $P_0 = 0$  dBm, zero level = -50 dB,  $S = 1$   $\mu\text{m}$ ,  $D = 260$   $\mu\text{m}$

$H$ ( $\mu\text{m}$ )	1	5	10	15	20
Width ( $\mu\text{m}$ )	228	233	252	261	275
Difference in %	3.6 %	5.5 %	13.6 %	17%	24%

**Table III-1:** Measured width as a function of probe stand-off distance  $H$  and the difference compared with the actual width,  $f = 2$  GHz, IFBW = 100 Hz,  $P_0 = 0$  dBm, zero level = -50 dB,  $S = 1$   $\mu\text{m}$ ,  $D = 260$   $\mu\text{m}$

As shown in Fig. III-4 and Table III-1, as expected, a smaller probe-sample distance returns a better lateral resolution. Thus, the best result is obtained when using the minimum stand-off distance. For this configuration the width retrieved by FWHM approach is 228  $\mu\text{m}$  which is only 7  $\mu\text{m}$  (3.6 %) larger than the actual slot width (220  $\mu\text{m}$ ). On the contrary, for a stand-off distance higher than 20  $\mu\text{m}$ , the error is very large (> 20%). For the following experiments, considering the compromise between the scanning noise, scanning height and the scanning resolution, we set the stand-off distance  $H$  to 10  $\mu\text{m}$ .

#### b) Scanning step size $S$

The impact of the scanning step size on the spatial resolution is evaluated in this part. The stand-off distance is set to 10  $\mu\text{m}$  and the probe with apex of 260  $\mu\text{m}$  is used. For the tests, different step sizes smaller than the slot width (220  $\mu\text{m}$ ) varying from 1

$\mu\text{m}$  (minimum step size offered by the platform) to  $200 \mu\text{m}$  (in the order of the slot width) are selected. The testing duration depends on the scanning step size and the scanning speed. With a typical speed of  $300 \text{ pixels/min}$  for the system, the resulting scanning duration to scan the line  $XX'$  varies from several seconds ( $S = 200 \mu\text{m}$ ) to about 3 minutes ( $S = 1 \mu\text{m}$ ). The results of the measurement width estimated when using different step sizes are presented in Fig. III-5.

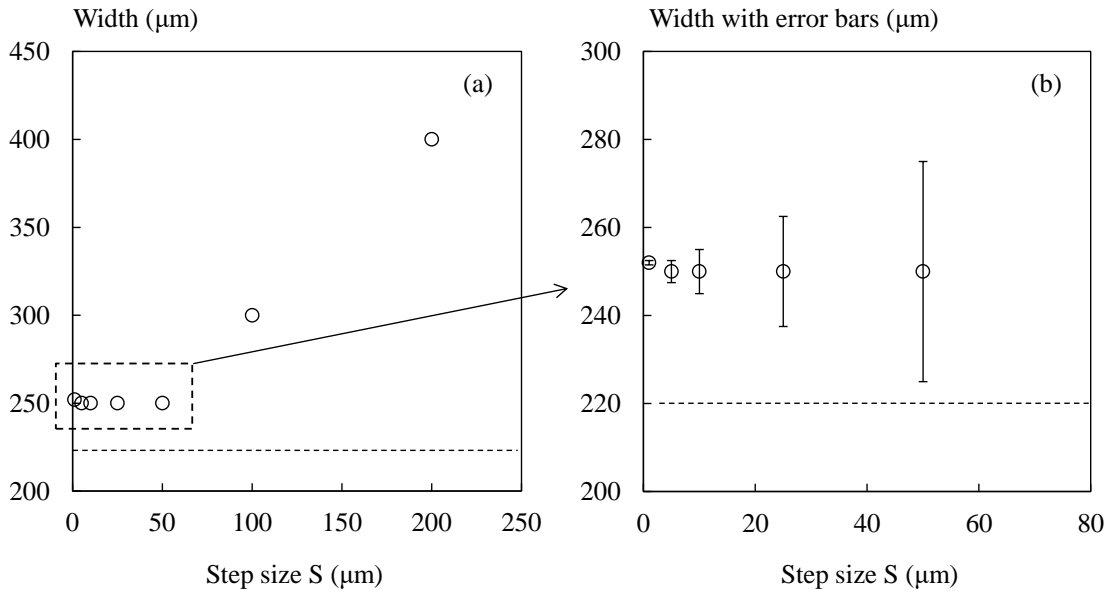


**Fig. III-5:** Measured width as a function of scanning step size  $S$ , (a): step size varying from  $1$  to  $200 \mu\text{m}$ , (b): step size from  $1$  to  $50 \mu\text{m}$ ,  $f = 2 \text{ GHz}$ ,  $\text{IFBW} = 100 \text{ Hz}$ ,  $P_0 = 0 \text{ dBm}$ , zero level =  $-50 \text{ dB}$ ,  $H = 10 \mu\text{m}$ ,  $D = 260 \mu\text{m}$

As shown in Fig. III-5.a, the lateral resolution is related to the scanning step size  $S$ . It can be retrieved from this figure that when the scanning step is below  $50 \mu\text{m}$ , the measured width remains almost stable (around  $250 \mu\text{m}$ ). But beyond this value, the width retrieved increases with the step size. Thus, a smaller step size leads to a better 1D scanning resolution. In addition, it should be highlighted that the use of a small step size improves the scanning precision. In Fig. III-5.b, the scanning results for five steps ( $1, 5, 10, 25$  and  $50 \mu\text{m}$ ) well below the slot width are plotted. In this figure, the error bars represent the errors brought by the step size selected. Generally, for a step size  $S$ , the measurement precision can be given as  $\pm S/2$ . For example, in Fig. III-5.b, the scanning results for  $S = 50 \mu\text{m}$  is estimated to  $250 \pm 25 \mu\text{m}$ . Thus, at the stand-off distance of  $10 \mu\text{m}$ , the result with the best scanning precision obtained is  $252 \pm 0.5 \mu\text{m}$  when  $S = 1 \mu\text{m}$  (minimum step of the x-y-z stage) is selected.

In the following part, an important probe parameter which is the probe apex size  $D$  is studied. The step size considered is  $1 \mu\text{m}$ .

### c) Probe apex size $D$

As it has been demonstrated, the probe apex plays a very important role in the scanning resolution achievable [KAN 03]. Thus, in this part the influence of the probe apex size on the 1D scanning results is evaluated. To that end, we compare the scanning results obtained by two probes whose apices are respectively  $260 \mu\text{m}$  and  $66 \mu\text{m}$ . For the demonstration, the slot width is measured by using the two probes at the same stand-off distance range [ $1-100 \mu\text{m}$ ]. The results, for a  $1 \mu\text{m}$ -scanning step size, are given in Fig. III-6.

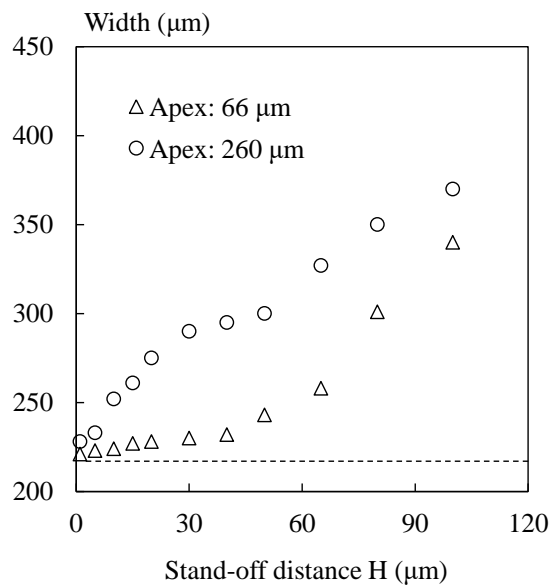


**Fig. III-6:** Comparison of the width measured by two probes with different apices:  $66 \mu\text{m}$  and  $260 \mu\text{m}$ ;  $f = 2 \text{ GHz}$ ,  $\text{IFBW} = 100 \text{ Hz}$ ,  $P_0 = 0 \text{ dBm}$ , zero level =  $-50 \text{ dB}$ ,  $S = 1 \mu\text{m}$

As shown in Fig. III-6, the two probes responses are quite different. Especially, for the probe with apex ( $66 \mu\text{m}$ ) the response varies almost exponentially with the distance. However, for the probe with larger apex ( $260 \mu\text{m}$ ), the response is roughly proportional to the distance. An explanation of this phenomenon can be found in the simulation results given in Fig. II-6. Actually, the E-field of the small probe decays exponentially with the distance while the E-field of the bigger one decreases almost linearly. In addition, as observed in Fig. III-6, for a very small distance  $H$ , the results obtained by the two probes are relatively close. For example, when the minimum

height (1  $\mu\text{m}$ ) is considered, the width measured is 221  $\mu\text{m}$  and 228  $\mu\text{m}$  for the probes with  $D = 66$  and 260  $\mu\text{m}$ , respectively. One can also note that for a given height  $H$ , the probe with small apex (66  $\mu\text{m}$ ) leads to a better scanning spatial resolution. Indeed, the electromagnetic energy is more confined around the probe with smaller apex size which leads to a better lateral resolution.

In Fig. III-7, the slot width is measured by using the two probes with a scanning step size ranging from 1 to 200  $\mu\text{m}$ . The probe-sample distance is set to 10  $\mu\text{m}$  (lower than the two probes apices) which guarantee a non-destructive scan in near-field.

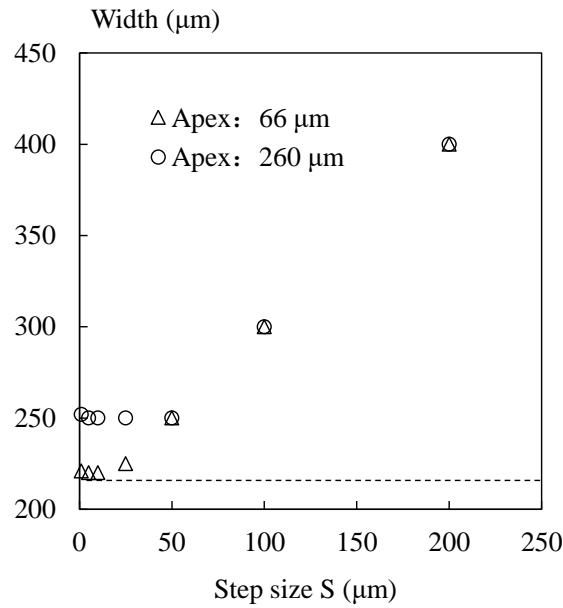


**Fig. III-7:** Comparison of the width measured by two probes with different apices: 66 and 260  $\mu\text{m}$ ,  $f = 2$  GHz, IFBW = 100 Hz,  $P_0 = 0$  dBm, zero level = -50 dB,  $H = 10$   $\mu\text{m}$

One can note that the step size also influences the scanning resolution in a great extent. As illustrated in Fig. III-7, the smaller the step size is, the better is the scanning quality obtained. Particularly, at minimum step size of 1  $\mu\text{m}$ , the measured width is  $228 \pm 0.5 \mu\text{m}$  and  $252 \pm 0.5 \mu\text{m}$  for the apex size: 66 and 260  $\mu\text{m}$ , respectively. Thus, considering a certain step size, the scanning resolution can be ever more improved by reducing the apex size.

As a conclusion of this study, we can note that the 1D lateral resolution is governed by the scanning parameters including the tip-sample distance  $H$ , the scanning step size  $S$  and the probe apex  $D$ . For the demonstration, we have linearly scanned a metal-dielectric-metal structure found on a common chip card. Generally speaking smaller are the parameters ( $S$ ,  $H$  and  $D$ ) better is the scanning quality. In our

case, the minimum controllable distance is 1  $\mu\text{m}$ , the minimum scanning step is 1  $\mu\text{m}$  and the smaller apex is 66  $\mu\text{m}$ . The scanning achieved with the set of parameters ( $H = 1 \mu\text{m}$ ,  $S = 1 \mu\text{m}$  and  $D = 66 \mu\text{m}$ ) leads to a width of 221  $\mu\text{m}$  which agrees well with the actual width of 220  $\mu\text{m}$ .

After this study for 1D scanning, in the following we are interested in 2D imaging. As it has been done for 1D scanning, we first demonstrate the benefit of adding an interferometer in terms of sensitivity measurement. Then, the investigation is also performed as a function of the scanning setting parameters (tip-sample distance  $H$ , scanning step size  $S$  and probe apex  $D$ ).

#### III.2.4 2D imaging sensitivity of iNFMM

One of the main features of NFMMs is the possibility to image samples whose size is much smaller than the free space wavelength ( $\lambda_0$ ) giving the opportunity for local characterizations [ANL 07], [TAB 99], [HAD 12b]. As we know the imaging ability is one of the important features of the scanning microwave microscope. In this part of the chapter, 2D scanning results of the proposed iNFMM are studied. The sample under test is still the chip area onto the chip card. In this section, the sensitivity is first investigated because it is an essential point of the NFMM imaging process. Practically, the imaging sensitivity of the iNFMM is evaluated by considering two configurations: without and with the interferometer. Considering the chip surface ( $11 \times 8 \text{ mm}^2$ ), a scanning speed of 300 pixels/min leads to a scanning duration of about 2 hours (step size of 50  $\mu\text{m}$ ). The 2D imaging process is achieved by using the probe with apex of 260  $\mu\text{m}$ . Instead of keeping 1  $\mu\text{m}$  for stand-off distance, we prefer to fix this distance to 10  $\mu\text{m}$  to avoid touching the device under test in case of a variation of the stand-off distance because of the undesirable tilt on the surface to be scanned or uniformities on the chip. Concerning the VNA, the setting parameters selected are 2 GHz for the operating frequency, 100 Hz for the IFBW and 0 dBm for the power. The zero level is first tuned to -50 dB on the plastic region of the chip card (reference). The images representing the contrast in terms of magnitude and phase shift are given in Fig. III-8.

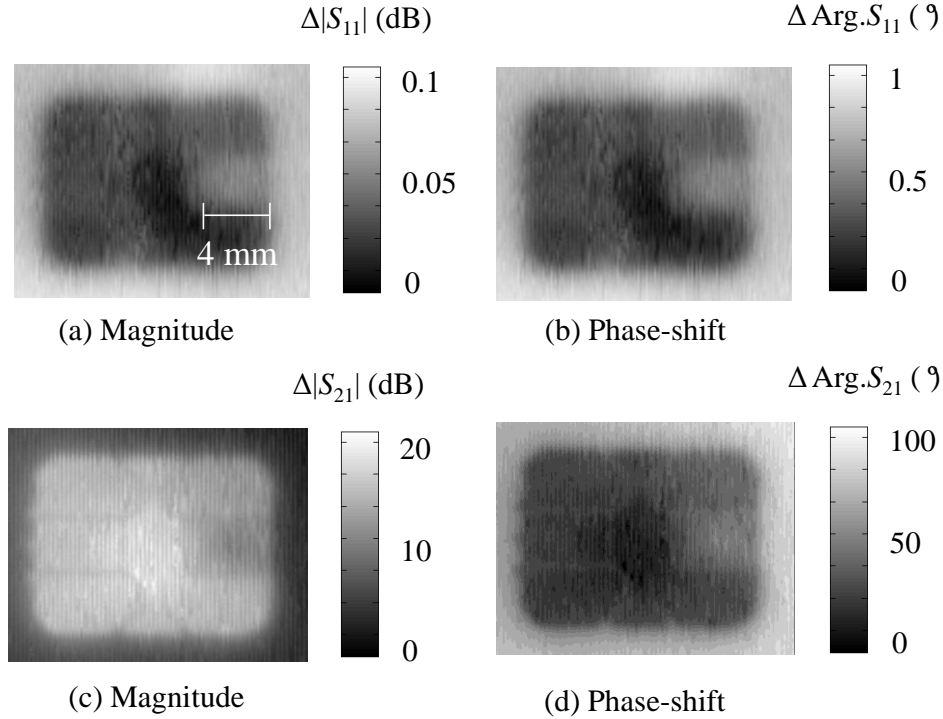


**Fig. III-8:** Measured magnitude and phase-shift of the S parameters in two system configurations, (a) and (b): without interferometer ( $S_{11}$  measured), (c) and (d): with interferometer ( $S_{21}$  measured);  $f = 2$  GHz, IFBW = 100 Hz, zero level = -50 dB,  $P_0 = 0$  dBm,  $H = 10$   $\mu\text{m}$ ,  $S = 50$   $\mu\text{m}$ ,  $D = 260$   $\mu\text{m}$

As shown in Fig. III-8, the interferometric technique permits a much higher sensitivity for both magnitude and phase-shift images. Indeed, contrasts of 20 dB and 100 ° respectively for the magnitude (Fig. III-8.c) and the phase-shift (Fig. III-8.d) are obtained whereas contrasts of only 0.1 dB (Fig. III-8.a) and 1 ° (Fig. III-8.b) have been observed in case of the no-interferometer configuration.

These results demonstrate the great advantage in using the interferometer-based setup. In this configuration, the zero level obtained from the wave reflected by the EMP and the one generated by the impedance tuner, impacts obviously the measurement sensitivity [GU 15a], [GU 15b]. So, we have also investigated the influence on the image contrast of the zero level chosen. As the magnitude and phase-shift images are very similar, once again to ease the presentation only magnitude plots are presented in the following. Three signal levels (-30, -50 and -70 dB) above the noise floor of the VNA (-90 dB) are evaluated in Fig. III-9. The probe retained for the study is the larger one ( $D = 260$   $\mu\text{m}$ ) and the stand-off distance is set to 10  $\mu\text{m}$ . The scanning duration is also about 2 hours.

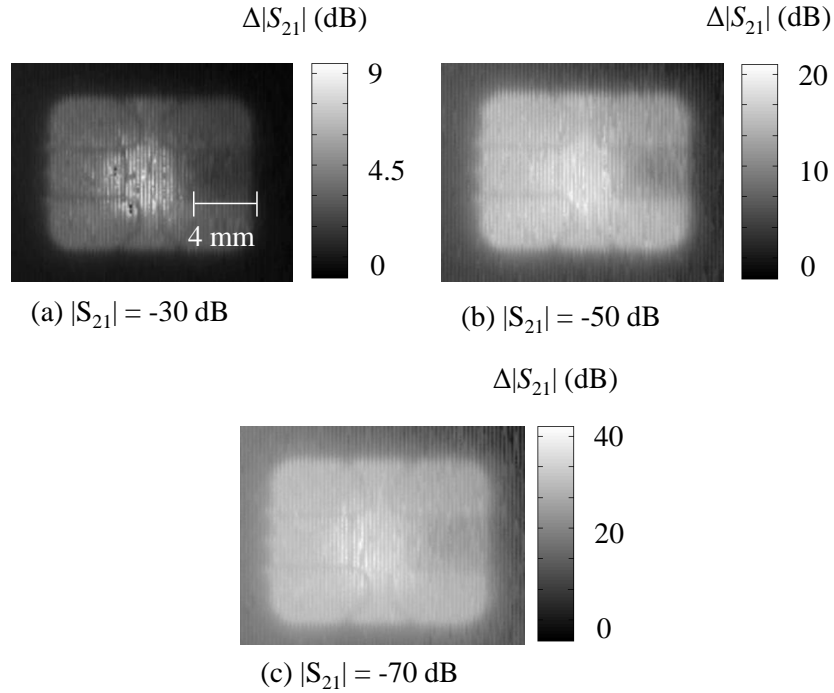


**Fig. III-9:** Measured magnitude of the transmission coefficient  $S_{21}$  for three zero levels, (a): -30 dB, (b): -50 dB and (c): -70 dB,  $f = 2$  GHz, IFBW = 100Hz,  $P_0 = 0$  dBm,  $H = 10$   $\mu\text{m}$ ,  $S = 50$   $\mu\text{m}$ ,  $D = 260$   $\mu\text{m}$

One can note that for the three zero levels selected (-30, -50 and -70 dB) the image of the chip area is returned. Nevertheless, the contrasts observed are quite different. The imaging contrast is 40 dB, 20 dB and 9 dB for signal levels of -70 dB, -50 dB and -30 dB respectively. One can say that in this case the imaging contrast roughly doubles (in dB) when the zero level falls by 20 dB. Nevertheless, as mentioned in Chapter II.4, a low signal level such as -70 dB leads to higher drift errors which in turns degrades the image quality (Fig. III-9.c). Therefore, a compromise between the sensitivity and the zero level has to be found. In this case -50 dB seems to be the best candidate for the zero level to construct an image with an acceptable duration (2 hours). In the following part, the impacts of the scanning parameters on the 2D imaging resolution are under investigation.

### III.2.5 Influence of the scanning parameters on the 2D imaging resolution

As mentioned in the previous part dedicated to the 1D scanning experiments, the spatial resolution of such an instrument is governed primarily by the scanning parameters namely the probe position with respect to the sample, the stand-off

distance  $H$ , the step size  $S$  during the scanning operation and the probe apex size  $D$ . In this part, we perform the same kind of experiments as conducted for 1D scanning to evaluate the impact of these parameters ( $H$ ,  $S$  and  $D$ ) on the imaging quality.

We know that a shorter scanning step naturally leads to a longer scanning duration. For 1D scanning, the duration is not an issue because the data acquisition process last less than a few minutes even with  $S = 1 \mu\text{m}$  (scanning speed  $\sim 300$  pixels/minutes). However, for 2D scanning whose duration usually accounts for several hours, a compromise between the step size and scanning duration has to be found. Besides, in this study, the scanning area is pretty large (around  $100 \text{ mm}^2$ , Fig. III-1), so a slight inclination of x-y-z stage is practically inevitable during the 2D imaging process. So, as already said, to avoid any damage of the probe, the minimum stand-off distance retained for the imaging process is  $10 \mu\text{m}$ . Additionally, for the measurement, the VNA setting parameters selected are 2 GHz for the operating frequency, 100 Hz for the IFBW and 0 dBm for the power.

#### **a) Probe-sample distance $H$**

In this section, we present the measured data (magnitude of the transmission coefficient  $S_{21}$ ) for several stand-off distances at the test frequency of 2 GHz. The step size retained is  $50 \mu\text{m}$  (duration of 2 hours). Comparing with the size of the probe apex ( $D = 260 \mu\text{m}$ ), three heights are chosen: one much smaller than the tip apex ( $10 \mu\text{m}$ ,  $D/H = 26$ ), one in the order of the probe apex ( $250 \mu\text{m}$ ,  $D/H \sim 1$ ) and the last one much larger than the tip apex ( $1000 \mu\text{m}$ ,  $D/H = 0.26$ ). The images constructed with the magnitudes collected by the iNFMM are given in Fig. III-10.

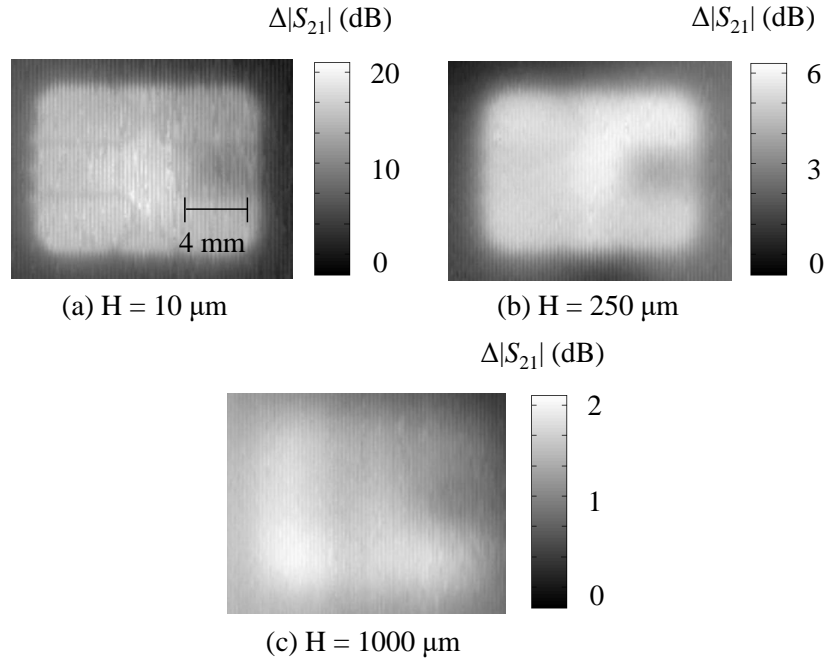


**Fig. III-10:** Measured magnitude of the transmission coefficient  $S_{21}$  over the chip area for three stand-off distances, (a):  $10 \mu\text{m}$ , (b):  $250 \mu\text{m}$  and (c):  $1000 \mu\text{m}$ ;  $f = 2 \text{ GHz}$ ,  $\text{IFBW} = 100 \text{ Hz}$ ,  $P_0 = 0 \text{ dBm}$ , zero level =  $-50 \text{ dB}$ ,  $S = 50 \mu\text{m}$ ,  $D = 260 \mu\text{m}$

As shown in the Fig. III-10, the spatial resolution decreases quickly with the increasing tip-sample distance  $H$ . Indeed, the collimation of the evanescent electrical fields diminishes with the increasing stand-off distance. One can conclude from these images that the higher the stand-off distance is, the less the contrast is. So, to ensure a good imaging quality, the distance  $H$  should be much smaller than the tip apex  $D$ . So, for the following experiments we set the stand-off distance  $H$  to the minimum height retained,  $10 \mu\text{m}$ .

### b) Scanning step size $S$

As the measured data are obtained by stepping the  $x$ - $y$ - $z$  stage motors point by point, the scanning step size also greatly influences the image resolution. To appreciate the influence of this parameter, four scanning steps ( $50, 100, 200, 500 \mu\text{m}$ ) are selected. The first three step sizes are smaller than the slot width on the chip area ( $220 \mu\text{m}$ ) while the last one ( $500 \mu\text{m}$ ) is more than two times larger. The probe apex is  $260 \mu\text{m}$  and the stand-off distance is set to  $10 \mu\text{m}$ . As the chip area is symmetric, the resulting images of half chip area at  $2 \text{ GHz}$  with these different step sizes are presented in Fig. III-11.

The resulting scanning duration for the four steps considered takes 1 h, 15 min, 4 min and 1 min respectively.

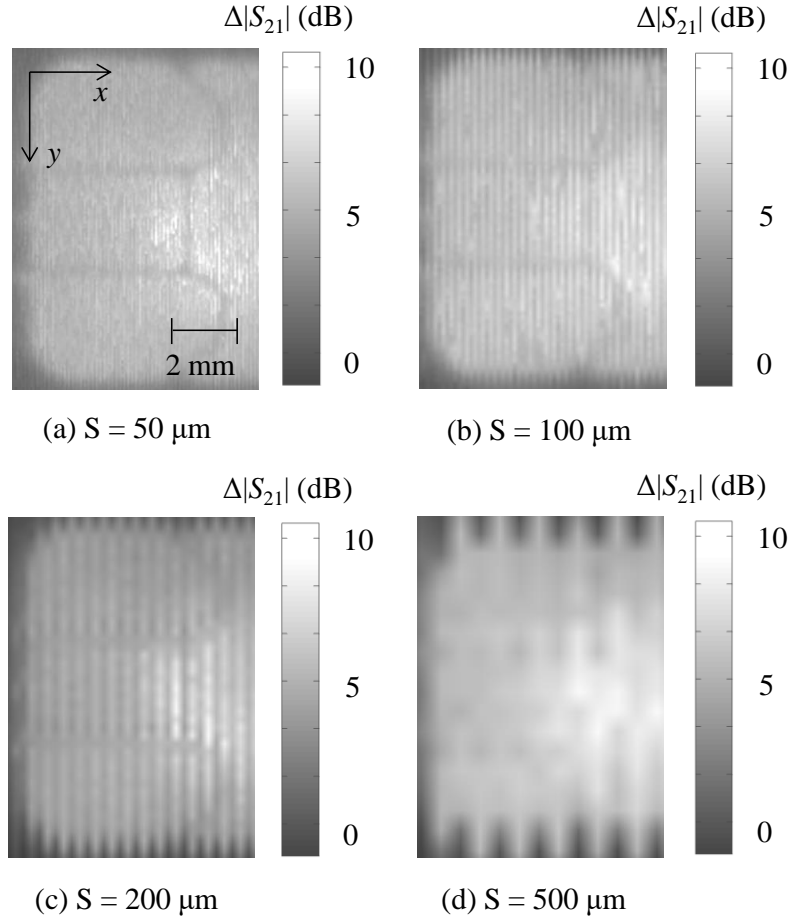


**Fig. III-11:** Measured magnitude of the transmission coefficient  $S_{21}$  over the chip area as a function of different scanning step sizes; (a): 50  $\mu\text{m}$ , (b): 100  $\mu\text{m}$ , (c): 200  $\mu\text{m}$  and (d): 500  $\mu\text{m}$ ,  $f = 2 \text{ GHz}$ ,  $\text{IFBW} = 100\text{Hz}$ ,  $P_0 = 0 \text{ dBm}$ , zero level = -50 dB,  $H = 10 \mu\text{m}$ ,  $D = 260 \mu\text{m}$

The 2D image is completed by moving the x-y-z stage in a zigzag path as already mentioned in Chapter II.4 (Fig. II-28: scan in one direction on y-axis followed by a certain step  $S$  in x-direction and a scan in the other direction on y-axis). Fig. III-11 demonstrates that the scanning quality is closely related to the step size. The images are blurred for larger step sizes such as 200  $\mu\text{m}$  (Fig. III-11.c) and 500  $\mu\text{m}$  (Fig. III-11.d). By contrast, a small step size such as 50  $\mu\text{m}$  leads to a better imaging quality but at the expense of a longer scanning time. Actually, when the step size is halved, the scanning duration is increased by a factor of 4. Therefore, a compromise between the step size and the scanning duration has to be made. In this case a step size of 50  $\mu\text{m}$

(Fig. III-11.a) seems to be a good candidate to acquire an image in an acceptable duration (1 hour) and quality.

### c) Probe apex size D

In this part, the impact of the apex size on the 2D resolution is evaluated. The same rigid tungsten probes with apex of 260  $\mu\text{m}$  and 66  $\mu\text{m}$  are considered for the tests. Based on the previous conclusions, the scanning parameters selected are a stand-off distance H of 10  $\mu\text{m}$  and scanning step size S of 50  $\mu\text{m}$ . The resulting scanning duration is about 1 hour. The scanned images constructed are given in Fig. III-12.

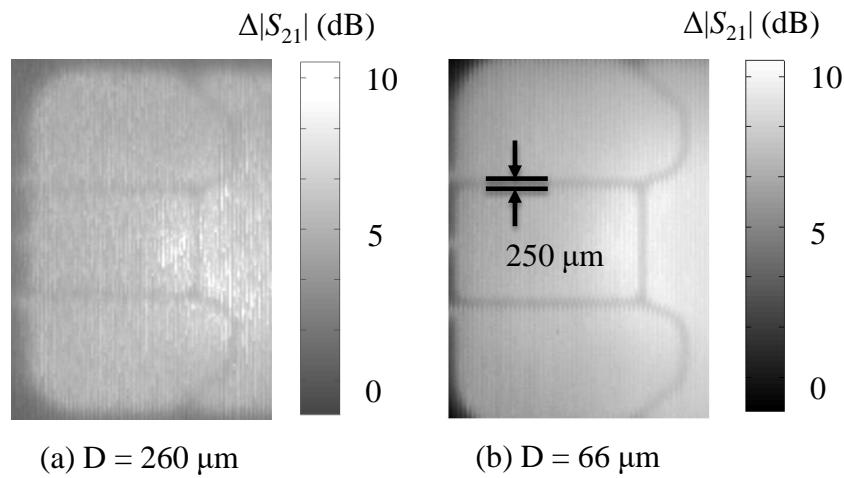


**Fig. III-12:** Measured magnitude of the transmission coefficient over the chip area for two different probe apex sizes, (a): 260  $\mu\text{m}$  and (b): 66  $\mu\text{m}$ ,  $f = 2 \text{ GHz}$ , IFBW = 100Hz,  $P_0 = 0 \text{ dBm}$ , zero level = -50 dB,  $H = 10 \mu\text{m}$ ,  $S = 50 \mu\text{m}$

This figure shows that the image obtained by means of the smaller tip (Fig. III-12.b) offers a better quality than the one acquired with the larger tip (Fig. III-12.a). Actually, the image constructed with the small tip (66  $\mu\text{m}$ ) provides a clearer result (Fig. III-12.b). Furthermore, the slot width measured is 250  $\mu\text{m}$  corresponding to about  $\lambda_0/550$  at 2 GHz in free space.

As the small probe brings better image quality, in the following measurements we keep the probe with apex of 66  $\mu\text{m}$ . As the probe size is much smaller than the previous one used for the tests, we have made a new evaluation by decreasing the step size so that we end up with a ratio  $D/S > 1$ . For the demonstration, a step size of 25  $\mu\text{m}$  is now applied, as displayed in Fig. III-13. The resulting scanning duration is 4 hours which is four times longer than the duration for a step of 50  $\mu\text{m}$  (1 hour).

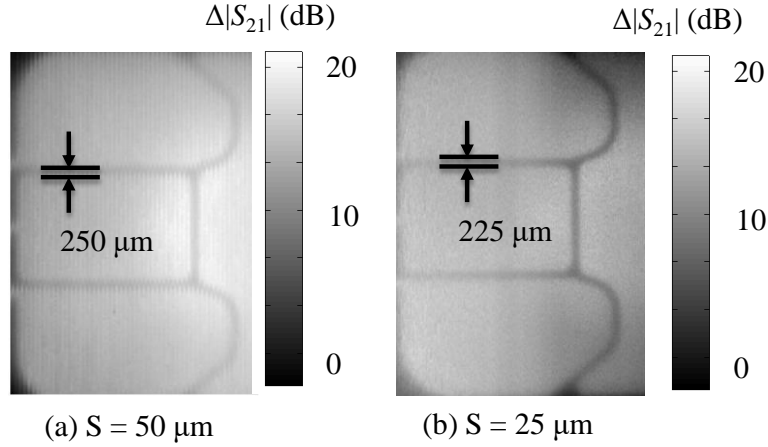


**Fig. III-13:** Measured magnitude of the transmission coefficient  $S_{21}$  over the chip area for two different step sizes; (a):  $260 \mu\text{m}$  and (b):  $66 \mu\text{m}$ ,  $f = 2 \text{ GHz}$ ,  $\text{IFBW} = 100\text{Hz}$ ,  $P_0 = 0 \text{ dBm}$ , zero level =  $-50 \text{ dB}$ ,  $H = 10 \mu\text{m}$ ,  $D = 66 \mu\text{m}$

As shown in Fig. III-13.b, a finer scanning step of  $25 \mu\text{m}$  returns a better image quality as the slot lines are clearer. Especially, the resulting slot width is  $225 \mu\text{m} \pm 12.5 \mu\text{m}$  while it is equal to  $250 \mu\text{m} \pm 25 \mu\text{m}$  for a step size of  $50 \mu\text{m}$ . Thus the scanning resolution and precision are enhanced by using the probe of small apex. However, the scanning process with a large step size leads to shorter duration (1 hour). Depending on the application targeted, this is an important parameter to consider.

As a conclusion of the study of 2D scanning resolution, first, we have shown that thanks to the interferometric technique, the iNFMM platform offers a high scanning sensitivity compared to the configuration without interferometer. It is retrieved that a low zero level also leads to a high measurement sensitivity. Furthermore, we find that the 2D imaging resolution is tightly dependent on the scanning parameters (the probe-sample distance  $H$ , the scanning step size  $S$  and the probe apex size  $D$ ). Typically, considering the compromise between the scanning resolution and an acceptable operation duration (in the order of 1 hour), the values of these parameters are set to  $D = 66 \mu\text{m}$ ,  $H = 10 \mu\text{m}$  and  $S = 50 \mu\text{m}$ .

The imaging resolution can be further improved by refining the step to  $25 \mu\text{m}$  or smaller, which of course results in a much longer scanning time ( $\geq 4$  hours). In this condition, the slot width retrieved is  $225 \mu\text{m}$  corresponding to a sub-wavelength lateral resolution of about  $\lambda_0/611$  at  $2 \text{ GHz}$  in free space.

In the following part, a method to enhance further the image resolution is introduced for a given set of scanning parameters ( $H$ ,  $S$  and  $D$ ).

### III.2.6 Resolution enhancement by position/signal difference method

The influence of the scanning parameters (stand-off distance  $H$ , scanning step size  $S$  and probe size  $D$ ) on the resolution has been finely analyzed above. In this part, an image resolution enhancement method is employed to improve the 1D and 2D scanning quality. This approach, named position/signal difference method, is performed by calculating the complex difference between the scanning results collected for two different distances ( $H_1$  and  $H_2$ ) [KAN 03]. By this means, the background noise during the scanning process can be effectively decreased, which helps to the improvement of the imaging quality.

To study the influence of the choice of the stand-off distance ( $H_1$  and  $H_2$ ) on the scanning quality, we first apply this method to the 1D scanning results. As the probe with small apex has already demonstrated good scanning resolution, here we focus on the resolution improvement of the bigger probe ( $D = 260 \mu\text{m}$ ). The step size is set to  $1 \mu\text{m}$ . For the demonstration, three values of  $H_1$  are considered: 1, 10 and  $50 \mu\text{m}$ . The signal processing method is applied on these three distances to evaluate the relation between the resolution improvement and the choice of the values ( $H_1$  and  $H_2$ ). To ease the presentation, the measured magnitude and phase-shift of the transmission coefficient as a function of the distance  $H$  is given in Table III-2.a. The complex difference between two sets of the parameters ( $H_1$  and  $H_2$ ) are calculated in Table III-2.b.

(a)

H ( $\mu\text{m}$ )	1	5	10	25	50	80	100	150	200
Width ( $\mu\text{m}$ )	228	233	252	280	300	350	370	389	386

(b)

$H_2$ ( $\mu\text{m}$ ) \diagdown $H_1$ ( $\mu\text{m}$ )	1	5	10	25	50	80	100	150	200
1	-	227	227	228	228	228	228	228	228
10	-	-	-	237	237	245	250	251	252
50	-	-	-	-	-	299	299	300	300

**Table III-2:** (a): Measured width as a function of the stand-off distance, (b): width as a result of the signal/position difference method applied to different tip-sample separation distances,  $f = 2 \text{ GHz}$ ,  $\text{IFBW} = 100\text{Hz}$ ,  $P_0 = 0 \text{ dBm}$ , zero level =  $-50 \text{ dB}$ ,  $S = 1 \mu\text{m}$ ,  $D = 260 \mu\text{m}$

As shown in Table III-2.b, the lateral resolution is improved after employing the signal processing method, compared to the width measured using only a stand-off distance ( $H_1 = 1, 10$  and  $50 \mu\text{m}$ ) in Table III-2.a. Actually, the choice of  $H_1$  and  $H_2$  has a strong influence on the resolution improvement. For example, for a very small distance  $H_1$  (i.e.  $1 \mu\text{m}$ ), the smallest width is  $227 \mu\text{m}$  by applying the signal difference method compared to the original value ( $228 \mu\text{m}$ ), which corresponds to a very slight resolution enhancement of  $1 \mu\text{m}$ . On the other hand, when concerning a relative high distance  $H_1$  (i.e.  $50 \mu\text{m}$ ), the resolution improvement is still very limited in the level of  $1 \mu\text{m}$ . However, when a moderate distance value of  $H_1$  (i.e.  $10 \mu\text{m}$ ) is considered, a maximum enhancement of  $15 \mu\text{m}$  (6 %) is achieved, which is much higher than the values obtained by other two cases. The performance of the signal processing method is also influenced by the distance  $H_2$ . When  $H_1$  is kept to  $10 \mu\text{m}$ , one can note a better resolution obtained for a smaller  $H_2$ . Therefore,  $H_1$  and  $H_2$  should be carefully selected to obtain a good resolution improvement.

As demonstrated above, we obtain a relative high enhancement of the scanning quality when considering the set of the distances ( $H_1 = 10 \mu\text{m}$ ,  $H_2 = 50 \mu\text{m}$ , Table III-2). Thus in the following, this signal processing method is applied on the imaging experiments based on the results of these two stand-off distances, as shown in Fig. III-14. The scanning step is set to  $50 \mu\text{m}$  for Fig. III-14.a and Fig. III-14.b while for zoomed area ( $2.5 \times 1.5 \text{ mm}^2$ ) in Fig. III-14.d and Fig. III-14.e, the scanning step is reduced to  $10 \mu\text{m}$  leading to a scanning duration of 2 hours.

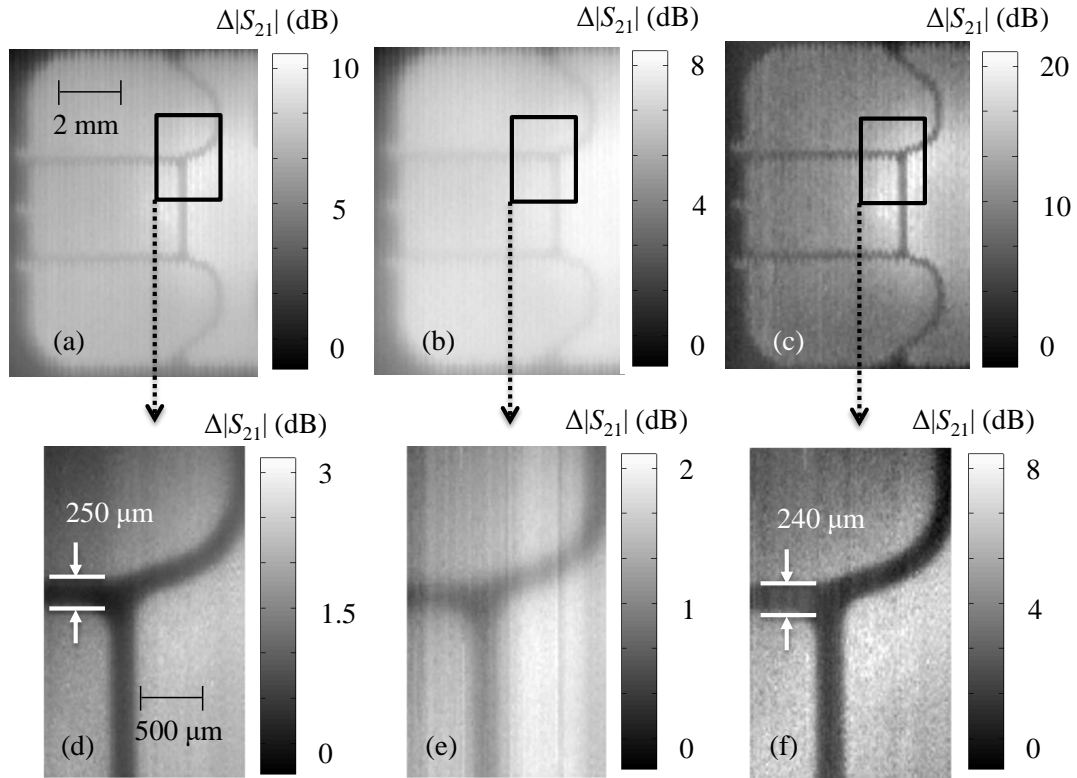


**Fig. III-14:** Resolution enhancement as a result of signal differences acquired for different tip-sample heights, the images represent the magnitude of the signal ( $S_{21}$ ); (a): Magnitude plot for height  $H = 10 \mu\text{m}$ , (b): magnitude plot for height  $H = 50 \mu\text{m}$ , (c): complex difference of magnitude plots (a) and (b); (d), (e) and (f) represent the zoomed area ( $2.5 \times 1.5 \text{ mm}^2$ ) of magnitude plots (a), (b) and (c) respectively;  $f = 2 \text{ GHz}$ ,  $\text{IFBW} = 100\text{Hz}$ ,  $P_0 = 0 \text{ dBm}$ , zero level =  $-50 \text{ dB}$ ,  $D = 260 \mu\text{m}$ ,  $S_1 = 50 \mu\text{m}$  for (a), (b) and (c);  $S_2 = 10 \mu\text{m}$  for (d), (e) and (f)

The magnitude images for two stand-off distances,  $10 \mu\text{m}$  and  $50 \mu\text{m}$ , are shown in the Fig. III-14.a and Fig. III-14.b. Fig. III-14.c represents the magnitude image of the complex difference between the signals obtained for these two stand-off distances. Compared with the images of a signal distance in Fig. III-14.a and Fig. III-14.b where the scanning contrast obtained is  $10 \text{ dB}$  and  $8 \text{ dB}$  respectively, an increase of the magnitude contrast of  $20 \text{ dB}$  is observed in Fig. III-14.c. Actually, thanks to the signal/position difference, the background signals generated by the probe body can be effectively eliminated, which leads to a contrast enhancement. To better visualize the slot line width on the chip area, the magnitude plots of a zoomed area ( $2.5 \times 1.5 \text{ mm}^2$ ) with a scanning step of  $10 \mu\text{m}$  are presented in Fig. III-14.d, Fig. III-14.e and. The image contrast acquired is  $8 \text{ dB}$  in Fig. III-14.f which is also much higher than the values ( $3 \text{ dB}$  and  $2 \text{ dB}$ ) obtained at distances ( $H = 10$  and  $50 \mu\text{m}$ ) in Fig. III-14.d and

Fig. III-14.e. As a result, the imaging lateral resolution in Fig. III-14.f is improved by 10  $\mu\text{m}$  compared to the original value of 250  $\mu\text{m}$  in Fig. III-14.d.

### III.2.7 Conclusion

The 1D and 2D scanning capability of the home-made iNFMM has been experimentally validated in this section. It has been demonstrated that thanks to the interferometric technique, the measured contrast is highly enhanced leading to a good measurement sensitivity. Another benefit of adding the interferometer is that the zero can be set to a desired level in a broad frequency range [2-18 GHz]. In this study we are interested in materials which size is larger than  $1000 \times 1000 \mu\text{m}^2$ . Because of the applications targeted we are not looking for an extremely high resolution but rather a sufficient one taking into account requirements such as image construction duration and robustness of the probe. For a demonstration, 1D scanning and 2D imaging experiments on a common chip card (surface under test:  $11 \times 8 \text{ mm}^2$ ) are experimentally demonstrated at 2 GHz.

The system establishes the capability of non-destructive and non-contact surface mapping with sub-millimeter spatial resolution through the study of the influence of the scanning parameters including the tip-sample distance  $H$ , the scanning step size  $S$  and the probe apex  $D$  on the scanning resolution. It should be mentioned that the minimum achievable  $H$  and  $S$  of the system is 1  $\mu\text{m}$  for both parameters which is sufficient for such a large scanning area. Instead of keeping 1  $\mu\text{m}$  for stand-off distance in 1D scanning, we prefer to fix this distance to 10  $\mu\text{m}$  in 2D imaging process to avoid touching the device under test in case of a variation of the stand-off distance because of the undesirable tilt on the surface to be scanned or uniformities on the chip. One can also note that, for the sake of robustness of the probe tip, the probes are selected with apex of tens and hundreds of microns (i.e. 66 and 260  $\mu\text{m}$ ) to avoid the too frequent impairment of the tip during the scanning experiments.

There is a compromise between the scanning duration and the scanning quality. For a 1D scanning process over a distance of 1000  $\mu\text{m}$ , the minimum step size (1  $\mu\text{m}$ ) is selected because the duration is only about 3 minutes (scanning speed = 300 pixels/min). The scanning conditions which offer the best scanning results (221  $\mu\text{m}$ ) is ( $H = 1 \mu\text{m}$ ,  $S = 1 \mu\text{m}$  and  $D = 66 \mu\text{m}$ ). However, for 2D imaging, the scanning step size should be carefully chosen to avoid a too long imaging duration leading to drift

errors as mentioned in the chapter II.4. The imaging resolution obtained is 250  $\mu\text{m}$  corresponding to about  $\lambda_0/550$  at 2 GHz under the conditions ( $H = 10 \mu\text{m}$ ,  $S = 50 \mu\text{m}$ , duration = 1 hour and  $D = 260 \mu\text{m}$ ).

Then, a signal/position difference method is used to improve the scanning quality. Actually, this method is based on the complex difference between the scanning results collected for two heights. The resulting signals return higher contrast than the original signal because the background noise is effectively lowered.

### III.3 Broadband microwave characterization of liquids by iNFMM

#### III.3.1 Introduction

In the last decade the understanding of the dielectric properties of biological samples such as cells, tissues and organs has attracted increasing attention owing to their large impact in many physiological, biological and physical processes [HAB 10], [SHI 15]. The evaluation, especially the local investigation, of the dielectric spectra in the microwave frequency band is expected for example to help to analyze the composing elements of biological materials in life sciences [TUC 16]. To this end, a well-designed microwave platform that provides high performance in terms of resolution and sensitivity is needed. Conventional microwave resonator methods including microstrip structures, cavity resonators and waveguides have been widely applied to dielectric characterizations [CHA 15], [FLO 14]. But in this case the frequency band of operation is very limited. Another weakness is that the measurement sensitivity falls rapidly in the presence of high-loss materials such as fluids. However, it is worth noting that methods based on parallel plate capacitors or open-ended coaxial transmission lines have been applied to measure fluids over a broad frequency range [STO 07]. Nevertheless, these approaches involve samples whose size is in the order of tens of square millimeters in terms of surface [STO 07], [GAO 04]. Recently, microwave microscopy has effectively established its potentials for local dielectric characterization of bio-samples by using sharpened tips [TUC 16], [FAR 12a], [FAR 12b], [BIA 16], [TSE 16]. Nonetheless, most of the microwave microscopes are based on resonators operating in a limited frequency band. Even though some researches have demonstrated dielectric characterizations in a wide frequency range [TSE 07], the sensitivity reported is not equally high in the entire frequency band investigated. Therefore, there is a demand for the development of a bio-sample dielectric spectroscopy.

To this end, we have proposed an interferometer-based microwave microscope offering both spatial resolution at the micro-scale and high measurement sensitivity [GU 16a], [HAD 15]. In this work, we take advantage of the high sensitivity feature of this platform demonstrated in the previous chapter to establish its capability in characterizing bio-samples in a wide and quasi-continuous frequency band [2-18 GHz].

In this purpose, the sample under test selected is a set of saline aqueous solutions. This choice is motivated by the fact that it is quite easy to obtain samples with calibrated concentrations and also because saline aqueous solutions are very commonly used to simulate biological fluids [PEY 07], [PEY 07]. The samples are investigated by using the same evanescent microwave probe employed in the previous scanning experiments. Thus, only a quite small volume related to the size of the probe apex is analyzed. In this preliminary study, we are mainly interested in the ability of our platform to perceive a very small variation in the sample under test [GU 16b]. This is a first step towards the final objective of quantitative microwave microscopy of biological structures.

First, Cole-Cole model is exploited to estimate the complex permittivity of different aqueous saline solutions. Secondly, the electromagnetic field distribution induced by the interaction between the probe and the liquid is analyzed. Then, the measurement sensitivity is evaluated by comparing two configurations: without and with interferometer. Finally, methods to retrieve the dielectric properties from the measured data are proposed. As mentioned in the chapter I there are basically two types of methods to calculate the dielectric properties: the transmission line method and the cavity perturbation method. The first approach extracts the electromagnetic parameters of materials through the magnitude and phase-shift parts of the measured transmission coefficient while the second one relates the measured quality factor and the resonant frequency shift of resonator-based structures to these parameters. In this work, based on an interferometric technique, the proposed system has the possibility to extract the dielectric properties by both means mentioned. The resulting complex permittivities are then compared to theoretical values calculated by Cole-Cole model to appreciate the performance of these methods.

### III.3.2 Permittivity study of saline solutions

It is well acknowledged that the permittivity of materials expresses their ability to polarize in response to an applied field and can be written as:

$$\varepsilon^* = \varepsilon' - j\varepsilon'' = \varepsilon'(1 - j \tan \delta)$$

where  $\epsilon^*$  is the complex permittivity,  $\epsilon'$  and  $\epsilon''$  are respectively the real and imaginary part of the permittivity, and  $\tan \delta$  is the loss tangent of permittivity.

The Cole-Cole model, given in Eqn.III-1, has been found to be very efficient for the representation of many systems over a wide frequency band [AHM 12], [PEY 07].

$$\epsilon^* = \epsilon_\infty + \frac{\epsilon_s - \epsilon_\infty}{1 + (j\omega\tau)^{1-\alpha}} + \frac{\sigma_i}{j\omega\epsilon_0} \quad \text{(III-1)}$$

$\epsilon_\infty$  and  $\epsilon_s$  are the limit of the permittivity at high and low frequencies,  $\sigma_i$  is the ionic conductivity,  $\tau$  is the relaxation time,  $\alpha$  is a distribution parameter and  $\epsilon_0$  is the permittivity of free space. After the calculation of all these parameters ( $\epsilon_s$ ,  $\epsilon_\infty$ ,  $\sigma_i$ ,  $\tau$  and  $\alpha$ ) at 25 °C, the complex permittivity can be determined. In Fig. III-15.a is retrieved the very well-known behavior of the water permittivity as a function of frequency.

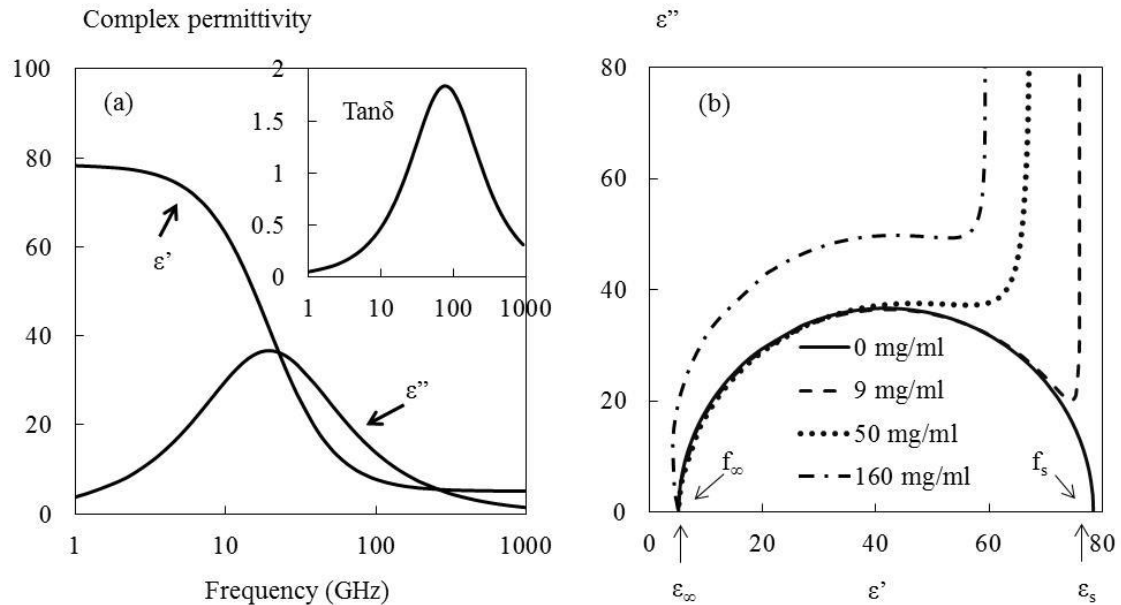


**Fig. III-15:** Complex permittivity of saline solutions based on Cole-Cole model at 25 °C, (a): frequency dependence of the complex permittivity for water,  $\tan \delta$  is given in the inset, (b): Cole-Cole plot for different saline concentrations (0, 9, 50 and 160 mg/ml)

As shown in Fig. III-15.a, the dielectric constant decays as a function of the frequency and the value is almost constant from 300 GHz to 1 THz. The dielectric loss reaches its peak value around 40 at 20 GHz. To visualize the frequency-dependent permittivity as a function of saline concentrations, Cole-Cole plots are drawn for 4 concentrations of sodium chloride ranging from 0 to 160 mg/ml (0 to 2.74 mol/L) (Fig. III-15.b). In this figure,  $\epsilon_\infty$  (5.8) represents the dielectric

constant at infinite frequency ( $f_\infty$ ) and  $\epsilon_s$  (77.7) is the static dielectric constant at low frequency ( $f_s$ ).

After having a global view of the frequency-dependent permittivity plots, now the permittivity behavior for a particular frequency is evaluated. As a demonstration, the results for saline concentrations ranging from 0 to 160 mg/ml (0 to 2.74 mol/L) are presented in Fig. III-16.a for a frequency of 2 GHz. Additionally, because the normal saline concentration of biological tissues fluid is in the order of 9 mg/ml, the responses at 2 GHz in the range [0-9 mg/ml] are also presented in Fig. III-16.b. The concentration 0 mg/ml represents deionized water (DI water).

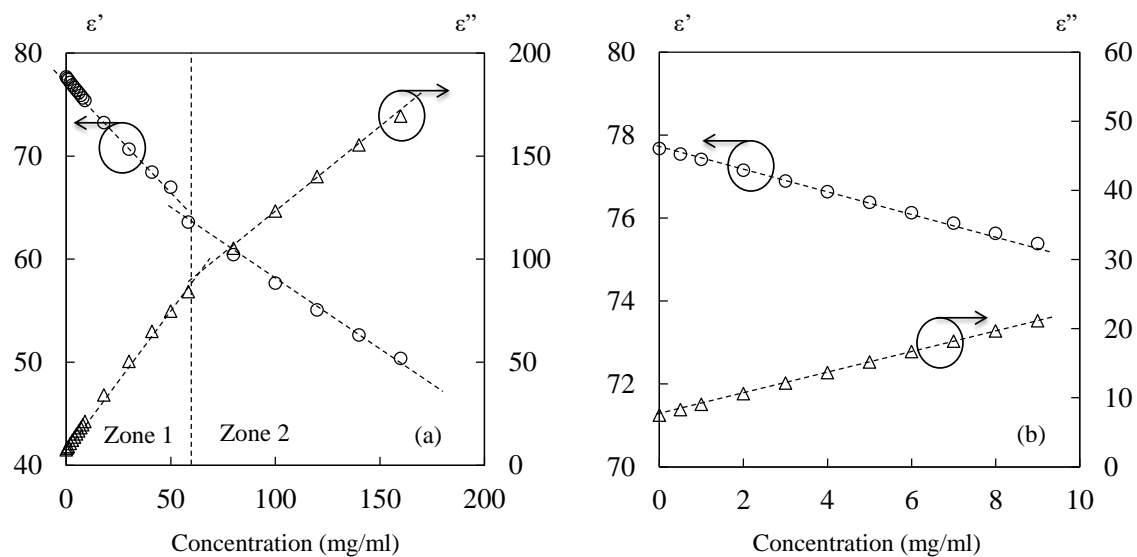


**Fig. III-16:** Complex permittivity of saline aqueous solutions calculated by Cole-Cole model, (a): NaCl concentration range from 0 to 160 mg/ml, (b): NaCl concentration range from 0 to 9 mg/ml,  $T = 25\text{ }^\circ\text{C}$ ,  $f = 2\text{ GHz}$

As shown in Fig. III-16.a, the real part of the permittivity (dielectric constant) decreases from 78 to 50 in the concentration range [0-160 mg/ml], while in the same range, the imaginary part of the permittivity (dielectric loss) increases from 7 to 170. Furthermore, one can note that the results of the complex permittivity exhibit linear behaviors as a function of the NaCl concentrations. Indeed, two linear zones can be identified in Fig. III-16.a: zone 1 for concentrations lower than 58 mg/ml (1 mol/L), and zone 2 for concentrations higher than 58 mg/ml. Thus, for saline concentrations in the range [0-58 mg/ml], the real and the imaginary part of the permittivity can be described by the following equations:

$$\varepsilon'_1 = -0.255C + 77.66 \quad (\text{III-2})$$

$$\varepsilon''_1 = 1.518C + 7.53 \quad (\text{III-3})$$

where C represents the concentration of sodium chloride. In the same way, the complex permittivity for concentrations ranging in [58-160 mg/ml] (Fig. III-16.a) can be expressed by:

$$\varepsilon'_2 = -0.130C + 70.91$$

$$\varepsilon''_2 = 0.837C + 37.7$$

On the other hand, the results for NaCl concentration spreading from 0 to 9 mg/ml are presented in Fig. III-16.b. In this case, the dielectric constant slightly decreases from 78 to 76, while in the same range, the imaginary part of the permittivity increases from 7 to 20. As this range is part of the zone 1, the complex permittivity is also governed by Eqn. III-2 and III-3.

Thanks to these linear equations, the complex permittivity around 2 GHz can be easily evaluated for any NaCl concentrations ranging from 0 to 160 mg/ml. Furthermore, the knowledge of the complex permittivity allows simulations to investigate the electromagnetic response of NaCl solutions by means of commercial software, such as ANSYS/HFSS<sup>TM</sup>.

### III.3.3 Simulation of the probe-liquid interaction

Simulations of the probe-liquid interaction have been performed using ANSYS/HFSS<sup>TM</sup> software to visualize the electromagnetic field distributions of the probe tip and the liquid under test. For the simulation, an excitation port (50 Ω) is directly connected to the same probe used in the previous measurements (diameter: 260 μm). The simulation data entries for the liquid (ε' and tanδ) are determined from the Cole-Cole equation. In Fig. III-17, the E-field distributions at the cross section along the probe are given for three typical positions: probe at 300 μm over the liquid surface (Fig. III-17.a), probe in contact with the liquid surface (Fig. III-17.b) and probe immersed into liquid at a depth of 300 μm (Fig. III-17.c). For these tests the liquid sample is DI water (0 mg/ml) and the frequency is set to 2 GHz.

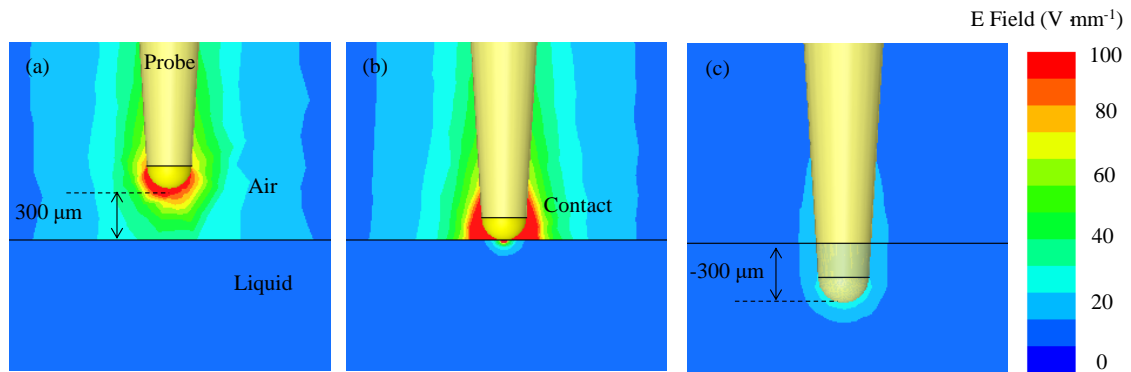


**Fig. III-17:** Numerical simulation (ANSYS/HFSS<sup>TM</sup>) of the EMP (apex = 260 μm) electric field magnitude at three probe positions, (a): probe at 300 μm over the liquid surface, (b): probe in contact with the liquid surface, (c): probe into the liquid at a depth of 300 μm, the images are taken at the cross section along the probe, liquid under test is DI water,  $T = 25\text{ }^{\circ}\text{C}$ ,  $f = 2\text{ GHz}$

As displayed in the Fig. III-17.a, because of the large dielectric constant difference between air ( $\epsilon' = 1$ ) and water ( $\epsilon' = 77.7$  at 2 GHz), the E-field penetration in liquid is extremely low even at a stand-off distance roughly equal to the apex size of the probe. The main part of the electromagnetic energy is reflected back at the air-liquid interface. Only when the probe is in contact or immersed in the liquid (Fig. III-17.b and Fig. III-17.c), one part of the E-field penetrates into the liquid. The E-field distributions cartography also demonstrates that as water presents higher dielectric losses than free space, the E-field maximum value decreases and the electromagnetic energy dissipation increases in liquid. It is also exhibited that the E-field is strongly spatially confined at the probe end and decays rapidly. This confinement allows very local characterizations [BAK 16] [GU 16b] [GU 16c]. Additionally, when the probe is immersed into water (Fig. III-17.c), the impedance mismatch between the probe-liquid system and the excitation port is reduced resulting in a lower reflection coefficient. Another advantage in case of an immersed probe is the immunity to water evaporation process at the liquid surface layer which can largely influence the air-liquid interface and the concentrations of saline solutions.

After the simulation of DI water, the E-field distribution of the saline solutions with different concentrations is also investigated. Four typical saline concentrations are considered in the simulation: two solutions (0 mg/ml and 9 mg/ml) in the linear zone 1 ( $C < 58\text{ mg/ml}$ ), and two others (80 mg/ml and 160 mg/ml) in the linear zone 2 ( $C > 58\text{ mg/ml}$ ). Fig. III-18 shows the distribution of the electric field magnitude at the

cross section along the probe. For these simulations the probe tip is immersed in the liquid solution at a depth of 300  $\mu\text{m}$  and the test frequency is 2 GHz.

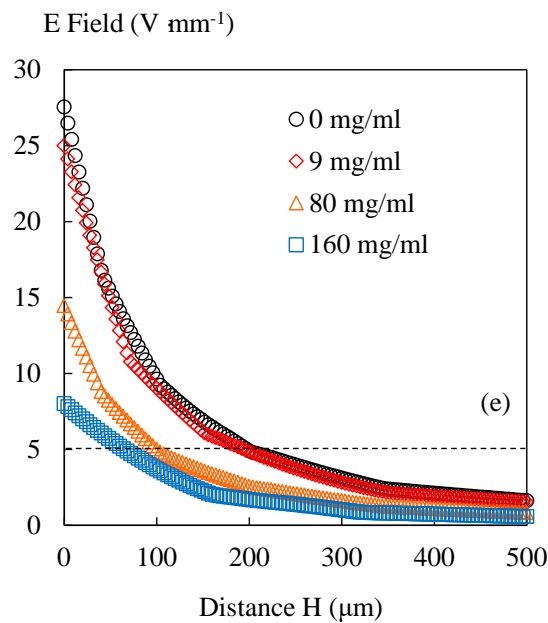
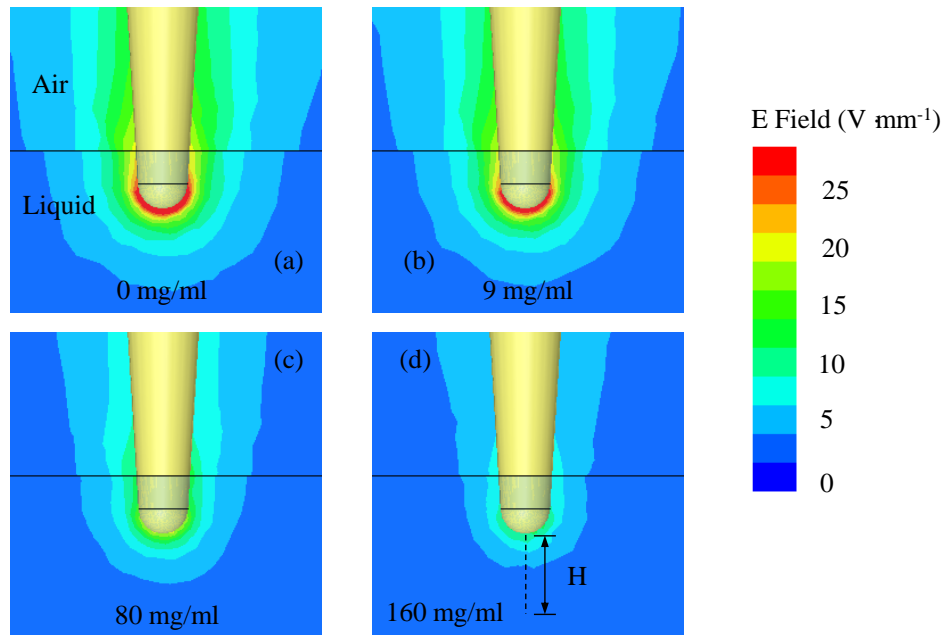


**Fig. III-18:** Simulation (ANSYS/HFSS<sup>TM</sup>) of the microwave probe (apex = 260  $\mu\text{m}$ ) electric field magnitude for different saline concentration levels, (a): 0 mg/ml, (b): 9 mg/ml, (c): 80 mg/ml and (d): 160 mg/ml, (e): E-field as a function of the distance  $H$  from the tip, probe immersed in liquid at a depth of 300  $\mu\text{m}$ ,  $T = 25 \text{ }^\circ\text{C}$ ,  $f = 2 \text{ GHz}$

Fig. III-18 also points out clearly that the simulated electrical field decays rapidly with the distance to the probe. As the electric field around the probe apex is much stronger than elsewhere (Fig. III-18.a-d), as already said, a local characterization of

materials can be achieved. The corresponding maximum E-field value varies with the saline concentrations. Actually, as shown in Fig. III-18.e, the E-field decays rapidly with the distance to the probe and its maximum diminishes with the concentration (27, 25, 14 and 8 V/mm respectively for 0, 9, 80 and 160 mg/ml). Indeed, the saline solutions absorb more electric energy generated by the microwave probe when the NaCl concentration level increases and the E-field penetration falls when the liquid becomes more conductive. For example when the E-field falls down from its maximum to 5 V/mm (Fig. III-18.e), the corresponding distance to the probe are 196, 192, 87, 66  $\mu\text{m}$  respectively for 0, 9, 80 and 160 mg/ml. When the concentration is increased, the distance is shortened.

After the simulation study of the probe-liquid interaction, the probe position control of the proposed iNFMM is studied in the following part.

### III.3.4 EMP position control in liquid

One of the great advantages of the technique proposed is the different modes offered: non-contact, contact and immersion. In this study, to guarantee a strong tip-sample interaction, the probe is plunged into the liquid. Nevertheless, one issue related to operation in liquid is the determination of the probe position. The method used to achieve an accurate positioning is the following. First the probe is immersed in the liquid and the zero level is tuned down to the order of -55 dB at 2 GHz by adjusting the impedance tuner. The IFBW is set to 100 Hz and the VNA power level ( $P_0$ ) is fixed at 0 dBm. To determine the contact position between the tip and the liquid, the probe is placed above the liquid and then pushed towards the liquid surface with a step of 1  $\mu\text{m}$  (minimum displacement allowed by the x-y-z stage with a precision of 0.1  $\mu\text{m}$ ) until the tip is immersed in the liquid at a depth of a few hundred microns. Fig. III-19 shows the evolution of the  $S_{21}$  with the probe tip position.

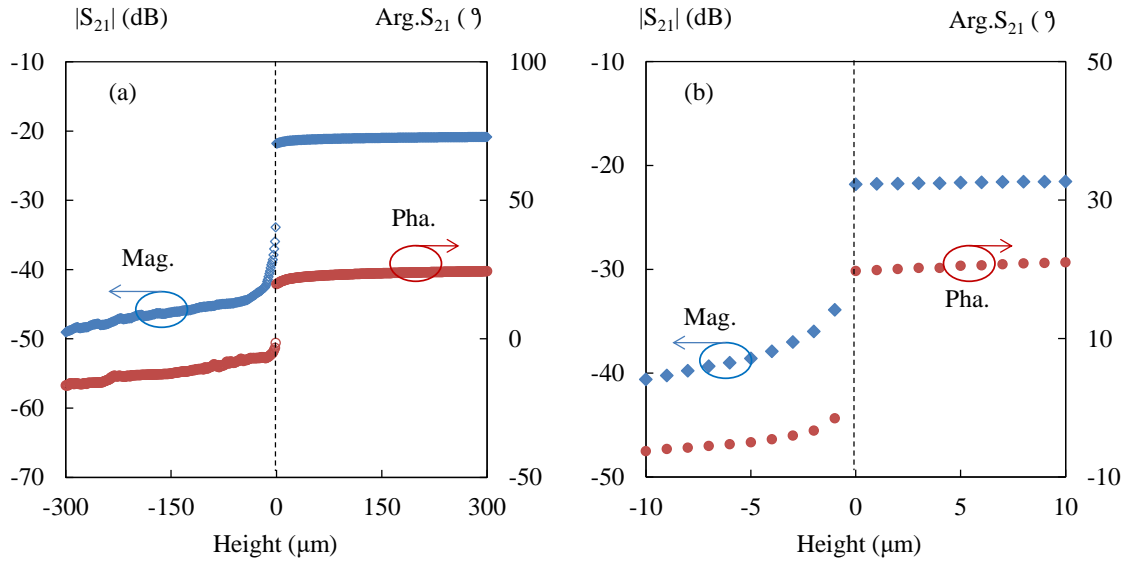


**Fig. III-19:** Transmission coefficient magnitude and phase-shift measured as a function of probe tip position, (a): from -300 to 300  $\mu\text{m}$ , (b): zoomed region from -10 to 10  $\mu\text{m}$ , liquid under test is DI water,  $T = 25\text{ }^{\circ}\text{C}$ ,  $f = 2\text{ GHz}$ ,  $\text{IFBW} = 100\text{ Hz}$ ,  $P_0 = 0\text{ dBm}$

Thanks to the strong interface effect shown in the simulation study, an abrupt change in both the magnitude and phase-shift of  $S_{21}$  can be observed. As illustrated in Fig. III-19.a, this frank break defines the contact position. Thus a plan that separates two probe statuses: probe in liquid and probe in air can be defined. To better locate this position, we zoom the region from -10  $\mu\text{m}$  to 10  $\mu\text{m}$  in Fig. III-19.b. A big jump for both magnitude ( $\Delta|S_{21}| = 12\text{ dB}$ ) and phase-shift ( $\Delta\varphi = 22.1\text{ }^{\circ}$ ) of  $S_{21}$  is caused by the passage from liquid to air. The EMP position is thus very well controlled thanks to the high precision provided by x-y-z stage. It is also observed in Fig. III-19 that when the tip is in air, constant values are measured. This is due to the fact that matching is done in the liquid to obtain a high sensitivity in the immersion mode.

After the probe position is well defined, in the following part, the microwave responses of the proposed iNFMM are experimentally validated considering the probe immersed in liquid. To demonstrate the performance of the interferometer-based microwave microscope, we compare the resulting measurement sensitivity with the value obtained when using the instrument without the interferometer setup.

### III.3.5 Evaluation of the measurement sensitivity

In this part, the response of the microwave microscope is experimentally evaluated. A plastic container ( $7.4 \times 7.4 \times 5.4\text{ mm}^3$ ) is used to hold the liquid solutions

under test. The setting parameters of the VNA are 2 GHz for the frequency, 0 dBm for the power and 100 Hz for the intermediate frequency bandwidth (IFBW). The probe with apex of 260  $\mu\text{m}$  is employed for the liquid characterization. As mentioned before, the microwave probe has potentials for local characterization as the E-field is well confined around the tip apex. During the measurement, the probe is immersed at a depth of 300  $\mu\text{m}$  in the liquid ensuring the whole tip apex is plunged in liquid under test. Thus a maximum tip-liquid electromagnetic coupling can be obtained.

As already mentioned, two configurations are considered: without interferometer (inset of Fig. III-20.a: reflection mode) and with interferometer (transmission mode). To evaluate the measurement sensitivity provided by these two working modes, low saline concentration levels, [0-9 mg/ml], are considered as the fluids under test. The choice of this NaCl solution concentration range is also motivated as already said by the fact the 9 mg/ml saline concentration level represents an essential component of the biological fluids. Thus, Fig. III-20 presents the measured microwave responses of saline concentrations from 0 to 9 mg/ml in the frequency band [1.996-2.004 GHz]. Actually, for the reflection mode the probe is connected directly to one port of the VNA without the impedance tuner and the coupler in-between (inset of Fig. III-20.a). In this configuration the reflection coefficient  $S_{11}$  is acquired.

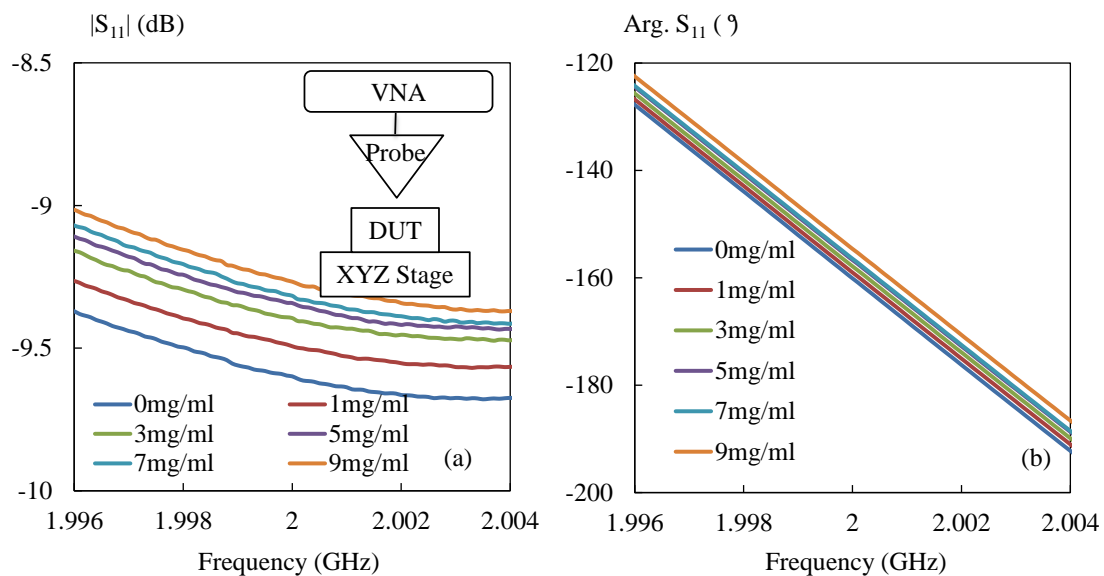


**Fig. III-20:** Measured reflection coefficient  $S_{11}$  of different saline aqueous solutions from 0 mg/ml to 9 mg/ml, (a): magnitude plot, (b): phase-shift plot,  $f = 2\text{GHz}$ ,  $P_0 = 0\text{ dBm}$ ,  $\text{IFBW} = 100\text{ Hz}$ ,  $T = 25\text{ C}^\circ$

As shown in Fig. III-20, the instrument without interferometer can distinguish the different saline concentrations from 0 to 9 mg/ml but with limited sensitivity. Indeed, in Fig. III-20.a, between the concentration limits (0 and 9 mg/ml), a variation of magnitude smaller than 0.5 dB is noticed at 2 GHz. Meanwhile, in Fig. III-20.b, a variation around 5 ° between these two saline concentrations is observed. Thus, the results collected by using this configuration return a measurement sensitivity of 0.06 dB/(mg/ml) and 0.6 °/(mg/ml) for magnitude and phase-shift respectively.

After the analysis of the instrument without interferometer, we present now the results for the system with interferometer. In this case, thanks to the impedance tuner made of variable attenuator and delay line, the tip is preliminary matched in DI water (0 mg/ml) by tuning  $|S_{21}|$  to -55 dB (35 dB above the noise floor of the VNA which is -90 dB) at 2 GHz. As described before, this level represents the zero level after combining the wave reflected by the probe and the wave generated by the impedance tuner. The saline solutions from 1 to 9 mg/ml are then sequentially measured and their responses in terms of transmission coefficient ( $S_{21}$ ) magnitude and phase-shift are collected in Fig. III-21.

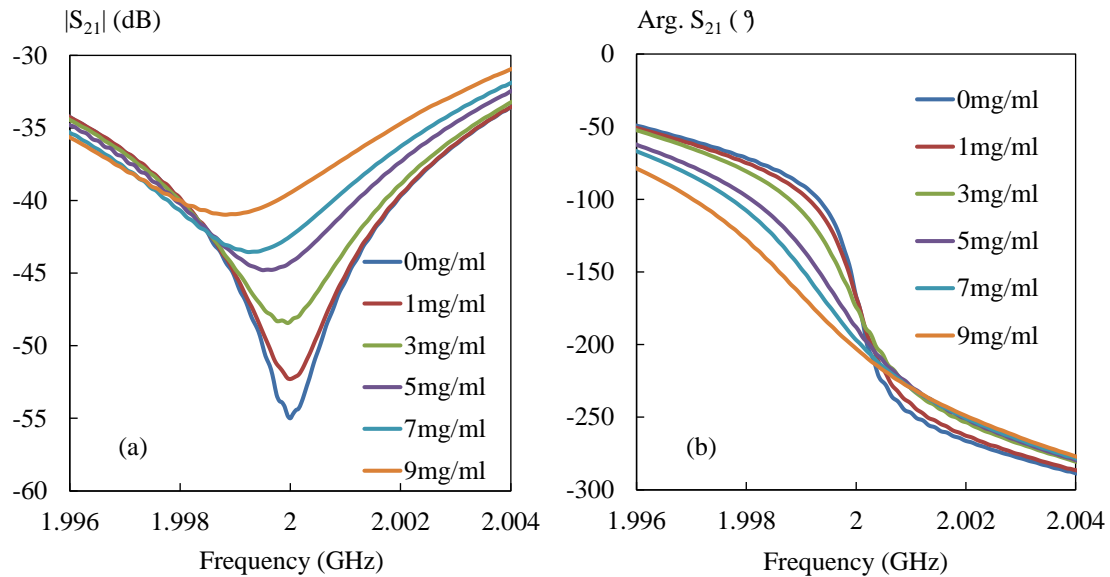


**Fig. III-21:** Measured transmission coefficient  $S_{21}$  for different saline solutions from 0 to 9 mg/ml, (a): magnitude plot, (b): phase-shift plot, 0 mg/ml (DI water) represents reference value,  $f = 2\text{GHz}$ ,  $P_0 = 0\text{ dBm}$ ,  $\text{IFBW} = 100\text{ Hz}$ , zero level = -55 dB,  $T = 25\text{ C}^\circ$

As demonstrated in Fig. III-21, the interferometer-based configuration can easily distinguish small saline concentrations from 0 to 9 mg/ml with high measurement sensitivity. We obtain at 2 GHz a maximum variation of the magnitude and the

phase-shift around 14.1 dB (Fig. III-21.a) and 35.7 °(Fig. III-21.b) respectively, which is much higher than the values obtained by the instrument without interferometer. To better appreciate the measurement sensitivity offered by the two working modes, we summarize the sensitivity values in Table III-3.

	Without interferometer	With interferometer
Magnitude	0.06 dB/(mg/ml)	1.56 dB/(mg/ml)
Phase-shift	0.6 °(mg/ml)	3.9 °(mg/ml)

**Table III-3:** Measurement sensitivity to saline concentration levels from 0 to 9 mg/ml with the two configurations considered: without interferometer (reflection mode) and with interferometer (transmission mode),  $f = 2\text{GHz}$ ,  $P_0 = 0\text{ dBm}$ ,  $\text{IFBW} = 100\text{ Hz}$

As shown in Table III-3, the measurement sensitivities reached when using the interferometer, 1.56 dB/(mg/ml) and 3.9 °(mg/ml) for magnitude and phase-shift respectively, are clearly much higher than the measurement sensitivities provided by the configuration without interferometer. Therefore, thanks to the interferometric technique, the proposed NFMM is able to precisely detect a very small variation of the saline concentration. Particularly, by using the impedance tuner, resonances with high quality factors are acquired. Additionally, it can also be observed in Fig. III-21.a that the resonance peak of  $|S_{21}|$  shifts to the left side (low frequencies) as the saline concentration level increases. So, a shift of the resonance frequency from the resonance frequency observed for the reference level can be evaluated for each concentration even for very small variations.

The proposed system also enables the characterization of saline solutions of a relatively large concentration range [0-160 mg/ml]. The zero level  $|S_{21}|$  is still matched to -55 dB in DI water at 2 GHz. The variation of the magnitude ( $\Delta|S_{21}|$ ) and phase-shift ( $\Delta\arg.S_{21}$ ) is highlighted in Fig. III-22.

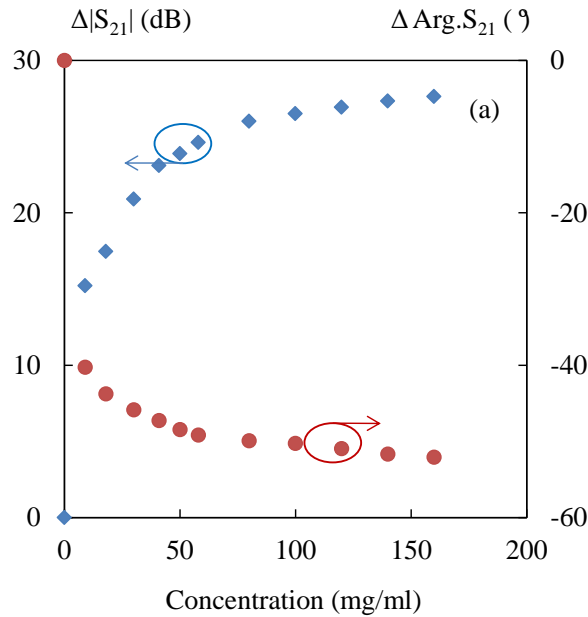


**Fig. III-22:** Measured transmission coefficient for saline concentrations [0-160 mg/ml], zero level is tuned to -55 dB considering 0mg/ml (DI water) as a reference value,  $f = 2$  GHz,  $T = 25$  °C, IFBW= 100 Hz,  $P_0 = 0$  dBm

Practically, for concentrations from 0 to 160 mg/ml, variations of 27.6 dB and  $42.1^\circ$  for magnitude and phase-shift at 2 GHz are respectively observed in Fig. III-22. This measurement sensitivity is much better than the value obtained by the typical resonator-based sensor [CHA 15]. Indeed, one of the advantages of the method is that the reference level can be adjusted at a desired concentration to enhance the sensitivity around this value. Finally, this procedure has been applied on the whole frequency range [2-18 GHz] with a step of 1 GHz to determine the complex permittivity of a set of saline solutions.

### III.3.6 Experimental retrieval of the complex permittivity

As mentioned in the chapter I there are basically two types of methods to calculate the dielectric properties: the transmission line method and the cavity perturbation method. The first approach allows the extraction of the dielectric parameters of materials through the magnitude and phase-shift of the measured transmission coefficients while the second one relates the measured quality factor and resonance frequency to these dielectric parameters. Actually, one of the benefits of the interferometric technique is the possibility to be exploited in case of both methods.

The performance of these two approaches will be compared with each other at the end of this section.

### III.3.6.1 Permittivity extraction by transmission line method

As the sample is placed in the near-field range of the tip and the tip radius is much smaller than the wavelength, the electromagnetic wave can be considered as quasi-static. Thus a lumped element model can be used to describe the tip sample impedance  $Z_S$ . It has been mentioned in Chapter I that the relation between  $Z_S$  and the material permittivity  $\varepsilon^*$  can be given by [ANL 07]:

$$Z_S = \frac{1}{i\omega\varepsilon_0\varepsilon^*D} \quad (\text{III-4})$$

where  $\omega$  is the angular frequency and  $D$  is the probe apex size. The reflection coefficient of the probe  $\Gamma_S$  can be written as a function of  $Z_S$ :

$$\Gamma_S = \frac{Z_S - Z_0}{Z_S + Z_0} \quad (\text{III-5})$$

with  $Z_0$  the VNA characteristic impedance (50  $\Omega$ ). Considering the matching network as a whole, an inversion procedure based on the one port calibration protocol can be performed to translate the measured data ( $S_{21}$ ) to the saline solutions dielectric properties. The complex transmission coefficient  $S_{21}$  can be expressed through the probe reflection coefficient  $\Gamma_S$  in the following form [TUC 16]:

$$S_{21} = e_{00} + \frac{(e_{10}e_{01})\Gamma_S}{1 - e_{11}\Gamma_S} \quad (\text{III-6})$$

$e_{00}$ ,  $e_{11}$  and  $e_{10}e_{01}$  are three complex errors parameters which are obtained from the calibration process. These terms can be extracted by measuring three transmission coefficients for three known calibration standards  $Z_{S1}$ ,  $Z_{S2}$  and  $Z_{S3}$  with reflection coefficients  $\Gamma_{S1}$ ,  $\Gamma_{S2}$  and  $\Gamma_{S3}$ . Once these calibration terms are determined, the complex permittivity can be calculated by exploiting the eqn.III-1 and eqn.III-4 to III-6. One point that makes the calibration task more difficult is that these errors terms change each time the operating frequency is modified. In this study, the inversion procedure is performed by stepping the frequency over the band [2-18 GHz] with a step of 1 GHz.

Different saline concentrations in the range [0-160 mg/ml] are characterized in the frequency band [2-18 GHz]. In Fig. III-23, the complex permittivities calculated

from the measured  $S_{21}$  by using the calibration model are compared to the theoretical values based on the Cole-Cole model. Five concentrations, 0, 40, 80, 120 and 160 mg/ml, are selected.

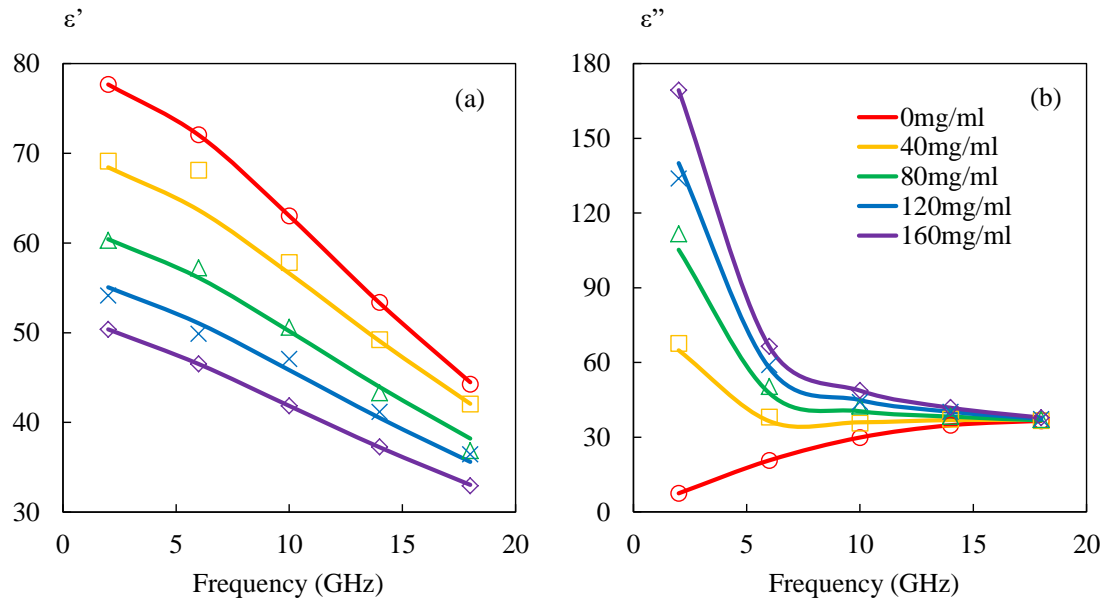


**Fig. III-23:** Frequency-dependent dielectric constant (a) and dielectric losses (b) for different saline concentrations from 0 to 160 mg/ml, Solid lines represent values based on the Cole-Cole model, Symbols are values retrieved by using the inversion procedure,  $T = 25\text{ }^{\circ}\text{C}$ , IFBW=100 Hz,  $P_0 = 0\text{ dBm}$ , zero level = -55 dB

First, a good agreement is observed between the dielectric spectra calculated by Cole-Cole model and the values retrieved from the inversion procedure. As shown in Fig. III-23.a, the dielectric constant decreases as the frequency increases. However, less variation of dielectric constant over the whole frequency band is obtained for higher NaCl concentrations. Fig. III-23.b exhibits a big difference between dielectric losses as a function of concentration at low frequencies (i.e.  $f < 5\text{ GHz}$ ). The curves gradually evolve towards a constant value (37) at 18 GHz. Actually, this convergence point represents a complete failure for dipole to follow the oscillation of applied electric field beyond which the liquid dipole remains freeze with no effective contribution to the dielectric loss [AHM 12].

### III.3.6.2 Permittivity extraction by cavity perturbation method

In this part, a model is proposed to relate the complex permittivity to the measured resonance frequency shift and quality factor. As a demonstration, this method is applied at 2 GHz.

Based on Fig. III-21.a, the resonance frequency shift ( $\Delta f$ ) and the quality factor ( $Q$ ) of the measured  $|S_{21}|$  are given in Fig. III-24. In fact,  $\Delta f$  represents the difference between the resonance frequency of the saline concentration considered ( $f_{meas}$ ) and the value ( $f_{ref}$ ) registered for DI water (reference solution):

$$\Delta f = f_{meas} - f_{ref}$$

For DI water, the corresponding  $f_{ref}$  is 2 GHz and  $Q_{ref}$  is around 2900. Thus, the resonance frequency shift  $\Delta f$  and  $Q$  factor of saline concentrations from 0 to 9 mg/ml are presented in Fig. III-24.

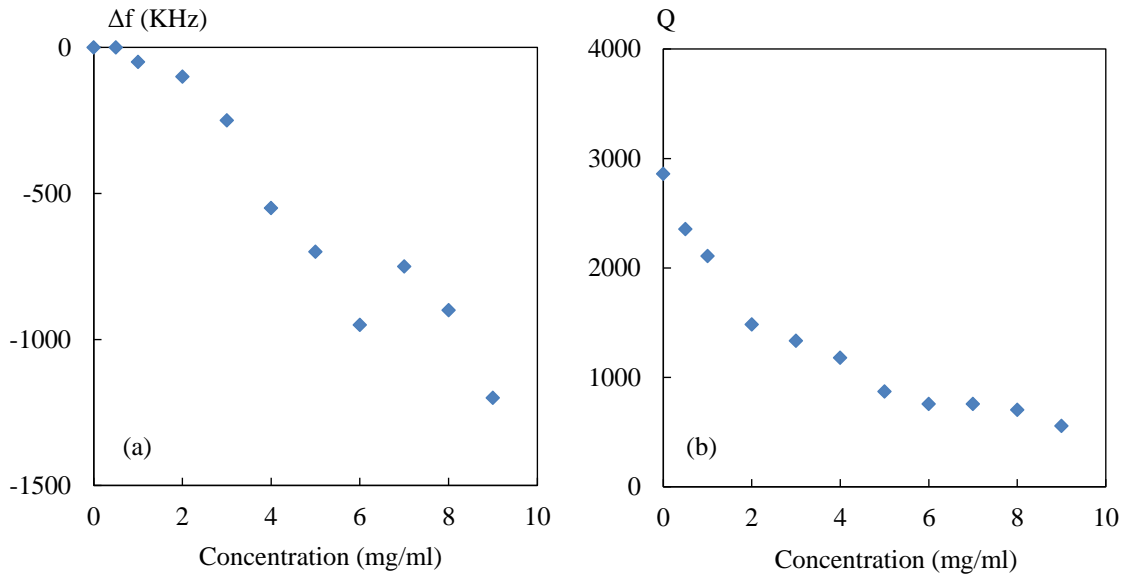


**Fig. III-24:** Resonance peak parameters obtained from the measured transmission coefficient  $|S_{21}|$  as a function of saline concentration, (a): resonance frequency shift  $\Delta f$ , (b): quality factor  $Q$ , 0 mg/ml = reference value,  $f_{ref} = 2\text{GHz}$ ,  $P_0 = 0\text{ dBm}$ , IFBW = 100 Hz, zero level = -55 dB

As shown in Fig. III-24.a, the resonance shift increases with the concentration level and the maximum shift is around 1200 kHz. On the other hand, it is observed in Fig. III-24.b that the quality factor decays as a function of the concentration. In particular, the maximum  $Q$  value (2900 obtained at 0 mg/ml - reference) decreases to 600 for a solution at 9 mg/ml, representing a reduction of almost a factor 5.

According to [LU 97], the resonance shift  $\Delta f$  is closely related to the variation of the dielectric constant  $\varepsilon'$  while the fall of the quality factor represents the variation of dielectric loss  $\varepsilon''$  of the material under test. The relation between the  $\Delta f$ ,  $Q$  and the complex permittivity can be expressed as:

$$\frac{\Delta f}{f_{ref}} = f(\Delta\varepsilon')$$

$$\Delta\left(\frac{1}{Q}\right) = \frac{1}{Q} - \frac{1}{Q_{ref}} = f(\Delta\varepsilon'')$$

Based on Fig. III-24, the quantities  $\Delta f/f_{ref}$  and  $\Delta(1/Q)$  measured as a function of saline concentration are given in Fig. III-25.

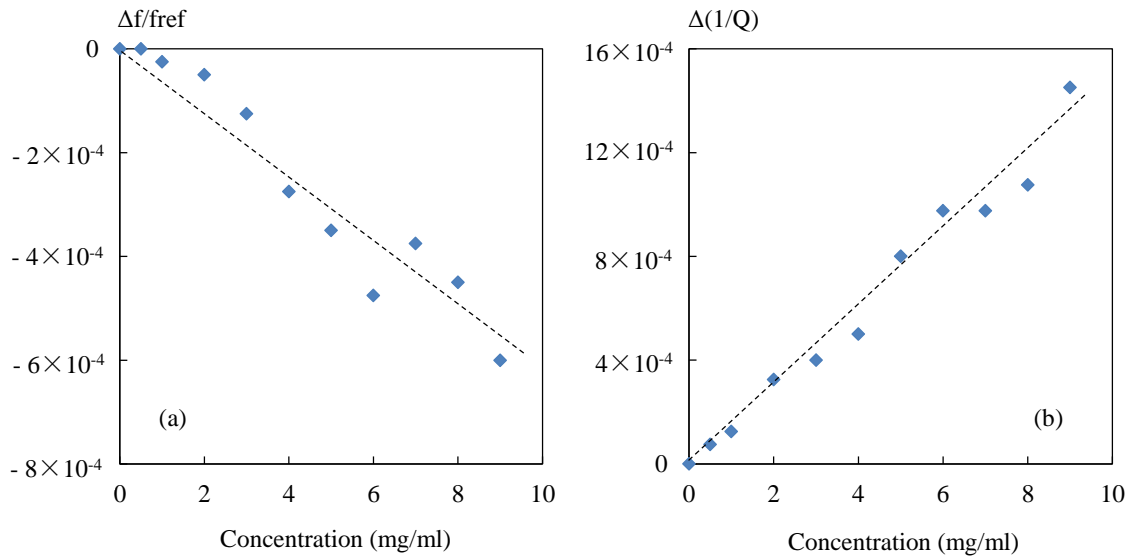


**Fig. III-25:** Resonance peak parameters obtained from the measured transmission coefficient  $|S_{21}|$  as a function of saline concentration, (a):  $\Delta f/f_{ref}$ , (b):  $\Delta(1/Q)$ , Dashed lines represent the fitted polynomial line at first order,  $0$  mg/ml is the reference value,  $f_{ref} = 2$ GHz,  $P_0 = 0$  dBm, IFBW = 100 Hz, zero level = -55 dB

As shown in Fig. III-25,  $\Delta f/f_{ref}$  and  $\Delta(1/Q)$  are practically proportional to the NaCl concentration level. So, the behavior of  $\Delta f/f_{ref}$  and  $\Delta(1/Q)$  can be expressed as a function of saline concentration ( $C$ ) by those equations:

$$\frac{\Delta f}{f_{ref}} = A' C \quad (III-7)$$

$$\Delta\left(\frac{1}{Q}\right) = A'' C \quad (III-8)$$

$A'$  and  $A''$  represent the slopes of the fitted polynomial line in Fig. III-25.a and Fig. III-25.b, respectively. Thus  $A' = -6.25 \times 10^{-5}$  ml/mg and  $A'' = 1.48 \times 10^{-4}$  ml/mg are

obtained. With these two parameters, the measured  $\Delta f/f_{ref}$  and  $\Delta(1/Q)$  are mathematically related to the saline concentration levels. In addition, thanks to the relations linking the complex permittivity and the NaCl concentrations discussed above (Eqn.III-2, III-3), the measured  $\Delta f/f_{ref}$  and  $\Delta(1/Q)$  can be related to the saline solutions complex permittivity by the following equations:

$$\epsilon' = -4.08 \cdot 10^3 \cdot \left(\frac{\Delta F}{F_{ref}}\right) + 77.66 \quad (III-9)$$

$$\epsilon'' = 1.022 \cdot 10^4 \cdot \Delta\left(\frac{1}{Q}\right) + 7.53 \quad (III-10)$$

Thanks to these equations, the measured complex permittivity in the concentration range [0-9 mg/ml] is then obtained. For comparison, the theoretical values calculated from Cole-Cole model are also presented in Fig. III-26.

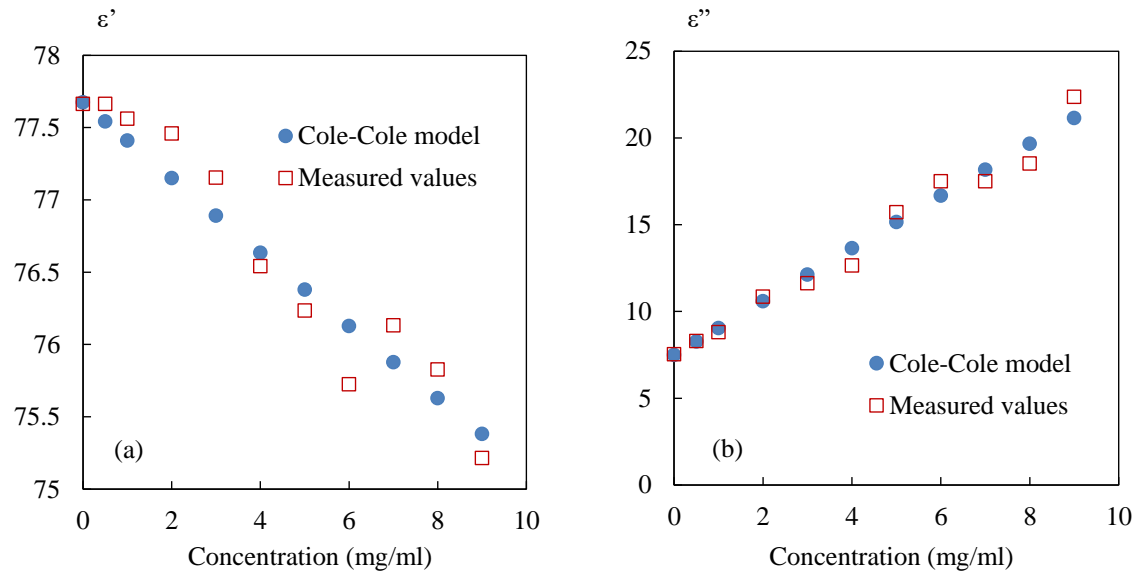


**Fig. III-26:** Complex permittivity as a function of saline concentration, (a): dielectric constant  $\epsilon'$ , (b): dielectric loss  $\epsilon''$ , round symbols represent values based on the Cole-Cole model, square symbols represent measured values, 0 mg/ml is the reference value,  $f_{ref} = 2\text{GHz}$ ,  $P_0 = 0 \text{ dBm}$ , IFBW = 100 Hz, zero level = -55 dB

This figure exhibits a good agreement between the theoretical and experimental complex permittivity at 2 GHz for the saline concentration range [0-9 mg/ml]. Thus, one can conclude thanks to the Eqn. III-9 and III-10 that the measured complex permittivity is successfully extracted. Actually, these equations remain available for the concentrations range [0-58 mg/ml] (linear zone 1 of Fig. III-16.a) and equivalent treatment can be applied by using them. Concerning the linear zone 2 (Fig. III-16.a), a similar extraction method based on  $\Delta f/f_{ref}$  and  $\Delta(1/Q)$  can be used and a new set of

equations is established. The results are gathered to represent the complex permittivity on the entire range of concentrations from 0 to 160 mg/ml in Fig. III-27.

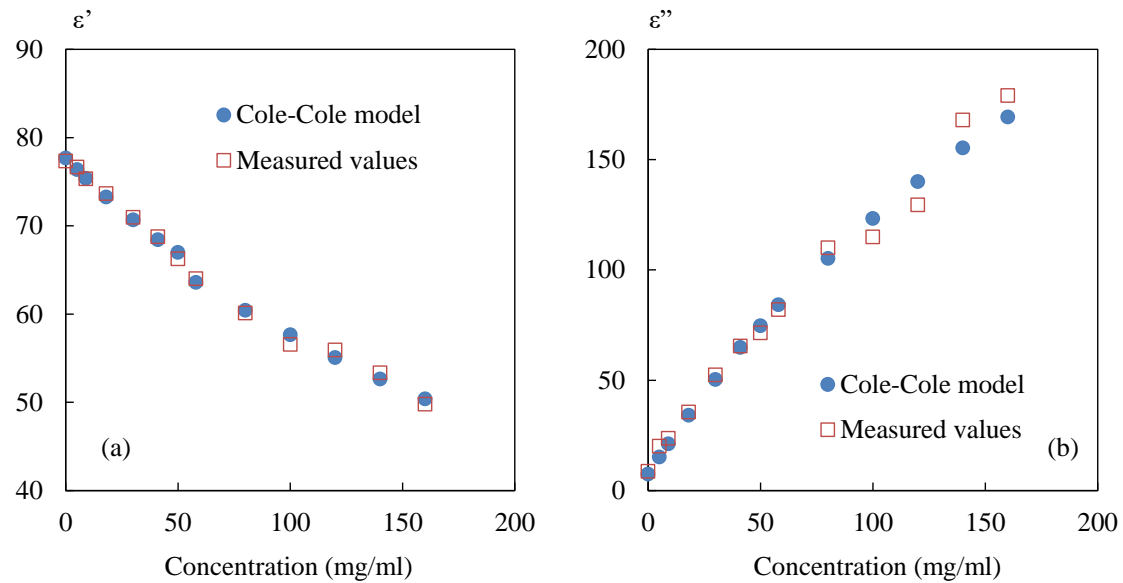


**Fig. III-27:** Complex permittivity as a function of saline concentration, (a): dielectric constant  $\epsilon'$ , (b): dielectric loss  $\epsilon''$ , round symbols represent values based on the Cole-Cole model, square symbols represent measured values, 0 mg/ml is the reference value,  $f_{\text{ref}} = 2\text{GHz}$ ,  $P_0 = 0\text{ dBm}$ , IFBW = 100 Hz, zero level = -55 dB

As shown in Fig. III-27.a, a good agreement is found between the permittivities calculated by the Cole-Cole model and the measured ones for such a large NaCl concentrations range spreading from 0 to 160 mg/ml. To investigate the measurement precision, the difference between measurement and theory for each concentration from 0 to 160 mg/ml is calculated and the average over the set of values is then computed. In this case, the averaged error is in the order of 1.6 % and 7.8 % for  $\epsilon'$  and  $\epsilon''$ , respectively. Higher discrepancy is noticed for the high concentrations from around 100 mg/ml (Fig. III-27.b). A way to increase the measurement sensitivity and precision in the upper range of concentrations is to consider as a reference value a higher concentration instead of 0 mg/ml (DI water). As a demonstration, 3 other concentrations are considered as the reference solution: the maximum concentration level (160 mg/ml) and two medium concentrations (58 and 100 mg/ml). For the setting parameters of the VNA, the operating frequency is kept at 2 GHz, 0 dBm for the power and 100 Hz for IFBW. The probe is still immersed at a depth of 300  $\mu\text{m}$  in the liquid under test. The zero level of  $|S_{21}|$  is tuned to -55 dB for the reference solutions. In Fig. III-28, we give

the measured quality factor for the 4 reference solutions selected: 0, 58, 100 and 160 mg/ml.

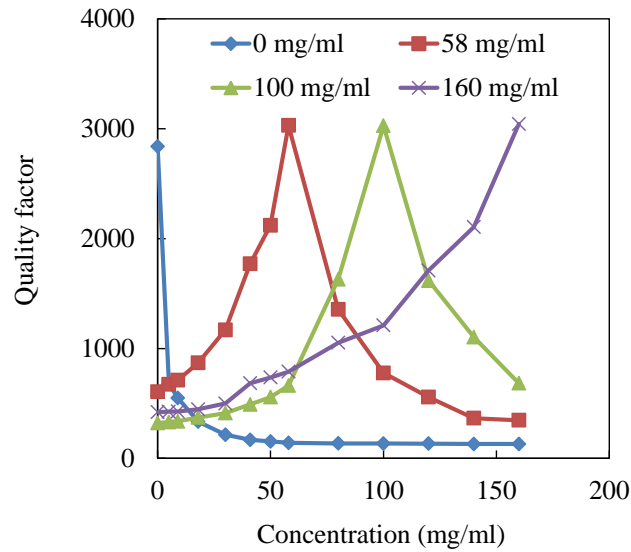


**Fig. III-28:** Quality factor as a function of saline solutions considering different reference solutions: 0, 58, 100 and 160 mg/ml,  $f_{\text{ref}} = 2\text{GHz}$ ,  $P_0 = 0\text{ dBm}$ , IFBW = 100 Hz, zero level = -55 dB

It can be noted from Fig. III-28 that the quality factor for the reference solution remains relatively stable around 3000, which means a high measurement sensitivity is obtained for these concentrations. This possibility of tuning the quality factor as a function of concentration is one of the main assets of the iNFMM proposed, in particular when liquids are investigated. In the following, we evaluate the impact of the reference concentrations on the measured permittivity (Fig. III-29).

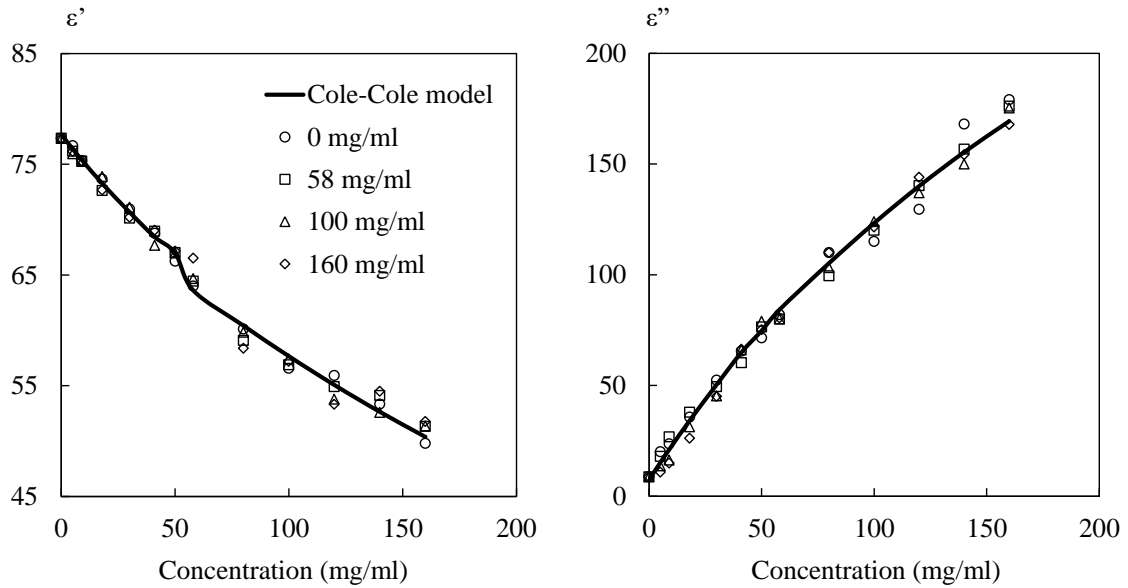


**Fig. III-29:** Complex permittivity for 4 NaCl reference concentrations: 0, 58, 100 and 160 mg/ml, (a): dielectric constant  $\epsilon'$ , (b): dielectric loss  $\epsilon''$ , Solid lines represent values based on the Cole-Cole model, symbols represent measured values, zero level equals to -55 dB for the 4 reference concentrations,  $f_{\text{ref}} = 2\text{GHz}$ ,  $P_0 = 0\text{ dBm}$ ,  $\text{IFBW} = 100\text{ Hz}$

Generally speaking, the measured permittivity is in a good agreement with the values based on Cole-Cole model for the entire concentration range [0-160 mg/ml] whatever the reference concentration is. Nevertheless, one can note that the reference concentration levels influence to some extent the measured permittivity values. In Fig. III-29.a, for a given NaCl concentration, for example 120 mg/ml, the theoretical value  $\epsilon'$  is 54.9 whereas the measured results retrieved when using the 4 reference concentrations (0, 58, 80 and 160 mg/ml) are 55.9, 54.8, 53.5 and 53.3 respectively. Besides, in Fig. III-29.b for the same NaCl concentration of 120 mg/ml, the measured  $\epsilon''$  obtained when using the 4 reference concentrations (0, 58, 80 and 160 mg/ml) are 129, 136, 135 and 143 respectively compared with the theoretical value of 140. These results show that especially for  $\epsilon''$  the difference between the measured value and the theoretical data is enlarged when the tested solution presents a concentration that is moved away from the reference solution. Thus, the measurement quality of the complex permittivity is closely associated to the reference concentration level. To better appreciate the relation between the reference concentration and the measurement results, we summarize in Table III-4 the averaged error calculated from the difference between the measured permittivities and the theoretical values for each concentration for the 4 cases envisaged (reference level = 0, 58, 100, and 160 mg/ml).

	0 mg/ml	58 mg/ml	100 mg/ml	160 mg/ml
$\epsilon'$	1.6 %	0.9 %	0.9 %	1.6 %
$\epsilon''$	7.8 %	7.0 %	7.1 %	8.5 %

**Table III-4:** Averaged errors in percentage for different reference concentration levels (0, 58, 100 and 160 mg/ml),  $f_{\text{ref}} = 2$  GHz,  $P_0 = 0$  dBm, IFBW = 100 Hz, zero level = -55 dB

As shown in Table III-4, the maximum averaged error reported is 1.6 % and 8.5 % for the real and imaginary parts of the permittivity, respectively. One can also note that a lower error is obtained for both  $\epsilon'$  and  $\epsilon''$  for reference concentrations at 58 and 100 mg/ml. This result confirms that a better measurement precision can be found when the reference concentration is not taken at the limit of range investigated. Thus, to guarantee a precise measurement, the intermediate concentrations (e.g. 58 and 100 mg/ml) should be preferentially selected as reference concentrations instead of the minimum (0 mg/ml) or maximum concentrations (160 mg/ml). Actually, thanks to the interferometer which is equipped with variable attenuator and delay line, high measurement sensitivity can be easily guaranteed at any desired reference concentrations. So, it is relatively simple to choose for example the middle of the range of interest as the reference concentration level.

As a conclusion, the saline solutions with a large concentration range [0-160 mg/ml] are effectively characterized in a wide frequency range [2-18 GHz]. We determine the complex permittivity of the materials by means of the transmission line and the cavity perturbation methods. Good agreement is found between the theoretical values obtained from the Cole-Cole equation and the experimental values. Practically, for the transmission line approach, an inverse procedure based on the magnitude and phase-shift of the transmission coefficient is employed to retrieve the dielectric parameters. On the other hand, based on the cavity perturbation approach, a relation is found between the dielectric properties and the measured quality factor and resonance frequency shift. It should be mentioned that unlike the traditional resonator-based method whose quality factor is fixed, in this case, the interferometer-based NFMM offers the possibility to obtain a high quality factor at any desired saline concentration levels and frequencies. The results indicate that intermediate concentration levels should be chosen to guarantee a good measurement quality. Finally, the performances

of these two methods are compared in terms of averaged errors at 2GHz in Table III-5.

	Transmission line method	Cavity perturbation method
$\epsilon'$	0.5 %	0.9 %
$\epsilon''$	1.9 %	7.0 %

**Table III-5:** Averaged errors in percentage of two complex permittivity extraction methods,  $f_{\text{ref}} = 2 \text{ GHz}$ ,  $P_0 = 0 \text{ dBm}$ , IFBW = 100 Hz, zero level = -55 dB

As shown in Table III-5, the averaged errors on the permittivity obtained by the transmission line method are lower than the values by cavity perturbation method. One can note that the measurement accuracy of the extracted values depends on the quantification methods applied. Actually, for perturbation method, the measured  $Q$  and  $\Delta f$  is linearly fitted as a function of some known saline concentrations. Then,  $Q$  and  $\Delta f$  are related to complex permittivity. This linear polynomial fit, as an approximation, may introduces some errors into the calculation. However, for the transmission line method, the calibration procedure is well defined by considering three different saline concentrations as the standards. Thus the complex permittivity is extracted with better agreement with the theoretical values.

### III.3.7 Conclusion

The characterization of the complex permittivity based on near-field microwave microscopy is experimentally demonstrated. The method combines a vector network analyzer, an interferometric technique and an evanescent microwave probe to achieve high measurement sensitivity and accuracy. The electromagnetic simulation shows that the strongest electric field is focused around the probe apex (260  $\mu\text{m}$ ) enabling a local characterization of materials. As a demonstration, this study gives a fine description of the dielectric properties of saline solutions as a function of both NaCl concentration [0-160 mg/ml] and frequency [2-18 GHz] based on the home-made iNFMM.

The complex permittivity is first evaluated by using the Cole-Cole equation at 2 GHz. The probe-sample interaction studied by using the electromagnetic simulation software ANSYS/HFSS<sup>TM</sup> shows that the electromagnetic energy dissipates rapidly as a function of the saline concentration levels. After a fine study of the probe position, during the measurement, the probe is immersed at a depth of 300  $\mu\text{m}$  in the liquid

ensuring the whole tip apex is plunged in liquid under test. Thus a maximum tip-liquid electromagnetic coupling can be obtained. Another advantage in case of an immersed probe is the immunity to water evaporation process at the liquid surface layer which can largely influence the air-liquid interface and the concentration of saline solutions.

Then, the sensitivity measurement is demonstrated by comparing two configurations: without and with interferometer. The interferometer based system offers a sensitivity of 1.56 dB/(mg/ml) and 3.9 %/(mg/ml) for magnitude and phase-shift respectively in the saline concentration range [0-9 mg/ml] at 2 GHz. These values are much higher than the measurement sensitivities provided by the configuration without interferometer. Therefore, thanks to the interferometric technique, the proposed iNFMM is able to detect precisely a very small saline concentration variation.

After the theoretical study of aqueous saline solutions permittivity and the evaluation of the measurement sensitivity, two methods are proposed to relate the measured transmission coefficient ( $S_{21}$ ) to the complex permittivity of the liquid: the transmission line method and the cavity perturbation method. The first approach translates the measurement data ( $S_{21}$ ) to the dielectric properties ( $\epsilon'$  and  $\epsilon''$ ) and the second method quantifies the complex permittivity from the knowledge of the resonance frequency shift ( $\Delta f$ ) from a reference frequency and the quality factor ( $Q$ ) of  $|S_{21}|$ . For both methods good agreement is found between the measured data and the theoretical findings obtained by using Cole-Cole model. One can also note that the transmission line method turns to be a better candidate for the liquids characterization because of a better agreement with the theoretical values..

Furthermore, unlike the resonator-based method whose quality factor is fixed, in this case, the interferometric technique enables the measurement of a tunable quality factor and good sensitivity at any desired concentration levels and frequencies. Therefore, this method provides an effective solution to the issue of poor sensitivity encountered when measuring high-loss materials by means of resonator-based structures. This study is a contribution towards quantitative microwave microscopy of biological structures.

## **III.4 Broadband non-contact characterization of graphene by iNFMM**

### **III.4.1 Introduction**

In recent years, two-dimensional nanomaterials such as graphene have attracted significant attentions from the scientific community because of their unique physical properties [JAR 13] [BAE 10]. Graphene-based devices/structures have addressed numerous applications of high-speed electronics such as digital electronics and RF analog devices to name just a few them [JAR 13], [BAE 10], [SCH 10], [NOV 12]. For the realization of these devices, the characteristics of graphene must be carefully evaluated. So far, the electronic properties of graphene have been mostly investigated in dc or low frequency range by techniques such as transmission line method (TLM) and probing methods [WEI 15] [WEI 16]. The coplanar waveguide (CPW) method has also been applied to evaluate the surface impedance of the graphene flake [JEO 09]. However, these characterization methods require additional electrodes fabrication process which could degrade the electrical properties of sample tested. Furthermore, most of these methods such as TLM and CPW approaches are not convenient and efficient to investigate local properties of materials, which is quite an issue when testing inhomogeneous samples, for example. So, there is an urgent need for the development of a non-destructive and non-contact characterization tool with a good spatial resolution compatible with this kind of evaluation.

In fact, the NFMM has already been effectively employed for quantitative imaging of the local impedance of monolayer and multilayer graphene [KUN 09] [TAL 10]. Thanks to the use of probe-sample capacitive coupling and a relatively high frequency of a few GHz, this NFMM method allows the mapping of local conductivity without a dedicated electrode, with a nanometric scale spatial resolution. However, as most of these NFMMs are resonator-or quarter wavelength transmission line-based, their working frequency range is limited. So, a big challenge for the NFMM is to perform a wideband measurement with high sensitivity [TSE 07]. In addition, many NFMMs work in contact mode hence there is a risk of scratching the graphene flake by the probe tip. In this work, to meet the non-destructive, non-contact and broad frequency band requirements, we propose to use the iNFMM. To better understand the

electromagnetic interaction between the microwave probe and the graphene sample, the electric field distribution is simulated by using ANSYS/HFSS<sup>TM</sup>. Then, the extraction method to transform the measured data to the impedance is described. Finally, the impedance of the graphene tested in the frequency [2-18 GHz] is demonstrated.

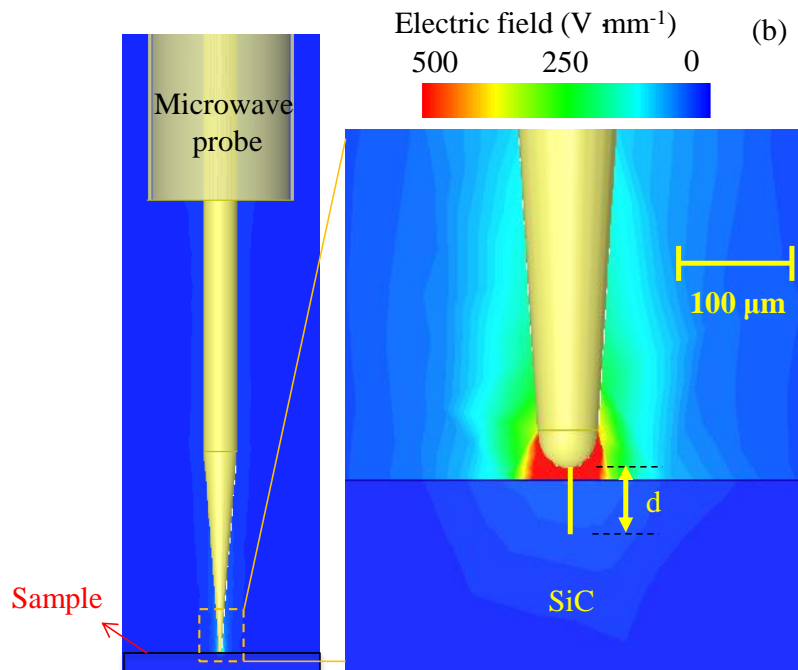
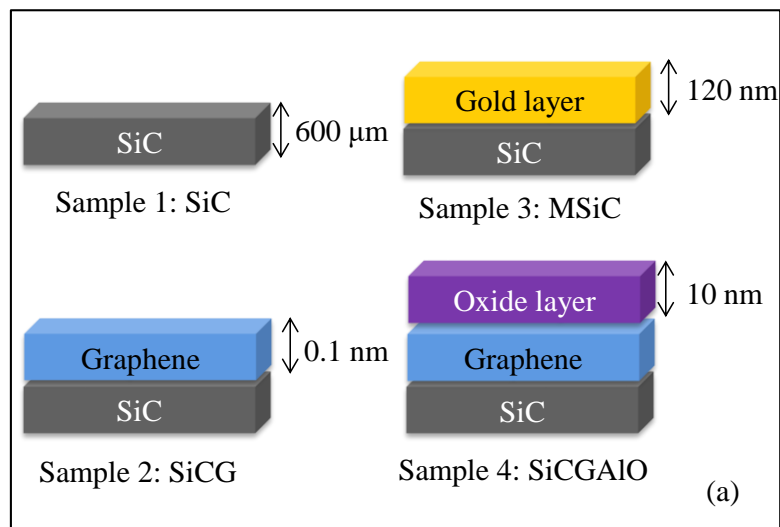
### III.4.2 Electromagnetic simulation of the probe-sample interaction

Simulation tools are available for a fine study of the electromagnetic properties of different kinds of structures. In this part, the electric field distribution between the probe and the sample is investigated by using an electromagnetic simulation software (ANSYS/HFSS<sup>TM</sup>). Graphene is a 2D material whose surface conductivity  $\sigma$ , from DC to optical frequencies, can be modeled by Kubo formula [GOM 12a] [AWA 16]:

$$\sigma(\omega) = -j \frac{q_e^2 k_B T}{\pi \hbar (\omega - j\Gamma)} \left( \frac{\mu_0}{k_B T} + 2 \ln \left( e^{-\frac{\mu_0}{k_B T}} + 1 \right) \right) \quad (\text{III-11})$$

where  $\omega$  is the radian frequency,  $\mu_0$  is the chemical potential,  $\Gamma$  is the scattering rate,  $T$  is the temperature,  $q_e$  is the charge of an electron,  $\hbar$  is the reduced Planck's constant, and  $k_B$  is Boltzmann's constant. The conductivity determined by using the Eqn.III-11 allows then to calculate the surface resistance of a monolayer graphene by  $R_{Gra} = 1/\sigma(\omega)$  [GOM 12a]. For example the surface resistance value computed at 2 GHz is (237+3j  $\Omega$ ). However, Kubo equation solves the surface conductivity of a monolayer of graphene without consideration on the type of graphene. Practically, the graphene impedance can be different from the one given by Kubo equation, because it is closely related to the preparation process of graphene. Actually, in the literature, different values of the ac surface resistance of graphene ranging from several hundreds of Ohms to hundreds of k $\Omega$  can be found depending on the graphene fabrication process such as mechanical exfoliation [AWA 16] [TAL 10] [MON 13], epitaxial method [ALA 11] [TSE 13] or chemical vapor deposition [GOM 12a] [GOM 12b] [TSE 12]. It can also be noticed that different kinds of characterization approaches including the rectangular waveguide [GOM 12a] [GOM 12b], the coplanar waveguide (CPW) [JEO 09] [TAM 12] [AWA 16], and the scanning microwave microscopy (SMM) [TSE 12] [TSE 13] [MON 13] [TAL 10] [KUN 09] have been exploited. In our case, the graphene flake is obtained by epitaxial method on silicon carbide. Thus, instead of employing the surface conductivity calculated by Kubo equation, we use for the simulations the value of 1

$k\Omega/\text{square}$  obtained by DC measurement. Furthermore, the probe retained for the simulation study is the one with an apex of  $66\ \mu\text{m}$ . Four samples have been considered for the simulation investigation: silicon carbide (SiC) used as a substrate, graphene fabricated by epitaxial method (SiCG), gold-metallized substrate (MSiC) with  $120\ \text{nm}$  in thickness and epitaxial graphene with a  $\text{Al}_2\text{O}_3$  layer prepared with static oxidation process on the top (SiCGAlO). These samples have been fabricated by Dr. Xin ZHOU from CARBON Group of IEMN. For the demonstration, the electric field distribution of the probe at  $2\ \text{GHz}$  for the four samples is shown in Fig. III-30. The probe is placed  $10\ \mu\text{m}$  over the sample surface, which guarantee a near-field and non-contact measurement.



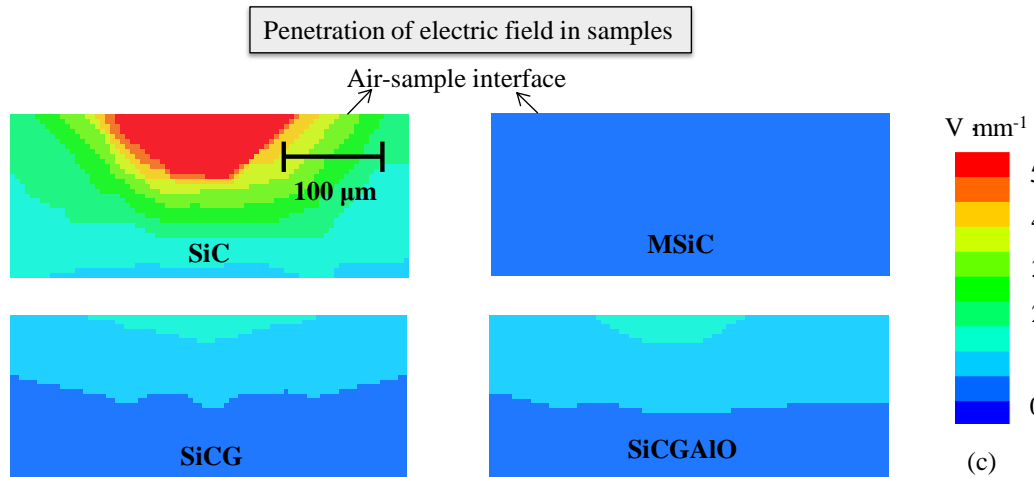


**Fig. III-30:** (a): Configuration of the samples tested: silicon carbide (SiC) substrate, epitaxial graphene on SiC substrate (SiCG,) metallized SiC substrate with gold layer on the top (MSiC) and SiCG structure with  $\text{Al}_2\text{O}_3$  layer on the top (SiCGAIO), (b): simulations of electric field at the cross-section along the probe, zoomed image of tip-sample (SiC) coupling and (c): electric field penetration in the samples (stand-off distance fixed at  $10 \mu\text{m}$ ),  $f = 2 \text{ GHz}$ , simulation tool: Ansys<sup>TM</sup>/HFSS

As shown in Fig. III-30.b, the electric field is well confined around the probe apex, which indicates the potential for local characterization of materials. A discontinuity of the electric field is found at the air-sample interface due to the strong air-sample mismatch. Indeed, most of the electric field is reflected at the air-sample interface, and only a small part penetrates into the sample (SiC). The field penetration is illustrated for the four samples in Fig. III-30.c. The penetration, as expected, depends on the sample under simulation. A significant electric field is noticed for SiC sample while for the metallic sample MSiC, there is obviously practically no electric field distribution inside the substrate, which means almost no charges induced by electric field is distributed in SiC. Compared with simple SiC substrate, the intensity of electric field in SiCG structure is much smaller due to existence of graphene layer, although the thickness of graphene layer is only  $0.1 \text{ nm}$ .

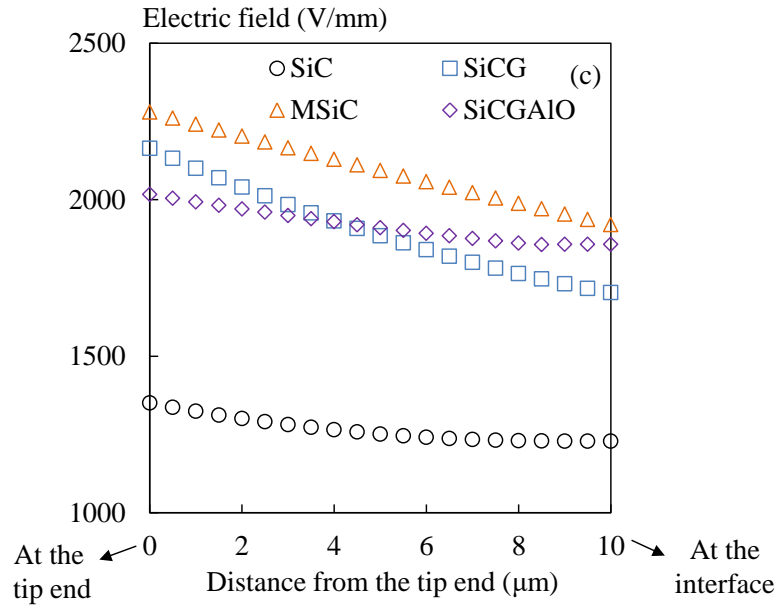


**Fig. III-31:** Electric field distribution for the samples as a function of the tip end to the sample surface,  $f = 2$  GHz

To better appreciate the electromagnetic coupling between the probe and the different samples, especially the electric field at the air-sample interface, the electric field distributions are plotted along a line from the tip end to the sample (Fig. III-30.b) for the four cases (SiC, MSiC, SiCG and SiCGAlO) in Fig. III-31. From this graph, it is retrieved that the sample under test influences the electric field distribution between the tip and the interface. Indeed, the four samples can be clearly distinguished by their electric field description, which indicates the high sensibility of this microwave probe. In Fig. III-31, the maximum electric field value obtained (at the tip end) is 1350, 2016, 2164 and 2280 V/mm for SiC, SiCGAlO, SiCG and MSiC samples respectively. Actually, MSiC has the highest electric field value at the tip end because the electric field can be strengthened in the presence of the metallized surface. However, as there is one part of the electric energy passes into the substrate, there are less electric field distribution in the air. One can also note that the electric field gradually decreases from the tip end to the interface.

The reflected microwave signal at the air-sample interface carries sample properties and gives actually the possibility to locally characterize the samples. This feature establishes the potential of the iNFMM to evaluate the electromagnetic properties of the materials such as the surface impedance and the dielectric parameters.

In the following the probe-sample interaction is studied by means of a lumped-element model and a calibration procedure of the platform is discussed.

### III.4.3 Calibration procedure of iNFMM

#### III.4.3.1 Modeling of the probe-sample interaction

Understanding NFMM measurements requires some insights into the interaction between the probe and sample under test. As the sample is placed in the near-field range of the tip and the tip radius is much smaller than the wavelength, the probe-sample interaction can be represented by a lumped element network in the quasi-static approximation [IMT 07]. We retake the schematic of this probe-sample interaction modelling which has been presented in Chapter I.3, as given in Fig. III-32.

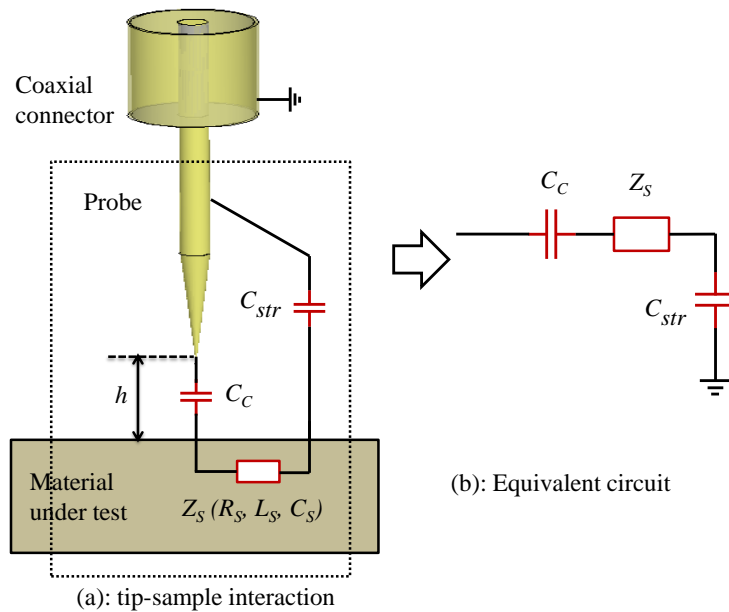


**Fig. III-32:** Schematic of a lumped element model of probe-sample interaction. Here,  $C_c$  is the coupling capacitance between the tip and the sample,  $Z_S$  is the material impedance to be measured, including the resistance  $R_S$ , inductance  $L_S$  and capacitance  $C_S$ .  $C_{str}$  (or  $C_{out}$ ) is the stray capacitance [GAO 98], [ANL 07]

In near-field region, the stray capacitance  $C_{str}$  can be neglected because it is much larger than  $C_c$  [IMT 07]. Thus the lumped element model of such a probe-sample interaction can be simplified as a coupling capacitance  $C_c$  in series with the material impedance  $Z_S$ . Particularly, the metallized substrate is usually regarded as the reference

sample. In this situation, in the first order of approximation, the interaction between the tip and the sample can be simplified and represented by a coupling capacitance  $C_c$ .

### III.4.3.2 iNFMM calibration procedure

A calibration procedure should be employed to transform the transmission coefficient  $S_{21}$  measured into the impedance of the device/material under test ( $Z_S$ ). The description of the calibration method and the material impedance extraction from the measured data (magnitude and phase-shift of the transmission coefficient) are illustrated in Fig. III-33.

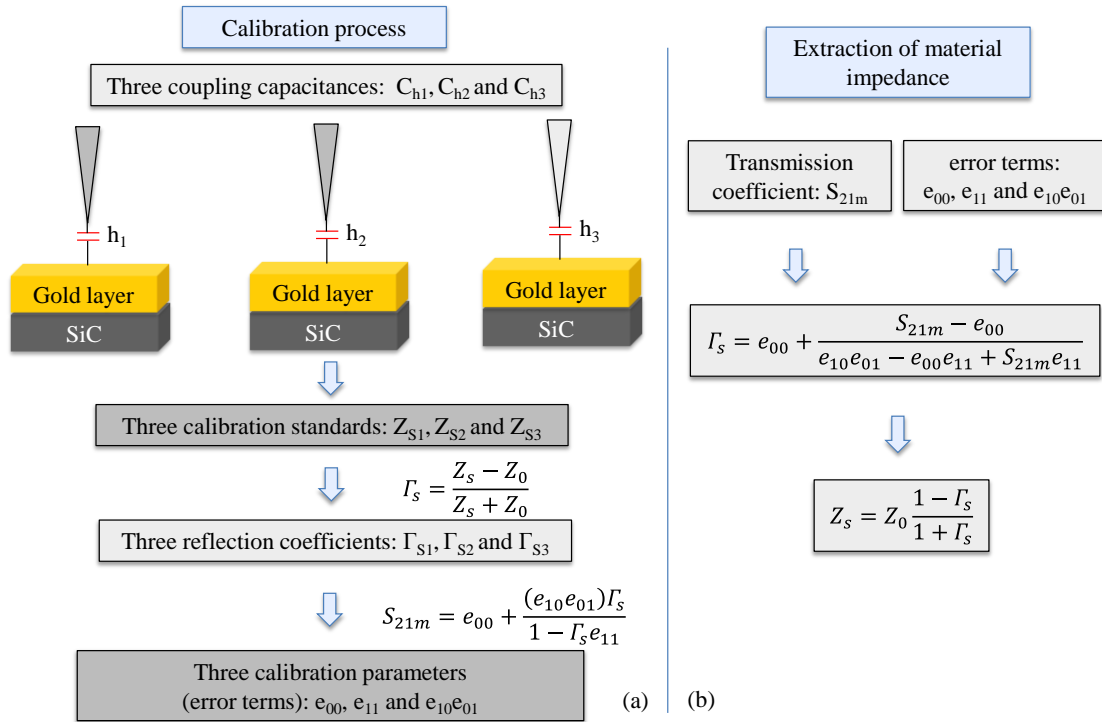


**Fig. III-33:** Calibration procedure of iNFMM (a) and extraction of the material impedance (b)

As shown in Fig. III-33, the process is derived from a one-port VNA calibration method, requiring three standard impedances. The metalized SiC substrate is selected as the standard material for the calibration process and the probe sample interaction is modeled as said before by a coupling capacitance  $C_c$ . In general, there are basically two methods to analytically solve this capacitance: the image method [GAO 98] and the surface integration method [HUD 98]. In this work, the image-charge method is used to determine the capacitance  $C_c$ . As the electromagnetic field is concentrated around the

probe tip of semi-sphere shape and according to [DUR 66] [GAO 99] works, the capacitance  $C_c$  between the semi-sphere and the metallic plane is given as follows:

$$C_c = 4\pi\epsilon_0 R_0 \sinh(\alpha) \sum_{n=2}^{\infty} \frac{1}{\sinh(n\alpha)} \quad (\text{III-12})$$

where  $\alpha = \cosh^{-1}(1+a')$  with  $a' = h/R_0$ .  $h$  stands for the stand-off distance between the tip and the sample.  $R_0$  is the tip radius. The impedance  $Z_s$  of the sample can be related simply to the reflection coefficient  $\Gamma_s$  [HUB 10] [MOE 14] by:

$$\Gamma_s = \frac{Z_s - Z_0}{Z_s + Z_0} \quad (\text{III-13})$$

where  $Z_0$  is the measurement system characteristic impedance (here 50  $\Omega$ : VNA impedance). When only the coupling capacitance  $C_c$  is considered,  $Z_s$  can be written as:

$$Z_s = \frac{1}{j\omega C_c} \quad (\text{III-14})$$

$\omega$  is the angular frequency. A traditional one port calibration model is used to link the transmission coefficient measured  $S_{21m}$  to the reflection coefficient  $\Gamma_s$ .

$$S_{21m} = e_{00} + \frac{(e_{10}e_{01})\Gamma_s}{1 - \Gamma_s e_{11}} \quad (\text{III-15})$$

The errors terms,  $e_{00}$ ,  $e_{11}$  and  $e_{10}e_{01}$ , are respectively the directivity, port match and tracking errors. They can be determined by measuring three reflection coefficients for three known calibration standards  $Z_{S1}$ ,  $Z_{S2}$  and  $Z_{S3}$  with reflection coefficients  $\Gamma_{S1}$ ,  $\Gamma_{S2}$  and  $\Gamma_{S3}$ . It should be mentioned that the calibration coefficients depend on the operating frequency. For example, based on the Eqn. III-12, we obtain 2.6 fF, 0.22 fF and 0.14 fF for the coupling capacitance of three stand-off distances 10, 260, and 410  $\mu\text{m}$ . One can note that the capacitance value decays rapidly with an increasing stand-off distance. Then, relying on the Eqns. III-13- III-15, the calibration parameters retrieved at 2 GHz are  $e_{00} = 0.015/-81.1^\circ$ ;  $e_{11} = 3.9 \times 10^{-6}/-178.7^\circ$  and  $e_{01}e_{10} = 0.99/-0.024^\circ$ . Once these three calibration parameters are determined, the electrical properties are extracted from the transmission coefficient according to the flow-chart given in Fig. III-33.b.

### III.4.4 Results and discussions

#### III.4.4.1 Evaluation of the measurement sensitivity

The quality factor of the iNFMM represents one of the most effective manners to demonstrate the measurement sensitivity [STE 98], [LAI 09]. As reported in the literature, the transmission-line-based structures usually exhibit a quality factor in the order of 1000 [TAB 00], [KLE 06], [WEB 12]; while the resonator-based platforms present higher  $Q$  values around 5000 [SUN 14], [GRE 16]. Unfortunately, all these platforms are narrow band and thus enable high measurement sensitivity in a limited frequency band. On the contrary, an interferometer-based structure has potentials to achieve a good sensitivity in a broad frequency band. For example, Bakli *et al.* obtained a  $Q$  varying from 5300 to 9400 in the frequency band [2-6 GHz] in free space [BAK 14] considering the zero level of -60 dB (30 dB above the noise floor of -90 dB). In this work, we extend the working frequency range up to 18 GHz with an excellent sensitivity ( $Q$  in the order of 53000). The zero level is set around -75 dB (15 dB above the noise floor of -90 dB) by carefully tuning the attenuator and the delay line when the probe is placed in air. The intermediate frequency bandwidth (IFBW) and power of the VNA ( $P_0$ ) are set to 100 Hz and 0 dBm, respectively.

Generally,  $\lambda/4$  or  $\lambda/2$  coaxial resonators based NFMMs are used to retrieve the materials/devices under test properties from the measurement of the quality factor and resonant frequency [STE 98]. Nevertheless, since recently, the transmission line method is more and more exploited in AFM-based NFMM [HUB 10], [GRA 14]. The proposed iNFMM has the advantage to be operable with both resonator and transmission line methods. First, the measured quality factor ( $Q$ ) and the resonance frequency shift ( $\Delta f$ ) as a function of the probe-sample distance are shown in Fig. III-34. In fact,  $\Delta f$  represents the difference between the resonance frequency obtained when measuring the sample under test ( $f_{meas}$ ) and the reference resonance frequency ( $f_{ref}$ ) measured without sample under test. In this study, the reference frequency selected is 2 GHz. The minimum probe-sample distance is kept as 10  $\mu\text{m}$  to guarantee the tip-sample interaction is well in the near field.

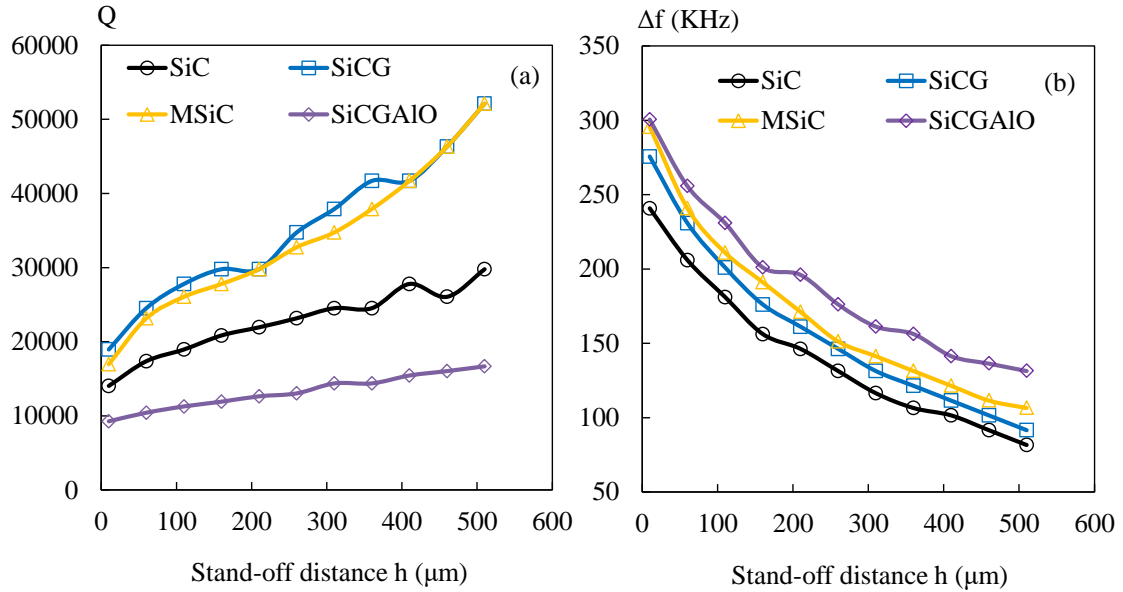


**Fig. III-34:** Measured quality factor (a) and resonance frequency shift (b) of measured transmission coefficient  $|S_{21}|$  as a function of the stand-off distance,  $f_{\text{ref}} = 2 \text{ GHz}$ ,  $\text{IFBW} = 100 \text{ Hz}$ ,  $P_0 = 0 \text{ dBm}$ , the wave-cancelling process is done considering the probe in air with zero level =  $-75 \text{ dB}$

We first notice that the four samples have different microwave responses in terms of the quality factors and the resonance frequency shifts qualifying the method for analysis of the material quality. It is observed in Fig. III-34.a that the quality factor increases with the tip-sample distance  $h$ . This is due to the fact that for the reference measurement (no sample under test) the quality factor ( $Q_{\text{Ref}}$ ) is tuned to the max (53000). One can also note that the shift of resonance frequency decreases with the stand-off distance, the maximum shift is around 300 KHz. From these results one can conclude that the method is sensitive enough to extract some materials properties.

If we look now at the second treatment method of the data we can plot the magnitude and phase-shift of the transmission coefficient  $S_{21}$  (Fig. III-35).

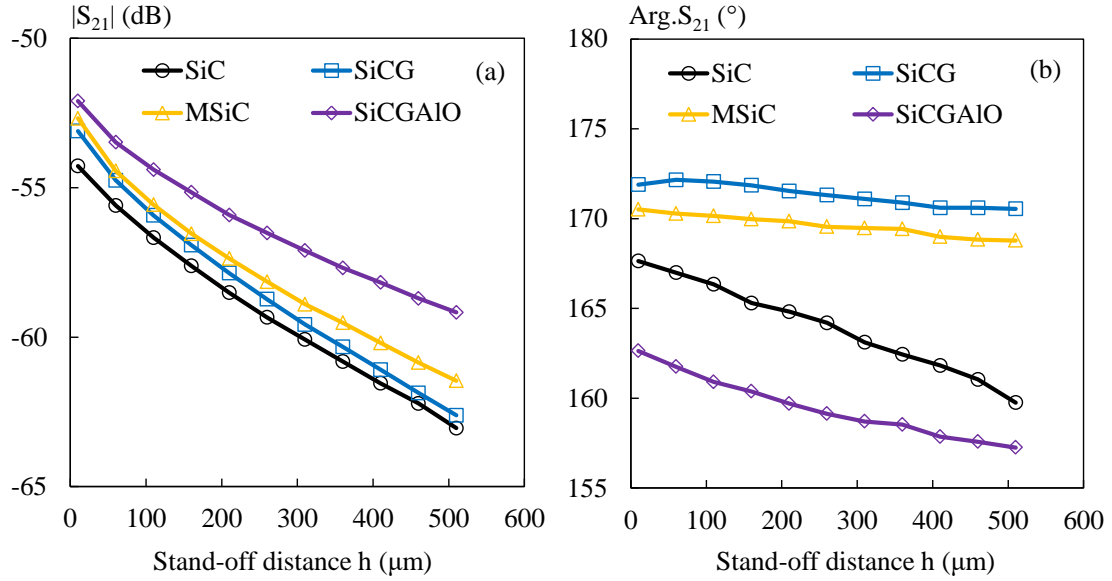


**Fig. III-35:** Measured magnitude and phase-shift of the transmission coefficient  $S_{21}$  as a function of the stand-off distance,  $f_0 = 2$  GHz, IFBW = 100 Hz,  $P_0 = 0$  dBm, the wave-cancelling process is done considering the probe in air with zero level = -75 dB

As shown in both the magnitude and phase-shift plots the four samples can be easily distinguished by the proposed iNFMM. One can also note that as the zero level selected is adjusted (-75 dB) when the probe is in air, the  $|S_{21}|$  decays as a function of the stand-off distance. The phase-shift spectra of  $S_{21}$  are also affected by the distance separation between the probe and the materials but in proportions depending on the material under test. Thus, this technique demonstrates its potential for the investigation of the local electromagnetic properties of samples with high sensitivity. In order to benefit from the measurement sensitivity of the proposed system, the probe-sample distance should be kept as small as possible compared to the apex size of the probe.

Now, for the demonstration, based on the magnitude and phase-shift of the transmission coefficient, we present the results of the implementation of the calibration process described before to extract the electric properties of the material under test.

#### III.4.4.2 Extraction of the materials under test impedance

When the iNFMM operates in non-contact mode, the measurement accuracy can be influenced by the separation between the probe and the sample. Thus, the extracted electric properties are evaluated as a function of the stand-distance. For the demonstration, the substrate (SiC) is selected as the sample under test. Thanks to the

calibration process detailed before, the measured transmission coefficient  $S_{21}$  is translated to the impedance of the sample under test. The probe-SiC interaction is simply modeled as a coupling capacitance ( $Z_C$ ) in series with the impedance of SiC ( $Z_{SiC}$ ), and thus  $Z_{SiC}$  can be extracted by subtracting the  $Z_C$  from the total impedance  $Z_{SI}$  ( $Z_{SI} = Z_C + Z_{SiC}$ ). Then, from the knowledge of  $Z_{SiC}$  the dielectric properties of SiC can be determined. In Fig. III-36, the extracted  $\epsilon'$  and  $\tan\delta$  of SiC versus the stand-off distance and also versus the frequency are presented at 2 GHz.

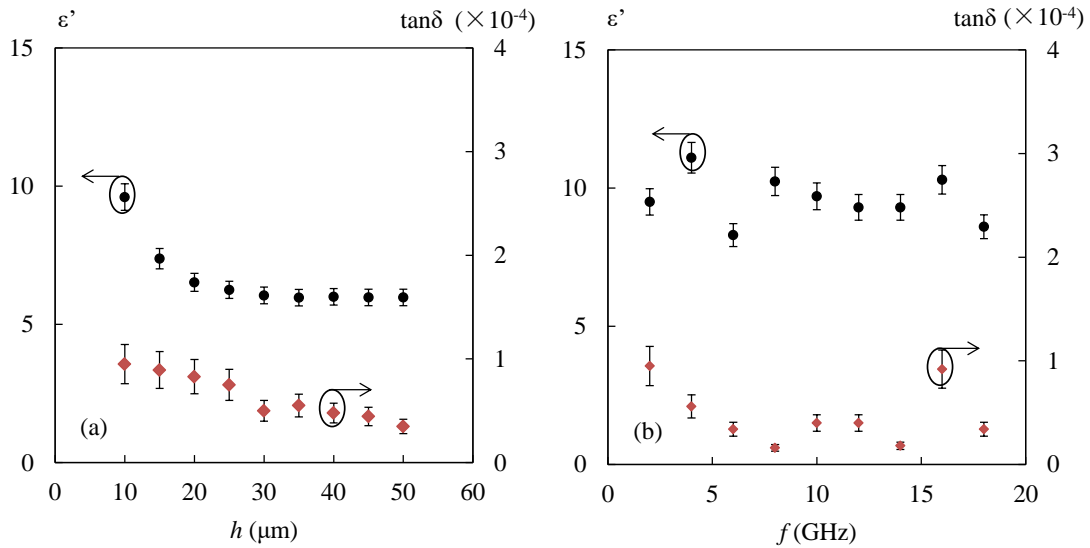


**Fig. III-36:** Extracted dielectric parameters of SiC after the calibration procedure, (a):  $\epsilon'$  and  $\tan\delta$  as a function of the stand-off distance  $h$  at 2 GHz, (b):  $\epsilon'$  and  $\tan\delta$  as a function of the frequency when the stand-off distance is kept to  $10 \mu\text{m}$

In this graph, the dielectric constant obtained at a small distance ( $10 \mu\text{m}$ ),  $\epsilon' = 9.6$ , agrees well with the value found in the literature [PAT\_70]. This value diminishes with the stand-off distance from  $0 \mu\text{m}$  to  $30 \mu\text{m}$  and then is almost constant around 6. Indeed, with the increasing stand-off distance, the electromagnetic coupling between the probe and the sample is weakened, resulting a reduced wave penetration into the SiC substrate and a larger influence of the air gap between the samples and the tip. Thus, to guarantee a good performance of the platform, the stand-off distance is kept as small as  $10 \mu\text{m}$  for the following. Additionally, the dielectric loss ( $\tan\delta$ ) retrieved is below 0.0001, which is also close to values found in the literature. Then, the broadband behavior of the dielectric parameters from 2 to 18 GHz is shown in Fig. III-36.b. The extracted dielectric parameters are also comparable to the theoretical values found in the literature [PAT\_70].

Thanks to the knowledge of the SiC properties, the impedance of the graphene flake ( $Z_{\text{Gra}}$ ) can be solved in a similar manner. As modeled in Fig. III-37.a,  $Z_{\text{Gra}}$  can be extracted from  $Z_{\text{S2}}$  which consists of three impedances in series:  $Z_{\text{C}}$ ,  $Z_{\text{Gra}}$  and  $Z_{\text{SiC}}$ . The real and imaginary parts of impedance retrieved for graphene are presented in Fig. III-37.b.

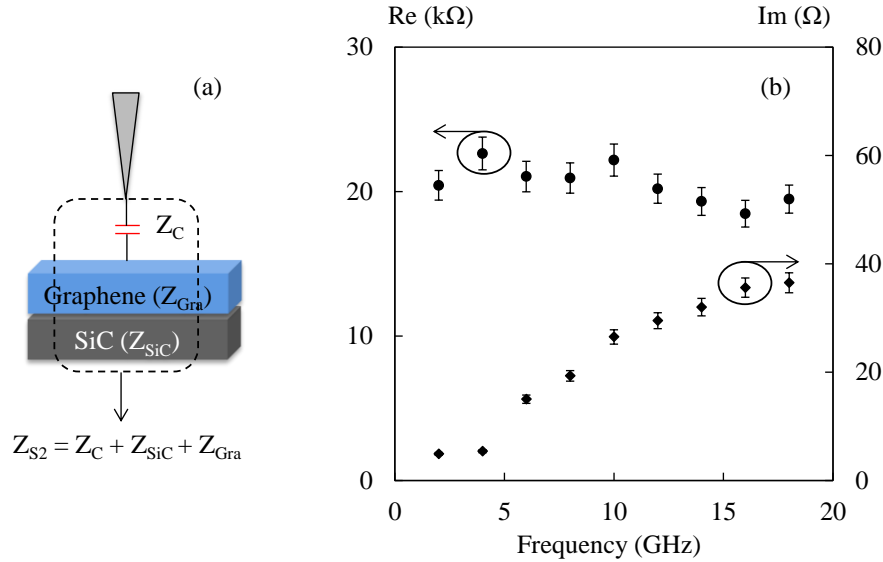


**Fig. III-37:** Modeling of the probe-SiCG interaction (a) and extracted complex impedance of graphene (b) as a function of frequency from 2 GHz to 18 GHz

As shown in Fig. III-37, the surface resistance of graphene is in the order of 20 kΩ from 2 GHz to 18 GHz. When compared the resistance obtained with the value measured by other approaches, we note that the resistance extracted by iNFMM is higher than the values obtained by dc probing and CPW methods, but corresponds to the values acquired by the SMM method ranging from tens to hundreds of kΩ [MON 13] [TAL 10] [KUN 09]. Actually, as a 2D material with a thickness in atomic scale, the graphene flake presents a dielectric behavior with low conductivity in the vertical direction [MON 12] [TSE 13]. This can explain the surface resistance measured by iNFMM. On the other hand, the imaginary part of the graphene impedance is also given in Fig. III-37. The reactance of the graphene is practically proportional to the frequency varying from 4.9 Ω to 36.5 Ω from 2 GHz to 18 GHz, which corresponds to an inductance about 360 pH. It is worth noting that these values extracted represent the local surface impedance of the graphene.

### III.4.5 Conclusion

In this section, a broadband non-destructive and non-contact characterization of epitaxial graphene is realized by using the iNFMM. Thanks to the interferometric technique, a high measurement sensitivity can be obtained at any desired operating frequency from 2 GHz to 18 GHz. The probe-sample interaction is numerically studied by using the electromagnetic simulation software, ANSYS/HFSS<sup>TM</sup>. Simulation results demonstrate a strong electromagnetic coupling between the probe tip and the sample, allowing a very local evaluation. Then, the measurement sensitivity is experimentally validated through the investigation of different samples including silicon carbide (SiC) used as a substrate, epitaxial graphene (SiCG), gold-metallized SiC (MSiC) and epitaxial graphene with Al<sub>2</sub>O<sub>3</sub> layer on the top (SiCGAlO). Furthermore, a high quality factor in air (53000) can be achieved, which is much higher than the platforms based on the transmission line and resonator methods. Finally, a calibration method is proposed to extract the complex impedance of a graphene flake grown on a silicon carbide substrate. Materials with known electrical properties are regarded as the calibrations standards. The graphene flake is characterized as a resistance (~20 k $\Omega$ ) and a small inductance (360 pH). The retrieved resistance is comparable with the values obtained by platforms such as AFM-based NFMM. The advantage of the proposed method is its non-contact and non-destructive features; there is no need to fabricate electrodes on the sample surface for the characterization. This work actually contributes to a preliminary study of the local characterization of graphene-based devices.

### **III.5 Conclusion**

In this chapter the usefulness of the home-made iNFMM for broadband local evaluations has been demonstrated. Examples of surface imaging and characterization of materials/structures are investigated to evaluate its performance. Indeed, rather than the limited frequency band offered by conventional microwave microscopes, the proposed interferometer-based platform enables a local analysis in a broad frequency band [2-18 GHz] with a high measurement sensitivity. Another benefit of the system is the capability to operate in different modes: contact, non-contact and immersion, which brings huge convenience to characterize various kinds of materials such as metals, dielectrics, semiconductors and liquids.

First, the 1D and 2D scanning lateral resolution is studied through a set of scanning parameters including the stand-off separation distance  $H$ , the scanning step size  $S$  and the probe apex size  $D$ . The scanning results show that, as expected, the set made of parameters with the minimum values available for the study ( $H=1\ \mu\text{m}$ ,  $S=1\ \mu\text{m}$  and  $D=66\ \mu\text{m}$ ) leads to the better lateral resolution. On the other hand, because of the applications targeted, we are not looking for an extremely high resolution but rather a sufficient one taking into account requirements such as scanning duration and robustness of the probe. Thus, some compromises for the scanning process are also discussed. The first one is between the scanning duration and the scanning quality. Actually, a sub-wavelength resolution of about  $\lambda_0/550$  is obtained at 2 GHz under the conditions  $H = 10\ \mu\text{m}$ ,  $D = 260\ \mu\text{m}$  and  $S = 50\ \mu\text{m}$  (scanning duration = 1 hour). This resolution can be further improved by refining the step but at the expense of a much longer imaging construction duration (i.e. 4 hours for  $S = 25\ \mu\text{m}$ ). There is also a hard compromise between the stand-off distance and the scanning quality. Instead of keeping  $1\ \mu\text{m}$  for stand-off distance like in 1D scanning, we prefer to fix this distance to  $10\ \mu\text{m}$  in 2D imaging process to avoid touching the device under test in case of a variation of the stand-off distance because of the undesirable tilt on the surface to be scanned or uniformities on the chip because of such a large-scale scanning ( $11 \times 8\ \text{mm}^2$ ).

After studying the lateral resolution of the iNFMM, a broadband characterization of liquid electrical properties is performed. Compared to the conventional microwave method for which the quality factor falls rapidly in the presence of the liquid, the

interferometric technique allows a high sensitivity in broadband frequency range. For the demonstration, a set of sodium chloride aqueous solutions is selected as the liquid under test. This choice is mainly motivated by the fact that it is a very commonly used sample to simulate the biological tissues. It is also very easy to obtain a large scale of NaCl concentrations. We give a fine description of the saline solutions dielectric properties as a function of both NaCl concentration [0-160 mg/ml] and frequency [2-18 GHz]. During the measurement, the probe is immersed in the liquid to avoid the water evaporation process at the liquid surface layer which can largely influence the air-liquid interface and the concentration of saline solutions. The complex permittivity of the saline concentration is extracted by two methods: the cavity perturbation and the transmission line methods. The experimental results based on both approaches agree well with the values theoretically retrieved by the Cole-Cole model.

The broadband investigation of iNFMM is also realized on the solid materials. As an example, epitaxial graphene, as a kind of 2D nanomaterial, is selected as the material under test. A calibration method is proposed to extract the complex impedance of a graphene flake grown on a silicon carbide substrate. The graphene flake is characterized as a resistance ( $\sim 20$  k $\Omega$ ) and a small inductance (360 pH). Compared to the other SMM method such as AFM-based NFMM which operates at a single frequency or in a limited frequency band (around 1 GHz), the platform proposed provides the impedance in a broad frequency range. The non-contact and non-destructive features of the method bring the advantage to not need the fabrication of electrodes on the sample surface for the characterization. This work actually contributes to a preliminary study of the local characterization of the graphene-based devices.

### III.6 References

(69 references, classified in alphabetical order)

- [AHM 12] Z. Ahmad, "Polymeric Dielectric Materials," *Dielectr. Mater.*, pp. 3–26, 2012.
- [ALA 11] J. Alaboson, Q. Wang, J. D. Emery, A. L. Lipson, M. J. Bedzyk, J. W. Elam, M. J. Pellin, and M. C. Hersam, "Seeding atomic layer deposition of high-k dielectrics on epitaxial graphene with organic self-assembled monolayers", *ACS nano*, vol.5, n<sup>o</sup>. 6, pp. 5223-5232, 2011.
- [ANL 07] S. M. Anlage, V. V. Talanov, and A. R. Schwartz, "Principles of near-field microwave microscopy," *Scanning Probe Microscopy: Electrical and Electromechanical Phenomena at the Nanoscale*, S. Kalinin and A. Gruverman, Eds. New York, Springer Sci., pp. 215 – 253, Aug. 2007.
- [AWA 16] S. A. Awan, A. Lombardo, A. Colli, G. Privitera, T. S. Kulmala, J. M. Kivioja, M. Koshino, and A. C. Ferrari, "Transport conductivity of graphene at RF and microwave frequencies," *2D Materials*, vol. 3, n<sup>o</sup>. 1 015010, 2016.
- [BAE 10] S. Bae, H. Kim, Y. Lee, X. Xu, J. Park, Y. Zheng, J. Balakrishnan, "Roll-to-roll production of 30-inch graphene films for transparent electrodes," *Nature nanotechnology*, vol.5, n<sup>o</sup>. 8, pp. 574-578, 2010.
- [BAK 14] H. Bakli, K. Haddadi, and T. Lasri, "Interferometric technique for scanning near-field microwave microscopy applications", *IEEE Trans. Instrum. Meas.*, vol. 63, n<sup>o</sup>. 5, pp. 1281–1286, 2014.
- [BAK 16] H. Bakli, K. Haddadi, and T. Lasri, "Modeling and Calibration in Near-Field Microwave Microscopy for Dielectric Constant and Loss Tangent Measurement", *IEEE Sensors Journal*, vol.16, n<sup>o</sup>.12, pp. 4667-4668, 2016.
- [BIA 16] M. C. Biagi, R. Fabregas, G. Gramse, M. Van Der Hofstadt, A. Juárez, F. Kienberger, L. Fumagalli, and G. Gomila, "Nanoscale Electric Permittivity of Single Bacterial Cells at Gigahertz Frequencies by Scanning Microwave Microscopy," *ACS Nano*, vol. 10, n<sup>o</sup>. 1, pp. 280–288, 2016.
- [CHA 15] A. Chahadih, P. Y. Cresson, Z. Hamouda, S. Gu, C. Mismar, and T. Lasri, "Microwave/microfluidic sensor fabricated on a flexible kapton substrate for complex permittivity characterization of liquids," *Sensors Actuators, A Phys.*, vol. 229, pp. 128–135, 2015.
- [DUR 66] E. Durand, *Electrostatique Tome II. Problèmes G é n é raux Conducteurs*. Masson, 1966.
- [FAB 11] S. Fabiani, D. Mencarelli, A. Di Donato, T. Monti, G. Venanzoni, A. Morini, T. Rozzi, and M. Farina, "Broadband Scanning Microwave Microscopy investigation of graphene", *Proc. IEEE MTT-S Int. Microw. Symp.*, Baltimore, MD, USA, pp. 1-4, June 2011.
- [FAR 12a] M. Farina, A. Di Donato, T. Monti, T. Pietrangelo, T. Da Ros, A. Turco, G. Venanzoni, and A. Morini, "Tomographic effects of near-field microwave microscopy in the investigation of muscle cells interacting with multi-walled carbon nanotubes," *Appl. Phys. Lett.*, vol. 101, n<sup>o</sup>. 20, 2012.
- [FAR 12b] M. Farina, A. Di Donato, D. Mencarelli, G. Venanzoni, and A. Morini, "High resolution scanning microwave microscopy for applications in liquid

- environment,” *IEEE Microw. Wirel. Components Lett.*, vol. 22, n<sup>o</sup>. 11, pp. 595–597, 2012.
- [FLO 14] J. M. Le Floch, C. Bradac, N. Nand, S. Castelletto, M. E. Tobar, and T. Volz, “Addressing a single spin in diamond with a macroscopic dielectric microwave cavity,” *Appl. Phys. Lett.*, vol. 105, pp. 133101, 2014.
- [GAO 98] C. Gao and X. Xiang, “Quantitative microwave near-field microscopy of dielectric properties,” *Rev. Sci. Instrum.*, vol. 69, n<sup>o</sup>. 11, pp. 3846–3849, 1998.
- [GAO 99] C. Gao, F. Duewer, X. Xiang, C. Gao, F. Duewer, and X. Xiang, “Quantitative microwave evanescent microscopy,” *Appl. Phys. Lett.*, vol. 75, n<sup>o</sup>. 19, pp. 3005, 1999.
- [GAO 04] C. Gao, B. Hu, P. Zhang, M. Huang, W. Liu, I. Takeuchi, “Quantitative microwave evanescent microscopy of dielectric thin films using a recursive image charge approach,” *Appl. Phys. Lett.*, vol. 84, n<sup>o</sup>. 23, pp. 4647–4649, 2004.
- [GOM 12a] D. Gomez, J. Sebastian, J. P. Carrier, P. Sharma, and A. Ionescu, “Non-contact characterization of graphene surface impedance at micro and millimeter waves”, *Jour. of Appl. Phys.*, vol.111, n<sup>o</sup>. 11 114908, 2012.
- [GOM 12b] D. Gomez, J. Sebastian, and J. Perruisseau-Carrier, “Microwave to THz properties of graphene and potential antenna applications”, In *Antennas and Propagation (ISAP), 2012 International Symposium*, pp. pp. 239-242, Nagoya, Japan, 2012.
- [GRA 14] G. Gramse, M. Kasper, L. Fumagalli, G. Gomila, P. Hinterdorfer, and F. Kienberger, “Calibrated complex impedance and permittivity measurements with scanning microwave microscopy.,” *Nanotechnology*, vol. 25, n<sup>o</sup>. 14, p. 145703, 2014.
- [GRE 16] A. P. Gregory, J. F. Blackburn, K. Lees, R. N. Clarke, T. E. Hodgetts, S. M. Hanham, and N. Klein, “Measurement of the permittivity and loss of high-loss materials using a Near-Field Scanning Microwave Microscope,” *Ultramicroscopy*, vol. 161, pp. 137–145, 2016.
- [GU 15a] S. Gu, K. Haddadi, A. El Fellahi, G. Dambrine and T. Lasri, “Measurement Accuracy and Repeatability in Near-Field Scanning Microwave Microscopy”, *International Instrumentation and Measurement Technology Conference (I<sup>2</sup>MTC)*, Pisa, Italy, May 2015
- [GU 15b] S. Gu, K. Haddadi, A. El Fellahi, and T. Lasri, “Near-field scanning microwave microscope for subsurface non-destructive characterization,” *European Microwave Conference (EuMC)*, Paris, France, pp. 155-158, Sept. 2015
- [GU 16a] S. Gu, K. Haddadi, A. El Fellahi and T. Lasri, “Setting Parameters Influence on Accuracy and Stability of Near-Field Scanning Microwave Microscopy Platform”, *IEEE Trans. Instrum. Meas.*, vol. 65, n<sup>o</sup>. 4, pp. 890–897, 2016.
- [GU 16b] S. Gu, T. Lin and T. Lasri, “Broadband dielectric characterization of aqueous saline solutions by an interferometer-based microwave microscope”, *Appl. Phys. Lett.*, vol. 108, 242903, 2016.
- [GU 16c] S. Gu, T. Lin, K. Haddadi and T. Lasri, “Saline Solutions Characterization by Near-field Microwave Microscopy”, *International Conference on*

- Electromagnetic Wave Interaction with Water and Moist Substances (ISEMA), pp.51-57, Florence, Italy, May, 2016.
- [GUI 11] J. P. Guillet, L. Chusseau, R. Adam, T. Grosjean, A. Penarier, F. Baida, and D. Charraut, "Continuous-wave scanning terahertz near-field microscope," *Microwave Opt. Technol. Lett.* vol. 53, pp. 580–582, 2011.
- [HAB 10] M. Habibi, D. P. Klemer, and V. Raicu, "Two-dimensional dielectric spectroscopy: Implementation and validation of a scanning open-ended coaxial probe," *Rev. Sci. Instrum.*, vol. 81, n° 7, 2010.
- [HAD 11] K. Haddadi, D. Glay, et T. Lasri, "A 60 Ghz Scanning Near-Field Microscope With High Spatial Resolution Sub-Surface Imaging", *IEEE Microw. Wireless Compon. Lett.*, vol. 21, n° 11, pp.625-627, Nov. 2011.
- [HAD 12a] K. Haddadi et T. Lasri, "60-GHz Near-Field Six-Port Microscope Using a Scanning Slit Probe for Subsurface Sensing", *IEEE Sensors Jour.*, vol. 12, n° 8, pp. 2575-2576, Aug. 2012.
- [HAD 12b] K. Haddadi, H. Bakli, and T. Lasri, "Microwave liquid sensing based on interferometry," *IEEE Microw. Wireless Compon. Lett.*, vol. 22, n° 10, pp. 542–544, 2012.
- [HAD 15] K. Haddadi, S. Gu, and T. Lasri, "Sensing of liquid droplets with a scanning near-field microwave microscope," *Sensors Actuators, A Phys.*, vol. 230, pp. 170–174, 2015.
- [HUB 10] H. P. Huber, M. Moertelmaier, T. M. Wallis, C. J. Chiang, M. Hochleitner, A. Imtiaz, Y. J. Oh, K. Schilcher, M. Dieudonne, J. Smoliner, P. Hinterdorfer, S. J. Rosner, H. Tanbakuchi, P. Kabos, and F. Kienberger, "Calibrated nanoscale capacitance measurements using a scanning microwave microscope," *Rev. Sci. Instrum.*, vol. 81, n° 11, 2010.
- [HUD 98] S. Hudlet, M. Saint Jean, C. Guthmann, and J. Berger, "Evaluation of the capacitive force between an atomic force microscopy tip and a metallic surface," *Eur. Phys. J. B*, vol. 10, n° 1, pp. 5–10, 1998.
- [IMT 07] A. Imtiaz, T. Baldwin, H. T. Nembach, T. M. Wallis, and P. Kabos, "Near-field microwave microscope measurements to characterize bulk material properties", *Appl. Phys. Lett.* vol. 90, 243105, 2007.
- [JAR 13] D. Jariwala , V. K. Sangwan, L. J. Lauhon, T. J. Marks, and M. C. Hersam, "Carbon nanomaterials for electronics, optoelectronics, photovoltaics, and sensing," *Chem. Soc. Rev.* vol. 42, n° 7, pp. 2824-2860, 2013.
- [JEO 09] D. Jeon, K. J. Lee, M. Kim, D. C. Kim, H. Chung, Y. Woo, and S. Seo, "Radio-frequency electrical characteristics of single layer graphene," *Japan. Jour. Appl. Phys.*, vol. 48, n° 9R, 091601, 2009.
- [KAN 03] R. Kantor, and I. V. Shvets. "Method of increasing spatial resolution of the scanning near-field microwave microscopy." *Jour. Appl. Phys.* Vol. 93, n° 9, pp.4979-4985, 2003.
- [KHA 07] S. Kharkovsky and R. Zoughi, "Microwave and millimeter wave nondestructive testing and evaluation – overview and recent advances", *IEEE Instrum. Meas.*, vol. 10, n° 5, pp. 26-38, 2007.

- [KLE 06] R. A. Kleismit, M. K. Kazimierczuk and G. Kozlowski. "Sensitivity and resolution of evanescent microwave microscope." *IEEE trans. Microwave theo. Tech.* vol. 54, n<sup>o</sup>. 2, pp. 639-647, 2006.
- [KUN 09] W. Kundhikanjana, K. Lai, H. Wang, H. Dai, M. A. Kelly, and Z. X. Shen, "Hierarchy of electronic properties of chemically derived and pristine graphene probed by microwave imaging," *Nano Lett.*, vol. 9, n<sup>o</sup>. 11, pp. 3762–3765, 2009.
- [LAI 09] K. Lai, W. Kundhikanjana, H. Peng, Y. Cui, M. A. Kelly, and Z. X. Shen, "Tapping mode microwave impedance microscopy," *Rev. Sci. Instrum.*, vol. 80, n<sup>o</sup>. 4, p. 043707, 2009.
- [LU 97] Y. Lu, T. Wei, F. Duerwer, Y. Lu, N. Ben Ming, P. G. Schultz, and X. D. Xiang, "Nondestructive Imaging of Dielectric-Constant Profiles and Ferroelectric Domains with a Scanning-Tip Microwave Near-Field Microscope," *Science*, vol. 276, n<sup>o</sup>. 5321, pp. 2004–2006, 1997.
- [MOE 14] M. Moertelmaier, H. P. Huber, C. Rankl, and F. Kienberger, "Continuous capacitance-voltage spectroscopy mapping for scanning microwave microscopy," *Ultramicroscopy*, vol. 136, pp. 67–72, 2014.
- [MON 12] T. Monti, A. Di Donato, and M. Farina, "High resolution imaging of few-layer graphene by near-field scanning microwave microscopy", In *Silicon Monolithic Integrated Circuits in RF Systems (SiRF)*, 2012 IEEE 12th Topical Meeting, pp. 109-112. Santa Clara, CA, USA, Jan, 2012.
- [MON 13] T. Monti, A. Di Donato, D. Mencarelli, G. Venanzoni, A. Morini, and M. Farina, "Near-field microwave investigation of electrical properties of graphene-ITO electrodes for LED applications", *Journal of Display Technology*, vol.9, n<sup>o</sup>. 6, pp. 504-510, 2013.
- [NOV 12] K. S. Novoselov, V. I. Fal, L. Colombo, P. R. Gellert, M. G. Schwab, and K. Kim, "A roadmap for graphene," *Nature*, vol.490, n<sup>o</sup> 7419, pp. 192-200, 2012.
- [OMA 15a] R. Omarouayache, P. Payet, J. Raoult, and L. Chusseau, "Millimeter-wave near-field imaging with bow-tie antennas", *Optics express*, vol. 23, n<sup>o</sup>. 9, pp.12144-12151, 2015
- [OMA 15b] R. Omarouayache, L. Chusseau, P. Payet, J. Raoult, and S. Jarrix, "60 GHz active microscopy with a bow-tie antenna as near-field probe," *IEEE International Instrumentation and Measurement Technology Conference, (I<sup>2</sup>MTC)* pp. 1189-1193, Pisa, Italy, 2015.
- [PAT 70] L. Patrick, and W. J. Choyke, "Static dielectric constant of SiC," *Physical Review B*, vol. 2, n<sup>o</sup>. 6, pp. 2255-2256, 1970.
- [PEY 07] A. Peyman, C. Gabriel, and E. H. Grant, "Complex permittivity of sodium chloride solutions at microwave frequencies," *Bioelectromagnetics*, vol. 28, n<sup>o</sup>. 4, pp. 264–274, 2007.
- [SCH 10] F. Schwierz, "Graphene transistors," *Nature nanotechnology*, v1o.5, n<sup>o</sup>. 7, pp. 487-496, 2010.
- [SHI 15] K. Shiraga, T. Suzuki, N. Kondo, T. Tajima, M. Nakamura, H. Togo, A. Hirata, K. Ajito, and Y. Ogawa, "Broadband dielectric spectroscopy of glucose aqueous solution: Analysis of the hydration state and the hydrogen bond network," *J. Chem. Phys.*, vol. 142, pp. 234504, 2015.

- [STE 98] D. E. Steinhauer, C. P. Vlahacos, S. K. Dutta, B. J. Feenstra, F. C. Wellstood, and S. M. Anlage, "Quantitative imaging of sheet resistance with a scanning near-field microwave microscope," *Appl. Phys. Lett.*, vol. 72, n<sup>o</sup>. 7, pp. 861–863, 1998
- [STO 07] M. R. Stoneman, M. Kosempa, W. D. Gregory, C. W. Gregory, J. J. Marx, W. Mikkelson, J. Tjoe, and V. Raicu, "Correction of electrode polarization contributions to the dielectric properties of normal and cancerous breast tissues at audio/radiofrequencies," *Phys. Med. Biol.*, vol. 52, pp. 6589–6604, 2007.
- [SUN 14] W. Sun, Y. Yang, Z. Wu, T. Feng, Q. Zhuang, L. M. Peng, S. Xu, and C. K. Ong, "Penetrative imaging of sub-surface microstructures with a near-field microwave microscope," *J. Appl. Phys.*, vol. 116, n<sup>o</sup>. 4, 2014.
- [TAB 99] M. Tabib-Azar, D.-P. Su, A. Pohar, S. R. LeClair, and G. Ponchak, "0.4  $\mu\text{m}$  spatial resolution with 1 GHz ( $\lambda=30\text{cm}$ ) evanescent microwave probe," *Rev. Sci. Instrum.*, vol. 70, n<sup>o</sup>. 3, pp. 1725–1729, 1999.
- [TAB 00] M. Tabib-Azar and S. R. Leclair, "Applications of evanescent microwave probes in gas and chemical sensors," *Sensors Actuators, B Chem.*, vol. 67, n<sup>o</sup>. 1, pp. 112–121, 2000.
- [TAL 09] V.V. Talanov and A.R. Schwartz, "Near-field scanning microwave microscope for interline capacitance characterization of nanoelectronics interconnect", *IEEE Trans. Microw. Theory Tech.*, vol. 57, n<sup>o</sup>. 5, pp. 1224-1229, May 2009.
- [TAL 10] V. V Talanov, C. Del Barga, L. Wickey, I. Kalichava, E. Gonzales, E. A. Shaner, A. V Gin, and N. G. Kalugin, "Few-Layer Graphene Characterization by Near-Field Scanning Microwave Microscopy," *ACS Nano*, vol. 4, n<sup>o</sup>. 7, pp. 3831–3838, 2010.
- [TAM 12] M., J. S. Tamagnone, D. Gomez, J. R. Mosig, and J. Perruisseau-Carrier. "Analysis and design of terahertz antennas based on plasmonic resonant graphene sheets", *Jour. Appl. Phys.* vol.112, n<sup>o</sup>. 11, 114915, 2012.
- [TSE 07] A. Tselev, S. M. Anlage, Z. Ma, and J. Melngailis, "Broadband dielectric microwave microscopy on micron length scales," *Rev. Sci. Instrum.*, vol. 78, n<sup>o</sup>. 4, 2007.
- [TSE 12] A. Tselev, N. V. Lavrik, I. Vlassiouk, D. P. Briggs, M. Rutgers, R. Proksch, and S. V. Kalinin, "Near-field microwave scanning probe imaging of conductivity inhomogeneities in CVD graphene," *Nanotechnology*, vol. 23, n<sup>o</sup>. 38, 385706, 2012
- [TSE 13] A. Tselev, V. K. Sangwan, D. Jariwala, T. J. Marks, L. J. Lauhon, M. C. Hersam, and S. V. Kalinin, "Near-field microwave microscopy of high- $\kappa$  oxides grown on graphene with an organic seeding layer", *Appl. Phys. Lett.* vol.103, n<sup>o</sup>. 24, 243105, 2013.
- [TSE 16] A. Tselev, J. Velmurugan, A. V. Ievlev, S. V. Kalinin, and A. Kolmakov, "Seeing through Walls at the Nanoscale: Microwave Microscopy of Enclosed Objects and Processes in Liquids," *ACS Nano*, vol. 10, n<sup>o</sup>. 3, pp. 3562–3570, 2016.
- [TUC 16] S. S. Tuca, G. Badino, G. Gramse, E. Brinciotti, M. Kasper, Y. J. Oh, R. Zhu, C. Rankl, P. Hinterdorfer, and F. Kienberger, "Calibrated complex impedance of CHO cells and *E. coli* bacteria at GHz frequencies using scanning microwave microscopy," *Nanotechnology*, vol. 27, n<sup>o</sup>. 13, p. 135702, 2016.

- [WEB 12] J. C. Weber, J. B. Schlager, N. A. Sanford, A. Imtiaz, T. M. Wallis, L. M. Mansfield, K. J. Coakley, K. A. Bertness, P. Kabos, and V. M. Bright, "A near-field scanning microwave microscope for characterization of inhomogeneous photovoltaics," *Rev. Sci. Instrum.*, vol. 83, n<sup>o</sup>. 8, 2012.
- [WEI 15] W. Wei, X. Zhou, G. Deokar, H. Kim, M. Moez Belhaj, E. Galopin, E. Pallecchi, D. Vignaud, and H. Happy, "Graphene FETs With Aluminum Bottom-Gate Electrodes and Its Natural Oxide as Dielectrics", *IEEE Trans. Electron Devices*, vol.62, n<sup>o</sup>. 9, pp. 2769-2773, 2015.
- [WEI 16] W. Wei, E. Pallecchi, S. Haque, S. Borini, V. Avramovic, A. Centeno, Z. Amaia, and H. Happy, "Mechanically robust 39 GHz cut-off frequency graphene field effect transistors on flexible substrates." *Nanoscale*, vol. 8, n<sup>o</sup>. 29, pp. 14097-14103, 2016.

## **General conclusion and perspectives**

In this thesis, a home-made near-field microwave microscope is described, analyzed in terms of resolution performance and frequency band of operation, and applied to the characterization of a large variety of materials such as metals, semiconductors, dielectrics, liquids and 2D nanomaterials. An interferometric technique is implemented in the near-field microwave microscope (NFMM) to match the high-impedance of the microwave probe with the  $50 \Omega$  characteristic impedance of the vector network analyzer (VNA). This solution permits to enhance the measurement sensitivity in a great extent. Furthermore, the evanescent microwave probe enables a very local characterization of materials with the sub-wavelength spatial resolution. The features of the proposed interferometer-based near-field microwave microscope (iNFMM) are summarized in three parts: the description of the platform, the measurement performance, and the possible applications.

Concerning the platform description, generally speaking, the microwave microscope is made of microwave and mechanical parts. The microwave part consists of a VNA, a coupler, an evanescent microwave probe (EMP) and an impedance tuner including a delay line and a motorized attenuator. On the other hand, as regards to the mechanical part, the platform is built on a motorized x-y-z stage (25 cm in x/y axis and 1 cm in z axis) with a minimum increment step in the three directions of  $1 \mu\text{m}$ , which actually is largely sufficient for the scanning applications targeted. One can also note that the sample is placed on the chuck fixed on the stage whereas the microwave part of the microscope remains fixed during the scans. Consequently, a better stability is obtained by moving the sample on the stage instead of moving the probe. Additionally, different operating is available including contact, non-contact, liquid environment modes.

The measurement performance of the whole platform is carefully evaluated through two main points: system repeatability and lateral spatial resolution. In the repeatability analysis of the iNFMM, we find the setting parameters (zero level, intermediate frequency bandwidth / IFBW and acquisition time) have a great influence on the measurement accuracy and stability. Generally speaking, the key parameters can be set to: zero level = -50 dB and IFBW = 100 Hz for both short-term

and long-term measurements. Considering the optimal setting parameters, it is demonstrated that for characterizations involving a fixed stage, the error is less than 3 %, while the error measured for applications requiring displacement (1D and 2D scanning) is less than 6 % in case of a 2-hour measurement, which is long enough for the applications targeted. As a second important feature, the performance of the iNFMM is also demonstrated by investigating the lateral resolution for 1D and 2D scanning processes. We study the influence of the scanning parameters including the tip-sample distance  $H$ , the scanning step size  $S$  and the probe apex  $D$  on the scanning lateral resolution. In this study we are interested in materials which size is larger than  $1000 \times 1000 \mu\text{m}^2$ . For the application targeted (e.g. quality inspection of microelectronics circuits), we are not looking for very high spatial resolution but rather a sufficient one taking into account requirements such as a suitable scanning stand-off distance, a short image construction duration and the robustness of the probe. Hence, we fix the stand-off distance to  $10 \mu\text{m}$  in 2D imaging process to avoid touching the device under test in case of a variation of the stand-off distance because of an undesirable tilt on the surface to be scanned or the presence of uniformities. Concerning the step size, for 1D scanning, the duration is not an issue because the data acquisition process last less than several minutes even with  $S = 1 \mu\text{m}$  (scanning speed  $\sim 300$  pixels/minutes). However, for 2D scanning whose duration usually accounts for several hours, a compromise between the step size and scanning duration has to be found. For the sake of robustness of the probe tip, one can note that the probes are selected with apex of tens and hundreds of microns (i.e.  $66$  and  $260 \mu\text{m}$ ) to avoid a too frequent impairment of the tip during the scanning experiments. The imaging resolution obtained is  $250 \mu\text{m}$  corresponding to about  $\lambda_0/550$  at  $2 \text{ GHz}$  under the conditions ( $H = 10 \mu\text{m}$ ,  $S = 50 \mu\text{m}$ , duration = 1 hour and  $D = 260 \mu\text{m}$ ), knowing that his value can be easily enhancement by refining the microwave probe tip size. Additionally, the scanning quality can still be enhanced by a simple signal processing method which is based on the complex difference between the scanning results collected for two different heights. As a result the background noise is effectively lowered.

After the performance evaluation of the iNFMM, we demonstrate in a final step the capability of the system in terms of possible applications from the characterization of various materials as different as metals, semiconductors, dielectrics, liquids and 2D

nanomaterials. Indeed, one of the benefits offered by the platform is that the zero level can be tuned as a function of the material under test. Another advantage brought by the system is the possibility to operate at any frequency in [2-18 GHz]. In fact, unlike many other NFMMs, in our case, the platform operates in a quasi-continuous band from 2 to 18 GHz opening the way to broadband characterizations. This feature actually establishes our iNFMM as a very efficient tool to investigate the frequency-dependent behavior of the materials properties. Additionally, the operating frequency range depends only on the limitations imposed by the characteristics of the microwave components in the system. Thus, characterization solutions can be provided at higher frequencies. Finally, the iNFMM demonstrates its ability in the extraction of the local electromagnetic properties of materials. When electromagnetic properties are aimed two widely used quantification methods which are cavity perturbation and transmission line methods are applied to translate the measured data (transmission coefficient) to the parameters of interest. It is worth mentioning that the electromagnetic properties for different kinds of materials have been successfully evaluated by using this instrument associated to these two quantification methods. In particular in case of liquids, the dielectric properties measured using both methods corresponds well to the values calculated by means of the Cole-Cole model. In case of the evaluation of graphene fabricated by epitaxial method, the surface impedance extracted by the transmission method has been found to be comparable to the values obtained by platforms such as AFM-based NFMM. Furthermore, it is important to note that there is no need to fabricate electrodes on the material under test, which protects the sample from the influence brought by the electrodes.

As a conclusion, the interferometer-based near-field microwave microscope is able to locally characterize the materials/structures in a broad frequency range with high measurement sensitivity. It provides a quantitative analysis of material properties to address cost-effective and non-destructive applications in many scientific fields.

Following this study a few research work directions have been identified.

First, concerning the instrumentation, the penetration of such tools in the industrial field can be considered if cost-effective, compact and easy to use systems are developed. In the industrial field, instead of an ultra-high sensitive instrument with noise floor better than -100 dB provided by the VNA, a solution with a lower sensitivity (i.e. noise floor around -60 dB) could be sufficient for applications considering the performance-cost aspect. For example, the six-port network analyzer could be a possible solution to meet the needs of high frequency characterization tools beyond the scope of laboratory use. Always from the instrumental point of view, to meet the current need for microwave characterization tools with high sensitivity and nanometric resolution, novel tip structures need to be designed for increasing signal-to-noise ratio and improving spatial resolution. For example, there are probe structures such as the miniaturized coplanar ground-signal-ground (GSG) waveguide probe fabricated on silicon-on-insulator (SOI) technology. On the other hand, a NFMM based on a multi-probe configuration is also of great interest for material characterizations. For example, one can think about a transmission-mode NFMM for the acquisition of both the reflection and transmission properties of the DUT. With the availability of such a measurement equipment, a solution integrating multiple emission-reception probes would have the possibility to offer an efficient, highly sensitive local characterization for the mass-production micro-/nano-electronics. In this case, probing algorithms need to be defined. Some ideas from the multiple-input and multiple-out (MIMO) technique in the telecommunication domain could be of great help.

Second, some investigations can be conducted for the non-contact, non-destructive local characterization of other materials for which only little information are available in the frequency range covered by the iNFMM. The potentials brought by the platform make it a good candidate of analyzing the novel materials for engineering and manufacturing applications. Possible directions are characterization of materials such as carbon-based materials, ferromagnetic materials, ferroelectric materials, and life-science materials (biological fluids and tissues) for example.

Finally, the microwave microscope enables sub-surface imaging which contains both the topography and the buried structures information of the samples. A challenge

in this kind of applications is the topographic influence inevitably appearing in microwave images during the scanning process. Indeed, topography-induced signals are convolved into the results, which makes it difficult to extract the electrical properties of the sample. Therefore, it is important to develop techniques which enable to remove topographic impact from microwave images to extract the electrical properties. Furthermore, many materials/devices are not simple bulk structures but are rather multilayered. This requires studies to describe the electromagnetic interaction between the tip and the stratified media. This can be done by using simulation tools like ANSYS<sup>TM</sup>/HFSS for example, or by developing dedicated theoretical models.



## **List of publications**

### **Journal:**

**S. Gu**, T. Lin and T. Lasri, “Dielectric properties characterization of saline solutions by near-field microwave microscopy”, *Meas. Sci. Technol.* vol. 28, 014014, 2017.

**S. Gu**, T. Lin and T. Lasri, “Broadband dielectric characterization of aqueous saline solutions by an interferometer-based microwave microscope”, *Appl. Phys. Lett.* vol. 108, 242903, 2016.

**S. Gu**, K. Haddadi, A. El Fellahi and T. Lasri, “Setting Parameters Influence on Accuracy and Stability of Near-Field Scanning Microwave Microscopy Platform”, *IEEE Trans. Instrum. Meas.*, vol. 65, n<sup>o</sup>. 4, pp. 890–897, 2016.

K. Haddadi, **S. Gu** and T. Lasri, “Sensing of liquid droplets with a scanning near-field microwave microscope”, *Sensors and Actuators A: Physical*, vol. 230, pp. 170-174, 2015.

A. Chahadih, P. Y. Cresson, Z. Hamouda, **S. Gu**, C. Mismar and T. Lasri, “Microwave/microfluidic sensor fabricated on a flexible kapton substrate for complex permittivity characterization of liquids”, *Sensors and Actuators A: Physical*, vol. 229, pp. 128-135, 2015.

### **International conference:**

**S. Gu**, T. Lin and T. Lasri, “Spatial resolution enhancement of near field microwave microscope”, 46<sup>th</sup> European Microwave Conference (EuMC), London, UK, Oct. 2016.

**S. Gu**, T. Lin and T. Lasri, “Materials Characterization by Near-field Scanning Microwave Microscopy”, 37<sup>th</sup> Progress in Electromagnetics Research Symposium (PIERS), pp. 1474-1475, Shanghai, China, Aug. 2016.

**S. Gu**, T. Lin, K. Haddadi and T. Lasri, “Saline Solutions Characterization by Near-field Microwave Microscopy”, International Conference on Electromagnetic Wave Interaction with Water and Moist Substances (ISEMA), pp.51-57, Florence, Italy, May, 2016.

**S. Gu**, K. Haddadi, A. El Fellahi and T. Lasri, “Near-field scanning microwave microscope for subsurface non-destructive characterization”, 45<sup>th</sup> European Microwave Conference (EuMC), pp. 155-158, Paris, France, Sept. 2015.

**S. Gu**, K. Haddadi, A. El Fellahi, G. Dambrine and T. Lasri, “Measurement Accuracy and Repeatability in Near-Field Scanning Microwave Microscopy”, International Instrumentation and Measurement Technology Conference (I<sup>2</sup>MTC), pp. 1735-1740, Pisa, Italy, May 2015.

**S. Gu**, K. Haddadi, and T. Lasri, “Near-field microwave microscopy for liquid characterization”, 44<sup>th</sup> European Microwave Conference (EuMC), pp. 628-631, Rome, Italy, Oct. 2014.

K. Haddadi, J. Marzouk, **S. Gu**, S. Arscott, G. Dambrine and T. Lasri, “Interferometric Near-field Microwave Microscopy Platform for Electromagnetic Micro-analysis”, 28<sup>th</sup> Eurosensors Conference, Procedia Engineering, vol. 87, pp. 388-391, Brescia, Italy, sept. 7-10, 2014.

### **National conference:**

T. Lin, **S. Gu**, and T. Lasri, “Conception et simulation d’un réflectomètre six-port ultra large bande”, 19<sup>èmes</sup> Journées Nationales du Réseau Doctoral en Micro-Nano électronique (JNRDM), Bordeaux, France, May 2016.

**S. Gu**, K. Haddadi and T. Lasri, “Contrôle non destructif par microscopie micro-ondes en champ proche”, 18<sup>èmes</sup> Journées Nationales du Réseau Doctoral en Micro-Nano électronique (JNRDM), Bordeaux, France, May 2015.

**S. Gu**, K. Haddadi, and T. Lasri, “Microscopie champ proche micro-ondes pour la caractérisation de liquides”, 17<sup>èmes</sup> Journées Nationales du Réseau Doctoral en Micro-Nano électronique (JNRDM), Villeneuve d'Ascq, France, May 2014.





---

## ABSTRACT

Near-field microwave microscopes are emerging instruments for materials characterization. In this work, a home-made near-field microwave microscope is first described and analyzed in terms of resolution performance and frequency band of operation. Then, it is applied to the characterization of a large variety of materials such as metals, semiconductors, dielectrics, liquids and 2D nanomaterials. The system is based on an interferometric technique to improve the measurement sensitivity in the entire frequency range of operation spanning from 2 to 18 GHz. The sensitivity and the different operating modes available (contact, non-contact, liquid environment) allow addressing a large variety of application fields.

The instrument allows a sub-wavelength lateral resolution which is more than two orders of magnitude smaller than the operating wavelength, opening the way to a local characterization. The cavity perturbation and transmission line approaches have been used to extract the electromagnetic properties of materials. In particular dielectric properties of saline aqueous solutions and complex impedance of graphene have been investigated in a broad frequency band. It provides a quantitative analysis of material properties in a non-destructive manner to address numerous applications in many scientific fields. Finally, all the results together show that the interferometer-based near-field microwave microscope has the potential to become an important metrology tool for characterizations in micro- and nano-electronics.

**Key words:** near-field microwave microscopy, evanescent microwave, interferometry, non-contact, non-destructive local characterization, aqueous saline solutions, 2D materials

## TITLE IN FRENCH:

### CONTRIBUTION A LA CARACTERISATION LOCALE DE MATERIAUX, EN LARGE BANDE, PAR MICROSCOPIE CHAMP PROCHE MICRO-ONDE

## RESUME

Les microscopes champ proche micro-ondes sont des instruments émergents pour la caractérisation de matériaux. Dans ce travail, un microscope champ proche micro-ondes fait maison est d'abord décrit et analysé en termes de résolution et de largeur de bande de fréquences de fonctionnement. Ensuite, il est mis en œuvre pour la caractérisation d'une grande variété de matériaux tels que par exemple des métaux, des semi-conducteurs, des diélectriques, des liquides et des nanomatériaux 2D. Le système intègre un interféromètre pour améliorer la sensibilité de la mesure pour des fréquences de fonctionnement couvrant la bande 2-18 GHz. La sensibilité et les différents modes de fonctionnement disponibles (contact, sans contact, environnement liquide) permettent d'adresser une grande variété de domaines d'applications.

La résolution latérale obtenue par cet instrument est plus petite de plusieurs ordres de grandeur que la longueur d'onde de fonctionnement, ouvrant ainsi la voie à une caractérisation locale. Les propriétés électromagnétiques des matériaux ont été extraites en utilisant la méthode de perturbation et celle de la ligne de transmission. En particulier, les propriétés diélectriques de solutions salines aqueuses et l'impédance complexe du graphène ont été étudiées dans une large bande de fréquence. Ce microscope champ proche micro-ondes basé sur une méthode interférométrique qui permet une analyse quantitative des propriétés des matériaux de manière non-destructive peut adresser un grand éventail d'applications dans de nombreux domaines scientifiques. Enfin, l'ensemble des résultats montre que potentiellement la microscopie champ proche micro-ondes dispose des atouts pour devenir un outil de métrologie important pour la caractérisation en micro- et nano-électronique.

**Mots clés:** microscopie champ proche micro-ondes, ondes évanescentes, interférométrie, caractérisation locale non destructive, sans contact, solutions salines aqueuses, matériaux 2D